Computational Modelling of Polyoxometalates: Progress on Accurate NMR Characterization and Reactivity

Magda Pascual Borràs

Magda Pascual Borràs

Computational Modelling of Polyoxometalates: Progress on Accurate NMR Characterization and Reactivity

PhD Thesis

Supervised by
Dr. Xavier López Fernández and Dr. Antonio Rodríguez Fortea

Departament de Química Física i Inorgànica
Grup de Química Quàntica

UNIVERSITAT ROVIRA i VIRGILI

Tarragona 2017

UNIVERSITAT ROVIRA I VIRGILI

Departament de Química Física i Inorgànica

Xavier López Fernández, Professor Agregat del Departament de Química Física i Inorgànica de la Universitat Rovira i Virgili, i Antonio Rodríguez Fortea, Professor Agregat del Departament de Química Física i Inorgànica de la Universitat Rovira i Virgili.

FEM CONSTAR QUE aquest treball, titulat

"Computational Modelling of Polyoxometalates: Progress on Accurate NMR Characterization and Reactivity"

que presenta Magda Pascual Borràs per a l'obtenció del títol de Doctor, ha estat realitzada sota la nostra direcció al Departament de Química Física i Inorgànica d'aquesta universitat i que acompleix els requeriments per poder optar a la Menció Internacional.

Tarragona, 3 de Març del 2017

Els directors de la tesi doctoral

Xavier López Fernández

Antonio Rodríguez Fortea

Acknowledgments

Després de cinc anys al grup de Química Quàntica, començo a escriure aquestes paraules, crec que les més difícils d'escriure de tota la tesi. Com en totes les coses hi han hagut moments bons i dolents, o si més no, difícils i amb molts entrebancs, però aquí no us vull fotre el *rotllo* dels problemes que et trobes quan realitzes una tesi, sí que vull remarcar els bons moments que he passat durant tots aquests anys, de les persones que he conegut i m'han recolzat i ajudat a fer front a aquestes 180 i pico pàgines que teniu per endavant!

Primer de tot, agrair als meus directors, els quals de manera oficial en són dos però realment n'han sigut tres: Josep Mª Poblet, Xavi López i Toni Rodríguez. Gràcies als tres per confiar en mi i deixar-me *parir* aquest treball. Crec que tot el que està aquí escrit no hi seria si no és per les vostres idees i consells, i a vegades, també petites bronques que m'han fet reaccionar per seguir endavant. Poblet, ja sé que sempre em dius que sóc molt negativa, però potser de tan que m'ho has dit, ara ja, a vegades, sé veure la part positiva de les coses. Xavi, ens hem topat amb molts entrebancs! Però crec que al final ha sortit un bon treball, si més no, jo n'estic orgullosa, gràcies! Toni, només hem treballat junts en una part de la tesi, però m'has ajudat molt i aportat bones idees, és molt fàcil tenir-te com a *jefe*.

Als altres membres sèniors del grup: Jordi, Rosa, Mar, Anna, Coen, Gerard gràcies per les bones estones de cafè, dinars, sopars, excursions... i també perquè sempre heu estat allà quan m'ha sorgit un dubte o un problema per tal de solucionar-lo. Als nostres informàtics: José, Elisenda i Moisès, els quals sense ells al grup li faltaria un pilar molt important. Gràcies per ajudar-me en tot el que he necessitat aquests anys!

Vaig arribar un bon dia al despatx 201 i em van posar en aquella taula petita (no tenia L!) i em van dir "Au, llegeix!", però súper ràpid em vaig adonar que dins el grup hi havia súper bon rotllo i gràcies a això em vaig adaptar molt ràpid. Què dir-vos! Jess, ja saps que ens assemblem molt i que hi ha coses que només tu i jo sabem, com per exemple, que parlar-nos pel matí és arriscar-se molt! Has sigut un pilar súper important durant els primers anys de la tesi, i estic súper contenta que ara, després de dos anys, encara no haguem perdut el contacte. Gràcies per les nostres estones de pitis, de rallades, de tes a les 6 de la tarda... ja saps que et trobo a faltar! Nuri, gràcies a tu vaig aprendre tantes coses, des de saber que és un RGB fins a quin és el color de moda de la temporada! jaja Ets increïble i t'admiro moltíssim. Gràcies per tots els consells i tot el que m'has ensenyat durant aquests anys. Xavi!!! M'has fet riure tant!!! M'encanta el bon rotllo que transmets i evidentment les teves imitacions, ets un crack! Trobo a faltar les estones de cafè que passàvem tots junts! Pablo A., como tu dices, siempre nos quedará París! Que buen equipo de POMs hicimos i que buenos ratos pasamos, era

tan facil explicarte cualquier cosa. Pablo J., espero que des de que te'n vas anar ningú t'hagi fet sortir sang del nas i ja saps que ets el nostre socorrista preferit. Marc M., quines bones esquiades que vam fer, espero que vagi súper bé per USA. Ximo, l'híbrid del grup, quins bons congressos que hem compartit, això sí, cap supera el de Lanzarote. Gian, echamos de menos tu locura italiana! I no oblidar-me dels meus companys de màster: Sergi! Quines bones farres ens hem fotut! Admiro el teu bon rotllo i *glamour* des de les 8 del matí. Gerard, gràcies per aguantar-me cada dia pel matí al tren mentre fèiem el màster, crec que és un bon mèrit.

Als d'ara, Diego ja fa molt que vas arribar al grup i hem compartit moltes birretes i confidències, espero que això mai canviï. Albert, el gran successor de les imitacions del Xavi, riem molt junts i hi ha coses que només ens fan gràcia a nosaltres dos. Que *tontos* som! (eeehhhh...) Els POMs ens han fet connectar molt i ens han aportat també moltes rallades, que la final hem superat! Te'n sortiràs, n'estic segura! Laura, la *organizer* del grup, a veure quan organitzes una bona esquiada! Roser, la nova de ful·lerens, ja saps que tens una gran responsabilitat en què els colors dels ful·lerens vagin a la moda de la temporada. Almu, fa poc que has arribat però ja t'has fet el teu lloc al grup, ja veuràs com al final no serà tant i això del magnetisme amb POMs estarà xupat! Marc A., a tu encara et queda un llarg camí per recórrer al grup, aprofita cada instant, és un període molt bonic, i gràcies per deixar que ens trobem el despatx calentet quan arribem. Antonio, el mateix et dic, aprofita cada moment i bona sort en aquesta etapa. Jianfang, you are learning Spanish so quickly, so I will say some words for you: Buena suerte y disfruta mucho de tu tiempo en el grupo. Als demés que han passat o estan al grup: Zhongling, Mariano, Pep, Pedro... Molta sort en tot, estic segura que us anirà molt bé.

Now, It's time for Newcastle's people. John thanks a lot for teaching me all the experimental stuff. It's been a great pleasure for me to work in your lab. Thank you for trust in me, not one but twice! We have done a lot of work that is reflected in this thesis. Dan and Thompson, we had a great time together in the lab, thanks for all! Kate, I knew you the last time that I came to Errington's lab and you were really nice to me. It was great to spend time with you in the lab and in the last POMs' congress! I hope we can meet in the future!

A les borgenques, encara que no saben ben bé que faig i no hagin entès que no fem horari escolar, m'hagin sabut escoltar en els moments que m'han fet falta i quan ha calgut m'han ajudat a desconnectar! Gràcies Marina, Laia, Lídia, Neus, Alba, Riera, Sara, Sheila i la nostra adoptada Carlota. Per les nostres sortides de *Ladies*, que bé que ens ho passem! Marina, a tu gràcies per sempre estar disposada a escoltar-me i aconsellar-me, crec que ningú millor que tu sap els bons i *mals* (també) que he passat durant aquests anys! Encara que no us ho digui mai, us estimo!

Roger, encara que ja ho sàpigues tot, gràcies per aguantar-me en els mals moments i sempre estar disposat a treure'm una rialla. Sempre has sabut dir-me les paraules idònies per tal de tornar-me aixecar i evidentment, celebrar els bons amb una bona cerveseta o copa de vi! Gràcies per interessar-te en saber que són i per a què serveixen els nostres estimats *Polioxos*. T'estimo.

Als meus pares, sense ells no seria aquí, encara que no els hi expliqui moltes coses i no entenguin ben bé que és fer una tesi, sempre han sabut recolzar-me i deixar-me fer el que cregués convenient. Gràcies per ser-hi sempre!

A la resta de la meva família, encara que alguns no enteníeu ben bé que feia, gràcies. Padrina, ja sé que no em veus tot el que voldries i ho sento, però crec que et sentiràs súper orgullosa de mi quan tinguis un exemplar d'aquest llibre a les mans. Gràcies per tot!

I crec que no em deixo a ningú. Ara començo un nou camí, un camí incert però estic segura que valdrà la pena. Fins sempre!

Overview of the Thesis

This thesis can be divided in two different parts: i) NMR and ii) Reactivity. The common factor of both sections is Polyoxometalates (POMs). POMs are polymetallic molecular anions formed upon aggregation of octahedral MO_6 blocks made of early transition metals (TMs), in their higher oxidation states, and oxygen, that are connected commonly by vertices and edges, forming characteristic structures such as those of the Lindqvist, Keggin or Wells-Dawson anions, which follow the names of the first authors who reported them. The principal features of these POMs are that they are strong oxidizing agents, very acidic and really versatile compounds.

The first part of this thesis is related to the characterization of POMs. In particular, it is based on the calculation of nuclear magnetic resonance (NMR) spectroscopy parameters. NMR has been used for many years and it has become one of the most popular chemical characterization techniques. Despite the fact that oxygen is one of the most important elements, other nuclei such as ^{1}H, ^{31}P, ^{13}C or even ^{183}W have been prevalent in NMR studies of POMs.

First, we focused on ^{17}O nuclei due to their presence in all the POMs structures. We report a theoretical DFT analysis on ^{17}O NMR chemical shifts for a family of prototypical POMs anions. We first made an extensive exploration of density functionals and basis sets to establish a good strategy to determine accurate values. In addition, the diversity of POMs studied provides a unique opportunity to compare chemical shifts (δ) values of nuclei bonded to different transition metals, allowing us to clearly identify and understand factors contributing to these values. Therefore, we have established a DFT-based strategy to accurately compute and rationalize ^{17}O NMR chemical shifts of polyoxoanions. For a set of 75 signals, we show that calculations performed with GGA-type PBE functional, including spin-orbit and scaling corrections, provide a mean absolute error value (MAE) <30 ppm, a small value considering that the range of $\delta(^{17}O)$ chemical shifts in these systems is around 1200 ppm (2.5%). We explored the paramagnetic contribution to the shielding, which dominates the ^{17}O chemical shift. It depends on the transition from occupied orbitals to unoccupied ones, which has higher contributions in oxygen atoms. We have shown that the electronegativity of the metal linked to the oxygen is a key factor in order to understand the chemical shift values. The paramagnetic shielding correlates with the M-O distance and also has a linear dependence with the reciprocal of the energy gap of the principal transition, which governs that shielding. Finally, we explored the effect of the protonation on $\delta(^{17}O)$ and demonstrated that ^{17}O NMR can be a powerful tool to identify the site(s) of protonation. DFT helps understanding how important protonation is and how it must be properly taken into account to reproduce and correctly interpret $\delta(^{17}O)$ in oxometalates. When a molecule has many similar or equivalent oxygen sites

that can accept an itinerant proton, the change in $\delta(^{17}O)$ signals is almost undetectable. On the other hand, when a molecule has very few distinctively basic sites, the proton gets trapped in one or a few sites and the change in $\delta(^{17}O)$ signals is more evident.

NMR of other nuclei which can be part of POMs such as ^{31}P, ^{29}Si, ^{79}Ga and ^{73}Ga offers the possibility to thoroughly study their structure and bonding. One of the most active nuclei used is ^{31}P, which provides straightforward structural information. In the case of POMs, the range of ^{31}P NMR is small (10 ppm), which implies a difficult assignment, but it is considered a powerful technique in structural characterization and monitoring of chemical reactions in the field of POMs. In chapter 4, we present a search for the best density functional strategy for the determination of ^{31}P NMR chemical shifts in POMs. The main computational parameters affecting the quality of such properties are the density functional and the basis set size, as well as the spin-orbit and solvent effects. The influence of the first two parameters on the quality of the ^{31}P NMR chemical shifts was investigated on a large family of compounds based on $[XM_{12}O_{40}]^{n-}$ and $[X_2M_{18}O_{62}]^{n-}$ frameworks. The work concludes that using a TZP/PBE for the NMR calculation step and a TZ2P/OPBE for geometry optimization is the best procedure for the accurate determination of ^{31}P NMR chemical shifts. The results obtained with the mentioned methodology presented a MAE of 2.64 ppm. The main variations in $\delta(^{31}P)$ come from the paramagnetic contribution to the shielding, which is directly related to occupied-virtual orbital transitions with phosphorous contribution. Thus, the variations in $\delta(^{31}P)$ are linked to the energy gap of these transitions.

The work presented in chapter 5 describes the first thallium containing polyoxometalate, which was synthetized and structurally determined. This project has been done in collaboration with two research groups: Dr. Kortz group and Dr. Tóth group. Our role in this project was to study the stability of the polyanion $[Tl_2\{B\text{-}\beta\text{-}SiW_8O_{30}(OH)\}_2]^{12-}$. Moreover, a detailed study of $^{203/205}Tl$ NMR has been performed in order to reproduce the experimental values. The optimized geometry reproduces correctly the X-ray geometry. We studied the most likely positions of the two protons of the molecule in solution. The results showed that there are relatively low energy differences obtained for different di-protonated anions, implying the possibility of mobile protons in solution. In solid state, the protons are linked to O_C due to the inaccessibility to the other oxygen types, which are blocked by countercations. The $\delta(^{205}Tl)$ are really well reproduced with DFT methodology. However, in the spin-spin coupling, there are large differences between calculated and experimental $^2J(^{205}Tl\text{-}^{203}Tl)$. $^2J(^{205}Tl\text{-}^{203}Tl)$ depends so much on the protonation and we would need to consider all the species present in solution in order to accurate reproduce $^2J(^{205}Tl\text{-}^{203}Tl)$. We have also searched for the best methodology to reproduce $^2J(^{205}Tl\text{-}^{203}Tl)$. All the results obtained so far show large deviations for the $^2J(^{205}Tl\text{-}^{203}Tl)$ compared to experiment and we are still working on it.

The second part of this thesis includes studies of POMs reactivity. The first project has been done in collaboration with Prof. Anna Proust and Dr. Guillaume Izzet. It is well known that many POMs have the ability to capture electrons with minor structural changes, and then in some media these electrons can be released generating new molecules. The efficient solar light-driven photochemical generation of fuels such as H_2 is a highly interesting topic and still a scientific challenge after decades of research. Matt *et. al.* (Energy Environ. Sci. **2013**, 6, 1504) designed a covalent Ir(III)-photosensitized polyoxotungstate, capable of efficiently evolving H_2 in presence of an excess of acid and a sacrificial electron donor. The stepwise mechanism of visible light harvesting, formation of charge-separated species and the proton reduction has been analysed by DFT and time-dependent-DFT (TD-DFT). We characterise the POM-based photosensitised reactant and intermediate species formed during the reaction mechanism, discussing photo- and electrochemical aspects. Electronic structure calculations show that the orbitals involved in the processes described here can be clearly classified as antenna- or POM-like upon their nature. Photochemistry, studied with the TD-DFT formalism, confirm that, upon absorption of UV-vis light by the reactant, the most probable electron excitation involves the [Ir] chromophore localized in the antenna. Partial relaxation of the excited state generated might populate a d(W)-like empty orbital of the POM fragment, producing the charge-separated species. Triethylamine (NEt_3) restores iridium to its initial oxidation state. After two excitation + reduction steps, the electron-rich species has extra electrons located in the POM framework. We have revealed that the two-electron reduced POM would be protonated in the reaction conditions. From the electrochemical point of view of the reaction, we have identified the orbitals of the POM that are found at considerably more positive energies in DMF with respect to aqueous medium, whereas the energy of the empty orbital of H^+ is not as dependent on the solvent. The energy of the hydrogen evolution process was computed in water and DMF media to check if the previous arguments are solid, revealing a more favourable process in DMF than in water. Such dissimilar reaction energies bring to light one of the greatest advantages of using DMF instead of water as solvent for H_2 evolution. However, the intricacy of the electron transfer from the two-reduced POM to H^+ is still now an open issue.

Finally, we wish to remark that reduced hybrid POMs have been used for CO_2 reduction, where a Re-organic decorated phosphotungstate Keggin cluster acts as photo-sensitizer, electron reservoir and electron donor. We cannot discard that in parallel to the outer-sphere hydrogen evolution on the surface of the electron-rich POM, a fraction of excited electrons return to the Ir centres and then a hydride is formed. Many organometallic complexes, which contain transition metals, can form hydrides to produce molecular hydrogen. Some studies focus on iridium (III) as catalyst. One of the most discussed mechanisms is the formation of a metal hydride that can react with a proton, resulting in H_2. We have checked that this species can

evolve H_2 with relatively low energy barriers although this hypothesis needs experimental confirmation. So, more studies are needed in this direction.

The last part of this thesis is done in collaboration with Dr. Errington's group. Heterometallic POMs are of particular interest and they provide a unique opportunity to study the reactivity of isolated heterometal site linked to a matrix of another metal at the molecular level and, hence, to establish a basis of understanding for the activity of a mixed oxide catalyst. The motivation of this collaboration comes from the difficulty to explain the behaviour of different heterometallic POMs in front of the protonolysis reaction. In chapter 7, we report a computational study to investigate (a) the effects of different lacunary oxide ligands $\{M_5O_{18}\}^{6-}$ on the protonolysis of the M'-OR bond and (b) the effects of different M' on the hydrolysis of heterometallic tungstates, $[(RO)M'W_5O_{18}]^{n-}$. We have found a consistent explanation based on DFT calculations of why and how the reactions take place from different heterometallic molecules. The mechanism of protonolysis of different heterometallic Lindqvist and Keggin anions was thoroughly studied. An understanding of the comparative differences in behaviour between polyoxomolybdates and -tungstates is not complete, since our calculations predict the same mechanism in both cases. These results prompted further investigations of these systems and it is worth noting that recent 2D EXSY 1H NMR studies reinforce the conclusions of the computational studies described in this thesis. Moreover, substituted Ti- and Sn- substituted Lindqvist and Keggin polyoxotungstates were also compared. The experimental trends have been reproduced by calculations, and relative stabilities and energy barriers are in complete agreement with measurements.

In the last section of the chapter an experimental study about the protonation of heterometallic tungstate dimers is reported. Two different pathways to the di-protonated form of $(TBA)_6[(\mu\text{-}O)(TiW_5O_{18})_2]$ were studied. We have found that the protonated form is stable and it is easily synthesized. This leads us to predict the behaviour of electrophiles when they interact with this class of oxo-bridged dimer. This study provides an understanding about the behaviour towards electrophiles in reactions that are producing a new family of functionalized POMs, where they act as chelating or pincer ligands.

Contents

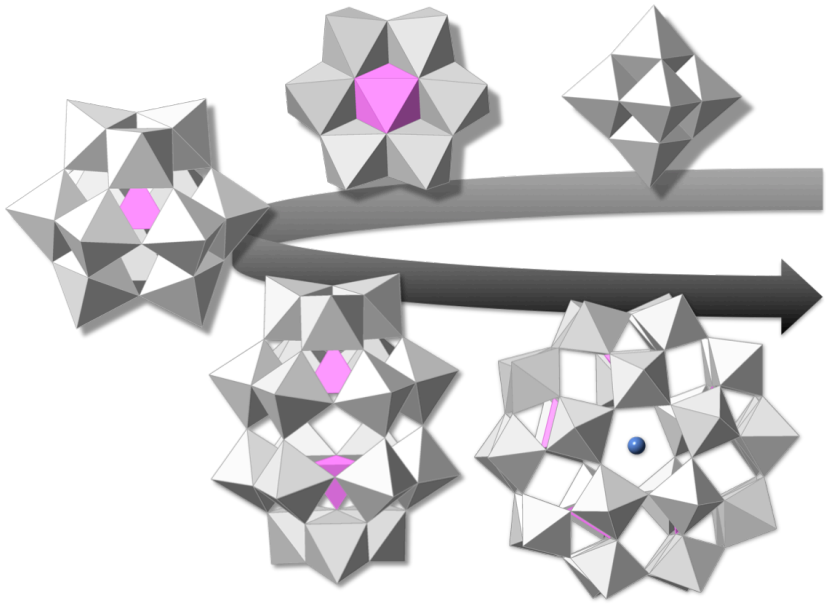

CHAPTER 1

Getting into the World of Polyoxometalates

CHAPTER 1

Getting into the World of Polyoxometalates

This chapter introduces the amazing world of polyoxometalates (POMs) to the reader, highlighting the fundamental characteristics and most relevant features of this class of compounds. First, the history, classification and the most common properties are presented. Afterwards, we describe the main applications related to POMs and how Computational Chemistry can help to understand and develop them.

1.1. Brief history of the beginnings of POMs

It was in 1778 when the first paper of what are known today as Polyoxometalates (POMs) was published by the Swedish chemist C. W. Sheedle. He studied for the first time "blue water", also known as "molybdenum blue", formed by oxidation of MoS_2. It was observed in some springs in Idaho Springs (Colorado) and in the Valley of Ten Thousand Smokes (Alaska). He was the first to describe a reproducible experiment about this compound, which was published in a Swedish journal under the name of *"Chemische Untersuchung über das Molybdänum oder Wasserbley"* (Chemical studies on molybdenum or water lead), being aware that the compound was a reduced molybdenum oxide.[1] It was considered a really distinguished work and it was translated from Swedish to French under the name "*Sur la Mine de Plomb ou Molybdène*", in the series of "*Observations sur la Physique, sur l'Histoire Naturelle et sur les Arts"*, which collected the most exciting findings at that time.

It was fifteen years after when Berzelius reported that the yellow precipitate that appeared when ammonia molybdate was added under a solution of phosphoric acid

was what is known nowadays as phosphomolybdic acid, $H_3PMo_{12}O_{40}$.[2] However, the nature and structure of the compound was still unknown. It was not before 1862 that C. Marignac carried out a systematic study of the composition of silicotungstic acid, $H_3SiW_{12}O_{40}$.[3] In this work, he reported two structural forms known nowadays as the α and β isomers, and different salts. During the next years, these polymolybdates and polytungstates were used to determine the content of ammonium, phosphorus or silicon in different samples.

It not was until the 20th century when the structure of POMs started to be revealed. The first attempt was performed by Miolati and Pizzighelli.[4] Pauling also contributed to their structural determination, noticing that Mo^{VI} and W^{VI} had an appropriate ionic radii for octahedral coordination. However, he only proposed the possibility of structures containing corner sharing (not edge sharing) MO_6 units.[5] Finally, in 1933, J. F. Keggin, thanks to the development of increasingly powerful spectroscopic techniques, solved the first X-ray structure for the phosphotungstic acid, $H_3[PW_{12}O_{40}]\cdot 5H_2O$.[6] He showed that the anion was indeed based on MO_6 octahedral units as suggested, but these octahedra were linked by edges as well as by corners. Later on, A. J. Bradley and J. W. Illingworth confirmed the POM structure by Keggin.[7] The study of POMs slowly progressed in the following years. Until 1971, just 25 new X-ray structures were reviewed by T. H. Evans.[8]

The improvements in crystallographic techniques increased the number of newly published structures during the following years. The emergence of new spectroscopic techniques, combined with more precise electrochemical and analytical techniques, helped characterizing new and more complex species. During recent decades, the popularity of POM has rapidly grown. Pope and Müller reviewed the status of POMs in 1991.[9] Later on, in 1998, a special issue on POMs was published in Chemical Reviews with C. Hill as Guest Editor, summarizing the history, developments and applications of many areas covered by POM Chemistry.[10] Thereafter, the number of works grew very rapidly and turned into a key field allowing the synthesis of numerous molecule-based materials. The rise of POMs popularity during the last decade can be grasped in a special issue of *Chem. Soc. Rev.*, which collects the most relevant research done in this field both experimentally and the theoretically.[11-14] In recent years, theoretical chemistry has lead to reproduce, understand and rationalise many physical and chemical properties related to POM Chemistry. All this progress is reflected in the review reported by López *et. al.*,[15] which includes a complete review of the computations done in this area.

At present, POM chemistry is a key area that promises development of sophisticated designer molecule-based materials and devices to be exploited in instrumentation, nanoscale science and material fabrication methods.

1.2. Structure and Design Principles

POMs are polymetallic molecular anions formed upon aggregation of octahedral MO_6 blocks made of early transition metals (TMs) and oxygen, that are commonly connected by vertices and edges,[16] although in some cases these fundamental units can share faces, forming compact frameworks. Their general formula is $(MO_X)_n$ where M are the addenda atoms and x typically being 6 although and less commonly 4, 5 or 7.[17] Most of these inorganic molecular aggregates contain Mo, W or V in their highest oxidation states (d^0 or d^1 electronic configurations), or a mixture of them. Many other early and late TMs have been incorporated to POM structures, such as Nb, Ta, Fe, Tc, amongst many others. Apart from M and O atoms, other elements can take part in the structure. They are the so-called central atoms or *heteroatoms* (labelled X in the following). The numerous elements that can take part in POMs and the way the fundamental building blocks can be connected make this family of compounds a continuously growing field. Figure 1.1 shows the most representative and well-known POM structures. Different attempts have been made to classify and rationalize the entire POM family, one of the most usual being their composition.

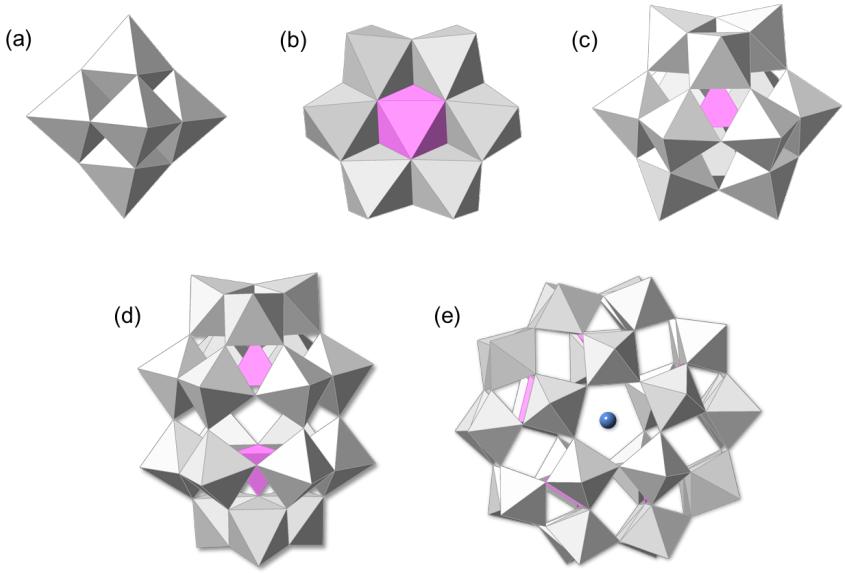

Figure 1.1 Polyhedral representation for typical isopoly-and heteropolyanions: (a) Lindqvist $[M_6O_{19}]$; (b) Anderson-Evans $[XM_6O_{24}]$; (c) Keggin, $[XM_{12}O_{40}]$; (d) Wells-Dawson, $[X_2M_{18}O_{62}]$ and (e) Preyssler, $[XP_5W_{30}O_{110}]$. Pink polyhedra contains the heteroatom, grey octahedra represents MO_6 units.

Upon this criterion, we can distinguish two different subfamilies:

Heteropolyanions (Figure 1.1b-e) are metal oxide clusters that include heteroanions such as SO_4^{2-}, PO_4^{3-}, AsO_4^{3-} and SiO_4^{4-} inside a metal-oxide cage. The general formula of this subset of POMs is $[X_zM_nO_y]^{n-}$. The most deeply studied is the catalytic activity of Keggin $[XM_{12}O_{40}]^{n-}$ and the Wells-Dawson $[XM_{18}O_{62}]^{n-}$ anions, where M is either Mo or W. X can be any element in principle since there is not a structural limitation for this position. Tungsten-based POMs are robust, and this fact has been exploited to develop tungsten-based Keggin and Dawson anions with vacancies (most commonly with one, two or three of them) that can be linked using electrophilic species to form larger aggregates in a controlled manner.

Isopolyanions are metal oxide clusters without internal heteroatom or heteroanion. The general formula is $[M_nO_y]^{n-}$ (Figure 1.1a). The most popular structure in this family is the Lindqvist anion, $[M_6O_{19}]^{n-}$. They are often much more unstable than their heteropolyanion counterparts.[18] However they also have interesting physical properties, such as a high charge density and more basic oxygens than heteropolyanions.

Molybdenum blue and molybdenum brown reduced POM clusters are related to molybdenum blue species, which were first reported by Scheele in 1783. Their composition was largely unknown until Müller *et. al.* reported the synthesis and structural characterization in 1995 of a high-nuclearity cluster $\{Mo_{154}\}$, which has a ring topology, that crystallized from a solution of molybdenum blue.[19] Changing the solution pH and increasing the amount of reducing agent along with incorporation of acetate ligands facilitates the formation of a $\{Mo_{132}\}$ spherical cluster.[20] This class of highly reduced POM clusters is one of the most exciting developments in POM Chemistry, with potential applications in nanoscience.

1.3. Synthesis and Functionalization

Generally, the approaches used to produce POM-based clusters are quite simple. They require a small number of steps, or even just one step (one-pot synthesis), during which acidification of an aqueous solution containing the relevant molybdate, tungstate or vanadate salt drives the condensation process and induces the aggregation towards the formation of specific archetypes. The aggregation process is controlled by a long list of experimental variables, which should be considered when planning the synthesis of a given POM, such as: 1) concentration/type of metal oxide anion, 2) pH, 3) ionic strength, 4) heteroatom type/concentration, 5) presence of

additional ligands, 6) reducing agent, 7) temperature of the reaction and processing, 8) solvent.

Based on the experience accumulated over the years, the vast growth in the number of assembled clusters may be attributed to thousands of combinatorial possible structural types, in which each building block can potentially adopt different isomeric forms itself.[14]

As mentioned, POM structures can also derive into lacunary species by removal of one or a few metal atoms of the plenary framework, forming vacancies that can occasionally be filled by other atoms. Depending on the POM, lacunary architectures can be obtained in different ways. One route is related to the basic hydrolysis of the plenary structure, although in some cases the lacunary species is obtained by increasing the pH under strictly controlled conditions.[21, 22] Then, a M=O vertex of the cluster vanishes. The lacuna generated is highly nucleophilic. Therefore, it can combine with other lacunary POMs so as to form larger and more intricate POMs. However, the great interest in lacunary POMs is related to their ability to fill the vacancy up with most of the elements of the periodic table or with organic groups, yielding functionalized and larger self-assembled metal-oxide structures. So, from a lacunary POM one can get a mixed-metal POM, such as $[PVW_{11}O_{40}]^{4-}$ or $[PMoW_{17}O_{62}]^{6-}$.

As a consequence, many new structures have been built from lacunary species, which have been increasingly used as rigid inorganic ligands to stabilize multinuclear metallic cores that could significantly change the functionality of the isolated material.[23] Cronin *et. al.* reported successful stabilization of a multinuclear $\{Fe_{12}(OH)_{18}\}$ core utilizing the trivacant polyanion $\{\alpha\text{-}P_2W_{15}O_{56}\}$, which forms the complex species $[KFe_{12}(OH)_{18}(\alpha\text{-}1,2,3\text{-}P_2W_{15}O_{56})_4]^{29-}$.[24] Another example is the $[Mn_{19}(OH)_{12}(SiW_{10}O_{37})_6]^{34-}$ (Figure 1.2) which was reported by Kortz *et. al.*, in this case the planar core $\{Mn_{19}(OH)_{12}\}$ is incorporated in the centre of six $\{SiW_{10}\}$ fragments.[25] Recently, Cronin's group have reported a supramolecular assembly mediated by control of $[Mo_2S_2O_2]^{2+}$ and SeO_3^{2-}, units ratio, leading to the formation of new types of buildings blocks to generate novel clusters with the general formula $\{(Mo_2O_2S_2)_x(OH)_y(SeO_3)_z(H_2O)_W\}^{n-}$.[26, 27]

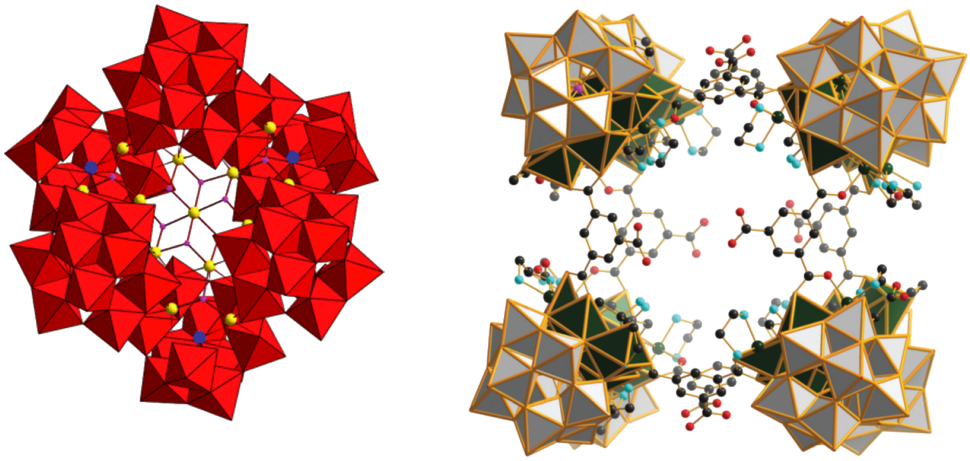

Figure 1.2. Right: Polyhedral representation of $[Mn_{19}(OH)_{\prime}Si_{12}W_{10}O_{37})_6]$. Colour code: W-red polyhedra Si-blue spheres, Mn-yellow spheres, O-red spheres (Figure obtained from Ref. [25]). Left: The POM structure $\{PW_9Ni_6\}$ is shown in polyhedral representation and the organic moieties in ball-and-stick mode. Colour code: W-grey polyhedral, Ni-dark green polyhedral, O-red spheres, N-light blue spheres, P-pink spheres, C-small black spheres. (Figure obtained from Ref. [14])

As said, the high nucleophilicity of the lacuna makes these positions accessible to organic groups and, therefore, the possibility to develop hybrid organic-inorganic materials.[28, 29] The structure and properties of hybrid POMs are totally dependent on both components. Therefore, the combination of organic ligands and inorganic POMs offers diverse options for their integration into functional materials and devices. POMs constitute ideal building blocks for targeting new multifunctional molecules. A new class of POM-based metal organic cages and POM-based MOFs (so-called POMOFs), which are built from the mutual connection of POMs through bridging organic linkers, are excellent candidates for the design of materials with tuneable functionality. Recently, Zhang-Ting Li *et. al.* have demonstrated that adsorbing anionic Wells–Dawson-type polyoxometalates in a one-cage-one-guest manner leads to efficient photocataytic hydrogen production in aqueous media and in organic media.[30]

1.4. Features of POMs

Their amazingly vast structural diversity promises applications in fields such as medicine, catalysis and material science, to mention just a few. These bring us an

interesting chance of physicochemical properties such as redox reactions, photoreactions, energy transfer and biological activity. POMs often present the following features:

- Electrochemical or photochemical reversible multi-electron redox processes
- High solubility in water and/or polar organic solvents
- Coordination of large amounts of water molecules
- Controlled synthesis of compounds of varied anion size, charge, structure and metal composition
- Possibility to obtain derivatives with a large variety of heteroatoms (75% of periodic table)
- Encapsulation of neutral molecules such as acetonitrile or water, or ions such as carbonate or thiocianate[31, 32]

Even though POMs can present countless structures, herein we will focus on the most common only.

1.4.1. Redox Properties

The variety of redox properties is one of the most important features of POM compounds, and provides a major motivation in the development of new functional systems. M. T. Pope classified POMs in two wide groups upon their redox properties:[17, 33]

Type I: Their metal atoms have one terminal oxygen, such as Keggin and Wells Dawson compounds. They are easily reduced and reoxidised. The redox potentials of type I compounds depend on the molecular structure and charge, and also on the nature of the metal elements constituting the metal-oxide framework.

Type II: Their metal atoms have two terminal oxygen atoms. Reductions of these POM anions are irreversible, leading to fragmentation or rearrangement to other structures.

Despite their negative charge, POMs are strong oxidizing agents. The explanation for this is given by the high oxidation state of the metal atoms present in the structures, typically featuring empty d valence shells. Therefore, they can accept electrons without appreciably changing the molecular structure. These electrons are usually delocalised over de MO_6 octahedra by virtue of the usual low interatomic hopping energy barrier.[34] Electron delocalisation has been an active research topic in past years.[35-39]

The degree of delocalisation depends on: (i) the local structure of M-O-M linkages, and (ii) the structural and chemical equivalency of the M sites. Then, the redox properties for the same type of cluster can be tuned by incorporating different heteroatoms or replacement of one metal ion on the cluster shell. For example, Dawson-type POMs disubstituted with phenylphosphonate, phenylsiyl, or tert-butylsilyl moieties can accept up to five electrons, and the organic substituents modify the first and second reduction potentials of the POM relative to the unsubstituted ion $[P_2W_{18}O_{62}]^{6-}$.[40] The Preyssler anion, $[M^{n+}P_5W_{30}O_{110}]^{(15-n)-}$, is able to accept electrons at low potentials, to selectively capture various metal cations and to undergo acid-base reactions. Poblet *et. al.* reported a linear relationship existing between the first one-electron reduction energy and the encapsulated X^{n+} charge.[41, 42]

1.4.2. Acidic Properties

POMs are also very acidic compounds, some of them featuring negative pK_a values, implying that all their protons can be readily released in water. However, some can be protonated in moderate or strongly acidic media. Because of the chemical characteristics of the M atoms, not all oxygen sites in a POM are identically basic. This depends on the following parameters: the molecular charge, the size of the POM, the M-O bond covalency and the number and physical nature of M neighbours. For many years, POMs' acidobasic properties have been studied theoretically and experimentally.[43]

Heteropolyacids in general are strong Brønsted acids. Therefore, the corresponding anionic forms have a very weak Brønsted basicity, and appear to be softer than simple nitrate or sulfate anions.[44, 45]

Some methods for heteropolyacid characterization involve titration with a base in order to establish or confirm the stoichiometry. In most of the cases, two phases can be detected, the first one related to neutralization of acidic protons and the second one related to the anion degradation, for example:

$$H_3[PW_{12}O_{40}] + 3OH^- \rightarrow [PW_{12}O_{40}]^{3-} + 3H_2O$$

$$[PW_{12}O_{40}]^{3-} + 23OH^- \rightarrow 12WO_4^{2-} + HPO_4^{2-} + 11H_2O$$

Another controversial question about acidity is where the protons are localized in the structure. The POM surface contains terminal and bridging oxygens, which are potential sites for protonation. In the solid state structures, the protons are thought to be mostly linked to bridging oxygens.[46-48] Thus, very few structures where protons are linked to the terminal oxygens have been reported.[49]

The identification of protons in solution is even more difficult than in the solid state because of their itinerant nature. One of the techniques used to study their behaviour is the pH dependency of ^{17}O NMR chemical shifts.[50] This issue will be discussed in Chapter 3.

1.4.3. Isomerism

Another important property of POMs is isomerism, which confers an additional richness to some of them. Various isomeric forms have been studied for the common $[XM_{12}O_{40}]^{n-}$ Keggin and $[X_2M_{18}O_{62}]^{n-}$ Wells-Dawson structures. Isomerism is relevant in POMs due to its implications in redox properties for instance, and therefore it has been largely studied and their properties profoundly analysed by theoretical and experimental groups.[34, 51-53]

The Keggin anion is the most studied POM due to its stability and ease of preparation. It is formed by twelve MO_6 octahedra arranged in four edge-sharing M_3O_{13} groups surrounding a central XO_4 tetrahedron. It possesses five geometrical isomers, proposed by Baker and Figgis,[51] known as α, β, γ, δ, and ε, the last four resulting from successive 60º rotations of the M_3O_{13} edge–sharing units about 3-fold symmetry axes of the α isomer.

A similar rotational isomerism exists for Wells-Dawson anion. It is an ellipsoidal structure formed by two M_3 rings at polar regions (caps) and two M_6 rings located at the equatorial region (belts). Inside the structure, there are two XO_4 anions encapsulated. There exist six rotational isomers of the Wells-Dawson structure, named α, β, γ, α*, β* and γ*. They were also postulated by Baker and Figgis in 1970.[51] They result of the rings rotation. One of the abilities of the Wells-Dawson structure is to generate lacunary species, and hence metal-substituted molecules. The replacement of one metal from the α structure can generate two different isomers, named α_1 (belt) and α_1 (cap), depending on the region of substitution, as shown in Figure 1.3.

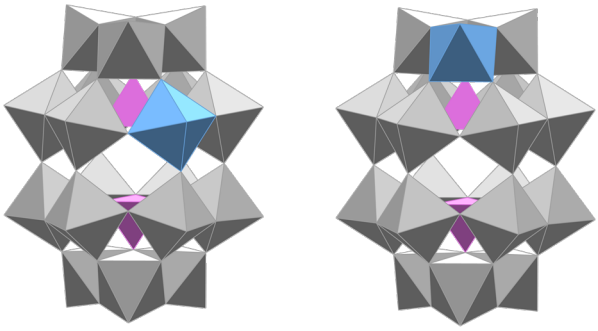

Figure 1.3. Polyhedral representation of addenda-substituted α_1 (right) and α_2 (left) of $[P_2M'W_{17}O_{62}]$ anions. Grey octahedra represent WO_6 groups, blue octahedral represent $M'O_6$ groups and pink tetrahedra represent XO_4.

1.5. Applications

Their wide structural diversity has derived into exciting applications in fields such as medicine, catalysis and material science, to mention just a few.[54] The main applications of POMs arise principally from the presence of many TM atoms. These bring us an interesting chance of physicochemical properties such as redox reactions, photoreactions, energy transfer, and biological activity.

POMs have a diverse range of electronic properties arising from the ability to form reduced species. This property combined with the ability to act as a well-defined ligands for polynuclear transition metal cluster, means they have a great potential for the discovery and design of new molecular magnetic devices. In fact, Mixed-Valence POMs may be ideal magnetic molecules to study the electrical control of the spin state. They can change their spin state by the application of an external field or by injection of extra electrons. For example, the $[PMo_{12}O_{40}(VO_2)]^{n-}$ cluster has been described as a possible fundamental spin qubit. The redox-active core unit of the Keggin cluster is capped on opposed positions by two $(V^{IV}=O)^{2+}$ groups, each containing a localized spin $S = 1/2$.[55] The last few decades have shown that containing vanadium POMs are ideal objects for magnetochemical studies and for the exploration of nanoscale molecular magnetism due to their intriguing magnetic features, ranging from geometrical spin frustration to single-molecule magnet characteristics.[56] The fact that POMs can be intrinsically electronic/redox active is one of the major strengths of POM-based ligands, especially in magnetic systems, as it offers an additional route by which the exchange pathways and electronic configuration of the system may be controlled.[57] Cronin *et. al.* reported one of the first POM-like single-molecule magnets

(SMMs), $[(GeW_9O_{34})_2\{Mn^{III}_4Mn^{II}_2O_4(H_2O)_4\}]^{12-}$. In this system, a central cationic mixed-valence hexameric manganese core is stabilized by two lacunary Keggin-like ligands.[58]

One of the most outstanding applications of POMs is catalysis owing to their properties as strong Brønsted acids and as fast reversible multielectron oxidants. POMs are applied in acid catalysis and in green selective oxidation with molecular oxygen and hydrogen peroxide. They can also act as bifunctional -acid and redox-catalysts, which make them promising compounds in the utilization of solar energy for molecular oxygen evolution from water oxidation. In 2008, two different groups reported, independently, a redox-active tetraruthenium POM $[Ru_4O_4(OH)_2(H_2O)_4(\gamma\text{-}SiW_{10}O_{36})_2]^{-10}$ (Figure 1.4a), which combined with $[Ru(bipy)_3]^{3+}$ was found to catalyse the rapid oxidation of H_2O to O_2 in water.[59, 60] In 2010, Hill reported the catalytic water oxidation activity of the tetracobalt-oxo-core sandwich-type POM $[Co_4(H_2O)_2(\alpha\text{-}PW_9O_{34})_2]^{10-}$.[61] During the last years, the molecular nature of the catalyst has been put into question,[62-65] since catalytically-active Co^{2+}(aq) cations may exist in solution in equilibrium with the cobalt-containing POMs. More recently, the group of Prof. J. R. Galán-Mascarós has shown that $[Co_9(H_2O)_6(OH)_3(HPO_4)_2(PW_9O_{34})_3]^{16-}$ is a robust homogenous catalyst in water oxidation.[66] Many review articles have covered the progress in this field, including recent reviews of green H_2O_2-based epoxidation reactions,[67] catalytic oxidation of organic substrates by molecular oxygen and hydrogen peroxide by multi-step electron transfer,[68] progress and challenges in POM-based catalysis and catalytic material chemistry[69, 70] and catalytic strategies for sustainable oxidation in water.[71] Herein, we particularly studied the H_2 evolution mechanism published by Artero, Izzet and co-workers. They showed that a covalent Ir(III)-photosensitized derivative of the Wells-Dawson structure ($P_2W_{18}O_{62}^{6-}$) in the presence of a sacrificial reducing agent leads to photocatalytic hydrogen evolution under UV-vis light.[72]

Another feature of POMs is that they can potentially interact with biomolecules. In recent years, a number of studies have been carried out employing POMs as anticancer and anti-viral agents. $[NH_3iPr]_6[Mo_7O_{24}]\cdot 3H_2O$ (Figure 1.4c) was found to be particularly effective in some tumour, namely showing activity against human colon cancer, human breast cancer and human lung cancer.[73] The interactions between POMs and general biological systems have also attracted interest, and it has been demonstrated that biopolymer-POM interactions are significant in the gelatin-decavanadate system.[74] Moreover, Xiaogang and co-workers have demonstrated that several POM structures are able to act efficiently as inhibitors towards amyloid β ($A\beta$) aggregation which can be one of the primary targets of therapeutic strategies for Alzheimer's disease.[75-78] Furthermore, proteins can ligate a remarkable variety of POMs that are formed from the interaction between the proteins and

molybdates/tungstates.[79, 80] Nowadays, several research groups are developing this type of chemistry with POMs.[81, 82]

In recent times, POMs have been applied for the design of memory devices. Vilà-Nadal *et. al.* showed that $[W_{18}O_{54}(SeO_3)_2]^{4-}$ (Figure 1.4b) has the right balance between structural stability and electronic activity to be an ideal candidate to act as flash memory device.[83] These findings have brought a new research area in POMs, showing that they have the potential for significant applications in molecular-based flash memory cells.

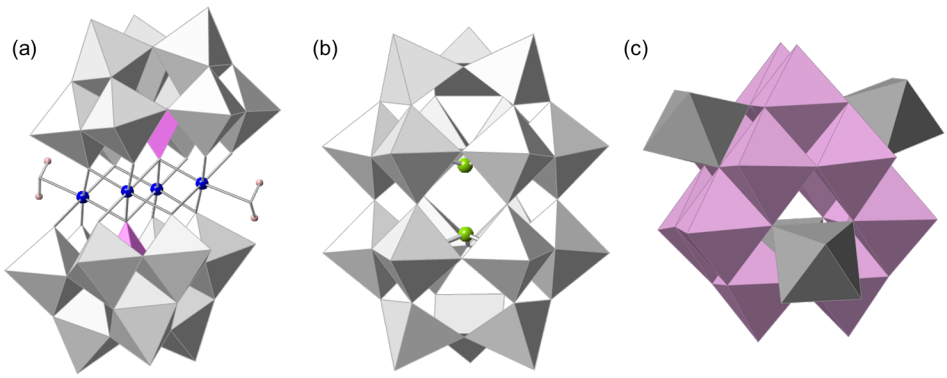

Figure 1. 4. Some examples of POMs used as a) Water splitting catalyst, $[Ru_4O_4(OH)_2(H_2O)_4(\gamma\text{-}SiW_{10}O_{36})_2]^{10-}$ b) Flash-memory Device, $[W_{18}O_{54}(SeO_3)_2]^{4-}$, c) Anticancer agent, $[NH_3iPr]_6[Mo_7O_{24}]\cdot 3H_2O$.

POMs are promising components in multifunctional nanomaterials, such as carbon-based nanostructures, and it has even been possible to image the sterically regulated translational and rotational motion of discrete $[W_6O_{19}]^{2-}$ inside carbon nanotubes.[84] Composites based on POMs and nanostructured carbon such as carbon nanotubes (CNTs) or graphene (Figure 1.5) have attracted widespread attention as they combine the unique chemical reactivity of POMs with the unparalleled electronic properties of nanocarbons. The exceptional properties of these composites have been employed in catalysis, energy conversion and storage, molecular sensors and electronics.[85-90] So, the arrangement of a group of functions into a hierarchy could allow the design of new materials in POM chemistry.

As it can be seen, the research in POMs is entering an exciting new period that is moving beyond the synthesis and the structural characterization of new cluster systems. The development of functional composites that utilize the intrinsic chemical and electronic properties, size, and self-assembly aspects promises to lead to increasingly sophisticated molecular systems that could be utilized as devices with a priori set up features.

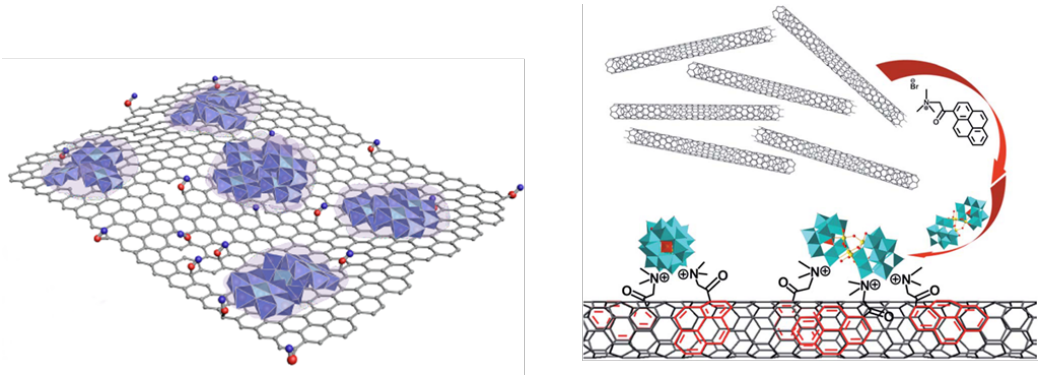

Figure 1. 5. Left: Anderson-type POM $[AlMo_6O_{24}H_6]^{3-}$ attached on Ethylenediamine-Decorated Reduced Graphene Oxide by electrostatic interaction (Figure obtained from Ref. [90]). Right: CNT-bound POM catalyst: the CNTs are functionalized with an amphiphilic cationic pyrene derivative by p–p stacking, the anionic $Ru_4(SiW_{10})_2$ is subsequently immobilized by electrostatic interactions. (Figure obtained from Ref. [89])

1.6. POMs in Computational Chemistry

From the theoretical point of view, POMs are fascinating and have captured the interest of the Quantum Chemistry research group in Tarragona since the mid-1990s because of the beauty of their symmetric structures, the presence of multiple metal atoms and their appealing physicochemical properties. Virtually all POMs' features have been tackled with computational tools: electronic structure, basicity, NMR chemical shifts, spectroscopy, magnetism, redox properties, solution dynamics, reactivity, and so on.[43, 91-97] Quantum mechanical calculations have dominated the theoretical publications on POMs during the last two decades, mainly based on density functional methods (DFT). These calculations mainly focused on the classical Lindqvist $[M_6O_{19}]$, Keggin $[XM_{12}O_{40}]$, Anderson-Evans $[XM_6O_{24}]$, Wells-Dawson $[X_2M_{18}O_{62}]$ and Preyssler $[XP_5W_{30}O_{62}]$ clusters. Thanks to the growing computational power, theoretical studies can presently solve almost any existing structure.

The theoretical modelling of POMs remained totally unexplored until 1986. The first published paper was an electronic structure study based on the $X\alpha$ method for the dodecamolybdophospate anion, $[PMo_{12}O_{40}]^{3-}$.[98] That work describes the properties of the most relevant molecular orbitals (MO). Using the same method, the electronic structures of other molybdates Keggin family were studied.[99] During the following years, some works using semi-empirical methods were published. Ritschl and co-workers studied a POM structure containing Cu^{II} and V^{IV} cations with the SCF CNDO/2 approach.[100-102] With the same method, the structure and bonding properties of the α

-Keggin anion[103, 104] and the stability and catalytic activity of the Wells-Dawson anion were published.[105]

During the 1990s, Bénard and co-workers applied the *ab initio* Hartree-Fock Self-Consistent (HF-SCF) method for studying the electronic structure of several polyoxovandates. The first work reports the different basicities of the external oxygen sites in the decavanadate $[V_{10}O_{28}]^{6-}$ anion.[106] Studies of other polyoxovanadtes featuring host-guest or endohedral activity were also reported.[107] They also performed HF calculations on $[V_{18}O_{32}]^{12-}$ and some related structures.[108]

The calculations mentioned above aimed to obtain qualitative information instead of accurate numerical data. For more detailed results, electron correlation has to be included in the calculations, thus DFT is an appropriate method at an accessible cost for studying POMs. The application of the DFT methodology to the study of POMs started more than twenty years ago.[39] Although DFT calculations were long due to the size of the POMs, nowadays this type of calculations has turned into routine because of the continuous development of increasingly powerful software and hardware. Present DFT calculations allow introducing additional physical effects not taken into account originally, such as the relativistic and the solvation effects, large atomic basis sets or hybrid functionals. The solvent effects are typically and cheaply included by means of continuum models (COSMO, PCM or SMD). These effects have revealed fundamental for the correct modelling of many POMs' properties, such as electrochemistry or reactivity.

Depending on the type of calculation or the accuracy wanted, the methodology varies. Pure GGA functionals and standard triple-zeta atomic basis sets may suffice to obtain good equilibrium geometries and correct electronic structures of most POMs. However, in some other calculations such as those describing NMR or electronic magnetism properties, a more accurate geometry is needed, which can only be achieved with larger basis sets, tight numerical integration and stabilizing solvent effects.[109, 110] This issue is tackled in Part I of this thesis. Moreover, hybrid functionals are used in reactivity since they provide better results than pure functionals in describing energy barriers.

Classical Molecular Dynamics (MD) has been also used to study the behaviour of POMs in solution. In these calculations no explicit quantum effects are involved. The diffusion of POM molecules within a solution and the distribution of water molecules and cations around the POM have been analysed.[111, 112] *Ab initio* or Car-Parrinello MD (CPMD) has been applied to model the nucleation process of fundamental metal oxide units to large clusters over time[113] and to study the behaviour of POMs in solution.[114]

These techniques were also applied in static DFT on the interaction between POM structures and metal surfaces.[115]

Correlated *ab initio* methods have also been applied to study POMs with unpaired electrons, namely properties involving small energy amounts such as the splitting between different spin states. These methods are much time-consuming and thus they are not applied routinely.

Some other recently published computational studies that deserve mention include the first theoretical study related to interactions between proteins and POMs[81], the reaction mechanism of water oxidation catalysed by Ru-containing POMs[116], dynamic calculations of a Keplerate-type $\{Mo_{132}\}$,[117] showing the behaviour in solution within cations, the electronic structure of $[W_{18}O_{54}(SeO_3)_2]^{4-}$ anion which is a candidate to act as a flash-memory device[83] and the isomerization of lacunary polyoxoanion [β_2-$SiW_{11}O_{39}]^{8-}$ into [γ –$SiW_{10}O_{36}]^{8-}$.[118]

Nowadays, computational chemists are able to reproduce and rationalise many physical and chemical properties of POMs such as redox potentials, reactivity of mixed-metal addenda, vibrational, electronic and NMR spectra of POMs in solution as well as absorbed on surfaces. Computational Chemistry has become an indispensable tool to understand the phenomena taking place at the nanoscale.

DFT methodology is implemented in many programs, codes and package. Although the computational details are described in each chapter of this thesis, a general description of why we use each methodology is presented in this section. The most widely used program during this thesis is *ADF*.[119-121] The principle feature of *ADF* code is the use of basis sets built with Slater-Type functions (STOs). A basis set is the mathematical ensemble of orbitals of a system used to perform theoretical calculations. Although numerical integration is more computationally demanding with STOs. It is generally accepted that STOs allows the construction of high-quality basis sets with relatively small number of functions. ADF also incorporates relativistic effects with the *zeroth-order regular approximation* (ZORA).[122-124] DFT methods calculate electron correlation using general functionals of the electron density. Becke-Perdew[125, 126] (PB86) is one of the most used functional using *ADF* related to POMs chemistry, which reproduce in very good agreement the X-ray structures.[34, 39, 127] Hybrid functionals are also implemented, but not in a very efficient way. Nowadays, geometrical optimization using this type of functionals is not suitable. During this thesis *ADF* code was useful to predict accurately NMR properties. NMR chemical shifts are very sensitive to tiny structural changes and, thus, extremely accurate geometries are necessary to accurately reproduce the experimental values. To do so, we have performed all-electron computations with large basis sets. As POMs structures contain

heavy atoms, it was necessary to treat them with relativistic effects, including ZORA approximation.

Gaussian package[128] is another of the most widely used programs. It can handle calculations of up to a few hundred atoms and it can predict the geometrical structures and electronic properties of large molecules with any type of atoms, including metals. In contrast to *ADF*, it uses a linear combination of Gaussian-type functions (GTOs) as atomic orbitals. It is worth mentioning that Slater orbitals are more accurate than the same number of Gaussian functions for molecular orbital computations. *Gaussian* has different pre-defined basis set, which are classified by the number and type of basis functions that they contain. Basis sets assign a group of basis functions to each atom within a molecule to approximate its orbital. Basis sets for atoms beyond the 3rd row of the periodic table are computed differently. In these heavy atoms, internal electrons are treated in an approximate way, via effective core potential (ECPs). This treatment includes part of relativistic effects, which are important in heavy atoms. Los Alamos National Laboratory pseudopotential with standard 2-double zeta (LANL2DZ) is one of the best-known basis set. One of the advantages of Gaussian is that hybrid functionals can be very efficiently used. As mentioned, it has been shown that hybrid functionals are very useful in reactivity studies due to the fact that it shows good results in energy barriers. The hybrid functional for excellence is B3LYP,[129, 130] it was employed in several studies of structural properties and reactivity of POMs.[15]

TD-DFT methodology is employed in the study of the physical properties that involve the participation of excited states. TD-DFT is applied in this thesis in order to reproduce and rationalize the UV-vis spectrum. A detailed analysis with several combinations of density functionals and basis sets for $[W_6O_{19}]^{2-}$ concluded that the UV spectrum should be predicted with hybrid or meta-hybrids type functionals.[131]

POMs exist in solution as negatively charged species stabilized by the solvent and the conterions. Therefore, the structures discussed in this thesis were optimized in the presence of a solvent model. The most common solvent models in POMs are Conductor-like Screening Model (COSMO)[132] implemented in *ADF* program package and Polarizable Continuum Model (PCM)[133] implemented in *Gaussian*. PCM and COSMO assume that the solute molecule may be placed within a cavity surrounded by solvent molecules. So, in this approximation the solvent is treated as a dielectric continuous material characterized by a constant (**ε**) placed around the studied solute molecule. Moreover, the geometries obtained with implicit solvent effects are considerably improved, in comparison to those obtained with gas phase calculations.

1.7. NMR Calculations on POMs

Since Part I of this thesis is devoted to the study of the nuclear magnetic resonance (NMR) properties of POMs, an introduction of the theoretical basis of this technique and a brief description of how calculations are carried out is done. The pioneering NMR calculations on POMs are also reviewed.

During the preparation of this thesis a contribution has been made to the structural characterisation of POMs. Nuclear magnetic resonance (NMR) is a powerful characterisation method both in solution and in the solid state. Consequently, the prediction of NMR shieldings of atoms present in POM structures has been a habitual subject of study in recent years. NMR analysis of the ^{183}W nucleus has revealed as one of the principal characterisation tools in solution, providing direct information about the tungsten atoms' environment in these rather complex frameworks. The first DFT calculations of tungsten chemical shifts were carried out for small and simple molecules such as $[WO_{4-x}S_x]^{2-}$, $W(CO)_6$, WF_6 and WCl_6[134, 135] for which almost linear correlation between experimental and theoretical values was found. The first attempts to calculate NMR chemical shifts for large POMs were partially unsuccessful because of the large systematic error related to the use of basis sets with effective core potentials.[136] Then, some improvements in the calculations gave qualitative agreement between theory and experiments for a large number of oxidized and reduced POMs with different architectures,[137] but these results were still far from being quantitatively acceptable.[138] Incorporating spin-orbit (SO) corrections with the zeroth-order regular approximation (ZORA) formalism and including solvent effects in the calculations, Bagno and co-workers[139, 140] reported accurate ^{183}W chemical shifts, reaching an average mean error of 35 ppm in a series of POMs.[139] Poblet and co-workers demonstrated that standard DFT methods can be useful to rationalize chemical properties of POMs. Using standard functionals such as BP86 and Slater basis sets of TZP or similar quality, the computed geometries for these molecular oxygen-metal clusters[39] are good enough to reproduce and analyse vibrational[141] and electronic spectra,[93] electrochemical properties,[41] reactivity[142, 143] and some magnetic properties.[144] However, since NMR chemical shifts are very sensitive to small structural changes and, they analysed how a better computed geometry significantly reduces the error between experimental and theoretical ^{183}W NMR chemical shifts.[109] Furthermore, they analysed the influence of the solvent on tungsten chemical shifts[109] since in previous studies it was shown that X-ray POMs structures are always better reproduced if the geometries are optimized in solution than in gas phase.[145] Using these ideas, Bagno and co-workers demonstrated that computed ^{183}W chemical shifts in solution are, in general, much better than those computed in gas phase[139] without enlarging

the basis set.[109] On the other hand, experimental structures obtained from X-ray or neutron diffraction are not the best ones to compute the ^{183}W chemical shifts since NMR experiments are usually performed in solution and it is accepted that the structure of POMs in these conditions is somewhat different from that in the solid state.

To sum up, the observed ^{183}W NMR chemical shifts for POMs can be nicely reproduced if the chemical shifts are computed with a middle-sized basis set of TZP quality, including the SO corrections and the solvent effects and using a highly precise geometry obtained using a large basis set of QZ4P quality and also including the solvent effects. The mean average error (MAE) for the set of ^{183}W NMR signals computed in this way was 7.3 ppm, a value within the experimental error.[109]

We herein make use of the previous experience in the calculation of $\delta(^{183}W)$ in POMs to make the best possible estimates of $\delta(^{17}O)$, $\delta(^{31}P)$ and $\delta(^{205}Tl)$ for polyoxanions in solution.

1.7.1. Calculation of NMR parameters

In its simplest form, NMR is the study of the properties of molecules containing magnetic nuclei (that is, those featuring a nonzero nuclear net spin, $I \neq 0$) by applying an external magnetic field and observing the frequency at which resonance between the incident electromagnetic radiation and the nuclear spin transition takes place. In this way a spectrum can be generated for a compound containing one or several NMR-active atoms (for instance ^{1}H, ^{19}F or ^{13}C). Furthermore, NMR is a spectroscopic technique, which allows obtaining information about the chemical environment of the nuclei of atoms thanks to the interaction between them and a magnetic field.

The Stern-Gerlach experiment in 1922 provided evidence for the spin of electrons.[146, 147] They observed two discrete spots on the detector, when a beam of silver atoms was passed through a magnetic field. This suggests that the electron has an intrinsic angular momentum, called spin. It turns out that many nuclei also possess a net spin angular momentum. Orbital and spin angular momenta give rise to magnetic moments. The magnetic moment of the individual silver atoms could be oriented parallel or antiparallel to the external magnetic field, which is the same as saying that an atom in the magnetic model would be either paramagnetic or diamagnetic.

Then, Isidor Rabi and co-workers[148] showed that, by using a magnetic field, the atom beam could be manipulated. The series of experiments culminated in 1937 when they discovered state transitions induced by time varying fields or radio frequency fields.

The explanation of those phenomena is that when a magnetic field, B_0, is applied to an atom, it induces circulations in the electron cloud surrounding the nucleus such that a magnetic moment, μ, opposed to B_0, is produced. This means that the local magnetic field at the nucleus, B_{local}, is smaller than the applied field. This effect corresponds to the magnetic shielding of the nucleus that reduces B_0 by an amount equal to σB_0, where σ is the so-called shielding constant.

$$B_{local} = B_0 (1 - \sigma) \quad (1.1)$$

Therefore, when a magnetic field is applied to a molecule, the situation, as mentioned, becomes more complicated and the electron circulation within the entire molecule must be considered. The ability of the applied magnetic field to induce an electronic current in a molecule, and thus to affect the strength of the local magnetic fields of the atoms, depends on the details of the electronic structure nearby each nuclei. This implies that nuclei of the same element have different shielding constant when they take part of different chemical groups.

Accurate calculation of shielding constants is very difficult, but the trends in this magnitude are quite well understood. Computational difficulties are evident in general, except for small molecules. Detailed information on the electron density distribution in the ground and excited states is required, as well as excitation energies of the molecule. Nevertheless, it is easier to understand the different contributions in observed shielding constants, which is the sum of three contributions: the local contribution is due to the electrons surrounding the studied nuclei, the neighbouring group contribution is due to atoms that form the rest of the molecule, and finally the solvent contribution, coming from the molecules of the solution. The value of the local contribution, σ, is the sum of the diamagnetic (σ^d) and the paramagnetic (σ^p) components of the induced electronic motion.

$$\sigma \text{ (local)} = \sigma^d + \sigma^p \quad (1.2)$$

The diamagnetic contribution opposes to the applied magnetic field and shields (protects) the nucleus in question. In contrast, the paramagnetic contribution reinforces the applied magnetic field and deshields the nucleus. Furthermore, the total local contribution is positive if the diamagnetic contribution dominates, and is negative otherwise.

The diamagnetic contribution manifests as a circulation of charge in the ground state generated by the external field applied. Its magnitude notably depends on the electron density in the region closest to the nucleus, being broadly proportional to the electron density of the atom containing the nucleus of interest. So, it arises that the

shielding is decreased if the electron density on the atom is withdrawn by the influence of an electronegative atom or group of atoms nearby.

The paramagnetic contribution appears from the ability of the applied field to force electrons to circulate through the molecule by rising their energy. This effect may be viewed as electrons making use of the orbitals that are unoccupied in the ground state.

From the interaction of the nuclear magnetic moment with an external magnetic field, B_0, it can be traced a nuclear energy level diagram characterized by a set of eigenvalues and eigenstates. The adsorption of energy, the transition between two of these states, can be detected and plotted as a spectral line, which is called resonance signal. It is conventional to express resonance frequencies in terms of an empirical quantity called chemical shift, which is related to the difference between the resonance frequency, ν, of the nucleus of interest and that of a reference sample, ν^0:

$$\delta\ (\text{ppm}) = 10^6 \left(\frac{\nu - \nu^0}{\nu^0}\right) \quad (1.3)$$

1.7.1.1. Chemical Shifts

The fundamental quantity underpinning the phenomenon of chemical shift of a nucleus is its magnetic shielding tensor, σ.

Formally, the shielding tensor of nucleus A, σ_A, is obtained as the second derivative of the total quantum mechanical energy E of the system with respect to the external magnetic field B_0 and the magnetic moment μ_A of the nucleus.[149]

$$\sigma_A = \left.\frac{\partial^2 E}{\partial_{\mu A}\partial_{Bo}}\right|_{B=\mu=0} \quad (1.4)$$

The shielding tensor is a second-rank tensor represented by a 3×3 matrix, which is fully described by its diagonal values. Therefore, diagonalitzation of the symmetric part of σ provides the principal axis system with its three orthogonal eigenvectors and the three eigenvalues σ_{ii}.

In general, the NMR shielding tensor can be written as the sum of two contributions,[150] the paramagnetic and the diamagnetic parts. Even though if the relativistic theory is taking into account spin-orbit contribution are further included.

$$\sigma = \sigma^d + \sigma^p + \sigma^{SO} \quad (1.5)$$

The diamagnetic part depends only on the ground-state wave function, and the paramagnetic shielding, which depends also on the excited states of the unperturbed system, expressed in terms of the virtual (unoccupied) MOs. Diamagnetic contributions for a given nucleus tend to be rather similar for most chemical environments, so that the actual chemical shifts are usually dominated by the paramagnetic part. The leading contribution to a σ^{p} is given by the coupling between occupied and virtual MOs, due to the external field $\overrightarrow{B_0}$.

$$\sigma_{st}^{p} \propto \sum_{i}^{occ} n_i \sum_{\mu}^{N} u_{ai} \left\langle \psi_i \middle| \left[\frac{\overrightarrow{r_N}}{r_N^3} \times \vec{\mathrm{p}}\right] \middle| \psi_a \right\rangle \tag{1.6}$$

ψ_a and ψ_i describe virtual and occupied MOs (with occupation number n_i) respectively, r_N is the electronic position operator and p is the electronic momentum operator.

The magnitude of the coupling is given by u_{ai}, which can be expressed as:

$$u_{ai} \propto -\frac{1}{2(\varepsilon_i^0 - \varepsilon_a^0)} \langle \phi_{\mathrm{a}} | \widehat{M_u} | \phi_{\mathrm{i}} \rangle \tag{1.7}$$

Where ε_i^0 and ε_a^0 are the orbital energies of the occupied and unoccupied MOs and the integral is the first-order magnetic coupling between the occupied and unoccupied orbitals.

The action of the magnetic operator $\widehat{M_u}$ on ϕ_{q} is simply to work with $\vec{L}_u^v$ on each atomic orbital χ_v. Here $\vec{L}_u^v$ is the u-component of the angular momentum operator with its origin at the center $\vec{R}_v$ on which χ_v is situated. The electron orbital angular momentum operator (l_x, l_y, l_z) acts on atomic wavefunctions. For example,

$$l_x|\mathrm{p_y}\rangle = i\hbar|\mathrm{p_z}\rangle \tag{1.8}$$

A significant magnetic coupling occurs when an occupied MO localized around the atomic nucleus of interest can have considerable overlap with an unoccupied MO after 90° rotation about the direction of the external magnetic field.

1.7.1.2. Spin-Spin Couplings

The chemical shift is not the only source of information encoded in an NMR spectrum. In fact, there is another extremely valuable information contained in most NMR spectra, namely the magnetic interactions between nuclei, known as spin-spin coupling, scalar coupling, or *J* coupling. Magnetic interactions between nuclei give rise

to extra NMR lines which give valuable clues to the arrangement of atoms in molecules.

Whenever there are groups of NMR active nuclei present in the molecule there will be scalar coupling between them. The nuclei can be of the same element –homonuclear coupling– or of different elements –heteronuclear coupling.

Scalar coupling arises because the nuclear magnetic moments of other NMR-active nuclei surrounding the nucleus under observation produce small "extra" magnetic fields in addition to the fields due to the spectrometer and chemical shift. Thus the observed nucleus sees not one resultant field but several, depending on the number and nature of the surrounding NMR-active nuclei. As we shall see, unlike chemical shielding, the magnitude of scalar coupling depends only on the interaction of the nuclear magnetic dipoles so it does not vary from one instrument to another and so are reported in Hertz.

Nuclear spin-spin coupling, or *J*-coupling, is also a property of the electronic system. It represents the electron-mediated magnetic interaction of two nuclear spin magnetic moments. The interaction energy between nucleus A and B is described by the phenomenological interaction energy:[151]

$$E = m_A \overline{K}_{AB} m_B \tag{1.9}$$

where K_{AB} is the rank 2 indirect-reduced nuclear spin-spin coupling tensor and m_A, m_B are the nuclear spin magnetic moment vectors and can be written as the second derivative of the molecular energy E with respect to the nuclear moments $\mu_A=\gamma_A I_A$,

$$\mathrm{K_{jk}(A,B)} = \left.\frac{\partial^2 \mathrm{E}}{\partial \mu_{\mathrm{Aj}} \partial \mu_{\mathrm{Bk}}}\right|_{\mu_{\mathrm{Aj}}=\mu_{\mathrm{Bj}}=0} \tag{1.10}$$

The relation of the magnetic moment to the (dimensionless) nuclear spin vector is $m_A = \gamma_A \hbar I_A$. The rotational average of the tensor $\overline{K_{AB}}$ is the isotropic reduced indirect nuclear spin-spin coupling constant $K_{NM.}$ The term reduced refers to the definition of $\overline{K_{AB}}$ and its isotropic average as being independent of the nuclear magnetogyric ratios. The experimentally determined *J*-coupling constant is related to the reduced coupling via[152, 153]

$$J_{\mathrm{AB}} = \mathrm{h}\frac{\Upsilon_{\mathrm{A}}}{2\pi}\frac{\Upsilon_{\mathrm{B}}}{2\pi}\mathrm{K_{AB}} \tag{1.11}$$

As said, *J* coupling is the intramolecular interaction between two magnetic nuclei mediated by electrons. There are two basic mechanisms. The magnetic field of a nucleus locally induces a magnetic moment in the electronic system. This electronic

magnetic moment can occur in the form of either (i) an electron spin polarization, that is, a local increase or decrease of the probability of finding spin-up (alpha) or spin-down (beta) electrons or (ii) by including orbital ring current. The motion of electrons in a many-electron system is coupled by their electrostatic Coulomb interaction. Thus, local effects such as the locally induced electronic magnetic moment will have an effect on the electronic structure elsewhere in a molecule. The local magnetic moment is transferred to other parts of the molecule, mainly through the chemical bonds, and is then experienced by other nuclei. Generally, a pronounced distance effect can be observed since the more bonds in between the two nuclei, or the larger the internuclear distance, the weaker the *J* coupling is. For a short-range coupling through one or a few bonds, usually the *Fermi Contact* mechanism is the dominant one.[154] This mechanism originates in the spin polarization of the electronic system right at one of the nuclei, and the resulting interaction of the transferred spin polarization *right at* another nucleus. In computations, atomic nuclei are usually treated as point charges and point magnetic dipoles. The contact term is then caused by the mutual interaction between the nuclear and the electron spins at the locations of nuclei. Clearly, for coupling to occur, the bonding electrons must be able to sense, or contact, the nucleus. Only s electrons have a finite density at the nucleus so it is expected that the amount of s character of the molecular orbitals making chemical bond plays an important role in the strength of the coupling. Percentage of s character will be influenced by factors such as the hybridization, the coordination number, the electronegativity of substituents or the oxidation state.

1.8. Bibliography

[1] C. W. Sheele, *in Sämtliche Physische und Chemische Werke*, Niederwaluf/Wiesbaden, **1971 (Original: 1793)**.
[2] J. J. Berzelius, *Pogg. Ann. Phys. Chem.* **1826**, *6*, 363.
[3] C. Marginac, *C. R. Acad. Sci.* **1862**, *55*, 888.
[4] A. Miolati, P. Pizzighelli, *J. Prakt. Chem.* **1908**, *77*, 417.
[5] L. C. Pauling, *J. Am. Chem. Soc.* **1929**, *51*, 2868.
[6] J. F. Keggin, *Nature* **1933**, *131*, 908.
[7] A. J. Bradley, J. W. Illingworth, *Proc. Roy. Soc.* **1936**, *157*, 113.
[8] H. T. Evans, *Perspect. Struct. Chem.* **1971**, *4*, 1.
[9] M. T. Pope, A. Müller, *Angew. Chem.* **1991**, *30*, 34.
[10] C. L. Hill, *Chem. Rev.* **1998**, *98*, 1.
[11] D.-L. Long, R. Tsunashima, L. Cronin, *Angew. Chem., Int. Ed.* **2010**, *49*, 1736.
[12] L. Cronin, A. Muller, *Chem. Soc. Rev.* **2012**, *41*, 7333.
[13] D. L. Long, E. Burkholder, L. Cronin, *Chem. Soc. Rev.* **2007**, *36*, 105.
[14] H. N. Miras, J. Yan, D.-L. Long, L. Cronin, *Chem. Soc. Rev.* **2012**, *41*, 7403.
[15] X. López, J. J. Carbó, C. Bo, J. M. Poblet, *Chem. Soc. Rev.* **2012**, *41*, 7537.
[16] M. T. Pope, *Inorg. Chem.* **1972**, *11*, 1973.
[17] M. T. Pope, A. Muller, *Angew. Chem., Int. Ed. Engl.* **1991**, *30*, 34.
[18] D.-L. Long, P. Kögerler, L. J. Farrugia, L. Cronin, *Angew. Chem., Int. Ed.* **2003**, *42*, 4180.
[19] A. Müller, E. Krickemeyer, J. Meyer, H. Bögge, F. Peters, W. Plass, E. Diemann, S. Dillinger, F. Nonnenbruch, M. Randerath, C. Menke, *Angew. Chem., Int. Ed. Engl.* **1995**, *34*, 2122.
[20] A. Müller, E. Krickemeyer, H. Bögge, M. Schmidtmann, F. Peters, *Angew. Chem., Int. Ed.* **1998**, *37*, 3359.
[21] G. Herve, A. Teze, *Inorg. Chem.* **1977**, *16*, 2115.
[22] J. Canny, A. Teze, R. Thouvenot, G. Herve, *Inorg. Chem.* **1986**, *25*, 2114.
[23] M. Ibrahim, Y. Lan, B. S. Bassil, Y. Xiang, A. Suchopar, A. K. Powell, U. Kortz, *Angew. Chem., Int. Ed.* **2011**, *50*, 4708.
[24] C. P. Pradeep, D.-L. Long, P. Kogerler, L. Cronin, *Chem. Commun.* **2007**, 4254.
[25] B. S. Bassil, M. Ibrahim, R. Al-Oweini, M. Asano, Z. Wang, J. van Tol, N. S. Dalal, K.-Y. Choi, R. Ngo Biboum, B. Keita, L. Nadjo, U. Kortz, *Angew. Chem., Int. Ed.* **2011**, *50*, 5961.
[26] H.-Y. Zang, J.-J. Chen, D.-L. Long, L. Cronin, H. N. Miras, *Chem. Sci.* **2016**, *7*, 3798.
[27] Y.-F. Song, R. Tsunashima, *Chem. Soc. Rev.* **2012**, *41*, 7384.
[28] P. Gouzerh, A. Proust, *Chem. Rev.* **1998**, *98*, 77.
[29] A. Dolbecq, E. Dumas, C. R. Mayer, P. Mialane, *Chem. Rev.* **2010**, *110*, 6009.
[30] J. Tian, Z.-Y. Xu, D.-W. Zhang, H. Wang, S.-H. Xie, D.-W. Xu, Y.-H. Ren, H. Wang, Y. Liu, Z.-T. Li, *Nat Commun* **2016**, *7*.
[31] A. Muller, M. Penk, R. Rohlfing, E. Krickemeyer, J. Doring, *Angew. Chem., Int. Ed. Engl.* **1990**, *29*, 926.

[32] P. C. H. Mitchell, *Nature* **1990**, *348*, 15.
[33] M. T. Pope, *Heteropoly and Isopoly Oxometalates*, Springer-Verlag Berlin, **1983**.
[34] X. López, J. M. Maestre, C. Bo, J. M. Poblet, *J. Am. Chem. Soc.* **2001**, *123*, 9571.
[35] C. Sanchez, J. Livage, J. P. Launay, M. Fournier, Y. Jeannin, *J. Am. Chem. Soc.* **1982**, *104*, 3194.
[36] C. Sanchez, J. Livage, J. P. Launay, M. Fournier, *J. Am. Chem. Soc.* **1983**, *105*, 6817.
[37] T. Yamase, *Polyhedron* **1986**, *5*, 79.
[38] X. López, C. Bo, J. M. Poblet, *J. Am. Chem. Soc.* **2002**, *124*, 12574.
[39] J. M. Poblet, X. López, C. Bo, *Chem. Soc. Rev.* **2003**, *32*, 297.
[40] M. Boujtita, J. Boixel, E. Blart, C. R. Mayer, F. Odobel, *Polyhedron* **2008**, *27*, 688.
[41] J. A. Fernández, X. López, C. Bo, C. de Graaft, E. J. Baerends, J. M. Poblet, *J. Am. Chem. Soc.* **2007**, *129*, 12244.
[42] M.-H. Chiang, M. R. Antonio, L. Soderholm, *Dalton Trans.* **2004**, 3562.
[43] J. A. Fernández, X. López, J. M. Poblet, *J. Mol. Catal. A: Chem.* **2007**, *262*, 236.
[44] Y. Izumi, K. Matsuo, K. Urabe, *J. Mol. Catal.* **1983**, *18*, 299.
[45] Y. Izumi, K. Urabe, M. Onaka, *Zeolite, Clay, and Heteropoly Acid in Organic Reactions*, VCH, Weinheim, New York, **1992**.
[46] K. M. Barkigia, L. M. Rajkovic-Blazer, M. T. Pope, E. Prince, C. O. Quicksall, *Inorg. Chem.* **1980**, *19*, 2531.
[47] H. T. Evans, E. Prince, *J. Am. Chem. Soc* **1983**, *105*, 2531.
[48] M. I. Khan, J. Zubieta, P. Toscano, *Inorg. Chim. Acta* **1992**, *193*, 17.
[49] M. Isobe, F. Marumo, T. Yamase, T. Ikawa, *Acta Crystallogr.* **1978**, *B34*, 2728.
[50] W. G. Klemperer, W. Shum, *J. Am. Chem. Soc.* **1977**, *99*, 3544.
[51] L. C. W. Baker, J. S. Figgis, *J. Am. Chem. Soc.* **1970**, *92*, 3794.
[52] G. Herve, A. Teze, *Inorg. Chem.* **1977**, *16*, 2115.
[53] X. López, C. Bo, J. M. Poblet, *Inorg. Chem.* **2003**, *42*, 2634.
[54] X. López, P. Miró, J. J. Carbó, A. Rodríguez-Fortea, C. Bo, J. M. Poblet, *Theor. Chem. Acc.* **2011**, *128*, 393.
[55] J. Lehmann, A. Gaita-Arino, E. Coronado, D. Loss, *Nat Nano* **2007**, *2*, 312.
[56] K. Y. Monakhov, W. Bensch, P. Kogerler, *Chem. Soc. Rev.* **2015**, *44*, 8443.
[57] J. M. Clemente-Juan, E. Coronado, A. Gaita-Arino, *Chem. Soc. Rev.* **2012**, *41*, 7464.
[58] C. Ritchie, C. Streb, J. Thiel, S. G. Mitchell, H. N. Miras, D.-L. Long, T. Boyd, R. D. Peacock, T. McGlone, L. Cronin, *Angew. Chem., Int. Ed.* **2008**, *47*, 6881.
[59] A. Sartorel, M. Carraro, G. Scorrano, R. D. Zorzi, S. Geremia, N. D. McDaniel, S. Bernhard, M. Bonchio, *J. Am. Chem. Soc.* **2008**, *130*, 5006.
[60] Y. V. Geletii, B. Botar, P. Kögerler, D. A. Hillesheim, D. G. Musaev, C. L. Hill, *Angew. Chem., Int. Ed.* **2008**, *47*, 3896.
[61] Q. Yin, J. M. Tan, C. Besson, Y. V. Geletii, D. G. Musaev, A. E. Kuznetsov, Z. Luo, K. I. Hardcastle, C. L. Hill, *Science* **2010**, *328*, 342.
[62] J. J. Stracke, R. G. Finke, *J. Am. Chem. Soc.* **2011**, *133*, 14872.
[63] J. J. Stracke, R. G. Finke, *ACS Catal* **2013**, *3*, 1209.
[64] J. J. Stracke, R. G. Finke, *ACS Catal* **2014**, *4*, 79.
[65] M. Natali, S. Berardi, A. Sartorel, M. Bonchio, S. Campagna, F. Scandola, *Chem. Commun.* **2012**, *48*, 8808.

[66] S. Goberna-Ferrón, L. Vigara, J. Soriano-López, J. R. Galán-Mascarós, *Inorg. Chem.* **2012**, *51*, 11707.
[67] N. Mizuno, K. Yamaguchi, *Chem. Rec.* **2006**, *6*, 12.
[68] J. Piera, J. E. Backvall, *Angew. Chem., Int. Ed.* **2008**, *47*, 3506.
[69] C. L. Hill, *J. Mol. Catal. A: Chem.* **2007**, *262*, 2.
[70] S.-S. Wang, G.-Y. Yang, *Chem. Rev.* **2015**, *115*, 4893.
[71] M. Carraro, A. Sartorel, G. Scorrano, T. Carofiglio, M. Bonchio, *Synthesis* **2008**, 1971.
[72] B. Matt, J. Fize, J. Moussa, H. Amouri, A. Pereira, V. Artero, G. Izzet, A. Proust, *Energy Environ. Sci.* **2013**, *6*, 1504.
[73] H. Yanagie, A. Ogata, S. Mitsui, T. Hisa, T. Yamase, M. Eriguchi, *Biomed. Pharmacother.* **2006**, *60*, 349.
[74] F. Carn, N. Steunou, M. Djabourov, T. Coradin, F. Ribot, J. Livage, *Soft Matter* **2008**, *4*, 735.
[75] N. Gao, H. Sun, K. Dong, J. Ren, T. Duan, C. Xu, X. Qu, *Nat Commun* **2014**, *5*.
[76] J. Geng, M. Li, J. Ren, E. Wang, X. Qu, *Angew. Chem., Int. Ed.* **2011**, *50*, 4184.
[77] N. Gao, K. Dong, A. Zhao, H. Sun, Y. Wang, J. Ren, X. Qu, *Nano Research* **2016**, *9*, 1079.
[78] M. Li, C. Xu, J. Ren, E. Wang, X. Qu, *Chem. Commun.* **2013**, *49*, 11394.
[79] J. Schemberg, K. Schneider, D. Fenske, A. Müller, *ChemBioChem* **2008**, *9*, 595.
[80] J. Schemberg, K. Schneider, U. Demmer, E. Warkentin, A. Muller, U. Ermler, *Angew. Chem., Int. Ed.* **2007**, *46*, 2970.
[81] A. Solé-Daura, V. Goovaerts, K. Stroobants, G. Absillis, P. Jiménez-Lozano, J. M. Poblet, J. D. Hirst, T. N. Parac-Vogt, J. J. Carbó, *Chem. Eur. J.* **2016**, *22*, 15280.
[82] H. G. T. Ly, G. Absillis, R. Janssens, P. Proost, T. N. Parac-Vogt, *Angew. Chem., Int. Ed.* **2015**, *54*, 7391.
[83] C. Busche, L. Vila-Nadal, J. Yan, H. N. Miras, D.-L. Long, V. P. Georgiev, A. Asenov, R. H. Pedersen, N. Gadegaard, M. M. Mirza, D. J. Paul, J. M. Poblet, L. Cronin, *Nature* **2014**, *515*, 545.
[84] J. Sloan, G. Matthewman, C. Dyer-Smith, A. Y. Sung, Z. Liu, K. Suenaga, A. I. Kirkland, E. Flahaut, *ACS Nano* **2008**, *2*, 966.
[85] K. Kume, N. Kawasaki, H. Wang, T. Yamada, H. Yoshikawa, K. Awaga, *J. Mater. Chem. A* **2014**, *2*, 3801.
[86] S. Herrmann, C. Ritchie, C. Streb, *Dalton Trans.* **2015**, *44*, 7092.
[87] R. Liu, G. Zhang, H. Cao, S. Zhang, Y. Xie, A. Haider, U. Kortz, B. Chen, N. S. Dalal, Y. Zhao, L. Zhi, C.-X. Wu, L.-K. Yan, Z. Su, B. Keita, *Energy Environ. Sci.* **2016**, *9*, 1012.
[88] J.-S. Li, Y. Wang, C.-H. Liu, S.-L. Li, Y.-G. Wang, L.-Z. Dong, Z.-H. Dai, Y.-F. Li, Y.-Q. Lan, *Nat Commun* **2016**, *7*.
[89] Y. Ji, L. Huang, J. Hu, C. Streb, Y.-F. Song, *Energy Environ. Sci.* **2015**, *8*, 776.
[90] J. Xie, Y. Zhang, Y. Han, C. Li, *ACS Nano* **2016**, *10*, 5304.
[91] S. Romo, N. S. Antonova, J. J. Carbó, J. M. Poblet, *Dalton Trans.* **2008**, 5166.
[92] X. López, C. Nieto-Draghi, C. Bo, J. B. Avalos, J. M. Poblet, *J. Phys. Chem. A* **2005**, *109*, 1216.
[93] J. M. Maestre, X. López, C. Bo, J. M. Poblet, C. Daul, *Inorg. Chem.* **2002**, *41*, 1883.

[94] J. M. Maestre, J. M. Poblet, C. Bo, N. Casan-Pastor, P. Gómez-Romero, *Inorg. Chem.* **1998**, *37*, 3444.
[95] B. B. Bardin, R. J. Davis, M. Neurock, *J. Phys. Chem. B* **2000**, *104*, 3556.
[96] N. Suaud, A. Gaita-Arino, J. M. Clemente-Juan, E. Coronado, *Chem. Eur. J.* **2004**, *10*, 4041.
[97] A. E. Kuznetsov, Y. V. Geletii, C. L. Hill, K. Morokuma, D. G. Musaev, *Inorg. Chem.* **2009**, *48*, 1871.
[98] H. Taketa, S. Katsuki, K. Eguchi, T. Seiyama, N. Yamazoe, *J. Phys.Chem.* **1986**, *90*, 2959.
[99] K. Eguchi, T. Seiyama, N. Yamazoe, S. Katsuki, H. Taketa, *J. Catal.* **1988**, 336.
[100] F. Ritschl, R. Fricke, *J. Chem. Soc., Faraday Trans. 1* **1987**, *83*, 1041.
[101] G. Scholz, R. Luck, R. Stosser, H. J. Lunk, F. Ritschl, *J. Chem. Soc., Faraday Trans.* **1991**, *87*, 717.
[102] G. Scholz, R. Stosser, F. Ritschl, R. Luck, *Z. Chem.* **1990**, *30*, 183.
[103] S. A. Jansen, D. J. Singh, S. H. Wang, *Chem. Mater.* **1994**, *6*, 146.
[104] S. H. Wang, S. A. Jansen, D. J. Singh, *J. Catal.* **1995**, *154*, 137.
[105] S. A. Jansen, S. H. Wang, A. D. Eddowes, *Supermol. Sci.* **1997**, *4*, 51.
[106] J. Y. Kempf, M. M. Rohmer, J. M. Poblet, C. Bo, M. Benard, *J. Am. Chem. Soc.* **1992**, *114*, 1136.
[107] M. M. Rohmer, M. Bénard, *J. Am. Chem. Soc* **1994**, *116*, 6959.
[108] J. P. Biaudeau, M. M. Rohmer, M. Bénard, N. E. Ghermani, *C. R. Chimie* **1998**, *1*, 319.
[109] L. Vilà-Nadal, J. P. Sarasa, A. Rodríguez-Fortea, J. Igual, L. P. Kazansky, J. M. Poblet, *Chem. Asian J.* **2010**, *5*, 97.
[110] M. Pascual-Borràs, X. López, A. Rodríguez-Fortea, R. J. Errington, J. M. Poblet, *Chem. Sci.* **2014**, *5*, 2031.
[111] X. López, C. Nieto-Draghi, C. Bo, J. B. Avalos, J. M. Poblet, *J. Phys. Chem. A* **2005**, *109*, 1216.
[112] D. Volkmer, B. Bredenkötter, J. Tellenbröker, P. Kögerler, D. G. Kurth, P. Lehmann, H. Schnablegger, D. Schwahn, M. Piepenbrink, B. Krebs, *J. Am. Chem. Soc.* **2002**, *124*, 10489.
[113] L. Vilà-Nadal, S. G. Mitchell, A. Rodríguez-Fortea, H. N. Miras, L. Cronin, J. M. Poblet, *Phys. Chem. Chem. Phys.* **2011**, *13*, 20136.
[114] P. Jiménez-Lozano, J. J. Carbó, A. Chaumont, J. M. Poblet, A. Rodríguez-Fortea, G. Wipff, *Inorg. Chem.* **2014**, *53*, 778.
[115] X. Aparicio-Anglès, P. Miró, A. Clotet, C. Bo, J. M. Poblet, *Chem. Sci.* **2012**, *3*, 2020.
[116] S. Goberna-Ferrón, B. Peña, J. Soriano-López, J. J. Carbó, H. Zhao, J. M. Poblet, K. R. Dunbar, J. R. Galán-Mascarós, *J. Catal.* **2014**, *315*, 25.
[117] N. Watfa, D. Melgar, M. Haouas, F. Taulelle, A. Hijazi, D. Naoufal, J. B. Avalos, S. Floquet, C. Bo, E. Cadot, *J. Am. Chem. Soc.* **2015**, *137*, 5845.
[118] J. M. Cameron, L. Vilà-Nadal, R. S. Winter, F. Iijima, J. C. Murillo, A. Rodríguez-Fortea, H. Oshio, J. M. Poblet, L. Cronin, *J. Am. Chem. Soc.* **2016**, *138*, 8765.
[119] C. Fonseca Guerra, J. G. Snijders, G. te Velde, E. J. Baerends, *Theor. Chem. Acc.* **1998**, *99*, 391.

[120] G. te Velde, F. M. Bickelhaupt, E. J. Baerends, C. Fonseca Guerra, S. J. A. van Gisbergen, J. G. Snijders, T. Ziegler, *J. Comput. Chem.* **2001**, *22*, 931.
[121] ADF2013, SCM, Theoretical chemistry, Vrije Universiteit, Amsterdam, The Netherlands, https:// www.scm.com.
[122] E. V. Lenthe, E. J. Baerends, J. G. Snijders, *J. Chem. Phys.* **1993**, *99*, 4597.
[123] E. V. Lenthe, E. J. Baerends, J. G. Snijders, *J. Chem. Phys.* **1994**, *101*, 9783.
[124] E. V. Lenthe, A. Ehlers, E. J. Baerends, *J. Chem. Phys.* **1999**, *110*, 8943.
[125] A. D. Becke, *Phys. Rev. A* **1988**, *38*, 3098.
[126] J. P. Perdew, *Phys. Rev. B* **1986**, *33*, 8822.
[127] X. López, I. A. Weinstock, C. Bo, J. P. Sarasa, J. M. Poblet, *Inorg. Chem.* **2006**, *45*, 6467.
[128] M. J. T. Frisch, G. W.; Schlegel, H. B.; Scuseria, G. E.; Robb, M. A.; Cheeseman, J. R.; Scalmani, G.; Barone, V.; Mennucci, B.; Petersson, G. A.; Nakatsuji, H.; Caricato, M.; Li, X.; Hratchian, H. P.; Izmaylov, A. F.; Bloino, J.; Zheng, G.; Sonnenberg, J. L.; Hada, M.; Ehara, M.; Toyota, K.; Fukuda, R.; Hasegawa, J.; Ishida, M.; Nakajima, T.; Honda, Y.; Kitao, O.; Nakai, H.; Vreven, T.; Montgomery, J. A., Jr.; Peralta, J. E.; Ogliaro, F.; Bearpark, M.; Heyd, J. J.; Brothers, E.; Kudin, K. N.; Staroverov, V. N.; Kobayashi, R.; Normand, J.; Raghavachari, K.; Rendell, A.; Burant, J. C.; Iyengar, S. S.; Tomasi, J.; Cossi, M.; Rega, N.; Millam, J. M.; Klene, M.; Knox, J. E.; Cross, J. B.; Bakken, V.; Adamo, C.; Jaramillo, J.; Gomperts, R.; Stratmann, R. E.; Yazyev, O.; Austin, A. J.; Cammi, R.; Pomelli, C.; Ochterski, J. W.; Martin, R. L.; Morokuma, K.; Zakrzewski, V. G.; Voth, G. A.; Salvador, P.; Dannenberg, J. J.; Dapprich, S.; Daniels, A. D.; Farkas, Ö.; Foresman, J. B.; Ortiz, J. V.; Cioslowski, J.; Fox, D. J. Gaussian, Inc., Wallingford CT, (2009).
[129] A. D. Becke, *J. Chem. Phys.* **1993**, *98*, 5648.
[130] P. J. Stephens, F. J. Devlin, C. F. Chabalowski, M. J. Frisch, *J. Phys. Chem.* **1994**, *98*, 11623.
[131] D. Ravelli, D. Dondi, M. Fagnoni, A. Albini, A. Bagno, *J. Comput. Chem.* **2011**, *32*, 2983.
[132] A. Klamt, *J. Phys. Chem.* **1995**, *99*, 2224.
[133] S. Miertus, E. Scrocco, J. Tomasi, *Chem. Phys.* **1981**, *55*, 117.
[134] A. Rodríguez-Fortea, P. Alemany, T. Ziegler, *J. Phys. Chem. A* **1999**, *103*, 8288.
[135] M. Hada, H. Kaneko, H. Nakatsuji, *Chem. Phys. Lett.* **1996**, *261*, 7.
[136] A. Bagno, M. Bonchio, *Chem. Phys. Lett.* **2000**, *317*, 123.
[137] J. Gracia, J. M. Poblet, J. Autschbach, L. P. Kazansky, *Eur. J. Inorg. Chem.* **2006**, 1139.
[138] J. Gracia, J. M. Poblet, J. A. Fernández, J. Autschbach, L. P. Kazansky, *Eur. J. Inorg. Chem.* **2006**, 1149.
[139] A. Bagno, M. Bonchio, J. Autschbach, *Chem. Eur. J.* **2006**, *12*, 8460.
[140] A. Bagno, M. Bonchio, *Angew. Chem., Int. Ed.* **2005**, *44*, 2023.
[141] A. J. Bridgeman, *Chem. Eur. J.* **2006**, *12*, 2094.
[142] D. Quiñonero, Y. Wang, K. Morokuma, L. A. Khavrutskii, B. Botar, Y. V. Geletii, C. L. Hill, D. G. Musaev, *J. Phys. Chem. B* **2005**, *110*, 170.
[143] D. Kumar, E. Derat, A. M. Khenkin, R. Neumann, S. Shaik, *J. Am. Chem. Soc.* **2005**, *127*, 17712.

[144] H. Duclusaud, S. A. Borshch, *J. Am. Chem. Soc.* **2001**, *123*, 2825.
[145] X. López, J. A. Fernández, S. Romo, J. F. Paul, L. Kazansky, J. M. Poblet, *J. Comput. Chem.* **2004**, *25*, 1542.
[146] M. A. Nielsen, I. L. Chuang, *Quantum Computation and Quantum Information*, Cambridge University Press, **2000**.
[147] W. Gerlach, O. Stern, *Zeitschrift Fur Physik* **1922**, *9*, 353.
[148] Rabi, II, *Phys. Rev.* **1937**, *51*, 0652.
[149] J. Grotendorst, *Modern Methods and Algorithms of Quantum Chemistry: Winterschool, 21 - 25 February 2000, Forschungszentrum Jülich, Germany : Poster Presentations*, NIC Directors, **2000**.
[150] G. Schreckenbach, *Inorg. Chem.* **2002**, *41*, 6560.
[151] J. Autschbach, in *Encyclopedia of Analytical Chemistry*, John Wiley & Sons, Ltd, **2006**.
[152] J. Autschbach, T. Ziegler, *J. Chem. Phys.* **2000**, *113*, 9410.
[153] J. Autschbach, T. Ziegler, *J. Chem. Phys.* **2000**, *113*, 936.
[154] J. Autschbach, B. L. Guennic, *J. Chem. Educ.* **2007**, *84*, 156.

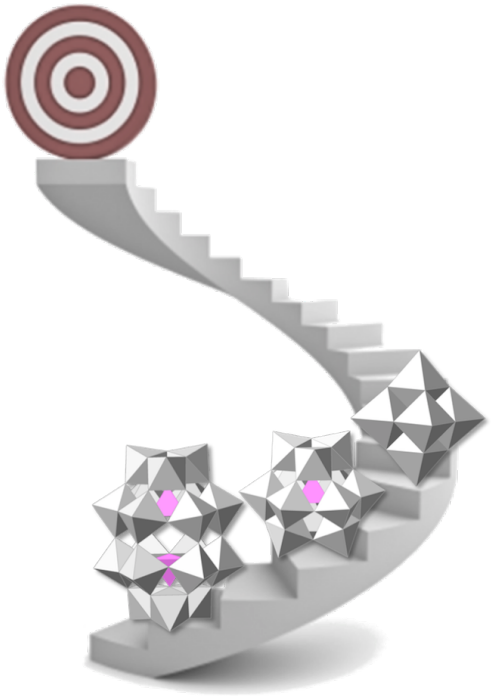

CHAPTER 2

Goals of this Thesis

CHAPTER 2

Goals of this Thesis

This thesis has contributed to enlarge our knowledge of some aspects related to Polyoxometalate chemistry. Some of the studies are collaborations with experimentalist groups studying Polyoxometalates, so we were able to take advantage of both disciplines, computational and experimental, in order to understand some aspects of this chemistry. During this research, we were interested in NMR calculations of POMs, including chemical shifts as well as spin coupling constants. On the other hand, we aimed to understand and rationalize the structure, properties and reactivity of different POMs. The specific objectives of each study are described below to clarify what were our thoughts at the begging of each project.

Chapter 3. ^{17}O NMR Chemical Shifts in Oxometalates

This work has been done in collaboration with Dr. John R. Errington's group (Newcastle University, UK).

One of the most used techniques for POM characterization is ^{17}O NMR. The Dr. Errington's masters this technique and we aimed to understand which factors affect the chemical shift of oxygen atoms in POMs. Therefore, the principal objectives were:

- to understand the features of calculations on NMR chemical shifts and the factors governing them,
- to develop an optimal computational strategy, in terms of cost and performance, in order to reproduce experimental ^{17}O NMR chemical shifts,

- to study the ^{17}O NMR chemical shift dependence on the metal, binding mode and protonation.

Chapter 4. ^{31}P NMR Calculations on Polyoxometalates

Following the knowledge acquired during the study of ^{17}O NMR chemical shifts, we pursued the understanding and rationalization of ^{31}P NMR, another powerful way for structural characterization and monitoring of chemical reactions of heteropolyanions. Then, the main goals were:

- to make use of the previous experience to find the best computational strategy for computing accurate $\delta(^{31}P)$ of solvated POMs,
- endeavour to understand how $\delta(^{31}P)$ depends on the geometrical and electronic properties of the molecule.

Chapter 5. Thallium(III) Containing POM: Structure and NMR

This work has been done in collaboration with two different research groups: Dr. Kortz's group (Jacobs University, Bremen, Germany) and Dr. Tóth's group (University of Debrecen, Hungary). All three groups aimed to identify and characterise a thallium-containing POM. Our objectives in this project were:

- Study the stability in solution of the thallium-containing POM by DFT calculations.
- Determine if the thallium-containing POM is protonated in solution and where are these protons localised.
- Reproduce the ^{205}Tl NMR chemical shifts and $^{203/205}Tl$-^{183}W spin-spin coupling constants.

Chapter 6. Photochemical H_2 Evolution by an Iridium (III)-photosensitized Polyoxometalate

This work has been done in collaboration with Prof. Anna Proust and Dr. Guillaume Izzet (Université Pierre et Marie Curie, Paris, France). They have designed a covalent Ir(III)-photosensitized POM, capable of efficiently evolve H_2 in the presence of excess acid and a sacrificial electron donor. We aimed to gain knowledge of the H_2 evolving

mechanism by means of DFT calculations and to rationalize the previously observed behavior. Therefore, the principal objectives were:

- to identify the species formed during the photoreduction of the POM,
- to characterize the species formed during the H_2 evolution reaction,
- to determine the catalytic species of the reaction,
- to reproduce the electrochemical and photochemical aspects of the reaction.

Chapter 7. Mechanistic Studies on Heterometallic Lindqvist and Keggin-type POMs

This work has been done in collaboration with Dr. John R. Errington's group (Newcastle University, UK). They studied experimentally the protonolysis of different heterometallic Lindqvist and Keggin POMs and they found different behaviors, which we aimed to unravel. Furthermore, some experimental work related to my stage in their group is reported in this chapter. The main goals were:

- to find differences in the methanolysis process for $(TBA)_3[(MeO)TiW_5O_{18}]$ and $(TBA)_3[(MeO)TiMo_5O_{18}]$,
- to determine the reaction mechanism for the protonolysis of Lindqvist- and Keggin-type POMs,
- to study how different metal atoms affect the hydrolysis reaction in heterometallic POMs,
- to rationalize the protonation of $(TBA)_6[(\mu\text{-}O)(TiW_5O_{18})_2]$ for future applications.

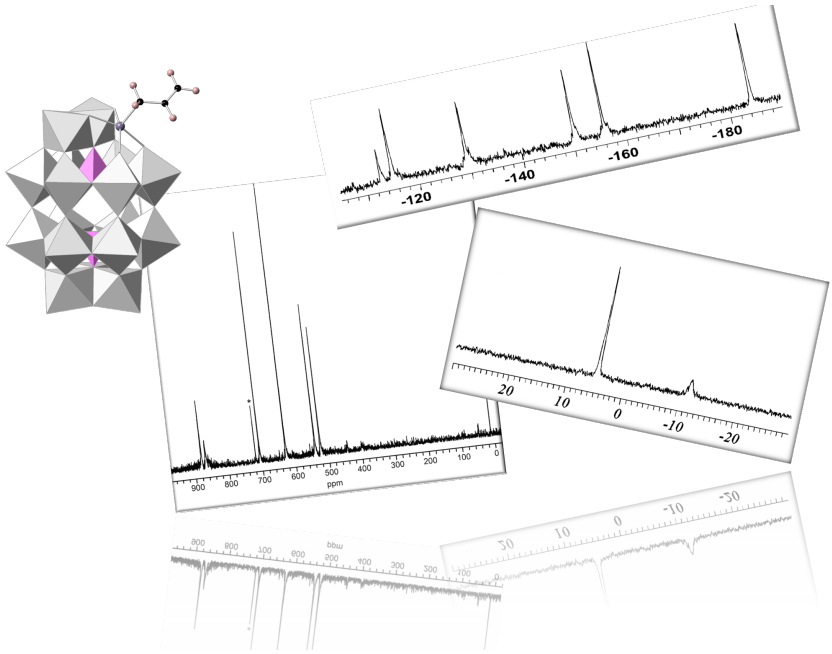

PART I

NMR Calculations

PART I

NMR Calculations

Nuclear Magnetic Spectroscopy (NMR) is the most used spectroscopic technique for compounds characterization. In POMs chemistry, ^{17}O, ^{1}H, ^{31}C, ^{31}P or even ^{183}W have been the most common nuclei in NMR characterization. Following the knowledge acquired from the study on ^{183}W chemical shift calculations published by our group, we whish we could reproduce ^{17}O NMR chemical shifts. Besides, our interest in ^{17}O NMR chemical shifts had increased and we finally reported the influences of these chemical shifts on bonding mode, metal and protonation. A similar study for ^{31}P NMR has been reported. ^{31}P is mostly used in monitoring chemical reactions in POMs. Afterwards, the ^{205}Tl project came up and we have been able to reproduce the ^{205}Tl NMR chemical shift. Furthermore, an extensive analysis of ^{203}Tl-^{205}Tl spin-spin couplings has been performed. The reader will find all these three projects in Part I of this thesis.

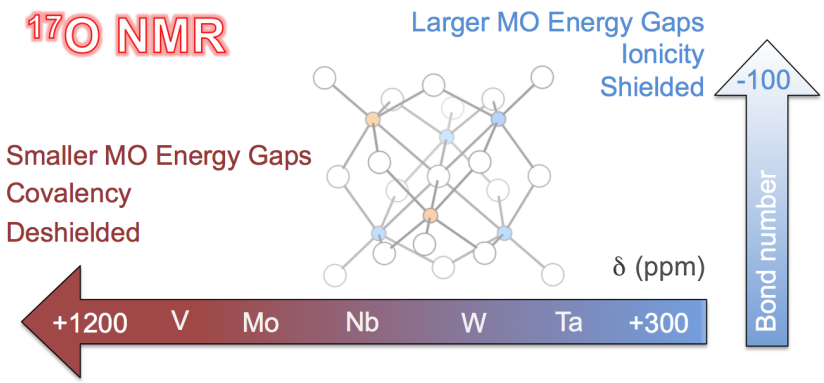

CHAPTER 3

^{17}O NMR Chemical Shifts in Oxometalates

Related publications:

M. Pascual-Borràs, X. López, A. Rodríguez-Fortea, R.J. Errington and J.M. Poblet, *Chem. Sci.* **2014**, 5, 2031.

CHAPTER 3

^{17}O NMR Chemical Shifts in Oxometalates

We report a theoretical analysis on ^{17}O NMR chemical shifts for a family of prototypical polyoxometalate anions. The huge diversity of structures and compositions in this family of oxometalates provides a unique resource for evaluating the influence of the metal type and connectivity over the resonance of ^{17}O nuclei. For a set of 75 signals, we show that DFT calculations performed with the GGA-type PBE functional, including spin-orbit and scaling corrections, provide a mean absolute error <30 ppm, a small value considering that the range of δ(^{17}O) values in these systems is ~1200 ppm. Moreover, the dependence of the δ(^{17}O) values on the neighboring metal atoms and bonding modes are also analysed. Finally, we explored the effect of protonation on δ(^{17}O) and demonstrated that ^{17}O NMR can be a powerful tool to identify the site(s) of protonation at low pH.

3.1. Introduction

From the pioneering studies on the magnetic properties of atomic nuclei, it was quickly understood that nuclear resonance frequencies depend on the chemical and electronic environment of the nuclei.[1-3] This property has been used for many years and, thus, nuclear magnetic resonance (NMR) has become probably the most popular chemical characterization technique. Despite the fact that oxygen is one of the most important elements chemically and biologically, other nuclei such as ^{1}H, ^{13}C, ^{31}P, or even ^{183}W have been prevalent in NMR studies of polyoxotungstates. The reasons are manifold, although the main shortcoming is the low natural abundance (0.037%) of the active I = 5/2 nucleus. Thus, enrichment of the sample with ^{17}O is needed. In addition,

$\delta(^{17}O)$ NMR signals are problematic to determine accurately compared with ^{1}H or ^{13}C because the nuclear quadrupolar interaction for ^{17}O is very often much larger than the magnetic shielding interaction, thus causing significant line broadening in NMR spectra. However, recent advances in instrumentation, the extremely large chemical shift (δ) range —up to 2000 ppm— and the availability of ^{17}O-enriched compounds have allowed an increasing use of ^{17}O NMR spectroscopy.[4, 5] In 1965, ^{17}O NMR was applied to the $Cr_2O_7^{2-}$ anion.[6, 7] Soon after, the ^{17}O NMR spectra of a range of other oxometalates were obtained.[8-10] In a systematic study of ^{17}O NMR parameters of POM structures, Klemperer and co-workers clearly established the relationship between chemical shift and metal-oxygen bond lengths.[11]

Modern quantum chemistry methods have always encountered more difficulties in describing systems containing transition metal atoms than simpler organic molecules, where approximate methods such as the density functional theory (DFT) have had great success from the beginning. However, the last two decades have seen the success of computational chemistry in tackling practically any physicochemical property related to POMs.[12] Quantum chemistry calculations of NMR properties in POMs started around 2000 with the study of $\delta(^{183}W)$ in several typical structures, though with rather poor accuracy.[13] Increasing accuracy was achieved in subsequent analyses that incorporated spin-orbit (SO) corrections, solvent effects and better geometry optimizations.[14-17] We herein make use of previous experience in the calculation of $\delta(^{183}W)$ in POMs[18] to calculate the best possible $\delta(^{17}O)$ values for mixed-metal polyoxoanions in solution. We first made an extensive exploration of density functionals and basis sets to establish a good strategy to determine accurate values. In addition, the diversity of POMs studied provides a unique opportunity to compare δ values of nuclei bonded to different transition metals, allowing us to clearly identify and understand factors contributing to these values. In the present work we focused on two main goals. First, we applied several computational methodologies based on the DFT to predict $\delta(^{17}O)$ with the best accuracy possible. Secondly, we sought to understand the dependence of $\delta(^{17}O)$ in POMs on the position, connectivity, vicinal metal atoms and degree of protonation of the relevant O atoms.

3.2. Computational Details

Density functional theory (DFT) calculations were performed using the ADF2010 package.[19] In the present work we apply a family of functionals, either GGA-type[20-27] or hybrid.[28-30] The latter include some % of exact Hartree-Fock exchange, which makes them more computationally demanding. The process for obtaining the ^{17}O NMR chemical shifts consists of (i) a geometry optimization step and (ii) a single-point NMR

calculation, a procedure expressed throughout the text as $Functional_{NMR}/Basis_{NMR}//Functional_{OPT}/Basis_{OPT}$. The basis sets utilized are all-electron of triple-ζ+ polarization (TZP) or triple-ζ+ double polarization (TZ2P) quality for all atoms with scalar relativistic corrections to the electrons via the zeroth-order regular approximation (ZORA).[31-33] We also tested the results for the large QZ4P basis set. The geometry optimizations were carried out under the constraints of the maximal point group symmetry of each molecule (reported in Figure 3.1) and with high numerical integration accuracy (parameter set to 6 in ADF). Since were dealing with anionic species in solution, we applied the effects of solvent and counterions as a continuum via the conductor-like screening model (COSMO), with a given dielectric constant (ε) that induces charge polarization on a surface around the molecule.[34, 35] Taking the optimized geometry, the NMR single-point calculation is done for the target and reference (H_2O) compounds introducing spin-orbit (SO) corrections and the GIAO method.[36-38] The calculated chemical shift is determined as $\delta_{cal} = \sigma_{ref} - \sigma_x$, where σ_x and σ_{ref} are the isotropic average shielding for the nucleus of the target and the reference compounds, respectively.

The quality of a given calculation is referred to the mean absolute error (MAEs) either per site or as an average of them. The reported MAE values have been obtained as:

$$\mathrm{MAE} = \frac{1}{N}\sum_i \left|\delta_{\mathrm{cal},i} - \delta_{\mathrm{exp},i}\right| \qquad (3.1)$$

where $\delta_{cal,i}$ and $\delta_{exp,i}$ are the calculated and experimental chemical shifts, respectively.

Figures 3.1 explain how the chemical shifts for oxygens of the *same type* (equivalent or not) are obtained from computations for $[MW_5O_{19}]^{n-}$ and $[M_2W_4O_{19}]^{n-}$, respectively.

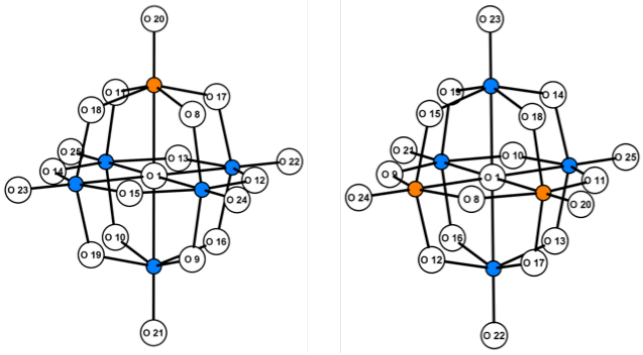

C_{4v}

Oxygen label	Nr. Of symmetry equivalent positions	Type	Compd. value		Tabulated value
1	x1	M_6O	δ_1		δ_1
20	x1	M=O	δ_2		δ_2
8,11,17,18	x4	MOW	δ_3		δ_3
22-25	x4	W=O	δ_4	}	$(4\cdot\delta_4 + \delta_5)/5$
21	x1	W=O	δ_5		
12-15	x4	W_2O	δ_6	}	$(\delta_6 + \delta_7)/2$
9,10,16,1,9	x4	W_2O	δ_7		

C_{2v}

Oxygen label	Nr. Of symmetry-equivalent positions	Type	Compd. value		Tabulated value
1	x1	M_6O	δ_1		δ_1
20,24	x2	M=O	δ_2		δ_2
8	x1	M_2O	δ_3		δ_3
12,15,17,18	x4	MOW	δ_4	}	$(4\cdot\delta_4 + 2\cdot\delta_5)/6$
9,10	x2	MOW	δ_5		
21,25	x2	W=O	δ_6	}	$(\delta_6 + \delta_7)/2$
22,23	x2	W=O	δ_7		
10	*x1*	*W_2O*	δ_8	}	$(\delta_8 + 4\cdot\delta_9)/5$
13,14,16,19	*x4*	*W_2O*	δ_9		

Figure 3. 1. Two examples illustrating how the ^{17}O chemical shifts for compounds featuring several non-equivalent oxygens *of the same type* are tabulated from computations. Oxygen labels for MW_5O_{19} and $M_2W_4O_{19}$ hexametalate compounds are displayed showing their point group symmetries. The molecular orientations are chosen to facilitate seeing the equivalence of sites. To the right, we specify how the different oxygen positions are grouped into types. In the chapter, the tabulated values refer to *oxygen types* and are listed as averaged values of the signals computed as indicated.

3.3. Results and Discussion

3.3.1. Calculation of accurate δ(^{17}O) for mixed-metal polyoxometalate

The family of POM structures represented in Figure 3.2 has been computed and analysed at the DFT level to provide a large set of δ(^{17}O) values. The compounds can be organized into two main groups:

(i) **Single- and mixed-metal hexametalate compounds** based on the Lindqvist framework, $[M_6O_{19}]^{n-}$ and $[M_{6-x}W_xO_{19}]^{n-}$. Single-metal compounds, $[M_6O_{19}]^{2-}$ (Figure 3.2a), feature terminal (M=O), bridging (M_2O) and central (M_6O) oxygen types. The latter, internal site is weakly connected to the six M atoms. The mixed-metal derivatives $[M_xW_{6-x}O_{19}]^{n-}$ with M = V^V, Ta^V or Nb^V (Figure 3.2b-d), present the same three types of structural oxygen types but they can be bonded to more than one metal type, introducing additional variability to the ^{17}O NMR values.

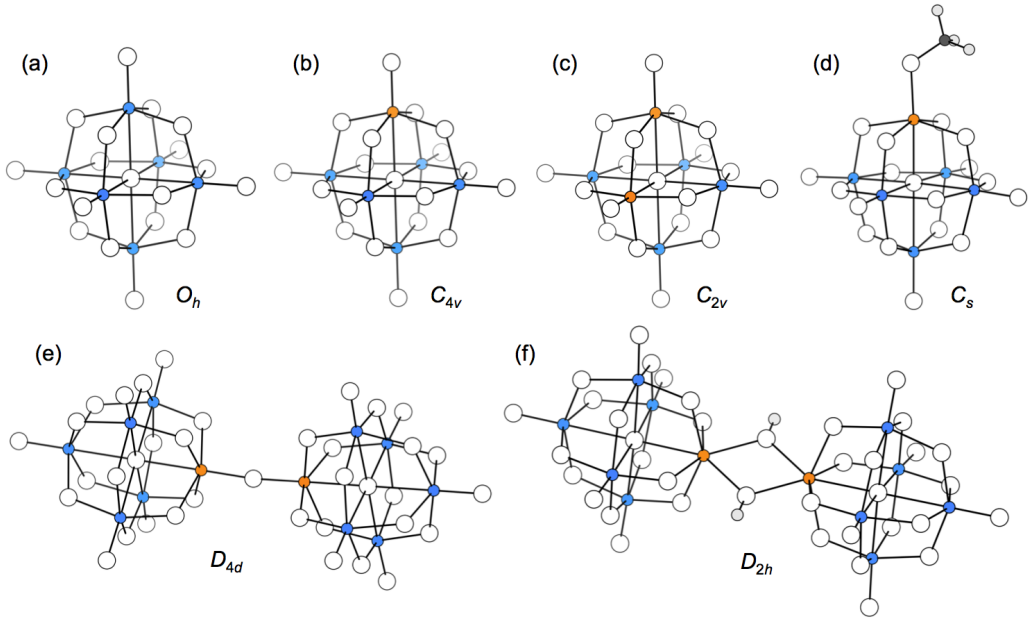

Figure 3. 2. Main structures analysed, with oxygens as white spheres: (a) $[M_6O_{19}]^{n-}$, (b) $[MW_5O_{19}]^{n-}$, (c) $[M_2W_4O_{19}]^{n-}$, (d) $[(MeO)MW_5O_{18}]^{n-}$, (e) $[(\mu\text{-}O)(TiW_5O_{18})_2]^{6-}$, (f) $[\{(\mu\text{-}HO)ZrW_5O_{18}\}_2]^{6-}$. Blue atoms are W, orange are M ≠ W. Point group symmetries are also shown.

(ii) **Larger structures:** dimers of the Lindqvist anion, $[(\mu\text{-O})(TiW_5O_{18})_2]^{6-}$ and $[\{(\mu\text{-HO})ZrW_5O_{18}\}_2]^{6-}$ (Figure 3.2e-f). The Keggin, $[XW_2O_{40}]^{n-}$ (X = P, Si), and Wells-Dawson $[P_2W_{18}O_{62}]^{6-}$ anions also feature terminal (M=O) and bridging (M_2O) oxygens, plus the internal (XOM_3) sites. Figure 3.3 shows the M-O connectivity modes of the POM structures presented.

Many variables affect the quality of the chemical shifts from computational techniques. A comprehensive analysis of the various sources of improvement in DFT calculations were studied for ^{99}Ru in $[Ru(CO)_3I_3]^-$.[39] The accurate determination is affected principally, besides the inclusion of the spin-orbit and solvent effects,[40] by the density functional and the basis set size. In the first part of this work we discuss the influence of the latter two on the quality of the computed ^{17}O NMR chemical shifts.

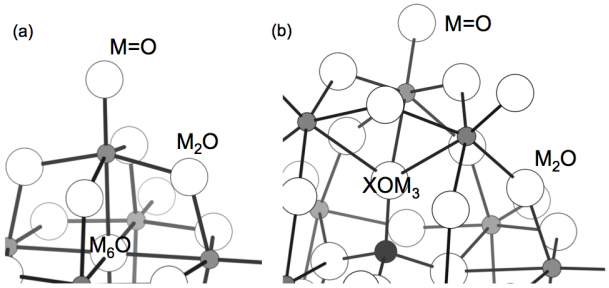

Figure 3. 3. Typical binding modes in (a) Lindqvist-type and (b) Wells-Dawson- and Keggin-type POMs. White spheres are oxygen atoms.

3.3.1.1. Selection of the density functional

We first focus on the effect of the density functional on the calculation of ^{17}O NMR chemical shifts. Table 3.1 shows a family of $\delta(^{17}O)$values computed for the simple $[W_6O_{19}]^{2-}$ structure. We carried out single-point calculations with various GGA and hybrid functionals after having optimized the geometry with the B3LYP functional and a TZP basis set. A comparison of the calculated values with the experimental ones shows that the three distinct oxygen types of $[W_6O_{19}]^{2-}$ (terminal, bridging and central) can be clearly resolved with any functional. However, there is an evident overestimation of the computed $\delta(^{17}O)$, that is, they are too positive with only a few exceptions. Recent theoretical studies[41, 42] on ^{17}O NMR of terminal transition-metal oxo compounds based on DFT using ZORA show that, in general, DFT calculations reproduce the experimental chemical shifts reasonably well but the results are not within the experimental error. In the present case, the accuracy achieved is modest, as shown in the rightmost column of Table 3.1, with averaged MAEs ranging 40–58 ppm.

The errors obtained with GGA functionals were found to be around 40–48 ppm, whereas the MAEs with hybrid functionals are ~10 ppm larger than GGA ones. GGA functionals perform very well for the tungsten terminal oxygen (W=O) whereas the error is larger for the bridging one (W_2O). Conversely, the central μ_6-O oxygen is better reproduced with hybrid functionals, probably because these are able to reproduce their special electronic properties, namely its more ionic nature, weakly bound and highly charged oxygen atom. We have observed that the GGA-type PBE and OPBE functionals perform better than the more time-consuming hybrid functionals (PBE0 and B3LYP). Previous studies testing a variety of density functional methods for small molecules also found that the OPBE performs remarkably well.[43, 44]

Table 3. 1.^{17}O chemical shifts[a] of the three oxygen positions of $[W_6O_{19}]^{2-}$ obtained with various functionals.

Functional	δ_{calc}			MAE
	W_2O	W=O	W_6O	
B3LYP	500	842	–57	58
PBE0	489	841	–62	52
BP86	497	790	–30	48
PW91	498	785	–31	47
SSB-D	458	728	–30	47
PBE	490	784	–32	44
OPBE	477	759	–36	40
δ_{exp}[b]	416	775	–80	

[a]Values in ppm. Methods are sorted by descending MAE. The geometry was optimized with the B3LYP functional and a TZP basis set. [b]Data taken from Ref. [17].

3.3.1.2. Effect of the basis set

The second issue to analyze is the effect of the basis set and the density functional on the geometry optimization step and, therefore, on the ^{17}O chemical shifts. We applied different combinations of these variables, as shown in Table 3.2, for the family of $[W_6O_{19}]^{2-}$ and $[M_2W_4O_{19}]^{4-}$ hexametalates (M = Ta, Nb, V) (Figure 3.2a,c). The nomenclature of the methodologies is described in the Computational Details section. Thus, for instance, the PBE/TZP//B3LYP/TZ2P method consists of a geometry optimization carried out with the B3LYP functional and a TZ2P basis set, whereas the single-point calculation for the NMR values is performed with a PBE functional and a TZP basis set. The number of $\delta(^{17}O)$ signals obtained with each methodology is 17 (see Tables A1–A9), sufficiently large to give reliable information about the quality of the

results. The MAEs are listed per specific oxygen type and an average of the 17 signals (rightmost column of Table 3.2) for each computational procedure.

Table 3. 2. Site-specific and average MAEs[a] for the $\delta(^{17}O)$ of $[W_6O_{19}]^{2-}$ and *cis*-$[M_2W_4O_{19}]^{4-}$ compounds (M = Ta, Nb, V) computed with different methodologies.[b]

NMR//OPT	Oxygen type						
	M_6O	W_2O	WMO	M_2O	W=O	M=O	Avg.
1- B3LYP/TZP//B3LYP/TZ2P	24	77	75	92	67	119	70
2- PBE/TZ2P//PBE/TZ2P	58	54	54	41	24	61	48
3- BP86/TZP//B3LYP/TZ2P	59	74	60	42	19	14	46
4- PBE/TZP//B3LYP/TZ2P	61	70	60	38	15	15	45
5- PBE/TZP//PBE/TZ2P	31	58	55	37	28	52	44
6- PBE/TZP//PBE/QZ4P	33	68	55	34	21	63	43
7- OPBE/TZP//OPBE/TZ2P	31	48	22	46	20	96	40
8- KT2/TZP//PBE/TZ2P	34	36	50	38	15	71	39
9- OPBE/TZP//PBE/TZ2P	27	40	41	41	24	76	39

[a]Values in ppm. Methods are sorted by descending average MAE. The experimental data can be found in parentheses in Table 3.3. [b]See Tables A1–A9 for the full list of computed chemical shifts.

First of all, we can confirm that the trends observed in Table 3.1 for $[W_6O_{19}]^{2-}$ are also followed in the mixed-metal compounds, namely, after using the B3LYP functional for the geometry optimization step, the single-point NMR calculation gives better results with GGA functionals than with B3LYP (entries 1, 3 and 4). In general, the NMR step gives better results with GGA functionals (PBE, OPBE). We also checked the relevance of the geometry optimization step with other functionals. Comparing entries 4 and 5 we can see what is the effect upon the total MAE of changing the geometry optimization step without changing the NMR calculation step (fixed to PBE/TZP). The MAEs do not significantly differ between B3LYP/TZ2P and PBE/TZ2P optimizations, confirming that the choice of the functional is more determinant in the NMR step than in the geometry optimization (as long as the latter is performed at least with a GGA functional and a TZP or TZ2P basis set). In addition, the difference in the average quality of the results when optimizations are performed with PBE or OPBE only differ by ~1 ppm, a fact showing how similar these two functionals are with respect to the geometry optimization step. Finally, the effect of the basis set in the geometry optimization step (entries 5 and 6) is residual when going from TZ2P to QZ4P. Therefore, structures optimized with a TZ2P basis set combined with the appropriate functional are good enough for NMR calculations.

To summarize, performing a test over a variety of methodologies (Table 3.2) shows that the best accuracy in ^{17}O NMR chemical shifts is achieved when GGA functionals are used. Except for the poor results obtained with the B3LYP/TZP//B3LYP/TZ2P procedure with an average MAE = 70 ppm, the rest of entries give much lower average MAEs, ranging 48–39 ppm. Notably, the last three methodologies in Table 3.2, characterized by GGA functionals, have very similar average MAEs (39–40 ppm) and, therefore, they are presumed of similar quality. For these methodologies, some positions are more accurately reproduced than others, such as W=O sites (MAE between 15 and 24 ppm with this set of molecules). On the other hand, the systematic error associated with terminal M=O positions is much larger (71 to 96 ppm), markedly influenced by the vanadium atom (i.e. 1015 ppm computed vs. 1217 ppm measured for V=O in $[V_2W_4O_{19}]^{4-}$). Excluding the values for V=O, the M=O MAE dramatically reduces. The deviations for bridging W_2O, WMO and M_2O positions are, on average, around 40 ppm. For the less chemically relevant central oxygen (M_6O), the accuracy of calculations is intermediate.

The knowledge gained from present calculations suggests that further improvement in ^{17}O NMR chemical shifts is not expected upon changes in the density functional or the basis set in the computational procedure. Also, the computed $\delta(^{17}O)$ values are systematically too positive.

3.3.2. Linear scaling to reduce the mean absolute errors in $\delta(^{17}O)$

From the results listed in Table 3. 2, we can choose any of the last three procedures to carry on our study. However, the OPBE/TZP//PBE/TZ2P procedure (last row of Table 3. 2 and Table A9) gives more constant deviations per site, whereas the KT2 functional has more fluctuating error values. In the following, all the values computed are referred to the OPBE/TZP//PBE/TZ2P computational procedure although one could consider using the KT2/TZP//PBE/TZ2P procedure with a comparable success.

For the chosen procedure, then, the average MAE = 39 ppm is still moderate despite the wide range of $\delta(^{17}O)$ ~1200 ppm in POMs. At this point we consider a general approach to overcome this issue. Empirical scaling is the application of corrections to the computed data derived from linear regression procedures using experimental data.[45] In this case, computed isotropic shieldings (σ) with the OPBE/TZP//PBE/TZ2P procedure and experimental chemical shifts (δ) are related via an equation of the form $\delta = b\cdot\sigma + a$. The major benefit of this analysis is that the slope (b) is a scaling factor to robustly account for the systematic errors in computed chemical shifts. This procedure is able to reduce errors from sources such as solvation effects, rovibratory effects and other methodological limitations.[46] Figure 3.4 shows the linear equation $\delta = -1.079\cdot\sigma$

+ 313.0 fitting the computed ^{17}O shielding to the experimental ^{17}O chemical shifts for the set of compounds listed in Table 3.3. So, using that equation we can reduce the systematic errors. A slope more negative than –1 indicates that the routinely computed chemical shifts were overestimated. A second linear regression was done with the bridging oxygens only, due to their larger error compared with the other oxygen types.

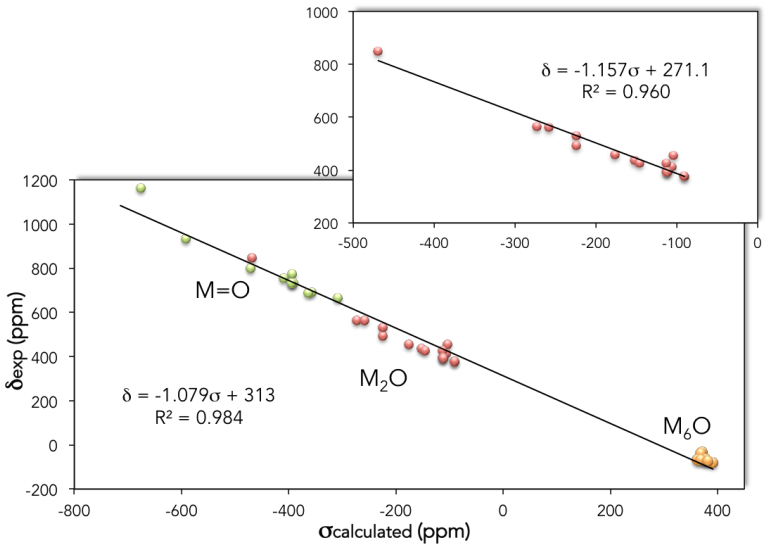

Figure 3. 4. Plot and linear regression of experimental chemical shifts, δ_{exp}, vs calculated shieldings, $\sigma_{calculated}$, for the oxygen positions taken from the hexametalate compounds listed in Table A10. Inlay contains the points and linear regression for the M_2O sites separately.

The values of $\delta(^{17}O)$ shown in Table 3.3 have been obtained with the mentioned linear equations. Notice that we have enlarged the number of compounds to which we applied the linear scaling to systems classified as (i) and (ii) in Section 3.3.1. The fitted values are more accurate in general than the non-fitted ones. The two of them coincide, though, in that the most accurately computed $\delta(^{17}O)$ values are those of terminal W=O oxygens. The empirical fitting also provides a quantitative accuracy for oxygens of the Keggin compound such as the internal XOM_3 position (MAE = 10 ppm). However, it does not perform so well for M_2O oxygens, maybe because the fitting includes a majority of values for W_2O oxygens. The improvement is therefore more evident for oxygens linked to W, although better results are also observed with the other metals, M.

Table 3. 3. Fitted and experimental[a] ^{17}O shifts for several Polyoxotungstates.[b]

Anion	M_6O	W_2O	WMO	M_2O	W=O	M=O	XOW_3	Ref.
$[W_6O_{19}]^{2-}$	-109 (-80)	394 (416)	-	-	738 (775)	-	-	[9]
$[TaW_5O_{19}]^{3-}$	-94 (-71)	401 (394)	440 (426)	-	737 (732)	645 (666)	-	[47]
$[NbW_5O_{19}]^{3-}$	-85 (-67)	400 (392)	475 (456)	-	735 (731)	821 (799)	-	[47]
$[VW_5O_{19}]^{3--}$	-99 (-75)	401 (392)	570 (562)	-	739 (731)	1083 (1217)	-	[9]
$[Ta_2W_4O_{19}]^{3-}$	-85 (-40)	379	401	391 (454)	702	608	-	
$[Nb_2W_4O_{19}]^{4-}$	-78 (-67)	376 (379)	447 (435)	530 (493)	698 (691)	755 (753)	-	[47]
$[V_2W_4O_{19}]^{4-}$	-95 (-65)	376 (378)	531 (530)	814 (848)	705 (687)	1042 (1162)	-	[9]
$[(MeO)SnW_5O_{18}]^{3-}$	25 (17)	394; 407 (363; 383)	376 (395)	-	718; 672 (720; 684)	-	-	[48]
$[(MeO)ZrW_5O_{18}]^{3-}$	-64 (-58)	387; 390 (385; 377)	478 (484)	-	719; 706 (711; 706)	-	-	[49]
$[(MeO)TiW_5O_{18}]^{3-}$	-71 (-58)	387; 393 (380; 390)	534 (525)	-	723; 716 (721; 713)	-	-	[50]
$[(\mu\text{-}O)(TiW_5O_{18})_2]^{6-}$	-81 (-63)	389; 397 (381; 390)	545 (534)	757 (697)	725; 721 (722; 714)	-	-	[50]
$[(\mu\text{-}HO)(ZrW_5O_{18})_2]^{6-}$	-78 (-58)	383; 393 (378; 387)	519 (479)	-	714; 703 (712; 692)	-	-	[49]
$\alpha\text{-}[PW_{12}O_{40}]^{3-}$	-	432; 456 (405; 431)	-	-	765 (769)	-	91 (80)	[11]
$\alpha\text{-}[SiW_{12}O_{40}]^{4-}$	-	428; 446 (405; 427)	-	-	761 (761)	-	37 (27)	[11]
$[P_2W_{18}O_{62}]^{6-}$	-	435 (418)	-	-	740; 760 (738; 759)	-	75; 106	[11]
MAE	17	13	14	48	6	60[c]	10	

[a]Values in parentheses. [b]Values in ppm. [c]This MAE decreases to 15 ppm if the vanadium-derived values are not considered. All the calculations were performed using CH_3CN as solvent except for $[W_6O_{19}]^{2-}$, which was performed with DMF

Table 3.4 summarizes the % improvement experienced when computed $\delta(^{17}O)$ are fitted using the linear equation in Figure 3.4. The systematic errors in $\delta(^{17}O)$ are notably reduced applying the linear fitting technique to the values computed with the OPBE/TZP//PBE/TZ2P procedure. The oxygens bonded to W atoms feature small MAEs between 7 and 17 ppm. On the other hand, the terminal V=O site is a special case since the computed chemical shift is still large after applying such fitting correction.

Table 3. 4. MAEs[a] for calculated and fitted $\delta(^{17}O)$ for hexametalate compounds.

Site	Calculated[b]	Fitted	Improvement
M_6O	38	17	55%
W_2O	60	13	78%
WMO	44	14	68%
M_2O	59	48	19%
W=O	7	6	14%
M=O[c]	69 (11)	60 (15)	13%
average[c]	46 (36)	26 (19)	44% (47%)

[a]Values in ppm. [b]Data in Table A10. [c]In parentheses, MAEs obtained excluding $\delta(^{17}O)$ of terminal V=O sites.

3.3.3. Influence of the metal on the chemical shift

To help us explain the ^{17}O NMR of complex POM systems, we firstly analyse its behaviour in the simpler and well-characterized MO_4^{n-} compounds, with M of groups 5, 6, 7 and 8 of the periodic table. These compounds were previously studied as models for the performance of theoretically methods in ^{17}O NMR properties.[51-53] Calculated and experimental $\delta(^{17}O)$ values are shown in Table 3.5. As stated above, the chemical shifts are governed by the paramagnetic term, σ^p, which in MO_4^{n-} anions is dominated by a *n*p(O)→ π*(M-O) electronic transition.

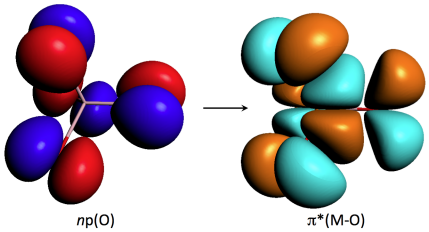

Scheme 1

where *n*p(O) is the occupied symmetry-adapted lone pair of the oxygen atoms (l.h.s. of Scheme 1). As mentioned in the chapter 1, the term u_{ai}, responsible for σ^p, depends on the reciprocal of the energy gap between these two orbitals, ΔE^{-1}, but also on the overlap (considering rotation due to the external magnetic field) between the oxygen atomic contributions in both orbitals.[17, 38] Figure 3. 5 shows that the energies of *n*p(O) and π* orbitals, defining ΔE^{-1}, decrease as we go right and up in the periodic table. Interestingly, the π* orbital does more dramatically. This is linked to the varying M-O bond polarization towards a larger oxygen character in the same sense. However, the occupied lone pair orbital remains constant at >95% p(O) character, its energy change being attributed to the different negative charges in the MO_4^{n-} family.

Table 3. 5. Calculated and experimental[a] ^{17}O NMR chemical shifts[b] for MO_4^{n-}.

VO_4^{3-}	CrO_4^{2-}	MnO_4^-	
548 (568)	758 (871)	1030 (1255)	
NbO_4^{3-}	MoO_4^{2-}	TcO_4^-	RuO_4
419 (–)	578 (576)	783 (786)	1071 (1142)
TaO_4^{3-}	WO_4^{2-}	ReO_4^-	OsO_4
332 (–)	452 (456)	597 (605)	800 (832)

[a]Data in parentheses from Refs. [54, 55] except for RuO_4 (Ref. [56]). [b]Values in ppm.

Within this series the correlation of ^{17}O chemical shifts with the orbital gaps is highly linear, as shown in Figure 3.5. When we move left and down in the periodic table, the ionicity of the metal-oxygen bond increases. After having analysed the computational results we can conclude that the numerator of the u_{ai} term is quite irrelevant (constant) vs. the chemical shift, the energy gap being entirely responsible for the trend in $\delta(^{17}O)$. Hence, for example, the contribution of p(O) to π*(M-O) is only 35% in WO_4^{2-} whereas it reaches up to 60% in RuO_4. This might affect the numerator of u_{ai}, but it does so only slightly and the varying % p(O) contributions have little effect, apart from the indirect effect on the energy of the π* orbital. Thus, the observed $\delta(^{17}O)$ resonance in WO_4^{2-} appears at 456 ppm, whereas that for RuO_4 is shifted 700 ppm downfield to 1142 ppm. The computed values are rather close to the observed ones, 452 and 1071 ppm, respectively. The mentioned downfield shift can be attributed in simple terms to the increase of covalency in the M-O bond and to the higher electron affinity of the metal. Both effects are present in the orbital gap mentioned. Likely, many chemists would prefer an interpretation based on atomic populations. It is true that the atomic charge of oxygens in WO_4^{2-} is larger than in RuO_4 (–1.00e vs. –0.46e, respectively, with multipole-derived atomic charges) but the reader should take into account that $\delta(^{17}O)$ correlates much better with the reciprocal of orbital energy gaps, ΔE^{-1}, than with

atomic populations (see Figure 3.5c). Both factors —orbital energy gap and, secondarily, orbital polarization— make the $n \rightarrow \pi^*$ electron transfer less accessible in the tungstate species.

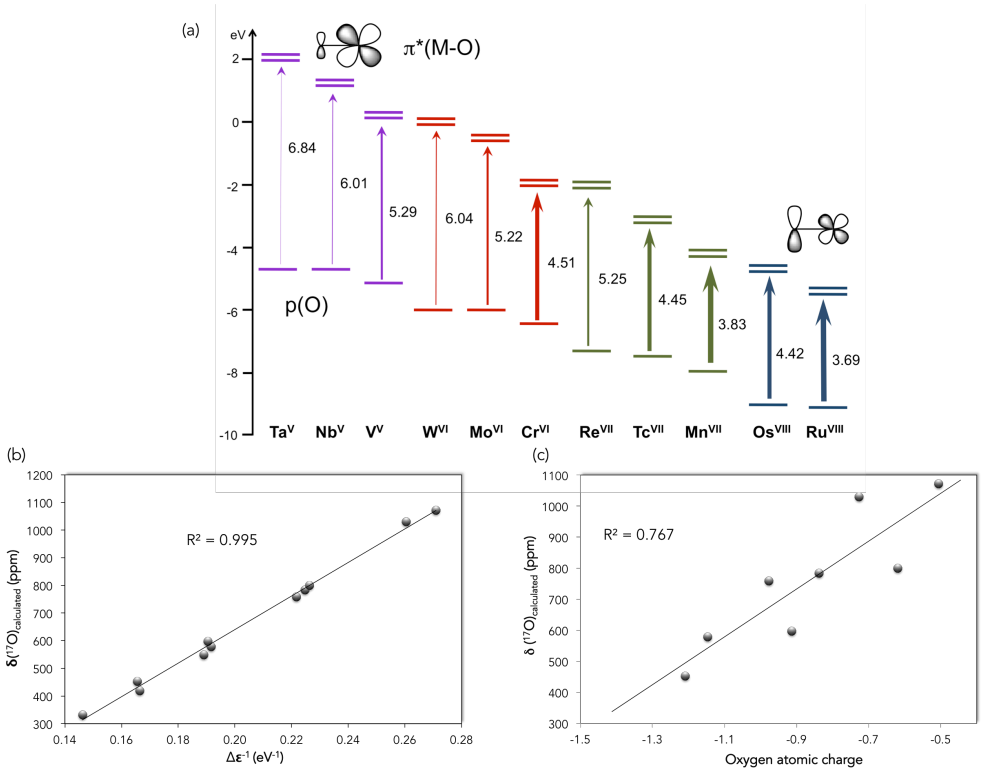

Figure 3. 5. (a) Dependence of ^{17}O chemical shifts on the energy gaps associated with the leading occupied → virtual electronic transitions in the σ^p component for the MO_4^{n-} series. Right: computed $n \rightarrow \pi^*$(M-O) energy gaps (in eV). More covalent M-O bonds are associated with smaller gaps (thicker arrows) and more deshielded nuclei. (b) Linear correlation of the calculated δ(^{17}O) vs. the reciprocal of the energy gap (ΔE^{-1}). (c) Linear correlation of the calculated δ(^{17}O) vs. the reciprocal oxygen atomic charge.

A deeper analysis of the MO_4^{n-} model set shows that the behavior of δ(^{17}O) can be rationalized mainly in terms of the orbital energy gap, the % contribution of p(O) in the implicated orbitals being indirect, affecting their relative energies.

The computed δ(^{17}O) values fitted by the expressions shown in Figure 3.4 for bridging MOW and MOM oxygens in hexametalate anions are listed in Table 3.6 along with experimental values. If we consider MOW sites, the variations in the chemical shift are within the range 400–600 ppm, smaller than in MO_4^{n-}. The changes are larger if we look at the MOM sites. Notably, an increase in the covalency of M-O bonds, going up in a group, produce larger chemical shifts. In a period, though, they remain fairly

constant (fitted and experimental values). Viewed as a whole, the $\delta(^{17}O)$ values for hexametalate POM compounds follow the same trends as the MO_4^{n-} set. Therefore their behaviours can be assigned to the same origin.

Table 3. 6. Fitted and experimental[a] $\delta(^{17}O)$ values[b] for MOW and M_2O positions in mixed-metal hexametalates.

MOW		MOM	
V		V	
570 (562)		814 (848)	
Nb	Mo	Nb	Mo
475 (456)	505 (485)	530 (493)	611 (563)
Ta	W	Ta	W
440 (426)	394 (413)	391 (454)	394 (413)

[a]In parentheses. [b]Values in ppm.

3.3.4. Relevance of the bonding mode

In addition to the metal atom bonded to the oxygen site, the nature of this interaction, related to the number of vicinal metal atoms, notably affects the chemical shift. For a family of polyoxotungstates computed (Figure 3.6a) it is relevant that the negative atomic charge assigned to the oxygen atom increases as $WO < W_2O < W_6O$, i.e. when more vicinal metal atoms and larger W-O distances are present. Thus, the W-O bonds become less covalent and the occupied and virtual orbitals split apart, lowering the $\delta(^{17}O)$ due to a decrease in the paramagnetic contribution to σ. Within any one type of oxygen (W_2O, for example), though, one cannot find any correlation between atomic charges and the associated chemical shifts.

Regarding the M-O bond distance, it provides an indication of the nature of the bond, which is important in determining the variations in $\delta(^{17}O)$. For MO_4^{n-}, we studied the main electronic transitions, but herein we focus on the relationship between V-O bond distances and $\delta(^{17}O)$ in $[V_{10}O_{28}]^{6-}$ due to the increase in the number of paramagnetic transitions, which makes the analysis of orbital couplings much more intricate (Figure 3.6b). We chose the decavanadate system (Figure 3.8) to illustrate this trend because it contains four different V_xO oxygen types (x = 1, 2, 3 and 6). The relationship between energy gaps and bond distances is used to explain the trends in the $\delta(^{17}O)$ in this oxovanadate. As can be seen in Figure 3.6b, as the V-O bond distance increases, the nature of the interaction becomes more ionic and the chemical shift decreases.

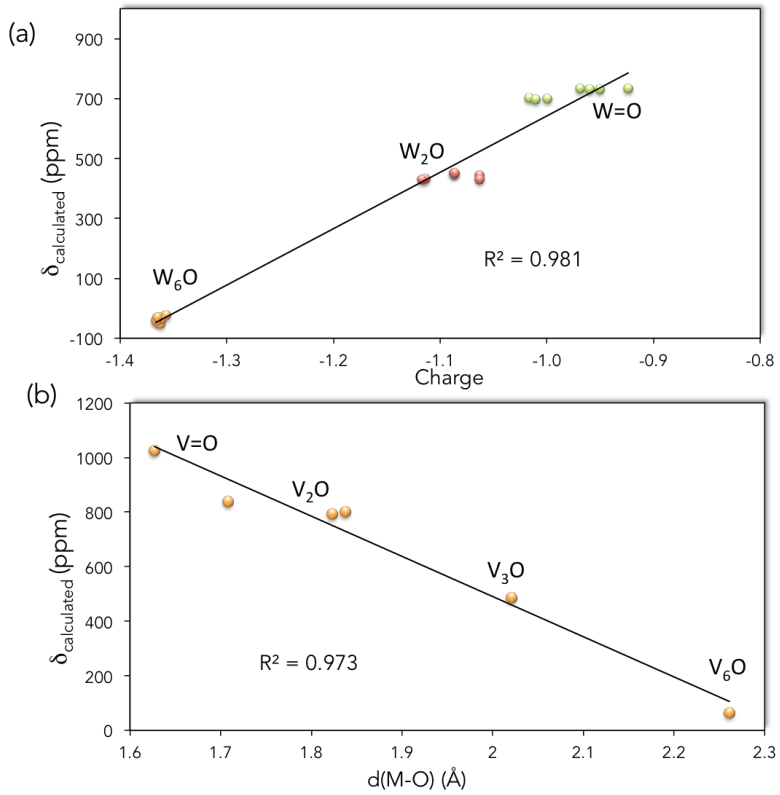

Figure 3. 6. Correlation of the calculated ^{17}O chemical shifts with (a) oxygen charges in substituted hexametalate anions, and with (b) V-O distances in the $[V_{10}O_{28}]^{6-}$ anion.

The paramagnetic contribution is the most important source of the shielding. Therefore, we further examined the main orbital transitions dominating this contribution in M=O and M_2O oxygen sites since they are the most common in POMs. In the models represented in Figure 3.7, there is one dominant contribution, namely the $\sigma \rightarrow \pi^*$ magnetic coupling, in terminal M=O sites, which accounts for about 40–70% of the total depending on the metal. On the other hand, the largest contribution to M_2O shifts comes from the *n*p(O) $\rightarrow \pi^*$ coupling, which accounts for about 30% of all transitions. Figure 3.7 schematically shows how if one rotates a σ or *n* orbital by 90° as indicated by the arrows, it overlaps with the empty π^* orbital, particularly in the region around the oxygen. As the number of metal atoms bonded to the oxygen increases, there is no single dominant transition any more, but many of them contribute to the paramagnetic term.

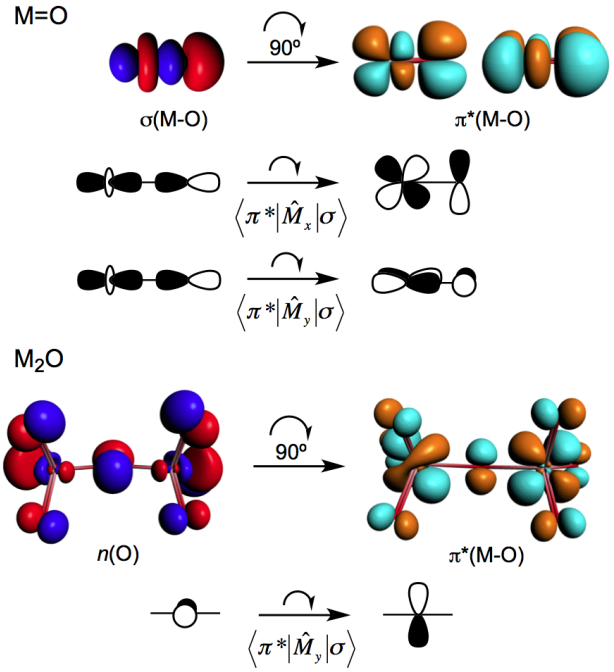

Figure 3. 7. Main contributions to the paramagnetic shielding for M=O (top) and M_2O (bottom) oxygen types obtained with simplified models. The symbolic representation of the σ and *n* occupied orbitals qualitatively illustrates how the action of the magnetic field rotates the atomic orbitals by 90°.

3.3.5. Effects of localised and mobile protons on the chemical shift

POMs are anionic species that can be protonated at neutral to acidic pH conditions, depending on their composition and charge. The identification of basic oxygens has significant implications regarding chemical reactivity and, more specifically, catalytic activity of metal oxides in general. However, the protonation sites in POMs are an elusive subject (i) naturally, since protons are itinerant in structures with chemically similar oxygen sites, and (ii) technically, due to the difficulties associated with the structural determination of H atom positions. Even so, in some cases, protonation sites have been determined experimentally using the empirical relationship between 'bond length' and 'bond strength'.[57] In other cases, positions can be proposed based on ^{17}O NMR spectra.[9, 57-61] Computationally, this subject has been tackled by many authors.[62-66] To analyse the effect of protonation on ^{17}O NMR of POMs, we focus on the well characterized decavanadate $[V_{10}O_{28}]^{6-}$ anion, represented in Figure 3.8, since it features seven structural oxygen sites, six of which are external and could potentially be protonated. In a series of experimental studies,[57-59] the location of protons in this compound and their effect on ^{17}O NMR was analysed. First, it must be stressed that

seven signals (labeled A-G) appear in the spectrum at any pH, proving that the effective C_{2h} symmetry is preserved irrespective of the protonation state of the species due to fast proton exchange at the NMR timescale.

Second, as the solution is acidified, two NMR signals, assigned to the bridging oxygens B (OV_3) and C (OV_2), experience an upfield shift ($\Delta\delta < 0$), whereas the other oxygen signals shift downfield ($\Delta\delta > 0$) by small amounts. Terminal positions F and G (V=O) are not basic. A general sequence of increasing negative charge has been proposed as $O_G \sim O_F < O_E < O_D < O_C < O_B < O_A$ that can be related to their basicity.[62] Because O_A is inaccessible to protons, O_B and O_C are effectively the most basic oxygens, with O_B slightly more basic than O_C.

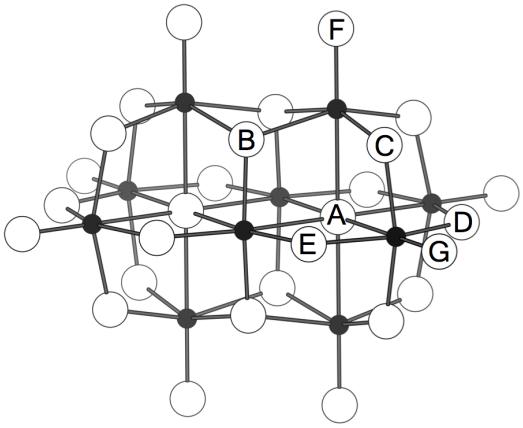

Figure 3. 8.The $[V_{10}O_{28}]^{6-}$ anion with labeling of one member of each set of symmetry-equivalent oxygens: A: V_6O; B: V_3O; C-E: V_2O; F-G: VO.

The main goal of our calculations was to reproduce and explain these experimental trends and to extract some general conclusions related to protonation in POMs. In general, calculations predict a huge and apparently unrealistic decrease of $\delta(^{17}O)$ when a single oxygen is protonated. For $V_{10}O_{28}^{6-}$, the computed change in $\delta(^{17}O)$ for the bridging OV_2 is $\Delta\delta(^{17}O) \approx -580$ ppm when protonation occurs considering the short timescale (a static protonated structure with a non-itinerant proton). In the same way, the bridging oxygens of the Lindqvist structure listed in Table 3.7 feature large $\Delta\delta(^{17}O)$ changes. However, basic oxygens (VOV) change their $\Delta\delta(^{17}O)$ more than non-basic ones, for which $\Delta\delta(^{17}O)$ ranges from –300 to –400 ppm for M = W, Nb. Hence, the change in chemical shift associated to protonation depends on the metal atoms linked to the oxygen.

Table 3. 7.Calculated $\delta(^{17}O)$ for non-protonated and protonated metal substituted Lindqvist structures, and their difference $\Delta\delta$.[a] The structural change, Δd(M-O), is shown.

	WOW	WONb	NbONb	WOV	VOV
non-prot.	445	516	563	563	808
protonated	152	150	171	149	237
$\Delta\delta(^{17}O)$	–293	–366	–392	–414	–571
Δd(M-O)[b]	+0.149		+0.159		+0.166

[a]Values in ppm. [b]M-O change upon protonation, in Å.

The geometrical effects of protonation might help us find an explanation for the variations in δ. The last row in Table 3.7 shows the change in some M-O distances if we attach a proton to a single oxygen site. It can be seen that the structural change is large, ranging from +0.149 Å for OW_2 to +0.166 Å for OV_2 at the present level of computation. Consequently, the protonated oxygens gain some ionic character and the δ moves upfield. We find that the smallest changes in chemical shift are associated with the smallest geometrical changes (M = W), and vice versa (OV_2). The geometrical changes encountered for W and V upon protonation are so similar in fact that we conjecture that the structural change is not the main reason for the wide range of 300 ppm of $\Delta\delta$ obtained. On the other hand, other M-O distances either elongate or shorten by about ±0.05 Å on average. There is also a correlation with the initial $\delta(^{17}O)$ position: the more downfield the initial value, the larger the upfield change after protonation. It is also important to mention that the neighboring oxygens of a protonated site experience positive $\Delta\delta(^{17}O)$ of several tens of ppm (Table A11) that must be taken into consideration for the final results. These trends may seem erroneous if compared to the small changes observed by ^{17}O NMR. However, they become logical at the NMR timescale, where the itinerant character of the proton emerges. To take into account such effects, we must consider the following facts:

(1) Taking static structures, the changes in $\delta(^{17}O)$ are either $\Delta\delta < 0$ for the protonated oxygen, and $\Delta\delta > 0$ for all the other non-protonated sites.

(2) Equivalence of oxygen sites and long timescales. $[V_{10}O_{28}]^{6-}$ belongs to the C_{2h} point group, with four O_B and eight O_C equivalent sites. If symmetry must be preserved in the protonated form, the ^{17}O chemical shift of the protonated oxygen ($\Delta\delta < 0$) and its non-protonated partner sites ($\Delta\delta > 0$) will be duly averaged to take into account

proton exchange between these N equivalent sites, in such a way that a unique signal is obtained for this set of sites.

(3) Coexistence of two protonated species. During the NMR measurements, more than one protonated species can be present in solution at sufficiently low pH, namely, $[V_{10}O_{28}]^{6-}$ can be protonated in oxygens B or C.

Table 3. 8. Evolution of the experimental and calculated $\delta(^{17}O)$ of external oxygens upon protonation.

	$[V_{10}O_{28}]^{6-}$	$HV_{10}O_{28}^{5-}$			$\Delta\delta_{cal}$[a]	$\Delta\delta_{exp}$[b]
		HO_B	HO_C	$60_B{:}40_C$		
O_B	498	433	520	468	–30	–28
O_C	785	803	734	776	–9	–7
O_D	791	814	818	816	25	23
O_E	826	830	837	833	7	11
$O_{F,\,G}$	1000	1020	1025	1022	22	17

[a]$\Delta\delta_{cal} = \delta(^{17}O, 60_B{:}40_C) - \delta(^{17}O, V_{10}O_{28}^{6-})$. See text for details. [b]$\Delta\delta_{exp} = \delta(^{17}O, \text{pH } 4.5) - \delta(^{17}O, \text{pH } 6)$. Data taken from Ref. [57].

Table 3.8 lists the computed $\delta(^{17}O)$ for the non-protonated, and the two protonated species derived from the decavanadate anion in the long timescale, along with the experimental changes in $\delta(^{17}O)$. The complete list of non-averaged chemical shifts for every individual oxygen position in the two protonated species can be found in Table A11. For each particular protonated species (columns 'HO_B' or 'HO_C'), one $\delta(^{17}O)$ decreases and the others increase compared to the non-protonated species. This behavior reveals that protonation does not only occur at the most basic site B but rather at both B and C sites, as their negative $\Delta\delta_{exp}$ values reveal. Column '$60_B{:}40_C$' shows the results if the two previous columns are combined as if $HV_{10}O_{28}^{5-}$ was 60% protonated in B and 40% protonated in C. We found that this balanced combination of the ^{17}O shieldings calculated for HO_B and HO_C reproduce the experimental data in the rightmost column, not only for protonated sites B and C, but also for non-protonated sites that shift downfield. Other ratios different from $60_B{:}40_C$ provided poorer estimations when comparing with experimental shifts (Table 3.9). The present procedure applied to DFT calculations prove that the observed $\delta(^{17}O)$ signals are a weighted mixture of those resonances assigned to equivalent oxygen types because they undergo mutual proton exchange in the timescale of ^{17}O NMR measurements. It has also been proven that oxygen B is more basic than C since the weighted combination that matches the experiments contains a higher % of $[HV_{10}O_{28}]^{5-}$

protonated at B. Therefore, the calculated values are only comparable with experimental ones if the effects discussed above are duly combined.

Table 3. 9. Changes in the experimental and calculated d(^{17}O) of external oxygens upon protonation, $\Delta\delta_{cal}$ = d(^{17}O, X_B:100-X_C) – d(^{17}O, $V_{10}O_{28}^{6-}$), for different HO_B:HO_C ratios.

	90_B:10_C	70_B:30_C	60_B:40_C	50_B:50_C	$\Delta\delta_{exp}$[a]
O_B	–57	–39	–30	–22	–28
O_C	12	–2	–9	–16	–7
O_D	24	24	25	25	23
O_E	5	6	7	7	11
$O_{F,\ G}$	21	22	22	23	17

[a] Δd_{exp}= d(^{17}O, pH 4.5) – d(^{17}O, pH 6). Data taken from Ref. [57].

Finally, the case of $V_2W_4O_{19}^{4-}$/$HV_2W_4O_{19}^{3-}$, that was experimentally analyzed,[9] revealed a change in the OV_2 site of –238 ppm upon protonation. Dramatic changes in δ(^{17}O) shifts were also detected and computed for various amide types.[67] Although it is much larger than Δδ = –7 ppm obtained for the chemically similar O_C in the decavanadate anion, it is still much smaller than our predicted value of Δδ = –571 ppm (Table 3.7). As described in this section, a small change in δ(^{17}O) when protonation occurs can be explained by proton delocalization over other equivalent or non-equivalent oxygen sites. In the case of $[V_2W_4O_{19}]^{4-}$, the absence of other similarly basic (equivalent or non-equivalent) sites discards the possibility of dissipation of Δδ by proton delocalization. As a matter of fact, there is a lone OV_2 position, and WOV sites are not expected to be protonated because of their relatively low basicity. We speculate that the protonated form $[HV_2W_4O_{19}]^{3-}$ represents only 30% of the total species present under the conditions specified by the authors. On the NMR timescale, the protonated and non-protonated forms would rapidly interconvert giving a single resonance.

3.4. Conclusions

We have established a DFT-based strategy to accurately com-pute and rationalize ^{17}O NMR chemical shifts of polyoxoanions. The lowest deviations between experimental and theoretical values were obtained at OPBE/TZP//PBE/TZ2P (NMR//optimization) level incorporating also solvent and relativistic effects. With this approach and using

linear fitting we predict δ values with mean absolute errors ~ 26 ppm for a set of 75 signals.

The paramagnetic contribution of the shielding (σ^p) dominates the ^{17}O chemical shift. It arises from the occupied → unoccupied orbital transitions with oxygen contribution promoted by the external magnetic field acting in NMR. The σ^p correlates in general with M-O bond distances. For terminal M=O oxygens, the σ → π* transition governs the shielding, which also has a linear dependence with the reciprocal of the energy gap. We used the simple MO_4^{n-} anion to clarify the dependence of δ vs. M. Electronegative ions such as V^V, Cr^{VI} or Ru^{VIII}, with rather deep π*(M-O) orbitals, lead to very positive δ(^{17}O). The less electronegative Nb^V or W^{VI} ions have the opposite behaviour. The number of metal ions linked to the oxygen atom also affect δ(^{17}O).

The effect of protonation on POMs has been analysed in detail for hexametalates and $[V_{10}O_{28}]^{6-}$. When proton-exchange occurs between chemically similar or equivalent sites, δ(^{17}O) signals of protonated oxygens move upfield (Δδ < 0), whereas the non-protonated ones slightly move downfield (Δδ > 0). When a molecule has many similar/equivalent oxygen sites that can accept an itinerant proton, the net effect of protonation is largely dissipated and the changes in δ(^{17}O) signals could become tiny or even undetectable by NMR as, for instance, the protonated Keggin $[HXW_{12}O_{40}]^{n-}$ anion. On the other hand, when a distinctively basic oxygen is present, as the bridging V_2O in $[V_2W_4O_{19}]^{4-}$, the proton gets trapped in one location and a large change (hundreds of ppm) in one ^{17}O NMR signal is observed upon protonation.

3.5. Bibliography

[1] I. I. Rabi, J. R. Zacharias, S.Millman, P. Kursch, *Phys. Rev.* **1938**, *53*, 318.
[2] E. M. Purcell, H. C. Torrey, R. V. Pound, *Phys. Rev.* **1946**, *69*, 37.
[3] E. M. Purcell, *Phys. Rev.* **1949**, *76*, 1262.
[4] I. P. Gerothanassis, *Prog. Nucl. Mag. Res. Sp.* **2010**, *56*, 95.
[5] I. P. Gerothanassis, *Prog. Nucl. Mag. Res. Sp.* **2010**, *57*, 1.
[6] J. A. Jackson, H. Taube, *J. Phys. Chem.* **1965**, *69*, 1844.
[7] B. N. Figgis, R. G. Kidd, R. S. Nyholm, *Can. J. Chem.* **1965**, *43*, 145.
[8] A. D. English, J. P. Jesson, W. G. Klemperer, T. Mamouneas, L. Messerle, W. Shum, A. Tramontano, *J. Am. Chem. Soc.* **1975**, *97*, 4785.
[9] W. G. Klemperer, W. Shum, *J. Am. Chem. Soc.* **1978**, *100*, 4891.
[10] M. Filowitz, W. G. Klemperer, L. Messerle, W. Shum, *J. Am. Chem. Soc.* **1976**, *98*, 2345.
[11] M. Filowitz, R. K. C. Ho, W. G. Klemperer, W. Shum, *Inorg. Chem.* **1979**, *18*, 93.
[12] X. López, J. J. Carbó, C. Bo, J. M. Poblet, *Chem. Soc. Rev.* **2012**, *41*, 7537.
[13] A. Bagno, M. Bonchio, *Chem. Phys. Lett.* **2000**, *317*, 123.
[14] A. Bagno, M. Bonchio, *Angew. Chem., Int. Ed.* **2005**, *44*, 2023.
[15] A. Bagno, M. Bonchio, J. Autschbach, *Chem. Eur. J.* **2006**, *12*, 8460.
[16] J. Gracia, J. M. Poblet, J. A. Fernández, J. Autschbach, L. P. Kazansky, *Eur. J. Inorg. Chem.* **2006**, 1149.
[17] J. Gracia, J. M. Poblet, J. Autschbach, L. P. Kazansky, *Eur. J. Inorg. Chem.* **2006**, 1139.
[18] L. Vilà-Nadal, J. P. Sarasa, A. Rodríguez-Fortea, J. Igual, L. P. Kazansky, J. M. Poblet, *Chem. Asian J.* **2010**, *5*, 97.
[19] E. J. Baerends, D. E. Ellis, P. Ros, *Department of Theoretical Chemistry: Vrije Universiteit: Amsterdam*.
[20] J. P. Perdew, K. Burke, M. Ernzerhof, *Phys. Rev. Lett.* **1996**, *77*, 3865.
[21] M. Swart, A. W. Ehlers, K. Lammertsma, *Mol. Phys.* **2004**, *102*, 2467.
[22] A. D. Becke, *Phys. Rev. A* **1988**, *38*, 3098.
[23] J. P. Perdew, W. Yue, *Phys. Rev. B* **1986**, *33*, 8800.
[24] T. W. Keal, D. J. Tozer, *J. Chem. Phys.* **2003**, *119*, 3015.
[25] J. P. Perdew, J. A. Chevary, S. H. Vosko, K. A. Jackson, M. R. Pederson, D. J. Singh, C. Fiolhais, *Phys. Rev. B* **1992**, *46*, 6671.
[26] M. Swart, M. Solà, F. M. Bickelhaupt, *J. Chem. Phys.* **2009**, *131*, 094103.
[27] M. Swart, M. Solà, F. M. Bickelhaupt, *J. Compt. Meth. Sci. Engi.* **2009**, *9*, 69.
[28] P. J. Stephens, F. J. Devlin, C. F. Chabalowski, M. J. Frisch, *J. Phys. Chem.* **1994**, *98*, 11623.
[29] S. Grimme, *J. Comput. Chem.* **2004**, *25*, 1463.
[30] M. Ernzerhof, G. E. Scuseria, *J. Chem. Phys.* **1999**, *110*, 5029.
[31] E. V. Lenthe, E. J. Baerends, J. G. Snijders, *J. Chem. Phys.* **1993**, *99*, 4597.
[32] E. V. Lenthe, E. J. Baerends, J. G. Snijders, *J. Chem. Phys.* **1994**, *101*, 9783.
[33] E. V. Lenthe, A. Ehlers, E. J. Baerends, *J. Chem. Phys.* **1999**, *110*, 8943.
[34] A. Klamt, *J. Phys. Chem.* **1995**, *99*, 2224.

[35] A. Klamt, V. Jonas, T. Bürger, J. C. W. Lohrenz, *J. Phys. Chem. A* **1998**, *102*, 5074.
[36] R. Ditchfield, *Mol. Phys.* **1974**, *27*, 789.
[37] K. Wolinski, J. F. Hinton, P. Pulay, *J. Am. Chem. Soc.* **1990**, *112*, 8251.
[38] G. Schreckenbach, T. Ziegler, *J. Phys. Chem.* **1995**, *99*, 606.
[39] J. Autschbach, S. Zheng, *Magn. Reson. Chem.* **2006**, *44*, 989.
[40] B. Le Guennic, K. Matsumoto, J. Autschbach, *J. Magn. Res. Chem.* **2004**, *42*, S99.
[41] A. Bagno, R. Bini, *Angew. Chem., Int. Ed.* **2010**, *49*, 1083.
[42] J. F. Zhu, T. Kurahashi, H. Fujii, G. Wu, *Chem. Sci.* **2012**, *3*, 391.
[43] Y. Zhang, A. Wu, X. Xu, Y. Yan, *Chem. Phys. Lett.* **2006**, *421*, 383.
[44] A. Wu, Y. Zhang, X. Xu, Y. Yan, *J. Comput. Chem.* **2007**, *28*, 2431.
[45] M. W. Lodewyk, M. R. Siebert, D. J. Tantillo, *Chem. Rev.* **2011**, *112*, 1839.
[46] W. Migda, B. Rys, *Magn. Reson. Chem.* **2004**, *42*, 459.
[47] C. J. Besecker, W. G. Klemperer, D. J. Maltbie, D. A. Wright, *Inorg. Chem.* **1985**, *24*, 1027.
[48] B. Kandasamy, C. Wills, W. McFarlane, W. Clegg, R. W. Harrington, A. Rodríguez-Fortea, J. M. Poblet, P. G. Bruce, R. J. Errington, *Chem. Eur. J.* **2012**, *18*, 59.
[49] R. J. Errington, S. S. Petkar, P. S. Middleton, W. McFarlane, W. Clegg, R. A. Coxall, R. W. Harrington, *J. Am. Chem. Soc.* **2007**, *129*, 12181.
[50] R. J. Errington, S. S. Petkar, P. S. Middleton, W. McFarlane, W. Clegg, R. A. Coxall, R. W. Harrington, *Dalton Trans.* **2007**, 5211.
[51] M. Kaupp, V. G. Malkin, O. L. Malkina, D. R. Salahub, *J. Am. Chem. Soc.* **1995**, *117*, 8492.
[52] M. Kaupp, O. L. Malkina, V. G. Malkin, *J. Chem. Phys.* **1997**, *106*, 9201.
[53] G. Schreckenbach, T. Ziegler, *Int. J. Quant. Chem.* **1997**, *61*, 899.
[54] B. N. Figgis, R. S. Nyholm, R. G. Kidd, *Proc. Roy. Soc. London* **1962**, *269*, 469.
[55] W. McFarlane, H. C. E. McFarlane, *In Multinuclear NMR*, Mason, J. Ed.; Plenum Press, New York, **1987**.
[56] C. Brevard, P. Granger, *J. Chem. Phys.* **1981**, *75*, 4175.
[57] W. G. Klemperer, W. Shum, *J. Am. Chem. Soc.* **1977**, *99*, 3544.
[58] V. W. Day, W. G. Klemperer, D. J. Maltbie, *J. Am. Chem. Soc.* **1987**, *109*, 2991.
[59] A. T. Harrison, O. W. Howarth, *J. Chem. Soc., Dalton Trans.* **1985**, *0*, 1953.
[60] O. W. Howarth, P. Kelly, L. Pettersson, *J. Chem. Soc., Dalton Trans.* **1990**, 81.
[61] J. R. Black, M. Nyman, W. H. Casey, *J. Am. Chem. Soc.* **2006**, *128*, 14712.
[62] J. Y. Kempf, M. M. Rohmer, J. M. Poblet, C. Bo, M. Benard, *J. Am. Chem. Soc.* **1992**, *114*, 1136.
[63] A. Dolbecq, A. Guirauden, M. Fourmigue, K. Boubekeur, P. Batail, M.-M. Rohmer, M. Benard, C. Coulon, M. Salle, P. Blanchard, *J. Chem. Soc., Dalton Trans.* **1999**, 1241.
[64] J. M. Maestre, J. P. Sarasa, C. Bo, J. M. Poblet, *Inorg. Chem.* **1998**, *37*, 3071.
[65] J. A. Fernández, X. López, J. M. Poblet, *J. Mol. Catal. A* **2007**, *262*, 236.
[66] S. Ganapathy, M. Fournier, J. F. Paul, L. Delevoye, M. Guelton, J. P. Amoureux, *J. Am. Chem. Soc.* **2002**, *124*, 7821.
[67] A. Bagno, G. Scorrano, *Acc. Chem. Res.* **2000**, *33*, 609.

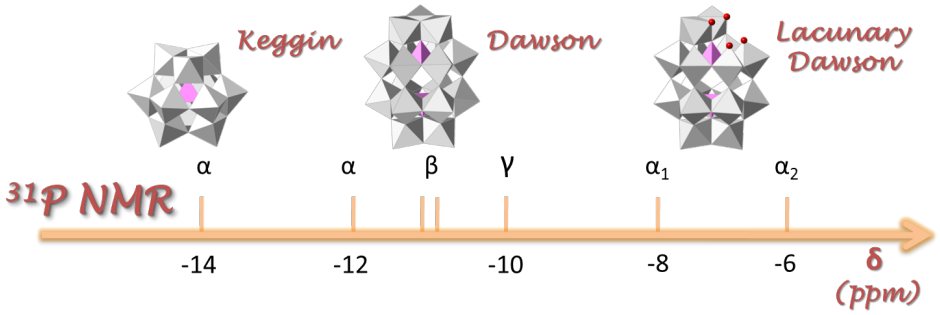

CHAPTER 4

^{31}P NMR Calculations on Polyoxometalates

Related publications:

M. Pascual-Borràs, X. López and J.M. Poblet, *Phys. Chem. Chem. Phys.* **2015**, 17, 8723.

CHAPTER 4

^{31}P NMR Calculations on Polyoxometalates

In this chapter, we present a search for the best density functional strategy for the determination of ^{31}P nuclear magnetic resonance (NMR) chemical shifts, $\delta(^{31}P)$, in polyoxometalates. Among the variables governing the quality of the quantum modeling, we tackle herein the influence of the functional and the basis set.

4.1. Introduction

Nuclear magnetic resonance (NMR) of the different active nuclei constituting IPAs and HPAs is nowadays considered a very powerful method to elucidate their molecular structures both in solution and in the solid state. ^{17}O, ^{51}V and ^{183}W nuclei attest to be the most effective ones for NMR due to their narrow lines and/or their wide range of chemical shifts, allowing a relatively easy assignment of the observed lines to atoms at different locations. Moreover, NMR of other nuclei that can be part of HPAs such as ^{31}P, ^{29}Si, ^{79}Ga and ^{73}Ga offers the possibility to thoroughly study their structure and bonding. One of the most active nuclei used for characterization of HPAs is ^{31}P, with a 100% abundance and a nuclear spin I = ½. ^{31}P NMR provides straightforward structural information falling into the range of roughly – 250 to + 250 ppm relative to 85% water solution of H_3PO_4, typically with well resolved signals resonating at characteristic frequencies. In the case of POMs, the range of ^{31}P NMR is much smaller (~10 ppm), implying a more difficult assignment, but it is considered a fundamental technique in structural characterization and monitoring of chemical reactions in POM science.

As mentioned, quantum chemical calculations are potentially able to reproduce and predict chemical shifts and coupling constants of many NMR-active ($I \neq 0$) nuclei, which can be used for spectral assignments of experimental data. However, it has been shown that NMR modelling is particularly demanding since a very accurate (expensive) description of the electron density in the vicinity of the NMR active nuclei is required. There are many studies dealing with the computation of ^{31}P NMR chemical shifts.[1-8] The Gauge-Including Atomic Orbital (GIAO)[9-10] method is one of the most widely used. It has been tested by comparison with experimental values of ^{31}P shielding tensors in $M(CO)_5PR_3$ (M = Cr, Mo and W) complexes.[1] Chesnut and collaborators[2-5, 11] also presented different NMR studies and quantum chemical investigations of $\delta(^{31}P)$ in a variety of phosphorus-containing compounds with very good agreements with experimental values. Recent theoretical studies[6, 12] focused on ^{31}P NMR based on density functional theory (DFT) show that, in general, calculations reproduce the experimental chemical shift reasonably well. Other recent studies[7-8] performed a comparison between DFT and perturbative MP2 methods in a representative series of organophosphorous compounds. They found that DFT calculations including relativistic and solvent effects give the best results. It must be noted that all the computational studies published so far are restricted to small molecules. Our challenge is to focus all these efforts in POM chemistry in order to help experimentalists in structural characterization and reactivity studies.

Computations of NMR properties of POMs, where many heavy nuclei are present, are challenging due to the large number of electrons occupying shells with high angular momentum and the associated relativistic effects playing an important role in all molecular orbitals (MOs). The task is even more complicated because POMs are negatively charged polyanions that must be modelled in the presence of a stabilising media to accurately reproduce their features. In the present study we will make use of the previous experience[13-16] to find the best methodology for computing accurate $\delta(^{31}P)$ of solvated POMs. In addition, we endeavour to understand how $\delta(^{31}P)$ depend on the geometrical and electronic properties of the molecule.

4.2. Computational details

DFT calculations were carried out with the ADF2013 package.[17-19] The calculations were performed with functionals characterised by the *generalised gradient approximation* (GGA). In the present work, the geometries were optimised with Slater type all-electron basis sets with the GGA-type PBE,[20] OPBE[21] and KT2[22] functionals. For NMR calculations, we used a Slater-type all-electron basis set and PBE, OPBE,

SSB-D,[23-24] KT2 and the B3LYP[25] and PBE0[26-27] hybrid functionals with spin-orbit (SO) corrections and a numerical integration accuracy parameter set to 6.0.

The notation for this procedure is expressed throughout the text as $Functional^{NMR}/Basis^{NMR}//Funcional^{OPT}/Basis^{OPT}$. We applied scalar relativistic corrections to the electrons via the *zeroth-order regular approximation* (ZORA)[28-30] that includes either only scalar or spin-orbit coupling as well. The stabilizing effect of an aqueous solution (liquid water and counterions, modelled as a continuum material) where our target molecules are immersed was approximated via *the conductor-like screening model* (COSMO).[31-32] The molecular cavities generated with this model are defined from VdW atomic radii. The effect of the atomic radii is minimal —much smaller than that of functionals or basis sets, as evaluated by us for ^{17}O NMR chemical shifts (unpublished results)— in ^{31}P NMR chemical shifts since construction of the molecule cavity must have a residual effect on the phosphorous environment (geometry and electronic structure). Thus, we did not evaluate this parameter in the present work.

The chemical shifts were referenced to 85% H_2PO_4 using PH_3 as a secondary standard following the method suggested by Van Wüllen,[33]

$$\delta(X_{calc}) = \sigma(PH_{3calc}) - \sigma(X_{calc}) - 266.1 \quad (4.\ 1)$$

where X is the phosphorus atom in the model system of interest and 266.1 is the difference in ppm between the absolute experimental chemical shielding of PH_3 (594.5 ppm) and 85% H_3PO_4 (328.4 ppm) at 300K.[5] The use of a secondary standard for ^{31}P NMR has become a frequent model of choice, as the theoretical chemical shielding for 85% H_3PO_4 is difficult to obtain.[6]

The fundamental quantity underpinning the phenomenon of chemical shift of a nucleus is its magnetic shielding tensor, σ. Although in general the NMR shielding tensor can be written as the sum of diamagnetic and paramagnetic contributions, we have also taken into account the relativistic phenomena with the spin-orbit (SO) contribution:

$$\sigma = \sigma^d + \sigma^p + \sigma^{SO} \quad (4.\ 2)$$

The diamagnetic contribution (σ^d) depends on the ground-state electron density only, whereas the paramagnetic shielding (σ^p) depends also on the excited states of the unperturbed system, expressed in terms of the virtual (unoccupied) MOs. The σ^d contributions of a given nucleus tend to be very similar for most chemical environments so that the actual chemical shifts' *differences* are usually dominated by the paramagnetic part. Therefore any change in δ is mainly determined by the σ^p term, whose principal contribution u_{ai} can be expressed as:

$$u_{ai} \propto -\frac{\langle \psi_a | \widehat{M} | \psi_i \rangle}{2\left(\varepsilon_i^0 - \varepsilon_a^0\right)} \quad (4.\ 3)$$

where ε_i^0 and ε_a^0 are the orbital energies of the occupied and unoccupied MOs involved in a given electronic transition, and the integral in the numerator is the first-order magnetic coupling between these orbitals. For a more accurate description see reference.[16]

To evaluate the quality of the calculated chemical shifts (δ), we computed different statistical indexes, such as the mean absolute error (MAE), the mean signed error (MSE) and the standard deviation (STD), obtained as:

$$\mathrm{MAE} = \frac{1}{N}\sum_i |\delta_{\mathrm{cal},i} - \delta_{\mathrm{exp},i}| \quad (4.\ 4)$$

$$\mathrm{MSE} = \frac{1}{N}\sum_i (\delta_{\mathrm{cal},i} - \delta_{\mathrm{exp},i}) \quad (4.\ 5)$$

$$\mathrm{STD} = \sqrt{\frac{1}{N-1}\sum_i (\mathrm{MSE} - (\delta_{\mathrm{cal},i} - \delta_{\mathrm{exp},i}))^2} \quad (4.\ 6)$$

were $\delta_{cal,i}$ and $\delta_{exp,i}$ are the calculated and experimental chemical shifts, respectively.

4.3. Results and discussion

We have computed and analysed the set of structures shown in Figure 4.1, containing a central phosphorous. They are all based on the basic Keggin, α-$[PM_{12}O_{40}]^{n-}$, and Wells-Dawson, α-$[P_2M_{18}O_{62}]^{n-}$, POM structures. The former is based on a central PO_4 tetrahedron surrounded by twelve MO_6 octahedra arranged in four groups of three edge-sharing units, M_3O_{13} (triads). These triads share corners with each other and with the central PO_4 (Figure 4.1a). At variance with the Keggin structure, Wells-Dawson compounds do not feature all-equivalent metal centres. One can distinguish between two mutually equivalent polar M_3O_{13} triads (also called *caps*) and two parallel M_6 rings at the equatorial region, mutually equivalent but not to caps, forming the *belt* (Figure 4.1b). We also studied the β and γ isomers of the Wells-Dawson structure, which arise from the α isomer after one and two 60° rotations of one and two M_3O_{13} polar triads, respectively. The accuracy of the possible best DFT procedure found on these simple compounds is extensively tested with larger and more complex structures, namely mixed-metal, isomeric, lacunary and functionalized Keggin and Wells-Dawson structures: (i) $[PW_{12-x}M_xO_{40}]^{n-}$ with M = Pd^{IV}, Nb^{V} and Ti^{IV}, (ii) α-$[P_2W_{18-x}M_xO_{62}]^{n-}$ with M = Mo^{VI}, V^{V} or Nb^{V}, (iii) $[P_2W_{17}O_{62}(M'R)]^{n-}$ with M' = Sn^{IV}, Ge^{IV} and Ru^{II} and R =

CH=CH_2,CH_2COOH or DMSO, (iv) α_2-$[P_2W_{17}O_{61}]^{10-}$ and α_1-$[P_2W_{17}O_{61}]^{10-}$, and (v) β-$[P_2W_{18}O_{62}]^{6-}$ and γ-$[P_2W_{18}O_{62}]^{6-}$.

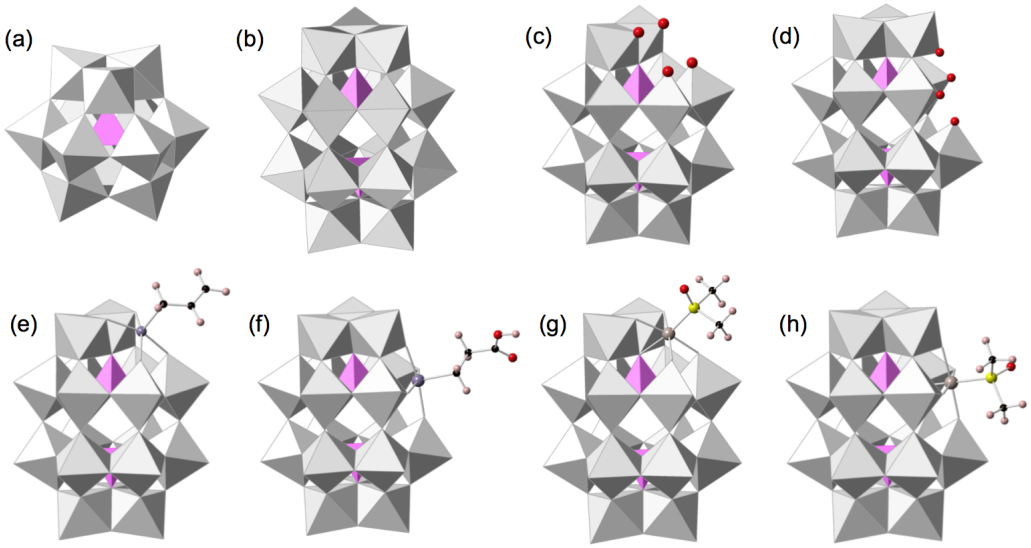

Figure 4. 1. Structures of (a) α-$[PW_{12}O_{40}]^{n-}$, (b) α-$[P_2W_{18}O_{62}]^{n-}$, (c) α_2-$[P_2W_{17}O_{61}]^{n-}$, (d) α_1-$[P_2W_{17}O_{61}]^{n-}$, (e) α_2-$[P_2W_{17}O_{62}M'(CH=CH_2)]^{7-}$ where M' = Sn^{IV} and Ge^{IV}, (f) α_2-$[P_2W_{17}O_{62}Sn(CH_2COOH)]^{7-}$, (g) α_2-$[P_2W_{17}O_{61}Ru(DMSO)]^{8-}$, (h) α_1-$[P_2W_{17}O_{61}Ru(DMSO)]^{8-}$. The β and γ isomers of structure b are not shown. P and W atoms are placed in the centre of pink tetrahedra and grey octahedra, respectively. Color code for spheres: Red - O, purple - Sn and Ge, brown - Ru, yellow - S, black - C, pink - H.

4.3.1. Optimal strategy for the calculation of δ(^{31}P) in POMs

It has been largely demonstrated by our group and others that standard DFT methods can help rationalising the chemical shifts of most POM-constituting elements.[34] We recently demonstrated that the most important factor for estimating chemical shifts theoretically is the choice of the density functional.[16] In general, GGA functional outperform hybrid ones. The best reproducibility and accuracy was obtained for OPBE or PBE functional and a triple-ζ + polarisation (TZP) basis set including the ZORA formalism for relativistic effects and a model solvent. In this regard, we focus this study on testing the different methodologies mentioned for ^{31}P NMR. Thus, the main goal is to calculate the best NMR chemical shift with the cheapest calculation possible. The ^{31}P NMR chemical shifts computed for $[PW_{12}O_{40}]^{3-}$ with different procedures and the P-O distances are shown in Table 4.1.

Table 4. 1. ^{31}P NMR chemical shifts (in ppm) of $[PW_{12}O_{40}]^{3-}$ and P-O distance obtained with different DFT methodology.

Entry	Computational procedure (NMR//OPT)	$\delta_{Calculated}$	d(P-O)/Å
1	B3LYP/TZP//OPBE/TZ2P	–37.3	1.535
2	KT2/TZP//OPBE/TZ2P	–34.5	1.535
3	PBE/QZ4P//PBE/QZ4P	3.64	1.544
4	SSB-D/TZP//OPBE/TZ2P	–30.9	1.535
5	OPBE/TZP//OPBE/TZ2P	–30.5	1.535
6	PBE/QZ4P//OPBE/QZ4P	–6.09	1.535
7	OPBE/TZP//PBE/TZ2P	–22.7	1.546
8	OPBE/TZP//PBE/QZ4P	–22.6	1.544
9	PBE/TZP//PBE/TZ2P	–9.7	1.546
10	PBE0/TZP//PBE/TZ2P	–18.6	1.546
11	KT2/TZP//KT2/TZ2P	–18.5	1.540
12	PBE/TZP//OPBE/TZ2P	–18.4	1.535
13	PBE/TZ2P//OPBE/TZ2P	–17.5	1.535
	Experimental value	–14.6[35]	1.530[36]

In this first selection of the computational procedures some trends can be extracted. First, the effect of the basis set in the geometry optimization step (compare entries 7-8) is minor and a TZ2P basis set suffices. Moreover, the comparison of entries 6 and 12 reveals that geometry optimisation using the large QZ4P basis instead of the TZ2P one does not affect much the final geometry for the cases examined. If a TZP basis set for the NMR step (entry 12) is replaced by a TZ2P (entry 13), a slightly more accurate result is obtained, but the CPU time for the latter doubles the former. Entry 3 in Table 4.1, although restricted to the PBE functional, suggest that using a large (QZ4P) basis set for the NMR calculation can produce unwanted, highly underestimated results, which sum up to a large CPU time increase. Comparison of entries 7, 9 and 10 with 1, 2, 4, 5, 12 and 13 suggests that, for a constant P–O distance, the calculated chemical shift is clearly varying from one functional to another.

Second, the adequacy of the functional must be considered not only in terms of quality but also concerning CPU time, knowing that hybrid functionals are more CPU-consuming than GGA ones. From the present results, we suggest that B3LYP NMR calculations may not be a good choice (entry 1). However, PBE0 (entry 10) performs

very well if compared with PBE or OPBE (entries 7 and 9) if the same geometry optimization step is carried out. If there are no CPU concerns, PBE0/TZP//PBE/TZ2P calculation is a good choice. It can also be seen that the KT2/TZP//KT2/TZ2P procedure performs very similarly to entry 10 and also to those with PBE or OPBE functionals. This originates in the similarity of these three functionals. The KT2 optimized geometry (P-O distances) is in between the PBE and OPBE ones. Thus, KT2 may be a good option for computation of ^{31}P NMR chemical shifts, albeit no all DFT codes have implemented this functional yet. This fact reinforces our preference to use the widely implemented PBE or OPBE functionals both in the NMR and the optimization steps. At this point we can confirm that the trends observed in our previous work on ^{17}O NMR are also valid for ^{31}P NMR.[16]

To complement these findings and refine the search for an optimal procedure of calculation of $\delta(^{31}P)$, we performed calculations on POM compounds with varied geometry and composition using the most relevant methods shown in Table 4.1. Table 4.2 lists computed and experimental $\delta(^{31}P)$ data for a set of well-characterized compounds shown in Figure 4.1, numbered following the rules of Figure 4.2, along with statistical indexes MAE, MSE and STD. We applied different combinations of OPBE and PBE functionals to the geometry optimization and NMR steps. The difference between PBE and OPBE functional lies in the electronic exchange part and this difference, as seen, affects the computed NMR chemical shift.

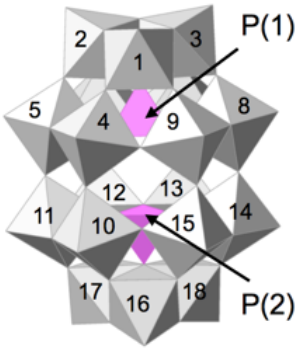

Figure 4. 2. Numbering of metal and P atoms in the Wells-Dawson structure $[P_2W_{18}O_{62}]^{6-}$ according to IUPAC rules.[37]

Table 4. 2. Computed and experimental ^{31}P NMR chemical shifts a (in ppm) for a set of Keggin, $[PM_{12}O_{40}]^{3-}$, and Wells-Dawson $[P_2M_{18}O_{62}]^{n-}$, compounds. The MAE, MSE and STD statistical indexes are also listed.

Anion	NMR//OPT						$\delta_{experimental}$		Ref.
	OPBE/TZP//PBE/TZ2P		PBE/TZP//PBE/TZ2P		PBE/TZP//OPBE/TZ2P				
	$\delta(P_1)^a$	$\delta(P_2)^a$	$\delta(P_1)^a$	$\delta(P_2)^a$	$\delta(P_1)^a$	$\delta(P_2)^a$	$\delta(P_1)^a$	$\delta(P_2)^a$	
α-$[PW_{12}O_{40}]^{3-}$	-22.70	-	-9.68	-	-18.37	-	-14.60	-	[35]
α-$[PMo_{12}O_{40}]^{3-}$	-14.68	-	-4.91	-	-9.66	-	-6.07	-	[38]
α-$[P_2W_{18}O_{62}]^{6-}$	-17.26	-	-6.89	-	-15.70	-	-12.44	-	[39]
α-$[P_2Mo_{18}O_{62}]^{6-}$	-15.60	-	-2.99	-	-6.78	-	-5.49	-	[38]
1-$[P_2VW_{17}O_{62}]^{7-}$	-15.77	-17.72	-4.98	-7.39	-13.55	-16.03	-10.84	-12.92	[39]
1-$[P_2vMo_{17}O_{62}]^{7-}$	-17.71	-19.09	-6.53	-6.79	-14.76	-15.76	-11.69	-12.45	[39]
α$_2$-$[PW_{17}O_{61}]^{10-}$	-9.32	-18.55	2.09	-7.80	-7.34	-16.72	-6.79	-13.93	[40]
MAE	6.05		5.14		2.62				
MSE	-6.05		5.14		-2.62				
STD	2.19		2.08		1.04				

[a]Figure 4.2 shows the numbering for internal P atoms.

Firstly, we checked if the trends observed with PBE/TZP//PBE/TZ2P also hold for mixed-metal compounds. The results in Table 4.2 roughly show the same behaviour as in Table 4.1, namely this procedure overestimates the $\delta(^{31}P)$ values (MSE = 5.14 ppm). In addition, the three procedures in Table 4.1 show largely systematic errors, meaning that the deviations from the experimental $\delta(^{31}P)$ all go in the same direction (|MSE| = MAE), around 5.1 ppm for PBE/TZP//PBE/TZ2P and 2.6 ppm in the case of PBE/TZP//OPBE/TZ2P. The MSE for OPBE/TZP//PBE/TZ2P reaches –6 ppm, substantiating a large underestimation of the measured values.

Figure 4.3 summarises graphically the computed and experimental $\delta(^{31}P)$ chemical shifts tabulated showing which procedures underestimate ($\delta_{calc} < \delta_{exp}$, circles and squares) and which overestimate ($\delta_{calc} > \delta_{exp}$, triangles) the experimental values. Comparing the performance of the above methodologies on simple compounds it can be concluded that one of the best DFT procedures to reproduce ^{31}P NMR in POMs is using PBE for NMR step with OPBE for optimised structures (PBE/TZP//OPBE/TZ2P), with a higher accuracy (MAE < 3 ppm) and a low dispersion (STD = 1.04 ppm).

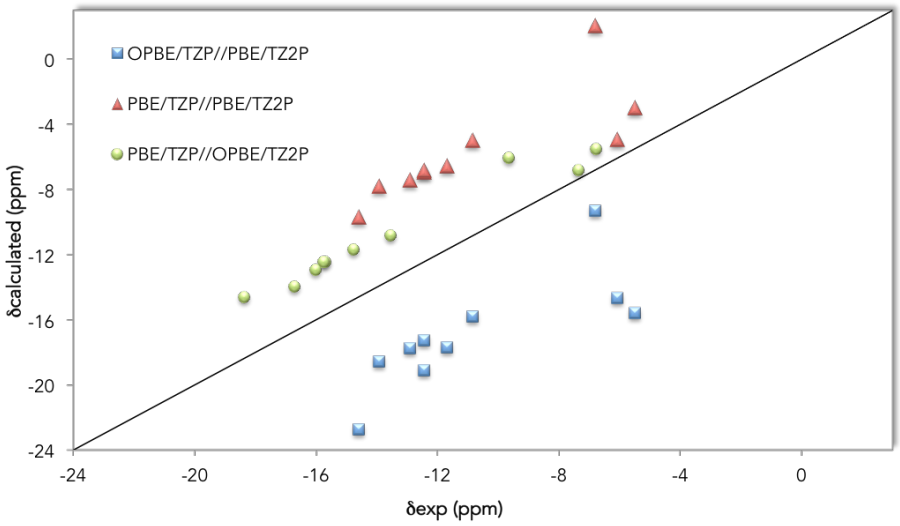

Figure 4. 3. Distribution of the experimental *vs.* calculated $\delta(^{31}P)$ values listed in Table 3.2. The straight line denotes coincidence between calculated and experimental values.

In Table 4.3, ^{31}P NMR chemical shifts computed with PBE/TZP//OPBE/TZ2P of the more complex structures previously classified (ii-iii) are listed for further testing. For the

chosen procedure, the MAE = 2.64 ppm is still moderate considering the narrow range of δ(^{31}P) values listed

Table 4. 3. Calculated (PBE/TZP//OPBE/TZ2P) and experimental ^{31}P NMR chemical shifts (in ppm) for a set of Wells-Dawson derived compounds. The MAE, MSE and STD statistical indexes are also listed.

Anion	$\delta_{calculated}$		$\delta_{experimental}$		Ref.
	$\delta(P_1)^a$	$\delta(P_2)^a$	$\delta(P_1)$	$\delta(P_2)$	
1,2-$[P_2V_2W_{16}O_{62}]^{8-}$	–11.19	–16.53	–8.82	–13.44	[39]
1,2,3-$[P_2V_3W_{15}O_{62}]^{9-}$	–8.28	–17.18	–6.25	–13.9	[39]
1,2,3-$[P_2MoV_2W_{15}O_{62}]^{8-}$	–9.78	–16.61	–7.7	–13.57	[39]
1,2,3-$[P_2Mo_2VW_{16}O_{62}]^{8-}$	–11.56	–16.07	–8.89	–13.04	[39]
1,2,3-$[P_2Mo_3W_{15}O_{62}]^{8-}$	–13.5	–15.36	–9.81	–12.34	[39]
1,2-$[P_2Mo_2W_{16}O_{62}]^{8-}$	–13.72	–14.86	–10.80	–12.40	[39]
4-$[P_2VW_{17}O_{62}]^{7-}$	–15.19	–15.56	–11.83	–12.90	[39]
4-$[P_2MoW_{17}O_{62}]^{6-}$	–14.77	–15.28	–11.6	–12.51	[39]
α_2-$[P_2W_{17}O_{61}]^{10-}$	–7.34	–16.72	–6.79	–13.93	[40]
α_1-$[P_2W_{17}O_{61}]^{10-}$	–9.34	–15.23	–8.53	–12.86	[40]
β-$[P_2W_{18}O_{62}]^{6-}$	–15.08	–13.62	–12.1	–11.3	[41]
γ-$[P_2W_{18}O_{62}]^{6-}$	–13.35	-	–10.8	-	[41]
α_2-$[P_2W_{17}O_{62}(SnR)]^{7-}$ (R=CH=CH_2)	–12.64	–16.07	–9.7	–11.8	[42]
1,2,3-$[P_2Nb_3W_{15}O_{62}]^{9-}$	–9.34	–16.92	–7.2	–13.8	[43]
MAE	2.64				
MSE	-2.64				
STD	0.76				

[a]Figure 4.2 shows the numbering for internal P atoms.

Empirical scaling can be applied to correct the computed data using a linear fitting to available experimental data.[44] In this case, based on our published study,[16] computed isotropic shieldings (σ) with the PBE/TZP//OPBE/TZ2P methodology and experimental chemical shifts (δ) are related via an equation of the form $\delta = b\cdot\sigma + a$, where the slope, *b*, is the scaling factor that reduces the systematic error of our results. This procedure is able to reduce errors from sources such as solvation effects, rovibratory effects or other methodological limitations. Figure 4.4 shows the linear fitting of the computed shieldings to the experimental ^{31}P chemical shifts for the compounds listed in Tables 4.2 and 4.3.

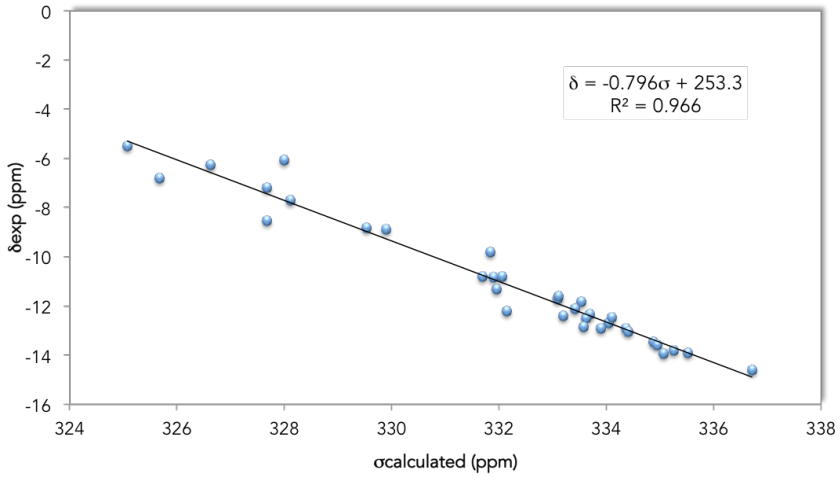

Figure 4. 4. Linear regression of the calculated shielding ($\sigma_{calculated}$) with the PBE/TZP//OPBE/TZ2P procedure vs. the experimental chemical shifts (δ_{exp}) for the ^{31}P signals listed in Tables 4.2 and 4.3.

The list of values in Table 4.4 was obtained with the mentioned linear equation, $\delta_{fitted} = -0.796 \cdot \sigma + 253.3$. Notice that we have enlarged the number of compounds from which we obtained this equation. Now, the 50 fitted values deviate much less form the experimental value (MAE = 0.57 ppm) and they are not systematically over- or underestimated with respect to experimental measurements (MSE = –0.05 ppm). Their dispersion is limited to STD = 0.70 ppm. This improvement from calculated to fitted values manifests upon comparison of the statistical indexes shown in Tables 4.3 and 4.4. Therefore, the fitting procedure reduces the systematic errors remarkably, obtaining accurate ^{31}P NMR chemical shifts. In addition, the ordering of the fitted chemical shifts is in good agreement with experimental ones.

Table 4. 4. Fitted and experimental ^{31}P chemical shifts (in ppm) for several polyoxometalates. The MAE, MSE and STD statistical indexes are also listed.

Anion	δ_{fitted}[a]		$\delta_{experimental}$		Ref.
	$\delta(P_1)$[b]	$\delta(P_2)$[b]	$\delta(P_1)$	$\delta(P_2)$	
α-$[PW_{12}O_{40}]^{3-}$	–14.7	-	–14.6	-	[35]
α-$[PMo_{12}O_{40}]^{3-}$	–7.78	-	–6.07	-	[38]
α-$[P_2W_{18}O_{62}]^{6-}$	–12.60	–12.60	–12.44	–12.44	[39]
α-$[P_2Mo_{18}O_{62}]^{6-}$	–5.49	–5.49	–5.49	–5.49	[38]
1-$[P_2VW_{17}O_{62}]^{7-}$	–10.88	–12.85	–10.84	–12.92	[39]
1-$[P_2MoW_{17}O_{62}]^{7-}$	–11.84	–12.64	–11.69	–12.45	[39]
1,2-$[P_2V_2W_{16}O_{62}]^{8-}$	–9.01	–13.26	–8.82	–13.44	[39]
1,2,3-$[P_2V_3W_{15}O_{62}]^{9-}$	–6.69	–13.77	–6.25	–13.9	[39]
1,2,3-$[P_2MoV_2W_{15}O_{62}]^{8-}$	–7.88	–13.32	–7.7	–13.57	[39]
1,2,3-$[P_2Mo_2VW_{16}O_{62}]^{8-}$	–9.30	–12.89	–8.89	–13.04	[39]
1,2,3-$[P_2Mo_3W_{15}O_{62}]^{8-}$	–10.84	–12.33	–9.81	–12.34	[39]
1,2-$[P_2Mo_2W_{16}O_{62}]^{8-}$	–11.02	–11.93	–10.80	–12.40	[39]
4-$[P_2VW_{17}O_{62}]^{7-}$	–12.19	–12.48	–11.83	–12.90	[39]
4-$[P_2MoW_{17}O_{62}]^{6-}$	–11.86	–12.26	–11.60	–12.51	[39]
α_2-$[P_2W_{17}O_{61}]^{10-}$	–5.94	–13.41	–6.79	–13.93	[40]
α_1-$[P_2W_{17}O_{61}]^{10-}$	–7.53	–12.22	–8.53	–12.86	[40]
β-$[P_2W_{18}O_{62}]^{6-}$	–12.10	–10.94	–12.10	–11.30	[41]
γ-$[P_2W_{18}O_{62}]^{6-}$	–10.70	–10.70	–10.80	–10.80	[41]
1,2,3-$[P_2Nb_3W_{15}O_{62}]^{9-}$	–7.53	–13.57	–7.20	–13.80	[43]
α_2- $[P_2W_{17}O_{61}Sn(CH{=}CH_2)]^{7-}$	–10.16	–12.89	–9.77	–11.80	[42]
α_2- $[P_2W_{17}O_{61}Sn(CH_2COOH)]^{7-}$	–7.48	–12.26	–6.70	–11.90	[42]
α_1-$[P_2W_{17}O_{61}Ru(DMSO)]^{8-}$	–10.35	–12.41	–9.67	–12.84	[45]
α_2-$[P_2W_{17}O_{61}Ru(DMSO)]^{8-}$	–10.36	–13.34	–8.61	–13.42	[45]
α_2-$[P_2W_{17}O_{61}Ge(CH{=}CH_2)]^{7-}$	–9.87	–12.95	–10.20	–13.53	[46]
α-$[PW_{11}O_{39}Pd]^{5-}$	–11.37	-	–13.20	-	[47]
α-$[PW_{11}NbO_{40}]^{4-}$	–13.65	-	–12.60	-	[48]
α-$[PW_{11}TiO_{40}]^{5-}$	–13.36	-	–13.34	-	[49]
MAE	0.57				
MSE	–0.05				
STD	0.70				

[a]Fitting procedure applied to values obtained with the PBE/TZP//OPBE/TZ2P procedure. [b]Figure 4.2 shows the numbering for internal P atoms.

Additionally, we performed a comparison between the three sets of results (experimental, computed and fitted). As mentioned above, the calculated $\delta(^{31}P)$ are

systematically too negative, this is why we decided to perform a scaling approach capable of correcting them. The improvement of the results upon fitting is clearly shown in Figure 4.5. The fitted values (red circles) feature much smaller errors than the calculated ones with respect to the experimental values. In general, the coincidence with the experimental ones after the fitting procedure is significant. The figure also shows that the most negative chemical shifts calculated need a major improvement and the fitting procedure properly accounts for it. Thus, for example, there is more difference between calculated and experimental $\delta(^{31}P)$ values for $[PW_{12}O_{40}]^{3-}$ or $[P_2SnW_{17}O_{61}R]^{n-}$ than $\delta(^{31}P)$ for $[PMo_{12}O_{40}]^{3-}$ or $[P_2W_{17}O_{61}]^{10-}$ ones. Even so, the chosen fitting procedure is able to reduce the deviations for these different ranges, giving remarkably good results.

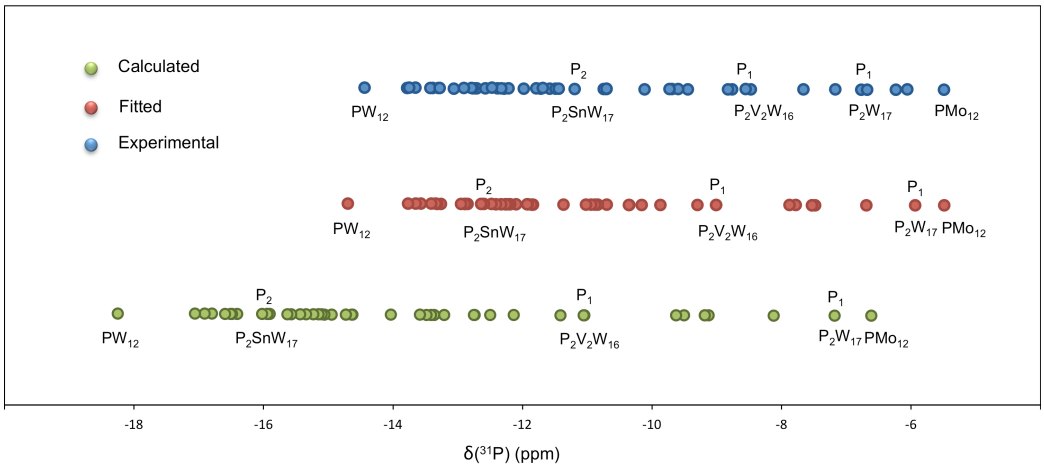

Figure 4. 5. Comparison of calculated, fitted and experimental $\delta(^{31}P)$ chemical shifts for ^{31}P signals listed in Tables 4.2, 4.3 and 4.4. Some signals have been labeled to monitor their variation from the calculated to the fitted value. The fitting procedure affects all the calculated values but to a different extent depending on their original position generating a final set of values that are in good agreement with the measured ones.

4.3.2. Dependence of $\delta(^{31}P)$ on electronic parameters

A step forward is to analyse the parameters affecting the $\delta(^{31}P)$, namely the electronic structure and the geometry. It is well-known that one depends on the other, so in this section we focus on the electronic part, pointing out which are the energy gaps of the main electronic transition governing the leading paramagnetic contribution of $\delta(^{31}P)$ (Eq. 4.2). The large number of atoms present in POM compounds makes this analysis a very intricate one. To simplify it, we built a suitable model to explore the main electronic transitions related only to the PO_4 fragment. In this model, all the atoms

except the target $P(1)O_4^{3-}$ unit are replaced by multipole derived atomic charges (MDC-q) obtained from a previous calculation (Figure 4.6).

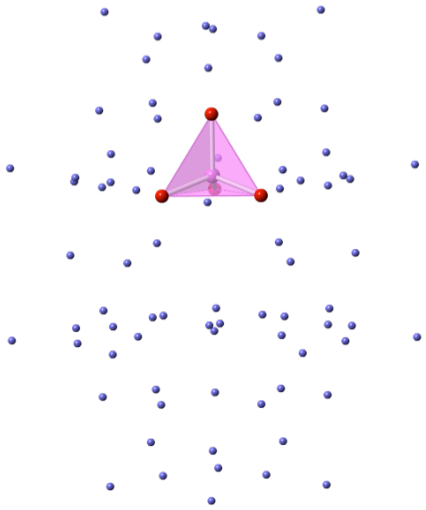

Figure 4. 6. Model applied for the study of the NMR parameters shown in Table 4.5. The pink tetrahedron represents the target $P(1)O_4^{3-}$ unit and purple spheres represent the positions of the multipole derived atomic charges (MDC-q).

The relevant NMR results obtained are shown in Table 4.5. Comparing the computed values for the full structure, σ_{real}, and the simplified model, σ_{model}, we find roughly coincident trends, that is, both parameters decrease from left to right in the table. We also see that some compounds present very similar σ values (third, fourth and fifth columns) and, certainly in these cases, the rationalisation of the real and model shieldings by the calculated electronic energy gaps is less obvious. Be that as it may, several contributions to σ^p exist besides the one related to the gap listed, which makes the overall analysis more complex.

Table 4. 5. Computed shieldings,[a] energy gaps and chemical shifts (in ppm) of ^{31}P(1) for several polyoxometalates.

	α-$[P_2W_{18}O_{62}]^{6-}$	1-$[P_2VW_{17}O_{62}]^{7-}$	α_2- $[P_2W_{17}O_{61}Sn(CH{=}CH_2)]^{7-}$	α_2-$[P_2W_{17}O_{61}Ru(DMSO)]^{8-}$	α_2-$[P_2W_{17}O_{61}]^{10-}$
σ_{real}	334.0	331.9	330.9	331.2	325.7
σ_{model}[a]	321.5	319.9	319.2	318.2	316.6
σ^p_{model}[a]	–655	–657	–658	–659	–661
Gap[b]	15.75	15.58	15.55	15.55	15.04
δ_{exp}	–12.44[39]	–10.84[39]	–9.77[42]	–8.61[45]	–6.79[40]

[a]The model structure contains one PO_4 unit surrounded by point charges (see text for details). Values obtained with the PBE/TZP//OPBE/TZ2P procedure. [b]Energy gaps (in eV) between the two orbitals involved in the electronic transition governing σ^p.

The following facts can be rationalised. Firstly, let us point out that changes in the diamagnetic part of the shielding, σ^d, are much smaller than those in the paramagnetic part. Consequently, the behaviour of $\delta(^{31}P)$ can be entirely attributed to the changes occurring in the paramagnetic shielding.

When the energy gaps between occupied and virtual orbitals decrease in the series, electronic transitions are allowed more easily, thus *deshielding* the P nucleus. The resulting σ^p contribution is reinforced (more negative) turning the total σ less positive. The overall effect on $\delta(^{31}P)$ is to make it more positive. Assuming that orbital gaps are just an approximation to the probability of electronic transitions, we can qualitatively relate these magnitudes to understand the nature of the NMR phenomena and their trends. Also, for a decreasing oxidation state of the metal$_{(1)}$ ($W^{VI} > V^V > Sn^{IV} > Ru^{II}$) the chemical shift becomes more positive. Moreover, when a lacuna is present, i.e. α_2-$[P_2W_{17}O_{61}]^{10-}$, the same behaviour is followed and $\delta(^{31}P)$ is even more positive. This is related to the energy gaps of the main transition(s) governing σ^p, since the σ^d is nearly constant for a given nucleus. When the oxidation state of the metal$_{(1)}$ decreases, the occupied MOs become less stabilised, being closer to the virtual MOs (smaller orbital gaps) and therefore the paramagnetic shielding, σ^p, becomes more negative. α_2-$[P_2W_{17}O_{61}]^{10-}$ presents the smallest energy gap (15.04 eV, more deshielded P nucleus) and the most negative σ^p = –661 ppm. On the contrary, α-$[P_2W_{18}O_{62}]^{6-}$ has the largest energy gap and the least negative σ^p = –655 ppm, with the most shielded P nucleus in Table 5, with $\delta(^{31}P)$ = –12.44 ppm. Recalling Eq. 4.3, it can be seen that when this energy gap increases, u_{ai} becomes less negative and therefore $|\sigma^p|$ is smaller giving more negative δ values.

4.4. Conclusions

The accurate determination of ^{31}P NMR chemical shifts in POMs has been tackled by DFT methods. The main computational parameters affecting the quality of such properties are the density functional and the basis set size, as well as the spin-orbit and solvent effects. The influence of the first two on the quality of the ^{31}P NMR chemical shifts was investigated on a large family of compounds based on $[XM_{12}O_{40}]^{n-}$ and $[X_2M_{18}O_{62}]^{n-}$ frameworks. This work suggests that using a TZP/PBE for NMR calculation step and TZ2P/OPBE for geometry optimization is the best DFT procedure for the accurate determination of ^{31}P NMR chemical shifts. Also the KT2 functional, somewhat less widespread than the PBE or OPBE ones, gives excellent results. As recently reported,[16] the more CPU demanding hybrid-type functionals do not clearly outperform GGA-type ones. The geometry optimization step does not need atomic basis sets larger than TZ2P. The results obtained with the PBE/TZP//OPBE/TZ2P procedure presented a MAE of 2.64 ppm that decreases to MAE = 0.6 ppm and MSE = – 0.05 ppm (for a set of 50 signals) applying a linear fitting to experimental data.

The dependency of $\delta(^{31}P)$ was analysed in terms of electronic structure parameters by means of a simplified model of PO_4 surrounded by point charges for the rest of atoms. The main variations in $\delta(^{31}P)$ come from the paramagnetic contribution to the shielding (σ^p), which is directly related to occupied-virtual orbital transitions with phosphorous contribution. The ^{31}P NMR chemical shifts can be linked with the energy of such transitions. As the oxidation state of the metal decreases ($W^{VI} > V^{V} > Sn^{IV} > Ru^{II}$), the orbital energy gap roughly becomes smaller due to destabilization of the occupied orbitals, giving more positive δ values.

4.5. Bibliography

[1] Y. Ruiz-Morales, T. Ziegler, *J. Phys. Chem. A* **1998**, *102*, 3970.
[2] D. B. Chesnut, B. E. Rusiloski, *Chem. Phys.* **1991**, *157*, 105.
[3] A. Dransfeld, D. B. Chesnut, *Chem. Phys.* **1998**, *234*, 69.
[4] D. B. Chesnut, *Chem. Phys. Lett.* **2003**, *380*, 251.
[5] D. B. Chesnut, *J. Phys. Chem. A* **2005**, *109*, 11962.
[6] J. Přecechtělová, P. Novák, M. L. Munzarová, M. Kaupp, V. Sklenář, *J. Am. Chem. Soc.* **2010**, *132*, 17139.
[7] B. Maryasin, H. Zipse, *Phys. Chem. Chem. Phys.* **2011**, *13*, 5150.
[8] S. V. Fedorov, Y. Y. Rusakov, L. B. Krivdin, *Magn. Reson. Chem.* **2014**, *52*, 699.
[9] G. Schreckenbach, Y. Ruiz-Morales, S. K. Wolff, J. Khandogin, T. Ziegler, S. Patchkovskii, *Abstr. Pap. Am. Chem. Soc.* **1999**, *218*, U322.
[10] G. Schreckenbach, T. Ziegler, *J. Phys. Chem.* **1995**, *99*, 606.
[11] D. B. Chesnut, L. D. Quin, *Tetrahedron* **2005**, *61*, 12343.
[12] A. Zheng, H. Zhang, X. Lu, S.-B. Liu, F. Deng, *J. Phys. Chem. B* **2008**, *112*, 4496.
[13] J. Gracia, J. M. Poblet, J. A. Fernández, J. Autschbach, L. P. Kazansky, *Eur. J. Inorg. Chem.* **2006**, 1149.
[14] J. Gracia, J. M. Poblet, J. Autschbach, L. P. Kazansky, *Eur. J. Inorg. Chem.* **2006**, 1139.
[15] L. Vilà-Nadal, J. P. Sarasa, A. Rodríguez-Fortea, J. Igual, L. P. Kazansky, J. M. Poblet, *Chem. Asian J.* **2010**, *5*, 97.
[16] M. Pascual-Borràs, X. López, A. Rodríguez-Fortea, R. J. Errington, J. M. Poblet, *Chem. Sci.* **2014**, *5*, 2031.
[17] G. te Velde, F. M. Bickelhaupt, E. J. Baerends, C. Fonseca Guerra, S. J. A. van Gisbergen, J. G. Snijders, T. Ziegler, *J. Comput. Chem.* **2001**, *22*, 931.
[18] C. Fonseca Guerra, J. G. Snijders, G. te Velde, E. J. Baerends, *Theor. Chem. Acc.* **1998**, *99*, 391.
[19] ADF2013, SCM, Theoretical chemistry, Vrije Universiteit, Amsterdam, The Netherlands, https:// http://www.scm.com.
[20] J. P. Perdew, K. Burke, M. Ernzerhof, *Phys. Rev. Lett.* **1996**, *77*, 3865.
[21] M. Swart, A. W. Ehlers, K. Lammertsma, *Mol. Phys.* **2004**, *102*, 2467.
[22] T. W. Keal, D. J. Tozer, *J. Chem. Phys.* **2003**, *119*, 3015.
[23] M. Swart, M. Solà, F. M. Bickelhaupt, *J. Chem. Phys.* **2009**, *131*.
[24] M. Swart, M. Solà, F. M. Bickelhaupt, *J. Comput. Methods Sci. Eng.* **2009**, *9*, 69.
[25] P. J. Stephens, F. J. Devlin, C. F. Chabalowski, M. J. Frisch, *J. Phys. Chem.* **1994**, *98*, 11623.
[26] S. Grimme, *J. Comput. Chem.* **2004**, *25*, 1463.
[27] M. Ernzerhof, G. E. Scuseria, *J. Chem. Phys.* **1999**, *110*, 5029.
[28] E. V. Lenthe, E. J. Baerends, J. G. Snijders, *J. Chem. Phys.* **1993**, *99*, 4597.
[29] E. V. Lenthe, E. J. Baerends, J. G. Snijders, *J. Chem. Phys.* **1994**, *101*, 9783.
[30] E. V. Lenthe, A. Ehlers, E. J. Baerends, *J. Chem. Phys.* **1999**, *110*, 8943.
[31] A. Klamt, *J. Phys. Chem.* **1995**, *99*, 2224.
[32] A. Klamt, V. Jonas, T. Bürger, J. C. W. Lohrenz, *J. Phys. Chem. A* **1998**, *102*, 5074.

[33] C. van Wüllen, *Phys. Chem. Chem. Phys.* **2000**, *2*, 2137.
[34] X. López, J. J. Carbó, C. Bo, J. M. Poblet, *Chem. Soc. Rev.* **2012**, *41*, 7537.
[35] M. Kozik, C. F. Hammer, L. C. W. Baker, *J. Am. Chem. Soc.* **1986**, *108*, 7627.
[36] G. M. Brown, M. R. Noe-Spirlet, W. R. Busing, H. A. Levy, *Acta Cryst.* **1977**, *B33*, 1038.
[37] Y. Jeannin, M. Fournier, *Pure Appl. Chem.* **1987**, *59*, 1529.
[38] L. A. Combs-Walker, C. L. Hill, *Inorg. Chem.* **1991**, *30*, 4016.
[39] M. Abbessi, R. Contant, R. Thouvenot, G. Hervé, *Inorg. Chem.* **1991**, *30*, 1695.
[40] R. Contant, M. Abbessi, R. Thouvenot, G. Hervé, *Inorg. Chem.* **2004**, *43*, 3597.
[41] M. A. Fedotov, R. I. Maksimovkaya, *J. Struct. Chem.* **2006**, *47*, 952.
[42] S. Bareyt, S. Piligkos, B. Hasenknopf, P. Gouzerh, E. Lacôte, S. Thorimbert, M. Malacria, *J. Am. Chem. Soc.* **2005**, *127*, 6788.
[43] K. Nomiya, M. Kaneko, N. C. Kasuga, R. G. Finke, M. Pohl, *Inorg. Chem.* **1994**, *33*, 1469.
[44] M. W. Lodewyk, M. R. Siebert, D. J. Tantillo, *Chem. Rev.* **2011**, *112*, 1839.
[45] S. Ogo, N. Shimizu, K. Nishiki, N. Yasuda, T. Mizuta, T. Sano, M. Sadakane, *Inorg. Chem.* **2014**, *53*, 3526.
[46] K. Nomiya, Y. Togashi, Y. Kasahara, S. Aoki, H. Seki, M. Noguchi, S. Yoshida, *Inorg. Chem.* **2011**, *50*, 9606.
[47] N. I. Kuznetsova, L. G. Detusheva, L. I. Kuznetsova, M. A. Fedotov, V. A. Likholobov, *J. Mol. Catal. A: Chem.* **1996**, *114*, 131.
[48] E. Radkov, Y. J. Lu, R. H. Beer, *Inorg. Chem.* **1996**, *35*, 551.
[49] O. A. Kholdeeva, R. I. Maksimovskaya, *J. Mol. Catal. A: Chem.* **2007**, *262*, 7.

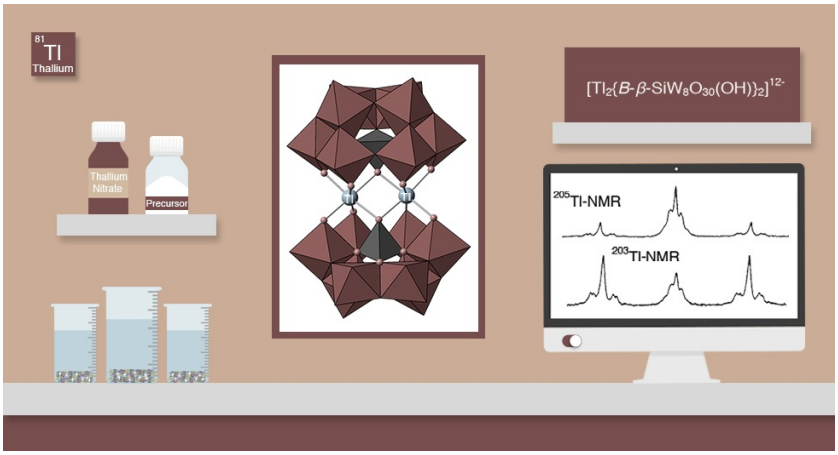

CHAPTER 5

Thallium(III) Containing POM: Structure and NMR

Related publications:

W. W. Ayass, T. Fodor, Z. Lin, R. M. Smith, X. Xing, K. Abdallah, I. Tóth, L. Zékány, M. Pascual-Borràs, A. Rodríguez-Fortea, J. M. Poblet, L. Fan, J. Cao, B. Keita, M. S. Ullrich, U. Kortz, *Inorg. Chem.* **2016**, 55, 10118.

CHAPTER 5

Thallium(III) Containing POM: Structure and NMR

The first discrete thallium-containing polyoxometalate was synthesized and structurally characterized. In this project, we have worked in collaboration with two groups: Dr. Kortz group from Jacobs University and Dr. Tóth group from University of Debrecen. All three groups aimed to identify and characterize this thallium-containing polyoxometalate. The polyanion $[Tl_2\{B\text{-}\beta\text{-}SiW_8O_{30}(OH)\}_2]^{12-}$ *was characterized in solid state and shown to be stable in solution by* $^{203/205}Tl$ *NMR, electrospray ionization mass spectrometry and electrochemical studies. Our role was to study the stability in solution by DFT calculations. Moreover, a detailed study of* $^{203/205}Tl$ *NMR has been performed and how* $^{203/205}Tl$ *NMR depends on protonation is also reported.*

5.1. Introduction

As mentioned, the structural and compositional variety in polyoxometalates is unmatched and hence such compounds are of interest in many different areas such as catalysis, medicine, magnetism and materials science.[1-3] Vacant (lacunary) heteropolytungstates can be considered as inorganic ligands which coordinate to all kinds of oxophilic electrophiles such as *d* or *f* block metal ions or main group elements. Tl-containing compounds are widely used in electrical, medical, and even glass manufacturing industries. However, little work has been done on Tl-containing POMs. Thallium(I) salts of conventional POMs such as the Keggin ion, paratungstate, and metatungstate have been prepared.[4-8] Thallium-containing metal-oxides with extended structures,[9-11] or Zintl phases containing thallium have also been reported.[12-14] In 1953, Magneli[15] first described the structure of hexagonal tungsten bronze

A_xWO_3, and later Shivahare[5] (1964) and Bierstedt[16] (1965) isolated $Tl_2W_4O_{13}$ and $Tl_{0.3}WO_3$, respectively. In 1980 Tourné's group reported a thallium(III)-containing Keggin ion as based on elemental analysis.[17] Considering that no structurally characterized discrete Tl-containing POM had been reported to date, the group of Dr. Kortz in Bremen decided to investigate the reactivity of Tl^{3+} ions with lacunary heteropolytungstates.

The aqueous solution chemistry of Tl^{3+} is dominated by a high tendency for hydrolysis, accompanied by formation of Tl^{3+}-hydroxo-complexes starting already at pH 0.5. Contrary to the lighter congeners of group 13, Tl^{3+} does not form polynuclear hydroxo-complexes,[18] and compounds with more than one Tl-atom are known mainly in organo-thallium chemistry.[19] Usually $^{203/205}$Tl NMR spectra showing ^{205}Tl-^{203}Tl spin-spin coupling are extraordinarily powerful tools for studying the structure and dynamics of compounds with more than one Tl-center.[20, 21]

In this chapter, we report the synthesis and both computational and experimental solution characterization of the novel, thallium(III)-containing 16-tungsto-2-silicate $[Tl_2\{B\text{-}\beta\text{-}SiW_8O_{30}(OH)\}_2]^{12-}$ in abbreviate form $Tl_2(SiW_8)_2$, which represents the first structurally characterized discrete thallium-containing metal-oxide. In polyanion $Tl_2(SiW_8)_2$, two octahedrally coordinated Tl^{3+} ions are sandwiched between two lacunary {B-β-SiW_8} Keggin-type fragments (Figure 5.1).

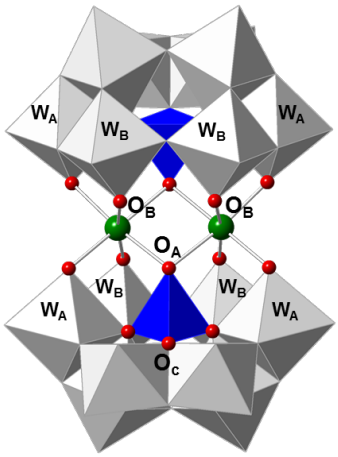

Figure 5. 1. Polyhedral and ball and stick structure of $Tl_2(SiW_8)_2$. Color code: Red balls-O, green balls-Tl, blue polyhedron-Si and grey polyhedron-W. The most basic oxygens are labeled as O_A, O_B and O_C. The W_A and W_B atoms have different $^{203/205}$Tl-^{183}W spin-spin coupling constants.

5.2. Experimental Characterization

The experimental work was done by the group of Dr. Kortz at Jacobs University and Dr. Tóth at Debrecen University. The results were extracted from ref. [22] in order to compare with the computational ones.

Single crystal X-ray analysis revealed that $Tl_2(SiW_8)_2$ crystallizes in a monoclinic crystal system with space group $P_{21/m}$. The $[Tl_2\{B\text{-}\beta\text{-}SiW_8O_{30}(OH)\}_2]^{12-}$ architecture presents a polyanion with idealized C_{2h} symmetry, which consists of two thallium(III) centers and two $\{B\text{-}\beta\text{-}SiW_8O_{31}\}$ POM units. The $\{B\text{-}\beta\text{-}SiW_8O_{31}\}$ units were formed from the $[\gamma\text{-}SiW_{10}O_{36}]^{8-}$ precursor by rotational isomerization and loss of tungsten. The first POM comprising a $\{B\text{-}\beta\text{-}SiW_8O_{31}\}$ unit was reported in 2005.[23] The $\{M_2(B\text{-}\beta\text{-}SiW_8O_{31})_2\}$ structure type has been seen before with M being 3d metal ions.[24] The two equivalent thallium(III) centers in $Tl_2(SiW_8)_2$ polyanion are both six-coordinated, and each thallium ion is coordinated to two $\{B\text{-}\beta\text{-}SiW_8O_{31}\}$ lacunary POM fragments via four terminal O atoms of the two complete tungsten-oxo triads and two terminal O atoms of two {SiO4} hetero groups. The Tl-O bond length ranges from 2.156(1) to 2.238(1) Å, and the distance between both thallium atoms is 3.338(1) Å. Bond valence sum (BVS) calculations[25] confirmed that the oxidation state of the two thallium centers is +3. As based on elemental analysis $Tl_2(SiW_8)_2$ is diprotonated and Bond Valence Sum (BVS) suggest that they are located on the two μ_3-O atoms (labeled O_C in Figure 5.1).

$NH_4K\text{-}Tl_2(SiW_8)_2$ is sufficiently soluble in water to record ^{205}Tl and ^{203}Tl NMR spectra of reasonable quality (Figure 5.2). Both isotopes have a nuclear I of 1/2, and a natural abundance of 70.5 % and 29.5%, respectively. At the first sight, both spectra appear as pseudo-triplets, attributed to the spin-spin coupling between two sterically identical Tl-atoms. The central peaks are assigned to polyanions with homonuclear $^{205}Tl\text{-}^{205}Tl$ or $^{203}Tl\text{-}^{203}Tl$ coupling, whereas the satellite peaks belong to heteronuclear $^{205}Tl\text{-}^{203}Tl$ coupled polyanions, respectively. The peak intensities of the pseudo-triplets agree very well with the expected ones based on the isotope ratios, 29.5/2 : 70.5 : 29.5/2 (^{205}Tl NMR), and 70.5/2 : 29.5 : 70.5/2 (^{203}Tl NMR). This finding is in full agreement with the solid-state structure having two Tl-atoms in identical positions, and it proves unequivocally that the dimeric structure of $Tl_2(SiW_8)_2$ is preserved in solution. The chemical shift difference between the satellite peaks represents the coupling constant, $^2J(^{205}Tl\text{-}^{203}Tl) = 2670$ Hz.

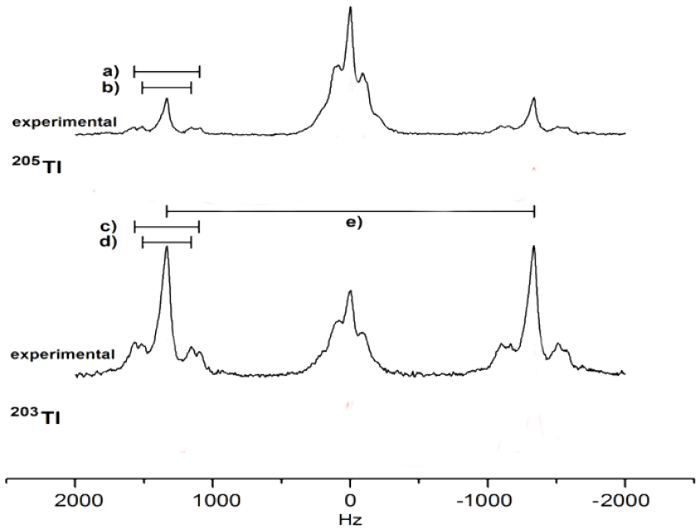

Figure 5. 2. Experimental 144.26 MHz ^{205}Tl (top) and 142.86 MHz ^{203}Tl NMR (bottom) spectra of $Tl_2(SiW_8)_2$, ~6 mM in 0.04 M acetic acid/sodium acetate buffer, pH = 4.1. Coupling constants shown: a) $^2J(^{205}Tl\text{-}^{183}W_A)$ ca. 475 Hz, b) $^2J(^{205}Tl\text{-}^{183}W_B)$ ca. 354 Hz, c) $^2J(^{203}Tl\text{-}^{183}W_A)$ ca. 470 Hz, d) $^2J(^{203}Tl\text{-}^{183}W_B)$ ca. 350 Hz and e) $^2J(^{205}Tl\text{-}^{203}Tl) = {}^2J(^{203}Tl\text{-}^{205}Tl)$ ca. 2700 Hz (same value in both spectra).

Interestingly, a closer look at the spectra indicates further fine structure of the recorded peaks caused by spin-spin coupling with ^{183}W atoms (14.3%). The two different values for $^2J(^{203}Tl\text{-}^{183}W)$ are ca. 470 and 350 Hz, respectively, and the corresponding values for $^2J(^{205}Tl\text{-}^{183}W)$ are ca 1% larger (see Figure 5.2 caption for details). These values can be rationalized by coupling to two structurally non-equivalent types of tungsten being two bonds away from the thallium centers. These couplings may actually be averaged effects of two types of ^{183}W centers (W_A, W_B) with similar chemical environments. The Tl···W distances are 3.64 and 3.65 Å for W_A, and 3.72 and 3.73 Å for W_B, respectively. However, the relatively broad spectral lines prohibit such a detailed investigation. The ^{1}H couplings do not play a role because of fast exchange, and the effects of ^{29}Si (I = 1/2, 4.7%) and ^{17}O (I = 5/2, 0.037 %) are also not detectable.

The chemical shift value of ca. 2206 ppm (the position of the central peaks, referenced to infinitely diluted $TlClO_4$ as 0 ppm) is consistent with a +3 oxidation state for the thallium atoms being six-coordinated to O atoms in an octahedral geometry in water.[26, 27] Comparing the $^2J(^{205}Tl\text{-}^{203}Tl)$ = 2670 Hz coupling constant to literature values is difficult, as published constants are mostly based on organothallium compounds in nonaqueous solvents. The $^2J(^{205}Tl\text{-}^{203}Tl)$ = 2560 Hz coupling constant for $(TlOEt)_4$ is very similar to ours,[28] but values ranging from 1920 to 19835 Hz for thallium-metal carbonyls have also been reported.[21]

5.3. Computational Details

All DFT calculations were carried out with the ADF2013 package.[29-31] The geometries and energies were computed with Slater-type basis sets of TZ2P quality using the GGA-type OPBE[32] and BP86[33, 34] functionals. We applied scalar relativistic corrections to the electrons via the *zeroth-order regular approximation* (ZORA)[35-37] that includes either only scalar or spin-orbit coupling as well. For NMR calculations, we used a Slater-type all-electron basis set and PBE,[38] JCPL[39, 40] GGA-type functionals and PBE0[41, 42] hybrid functional with spin-orbit (SO) corrections and a numerical integration accuracy parameter set to 6.0. The notation for this procedure is expressed throughout the text as Functional^{NMR}/Basis^{NMR}//Funcional^{OPT}/Basis^{OPT}. The stabilizing effect of an aqueous solution (liquid water and counterions, modelled as a continuum material) where our target molecules are immersed was approximated via *the conductor-like screening model* (COSMO).[43, 44] The molecular cavities generated with this model are defined from VdW atomic radii.

Now, we focus on the ^{205}Tl NMR chemical shift. The calculated chemical shift in ppm (δ) is determined as $\delta_{cal} = \sigma_{ref} - \sigma_x$, where σ_x and σ_{ref} are the isotropic average shielding for the nucleus of the target and the reference compounds, respectively. So, an accurate σ_{ref} is needed in order to get a reliable prediction for the NMR signal.

As shown in Figure 5.1, the $Tl_2(SiW_8)_2$ has two thallium atoms (green balls), which are equivalent. Then, we will only find one σ_x value. Note that we also need to compute the reference (σ_{ref}) in order to obtain the $\delta(^{205}Tl)$.

In the case of ^{205}Tl NMR, the reference is a salt of Tl(I), which is a bit tricky to compute. First of all, we have computed a Tl(I) solvated with different number of waters (4,5 or 6), as it is shown that the chemical shift is very sensitive to solvation in thallium cations.[45-47] However, these references lead to an overestimation of the results. This can be due to the incorrect description of the solvation.

Consequently, another way to determine the reference has been used. We have computed a set of $\sigma_x(^{205}Tl)$ of well-characterized thallium compounds (Table 5.1). Considering the equation, $\delta = \sigma_{ref} - \sigma_x$, and having the experimental $\delta(^{205}Tl)$ chemical shift, a much accurate σ_{ref} has been obtained. Moreover, this procedure is able to reduce errors from sources such as solvation effects, rovibratory effects or other methodological limitations.

Table 5. 1. Computed $\sigma(^{205}Tl)$ and $\delta_{exp}(^{205}Tl)$ chemical shifts for a set of thallium compounds.

Compound	$\sigma_{cal}(^{205}Tl)$	$\delta_{exp}(^{205}Tl)$	Ref
Me_3Tl	6487	5093	[48]
Me_2Tl^+	7629	3534	[49]
$[(CN)_5Pt\text{-}Tl(CN)_3]^{3-}$	9634	2224	[50]
$[(CN)_5Pt\text{-}Tl]$	12177	786	[51]
$[(CN)_5Pt\text{-}Tl(CN)_2]^{2-}$	9107	1975	[50]
$[(CN)_5Pt\text{-}Tl(CN)(H_2O)_4]^-$	9757	1371	[50]
$Tl(CN)_4^-$	9371	3010	[50]

The list of values in Table 5.1 were used to perform a linear regression, $\sigma_{ref} = \delta_{exp} + \sigma_x$. We have obtained a σ_{ref} of 11737 ppm. Now, we can use the *new* σ_{ref} to get a much proper estimation of the chemical shift, $\delta_{cal}(^{205}Tl)$. So, in order to obtain the $\delta_{cal}(^{205}Tl)$, we have used,

$$\delta_{cal}(^{205}Tl) = 11737 - \sigma_x \quad (5.1)$$

The spin-spin coupling constants do not require any data processing operation, meaning that the values obtained from the calculation can be directly compared with the experimental spin-spin couplings.

5.4. Computational characterization

Once being introduced, we show how the computational techniques play an important role in the identification of such a structure. First, the electronic structure and the geometrical parameters are discussed. Afterwards, a detailed study of how $^{205/207}Tl$ NMR depends on protonation is reported.

5.4.1. Electronic structure and geometry parameters

DFT calculations were performed in order to evaluate the most probable protonation sites and proton distribution on $Tl_2(SiW_8)_2$ in aqueous solution. The structure was optimized initially for the non-protonated anion $[Tl_2\{B\text{-}\beta\text{-}SiW_8O_{31}\}_2]^{14-}$ and the most characteristic X-ray bond distances (in parenthesis) were rather well reproduced: Tl-

O(Si) 2.28 Å (ca 2.20 Å), W-O(Si) 2.25 - 2.43 Å (2.27-2.34 Å), W-O(Tl) ca 1.81 Å (ca. 1.83 Å), and Tl···Tl 3.37 Å (3.34 Å).

Three types of oxygens in $Tl_2(SiW_8)_2$ were found to be the most nucleophilic according to molecular electrostatic potential distributions (see Figure 5.3), i.e. the triply bridging O_A and O_C oxygen sites, and the doubly bridging O_B sites. Protonation of O_B site only slightly modifies the structure of the non-protonated form, whereas when the two protons are attached to the two O_A or two O_C sites the distortion is much more important, inducing a lengthening in the O-Tl (~ 0.4 Å) and in O-W (~ 0.3 Å) bond lengths, respectively. It also modifies the Tl···Tl distance separation, which is also elongated.

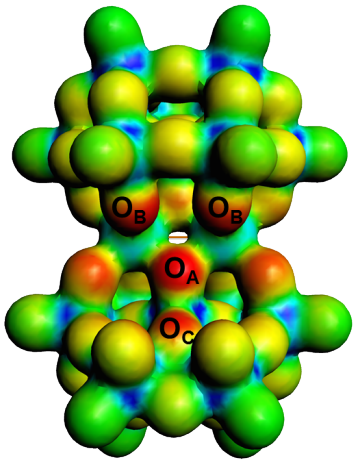

Figure 5. 3. Molecular electrostatic potential for $Tl_2(SiW_8)_2$. Red identifies more nucleophilic regions and green and blue denote less nucleophilic regions.

The most stable, diprotonated form of $Tl_2(SiW_8)_2$ has two protons on two of the four equivalent O_B sites. When the protons are placed on the O_C and O_A sites, the energy increase is only 2.1 and 3.9 kcal·mol^{-1}, respectively. Therefore, it is expected that the protons will likely move amongst these three positions in solution. In the solid state, the most accessible basic sites (O_A and O_B) are blocked by direct interactions with counter cations, making O_C the most favorable site to be protonated, as suggested by BVS.

On the other hand, we have analyzed the electronic structure of $Tl_2(SiW_8)_2$ (Figure 5.4). As a feature of polyoxometalates, the highest occupied molecular orbitals (HOMOs) are localized over the p_z oxygens orbitals, which cause the so-called oxo band. The first

two unoccupied molecular orbitals (LUMOs) are localized over the thallium atom, specifically at their 6s orbital. For LUMO+2 and higher-energy orbitals the electrons are localized mostly in the W and O atoms.

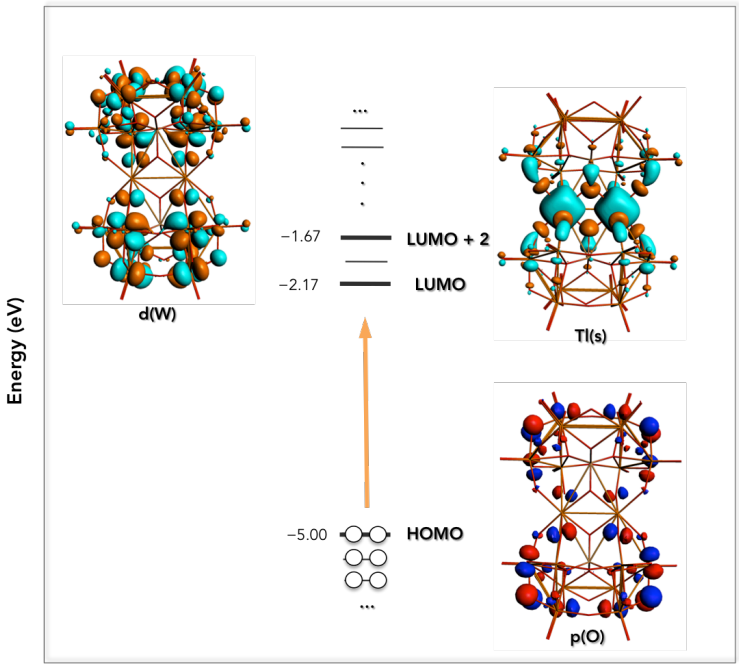

Figure 5. 4. Electronic structure representation of $Tl_2(SiW_8)_2$,with circles representing the electrons and values in eV. The 3D orbitals images are those labeled in the scheme.

The electrochemical properties of $Tl_2(SiW_8)_2$ were investigated in phosphate media by cyclic voltammetry (CV) and controlled potential electrolysis. The reduction pattern, at pH 4.3, is composed of three well-defined reduction waves peaking respectively at -0.593 V, -0.830V and -0.960V versus SCE. The first and third waves are attributed to the stepwise reduction of the Tl^{III} centers into Tl^0 state through the Tl^I state, in accordance with previous observations.[52] The second wave is attributed to the reduction of the W^{VI} centers.[23, 53] We have confirmed these trends by DFT calculations. We have calculated the two-electrons reduced $Tl_2(SiW_8)_2$ and we have obtained that the two extra electrons will be localized at the thallium s orbital, which corresponds to the LUMO in Figure 5.4.

5.4.2. Chemical Shift

The chemical shift for the two equivalent ^{205}Tl nuclei of the non-protonated anion is predicted to be 2140 ppm, which is rather similar to that found in experiment for $[Tl_2\{B\text{-}\beta\text{-}SiW_8O_{30}(OH)_2]^{12-}$ (2206 ppm). The ^{205}Tl chemical shift does not change appreciably with the protonation degree or with the protonation site. Di-protonated structures, as $[Tl_2\{B\text{-}\beta\text{-}SiW_8O_{30}(OH)_2]^{12-}$, showed very similar ^{205}Tl chemical shifts regardless of their protonation sites (A, B or C, see Figure 5.1 and Table 5.2), even thought the Tl···Tl distances might change appreciably (up to 3.99 Å for di-protonation in site A). A range between 2117 and 2245 ppm was found for the different protonation sites studied in this work. Tetra-protonation in sites B did not alter noticeably neither the ^{205}Tl chemical shifts nor the Tl···Tl distance (3.42 Å). The effect of the counterions was also considered by introducing explicitly two NH_4^+ cations making hydrogen bonds with the oxygens nearby the Tl atoms. It can be shown that there is not a considerable change when the counterions are introduced.

Table 5. 2 Computed ^{205}Tl chemical shifts, along with the Tl···Tl distances and relative energies for $[Tl_2\{B\text{-}\beta\text{-}SiW_8O_{30}(OH)\}_2]^{12-}$ protonated at different oxygen sites.[a]

Sites	Protons	$\delta(^{205}Tl)$	d(Tl···Tl)
-	0	2140	3.372
O_A	2	2245	3.997
O_B	2	2167	3.365
O_C	2	2117	3.515
O_A- O_B	2	2239	3.625
O_A- O_C	2	2230	3.721
O_B- O_C	2	2155	3.435
O_B	2 [b)]	2151	3.412
O_C	2 [b)]	2142	3.558
Exp	2	2210	3.34

a) $\delta(^{205}Tl)$ in ppm, Tl···Tl in Å and E_{rel} in kcal·mol^{-1}. b) two NH_4^+ are interacting through H bonds with the POM.

5.4.3. Spin-Spin Coupling

As we have introduced, two different spin-spin coupling are determined experimentally. Then, we have computed the coupling constant between the two Tl isotopomers, $^2J(^{205}Tl\text{-}^{203}Tl)$, which is the origin of the satellites found in the Tl NMR spectrum, as discussed previously (*vide supra*). In contrast to the results found for the chemical shifts, the $^2J(^{205}Tl\text{-}^{203}Tl)$ coupling constants depend critically on the

protonation degree and the protonation sites (see Table 5.3). For example, for the non-protonated anion $[Tl_2\{B\text{-}\beta\text{-}SiW_8O_{31}\}_2]^{14-}$, the computed $^2J(^{205}Tl\text{-}^{203}Tl)$ constant was 7845 Hz, very large compared to 2675 Hz, the experimental value for $[Tl_2\{B\text{-}\beta\text{-}SiW_8O_{30}(OH)\}_2]^{12-}$. For the di-protonated anion with two protons attached to two of the four equivalent sites O_B, the coupling constant is only slightly reduced to 7565 Hz, in line with the small change observed for the Tl···Tl distance, 3.365 Å (Table 5.3). However, when the protonation occurs on sites O_C, the coupling constant is reduced to 5222 Hz in accordance with the lengthening of the Tl···Tl distance to 3.515 Å. For sites O_A the elongation in the Tl···Tl separation reaches up to 3.997 Å and the coupling constant decreases very significantly up to 141 Hz, much smaller than the experimental value. For di-protonated species with each proton on different sites, the same trend was observed, meaning that as the Tl···Tl distance becomes larger, the coupling constant is smaller. As a case in point, when one site O_A and one site O_B are protonated, the coupling constant is reduced appreciably up to 4241 Hz, as the lengthening of the Tl···Tl distance is much larger reaching a value of 3.721 Å. However, when one site O_B and one site O_C are protonated, the Tl···Tl distance does not change too much and consequently the coupling constant is only reduced up to 6287 Hz. The effect of the counterions was also considered by introducing explicitly two NH_4^+ cations making hydrogen bonds with the oxygens nearby the Tl atoms. A decrease of the coupling constant of about 20% and 10% in sites O_B and O_C was computed for the di-protonated anion.

Table 5. 3. Computed $^2J(^{205}Tl\text{-}^{203}Tl)$ coupling constants, along with the Tl···Tl distances and relative energies for $[Tl_2\{B\text{-}\beta\text{-}SiW_8O_{30}(OH)\}_2]^{12-}$ protonated at different oxygen sites.[a]

Sites	Protons	$^2J(^{205}Tl\text{-}^{203}Tl)$	Tl···Tl	E_{rel}
	0	7845	3.372	-
O_A	2	141	3.997	0.0
O_B	2	7565	3.365	-3.9
O_C	2	5222	3.515	-1.8
O_A- O_B	2	5057	3.625	-0.6
O_A- O_C	2	4241	3.721	-0.6
O_B- O_C	2	6287	3.435	-0.5
O_B	2 [b)]	6034	3.412	
O_C	2 [b)]	4700	3.558	
Exp	2	2675	3.34	

a) $^2J(^{205}Tl\text{-}^{203}Tl)$ in Hz, Tl···Tl in Å and E_{rel} in kcal·mol^{-1}. b) two NH_4^+ are interacting through H bonds with the POM.

In addition, we performed a regression between the $^{2}J(^{205}Tl\text{-}^{203}Tl)$ and the thallium-thallium distance. Figure 5.5. shows that the correlation is almost directly. Then, using this regression we can extrapolate the distance between the two thalliums needed to get the experimental $^{2}J(^{205}Tl\text{-}^{203}Tl)$. This distance is around 3.78 Å, which is significantly longer than the one formed in the X-ray structure (3.34 Å). We believe that the difference between the computational and experimental $^{2}J(^{205}Tl\text{-}^{203}Tl)$ values is not only due to differences in geometry. A plausible interpretation of these results could be that in solution the Tl···Tl distance can vary due to the mobile character of the protons and it is seen as an average of those distances.

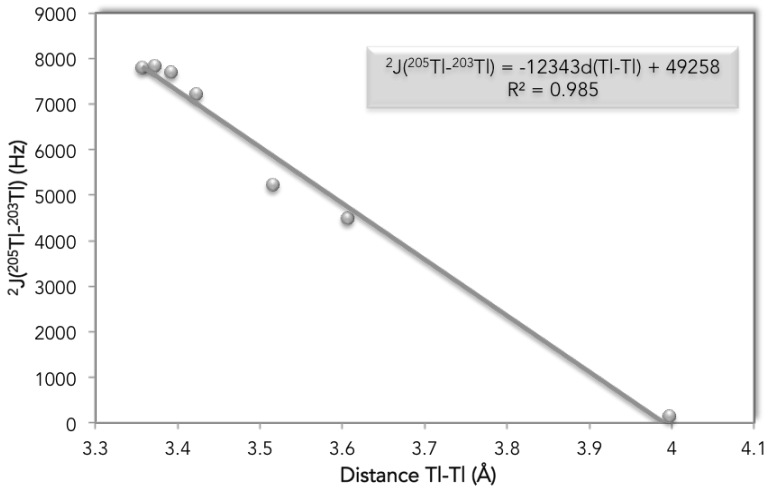

Figure 5. 5. Correlation between $^{2}J(^{205}Tl\text{-}^{203}Tl)$ in Hz and distance between the two thallium atoms in Å.

Gathering all these results, we conclude that the X-ray geometry must correspond to the di-protonated species with the two protons attached to O_c sites because the other two positions (O_A and O_B) are blocked by direct interactions with countercations. In solution, very likely the protons are mobile and they may be linked to O_B, O_C and O_A sites. Values in Table 5.3 clearly show that when one proton is attached to O_A or in less extension to O_C, the Tl···Tl separation increases and the $^{2}J(^{205}Tl\text{-}^{203}Tl)$ coupling decreases significantly. The relatively low energy differences obtained for different di-protonated anions gives support to this hypothesis. Instantaneous interactions of the relatively charged POM with the counterions may also affect to the central structure of the POM and consequently to the $^{2}J(^{205}Tl\text{-}^{203}Tl)$ coupling. Besides, we do not discard that our computational settings could overestimate $^{2}J(^{205}Tl\text{-}^{203}Tl)$.

Moreover, the coupling constant between Tl and W, $^{2}J(^{205}Tl\text{-}^{183}W)$, has also been calculated. Table 5.4. shows that the coupling between Tl and W are also dependent on protonation. In contrast with $^{2}J(^{205}Tl\text{-}^{203}Tl)$, for the non-protonated anion $[Tl_2\{B\text{-}\beta\text{-}SiW_8O_{32}]^{14-}$ the $^{2}J(^{205}Tl\text{-}^{183}W)$ are in good agreement with the experimental ones. For the di-protonated anion with two protons attached to two of the four equivalent sites O_B, the $^{2}J(^{205}Tl\text{-}^{183}W_B)$ decreases up to 50%, whereas $^{2}J(^{205}Tl\text{-}^{183}W_A)$ increases only a 12%. This is because the proton is directly linked to an O_B connected to a W_B (Figure 5.1). For the di-protonated anion with two protons attached to O_A analogous results are obtained, now the hydrogen is closer to W_A than W_B, and this is why an important decrease of $^{2}J(^{205}Tl\text{-}^{183}W_A)$ is shown. For the di-protonated anion with two protons in O_C no much change is observed.

Table 5. 4. Computed $^{2}J(^{205}Tl\text{-}^{183}W)$ coupling constants, for $[Tl_2\{B\text{-}\beta\text{-}SiW_8O_{30}(OH)\}_2]^{12-}$ protonated at different oxygen sites.[a]

Sites	Protons	$^{2}J(^{205}Tl\text{-}^{183}W_A)$	$^{2}J(^{205}Tl\text{-}^{183}W_B)$
-	0	412	381
O_A	2	93	495
O_B	2	460	189
O_C	2	441	450
Exp	2	470-475	350-354

a) $^{2}J(^{205}Tl\text{-}^{183}W)$ in Hz.

Taking in consideration the previous results, we should point out that the $^{2}J(^{205}Tl\text{-}^{183}W)$ results are much well reproduced than the $^{2}J(^{205}Tl\text{-}^{203}Tl)$. The error in the $^{2}J(^{205}Tl\text{-}^{203}Tl)$ results compared to experimental can be due to: (i) the mobile character of the protons in solution and we have to consider more than one protonated species, (ii) the computational methodology used. Therefore, we have tried to get better $^{2}J(^{205}Tl\text{-}^{203}Tl)$ varying the methodology.

5.4.4. Reproducing $^{2}J(^{205}Tl\text{-}^{203}Tl)$ coupling constants

In the early 2000's Autschbach and Ziegler published different pioneering works related to the calculation of NMR spin-spin couplings.[39, 54] They had a theoretical interest in NMR spectroscopy involving heavy nuclei like ^{183}W, ^{195}Pt ^{199}Hg or ^{205}Tl. It has long time before that it was discovered that a relativistic treatment of these systems containing such elements is necessary for the correct description of bonding. Since NMR spin-spin couplings are determined by features of the wave function at or very

close to the nuclei, one may expect enormously large relativistic effects. Autschbach *et. al.* studied in detail the NMR parameters of platinum-thallium bonded complexes.[45, 47, 48, 55] They reported that such spin-spin constants are very sensitive to the geometric and electronic structure as well as environment effects. In addition, for systems with as many electrons as those that they studied, it is difficult to calculate the NMR properties differing at least a 10% from experiments. It is well known that the Fermi Contact (FC) is the dominant contribution in the spin-spin coupling constants. The Fermi Contact term requires the density to be accurate near the nuclei and therefore, presumably, a good description of the function of s orbitals is important in order to reproduce correctly the values.[56] Thus, spin-spin couplings are quite sensitive to approximations used to describe the electron-electron interactions, the quality of the basis set, and every other approximation made in the computational model. The reliable calculation of coupling constants for heavy nuclei has some important theoretical requirements for the computational model, most importantly the inclusion of relativistic effects and electron correlation, basis sets that are capable of describing the large relativistic effects on J coupling, but other also more "exotic" features such as an adequate finite nuclei representation.[40] For a good description of the FC contribution Auschbach *et. al.* implemented the JCPL[39, 40] basis set in ADF program. This basis set is derived from the TZ2P basis of the ADF basis set library adapted for ZORA calculations which is a triple-ζ and core-double-ζ all-electron STO basis set with two sets of polarization functions. For the sixth-row elements, basis functions with exponents >> Z (Z= nuclear charge) were replaced by an even-tempered set of high-exponent s- and p- functions along with a set of accompanying density-fit functions. They reported[57, 58] a study for reproducing spin-spin coupling in thallium compounds. They concluded that in thallium compounds the inclusion of the spin-orbit coupling is crucial. Moreover, the spin-spin couplings in the Tl compounds are quite strongly dependent on the computational model. A spin-orbit relativistic formalism as well as the use of a hybrid functional appears to be overall beneficial. However, they pointed out that spin-orbit coupling does not improve the results in some compounds. Taking in consideration all previous studies, we decided to calculate the $^{2}J(^{205}Tl\text{-}^{203}Tl)$ with different methodologies (see Table 5. 5) and obviously make use of the JCPL basis set.

First, the effect of the basis set in the spin-spin coupling calculation (compare entries 1 and 2) is minor. Moreover, if the TZP basis set for NMR computation is replaced by a TZ2P, the CPU time for the latter is much larger and the $^{2}J(^{205}Tl\text{-}^{203}Tl)$ obtained is only slightly better. Second, the choice of the functional can be critical to compute $^{2}J(^{205}Tl\text{-}^{203}Tl)$. BP86 (entry 3) is not a good option. The $^{2}J(^{205}Tl\text{-}^{203}Tl)$ obtained with BP86 functional has an error higher than those obtained with the PBE (entry 1). As mentioned, the JPLC basis set was implemented for spin-spin coupling calculations. However, in our case this basis set (entries 5 and 6) does not improve the result. We

believe that error is due to the fact that JPLC is not implemented for W atoms and the Fermi Contact is not well reproduced.

Table 5. 5. Computed $^{2}J(^{205}Tl\text{-}^{203}Tl)$ coupling constants, for non-protonated $[Tl_2\{B\text{-}\beta\text{-}SiW_8O_{31}\}_2]^{14-}$ with different methodologies.[a]

Entries	Methodology	$^{2}J(^{205}Tl\text{-}^{203}Tl)$
1	TZP/PBE//TZ2P/OPBE	7845
2	TZ2P/PBE//TZ2P/OPBE	7230
3	TZP/BP86//TZ2P/PB86	8671
4	JCPL[b]/PBE//TZ2P/OPBE	9364
5	JCPL[c]//PBE//TZ2P/OPBE	9200
6	JCPL[c]//PBE0//TZ2P/OPBE	13867
	Experimental	2700

a) $^{2}J(^{205}Tl\text{-}^{203}Tl)$ in Hz. b) TZP were used for all the atoms except for Tl. c) TZP were used for all the atoms except for Tl and O.

It is worth mentioning that likely present calculations slightly overestimate the $^{2}J(^{205}Tl\text{-}^{203}Tl)$ constant. For example, for the organometallic complexes like $[Tl(OCH_2Me_3)]_4$, for which a $^{2}J(^{205}Tl\text{-}^{203}Tl)$ = 2540 Hz[59] was reported, we computed with the JCPL//PBE//TZ2P/OPBE methodology a value of 3305 Hz and with TZP//PBE//TZ2P/OPBE methodology a value of 2552 Hz. For complexes like, $Tl_2[Aryl_2P_4]$, for which a $^{2}J(^{205}Tl\text{-}^{203}Tl) \approx 12000$Hz[19] was reported, we computed values of ≈15000Hz and ≈19600 Hz with TZP//PBE//TZ2P/OPBE (+ JCPLC for Tl atoms) and TZP//PBE//TZ2P/OPBE methodologies, respectively.

5.5. Conclusions

We have structurally and electronically characterized the $Tl_2(SiW_8)_2$. We have shown that the optimized geometry reproduces correctly the X-ray geometry. Moreover, we studied the most likely positions of the two protons in solution. In solid state, these protons are linked to O_C because of O_A and O_B are blocked by direct interactions with countercations, making O_C the most favorable site to be protonated. In solution, the protons can be mobile and the relatively low energy differences obtained for different di-protonated anions supports this hypothesis. Moreover, we have determined NMR

parameters. The calculated ^{205}Tl chemical shifts are really well reproduced with DFT methodology. We have also computed different di-protonated $Tl_2(SiW_8)_2$ and we have shown that ^{205}Tl chemical shifts values do not depend much on the protonation. In the case of spin-spin coupling, however, there is a large difference between calculated and experimental $^2J(^{205}Tl\text{-}^{203}Tl)$ values. The $^2J(^{205}Tl\text{-}^{203}Tl)$ values depend so much on the protonation meaning that if there exist different di-protonated anions in solution we would need to consider more than one calculated $^2J(^{205}Tl\text{-}^{203}Tl)$ value and make a weighted average of those values in order to compare with the experimental one.

On the other hand, we have tested different methodologies to reproduce the $^2J(^{205}Tl\text{-}^{203}Tl)$ just for being sure that such difference between experimental and calculated $^2J(^{205}Tl\text{-}^{203}Tl)$ values was not due to methodology limitations. All the results obtained so far, even with those basis set optimized for NMR calculations, show large deviations for the $^2J(^{205}Tl\text{-}^{203}Tl)$ of the non-protonated $[Tl_2\{B\text{-}\beta\text{-}SiW_8O_{31}\}_2]^{14-}$ compared to experiment. We are currently working on this project.

5.6. Bibliography

[1] B. S. Bassil, U. Kortz, *Z. Anorg. Alleg. Chem.* **2010**, *636*, 2222.
[2] O. Oms, A. Dolbecq, P. Mialane, *Chem. Soc. Rev.* **2012**, *41*, 7497.
[3] S.-T. Zheng, G.-Y. Yang, *Chem. Soc. Rev.* **2012**, *41*, 7623.
[4] W. P. Thistlethwaite, W. T. Watson, *J. Inorg. Nucl. Chem.* **1962**, *24*, 1559.
[5] G. C. Shivahare, *Naturwissenschaften* **1964**, *41*, 406.
[6] M. A. Parent, J. B. Moffat, *Langmuir* **1996**, *12*, 3733.
[7] A. N. Kharat, M. Abedini, M. M. Amini, P. Pendleton, A. Badalyan, *Transition Met. Chem.* **2003**, *28*, 339.
[8] S. Mane, *Adv. Mater. Lett.* **2013**, *4*, 94.
[9] R. N. P. Choudhary, M. L. Nanda Goswani, S. Sharma, *Ind. J. Phys.* **1997**, *71*, 153.
[10] H. Y. Chang, S.-H. Kim, K. M. Ok, P. S. Halasyamani, *Chem. Mater.* **2009**, *21*, 1654.
[11] A. K. Paidi, R. N. Devi, K. Vidyasgar, *Dalton Trans.* **2015**, *44*, 17399.
[12] Z. Dong, J. D. Corbett, *J. Am. Chem. Soc* **1994**, *116*, 3429.
[13] M. M. Tillard-Charbonnel, C. H. E. Belin, A. P. Manteghetti, D. M. Flot, *Inorg. Chem.* **1996**, *35*, 2583.
[14] Z.-C. Dong, R. W. Henning, J. D. Corbett, *Inorg. Chem.* **1997**, *36*, 3559.
[15] A. Magneli, *Acta Chem. Scand.* **1953**, *7*, 315.
[16] P. E. Bierstedt, T. A. Bither, F. J. Darnell, *Solid State Commun.* **1966**, *4*, 25.
[17] F. Zonnevijlle, C. M. Tourné, G. F. Tourné, *Inorg. Chem.* **1982**, *21*, 2742.
[18] C. F. Baes, R. E. Mesmer, *The Hydolysis of Cations*, Wiley- Intersience Publication: New York, **1976**.
[19] A. R. Fox, R. E. Wright, E. Rivard, P. P. Power, *Angew. Chem. Int. Ed.* **2005**, *44*, 7729.
[20] G. M. Sheldrick, J. P. Yesinowski, *J. Chem. Soc., Dalton Trans.* **1975**, 870.
[21] J. W. van Hal, L. B. Alemany, K. H. Whitmire, *Inorg. Chem.* **1997**, *36*, 3152.
[22] W. W. Ayass, T. Fodor, Z. Lin, R. M. Smith, X. Xing, K. Abdallah, I. Tóth, L. Zékány, M. Pascual-Borràs, A. Rodríguez-Fortea, J. M. Poblet, L. Fan, J. Cao, B. Keita, M. S. Ullrich, U. Kortz, *Inorg. Chem.* **2016**.
[23] B. S. Bassil, S. Nellutla, U. Kortz, A. C. Stowe, J. van Tol, N. S. Dalal, B. Keita, L. Nadjo, *Inorg. Chem.* **2005**, *44*, 2659.
[24] R. S. Winter, D. L. Long, L. Cronin, *Inorg. Chem.* **2015**, *54*, 4151.
[25] I. D. Brown, D. Altermatt, *Acta Crystallogr., Set. B: Struct. Sci.* **1985**, *41*, 244.
[26] J. F. Hinton, *Bull. Magn. Reson.* **1992**, *23*, 90.
[27] I. Tóth, B. Györi, *Thallium: Inorganic Chemistry. In Encyclopedia of Inorganic Chemistry, Vol. 10*, 2nd ed., Wiley: New York, **2005**.
[28] W. G. Schneider, A. D. Buckingham, *Discuss. Faraday Soc.* **1962**, *34*, 147.
[29] G. te Velde, F. M. Bickelhaupt, E. J. Baerends, C. Fonseca Guerra, S. J. A. van Gisbergen, J. G. Snijders, T. Ziegler, *J. Comput. Chem.* **2001**, *22*, 931.
[30] C. Fonseca Guerra, J. G. Snijders, G. te Velde, E. J. Baerends, *Theor. Chem. Acc.* **1998**, *99*, 391.
[31] ADF2013, SCM, Theoretical chemistry, Vrije Universiteit, Amsterdam, The Netherlands, https:// www.scm.com.

[32] M. Swart, A. W. Ehlers, K. Lammertsma, *Mol. Phys.* **2004**, *102*, 2467.
[33] J. P. Perdew, *Phys. Rev. B* **1986**, *33*, 8822.
[34] A. D. Becke, *Phys. Rev. A* **1988**, *38*, 3098.
[35] E. V. Lenthe, E. J. Baerends, J. G. Snijders, *J. Chem. Phys.* **1993**, *99*, 4597.
[36] E. V. Lenthe, E. J. Baerends, J. G. Snijders, *J. Chem. Phys.* **1994**, *101*, 9783.
[37] E. V. Lenthe, A. Ehlers, E. J. Baerends, *J. Chem. Phys.* **1999**, *110*, 8943.
[38] J. P. Perdew, K. Burke, M. Ernzerhof, *Phys. Rev. Lett.* **1996**, *77*, 3865.
[39] J. Autschbach, T. Ziegler, *J. Chem. Phys.* **2000**, *113*, 936.
[40] J. Autschbach, *ChemPhysChem* **2009**, *10*, 2274.
[41] S. Grimme, *J. Comput. Chem.* **2004**, *25*, 1463.
[42] M. Ernzerhof, G. E. Scuseria, *J. Chem. Phys.* **1999**, *110*, 5029.
[43] A. Klamt, *J. Phys. Chem.* **1995**, *99*, 2224.
[44] A. Klamt, V. Jonas, T. Bürger, J. C. W. Lohrenz, *J. Phys. Chem. A* **1998**, *102*, 5074.
[45] J. Autschbach, B. Le Guennic, *J. Am. Chem. Soc.* **2003**, *125*, 13585.
[46] J. Autschbach, B. Le Guennic, *Chem. Eur. J.* **2004**, *10*, 2581.
[47] B. Le Guennic, K. Matsumoto, J. Autschbach, *Magn. Reson. Chem.* **2004**, *42*, S99.
[48] W. Chen, F. Liu, K. Matsumoto, J. Autschbach, B. Le Guennic, T. Ziegler, M. Maliarik, J. Glaser, *Inorg. Chem.* **2006**, *45*, 4526.
[49] C. Schramm, J. I. Zink, *J. Magn. Res.* **1977**, *26*, 513.
[50] F. Jalilehvand, M. Maliarik, M. Sandström, J. Mink, I. Persson, P. Persson, I. Tóth, J. Glaser, *Inorg. Chem.* **2001**, *40*, 3889.
[51] M. Maliarik, K. Berg, J. Glaser, M. Sandström, I. Tóth, *Inorg. Chem.* **1998**, *37*, 2910.
[52] T. D. Dolidze, D. E. Khoshtariya, M. Behm, G. Lindbergh, J. Glaser, *Electrochim. Acta* **2005**, 4444.
[53] L. Lisnard, P. Mialane, A. Dolbecq, A. J. Marrot, J. M. Clemente-Juan, E. Coronado, B. Keita, P. d. Oliveira, L. Nadjo, F.Sécheresse, *Chem. Eur. J.* **2007**, 3525.
[54] J. Autschbach, T. Ziegler, *J. Chem. Phys.* **2000**, *113*, 9410.
[55] J. Autschbach, T. Ziegler, *J. Am. Chem. Soc* **2001**, *123*, 5320.
[56] M. A. Watson, N. C. Handy, A. J. Cohen, T. Helgaker, *J. Chem. Phys.* **2004**, *120*, 7252.
[57] S. Moncho, J. Autschbach, *J. Chem. Theory Comput.* **2010**, *6*, 223.
[58] J. Autschbach, *J. Chem. Phys.* **2008**, *129*, 94105.
[59] C. A. Zechmann, T. J. Boyle, D. M. Pedrotty, T. M. Alam, D. P. Lang, B. L. Scott, *Inorg. Chem.* **2001**, *40*, 2177.

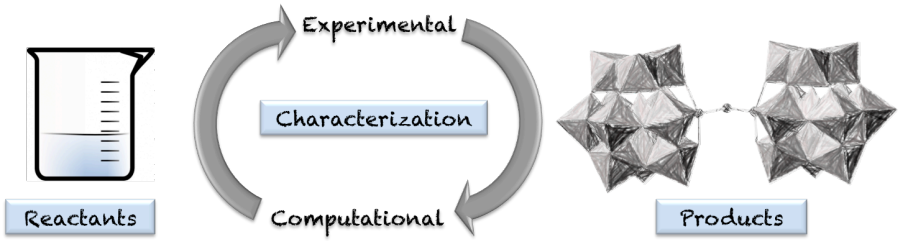

PART II

POMs Reactivity

PART II

POMs Reactivity

The reactivity of POMs is a widely studied research area, which is derived from the amazing structural diversity and the diverse range of physicochemical properties of this family of compounds. The Part II is focused on H_2 evolution reaction by a covalent iridium (III)-photosensitized polyoxometalate (POM) in the presence of acid and a sacrificial electron donor, and protonolysis reaction of Keggin and Lindqvist-type POMs. In both projects we have determined the possible reaction mechanism, studied the intermediates of the reactions and analysed some properties related to the intermediates. The last part of chapter 7 includes some experimental work. The reader will find all these projects in Part II of this thesis.

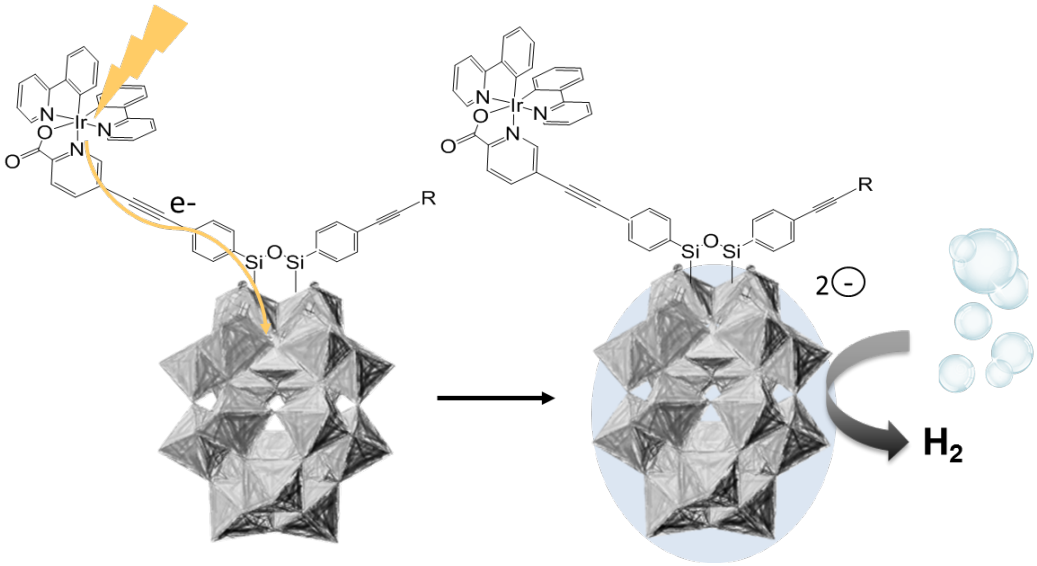

CHAPTER 6

Photochemical H_2 Evolution by an Iridium (III)-photosensitized Polyoxometalate

CHAPTER 6

Photochemical H_2 Evolution by an Iridium(III)-photosensitized Polyoxometalate

Many polyoxometalates have the ability to capture several electrons with minor structural or stability changes. In aqueous solution, only highly reduced forms of common POMs are able to reduce protons to H_2 but, in less polar organic solvents such as DMF, their electrons can be released in the presence of acid generating H_2. This idea was applied by Matt et al. (Energy Environ. Sci. **2013**, *6, 1504)[1] to design a covalent Ir(III)-photosensitized polyoxometalate (POM), capable of efficiently evolving H_2 in the presence of excess acid and a sacrificial electron donor. The stepwise mechanism of visible light harvesting, formation of the charge-separated species and proton reduction has been analysed with density functional theory and time-dependent-DFT. Herein, calculations tackle photochemical and electrochemical aspects of this complex reaction, shedding new light into the intricate process of photoinduced H_2 evolution assisted by hybrid POMs.*

6.1. Introduction

The efficient solar light-driven photochemical generation of fuels such as H_2 is a highly interesting topic and still a scientific and technological challenge after decades of research.[2-12] Many organometallic complexes made of cobalt, nickel, iridium or ruthenium have been used as molecular catalysts for photochemically- and electrochemically-driven H_2 evolution.[13] In the case of the environmentally friendly photochemical reactions, it is established that H_2 evolution relies on the formation of a photoinduced electronic charge separation with a suitable lifetime to permit further electron transfer.[14-19] In addition, the catalyst has to be able to use these

photogenerated charges to produce the chemical fuel as a major reaction outcome.[1] One of the greatest challenges is the integration, in a single molecular framework, of individual subunits able to bring together all these events. In the search for innovative materials for the photochemical production of fuels, POMs have attracted the attention of several research groups due to their unmatched chemical and structural versatility.[20-22] POMs are early transition-metal oxide clusters, most of which possess the ability to accept several electrons in a stepwise fashion,[23] in a number and at potentials that depend on their size, charge and composition.[24, 25] Reduced POMs have been tested in electrochemical assisted catalysis,[26-28] making them promising candidates for the development of artificial photosynthetic devices.[29] In recent years, the photochemical reduction of protons to H_2 has been a field of discussion.[13]

Some studies[30-38] showing that reduced POMs evolve H_2 via a photochemical process involve either strong UV light irradiation or the presence of a co-catalyst. However, in the last years, some reports have shown that visible light can also drive H_2 evolution aided by POM compounds.[1, 39-41] Artero, Izzet and co-workers[1] showed that a covalent Ir(III)-photosensitized derivative of the Wells-Dawson POM structure (denoted D_{Si}[Ir] in short) in the presence of a sacrificial reducing agent ($N(CH_2CH_3)_3$, or NEt_3) leads to efficient photoreduction of the POM fragment. Successive formation of the one- and two-electron reduced species was observed. Moreover, the system shows photocatalytic hydrogen evolution under visible light (hν) without a significant loss of performance over 1 week of continuous photolysis following the formal global reaction:

$$D_{Si}[Ir] + 2H^+ + 2NEt_3\ (+h\nu) \rightarrow D_{Si}[Ir] + H_2 + 2NEt_3^{\bullet+} \qquad (6.\ 1)$$

Figure 6.1a presents the reaction conditions reported in ref. 1 and the structure of the photoactive POM-based hybrid, D_{Si}[Ir]. It consists of an iridium(III)-containing double organosilyl antenna covalently linked to a Wells-Dawson-type POM compound depicted in blue. This system was efficiently synthesized by coupling a neutral unit made of Ir(III) bearing two 2-phenylpyridyl ligands (noted below as either ppy or (C^N)) and a pyridylcarboxylate ligand (noted below as either pic or (O^N)).

The proposed mechanism of POM photoreduction, schematically shown in Figure 6.1b, starts by light excitation of [Ir] leading to a charge-separation state. The electron is transferred from the π*[(O^N)] orbital to a low-energy tungsten-like POM orbital [1′]. Meanwhile, the trimethylamine (TEA) acts as a sacrificial electron donor, that is, the $[Ir]^+$ is reduced by the electron released by TEA. We assume that the active species responsible for the oxidation of the TEA is more likely the oxidized photosensitizer in the charge separation state rather than the excited form of the photosensitizer itself.

As shown below, the extra electrons in [2] and [3] are delocalized over the tungsten d orbitals of the POM framework.

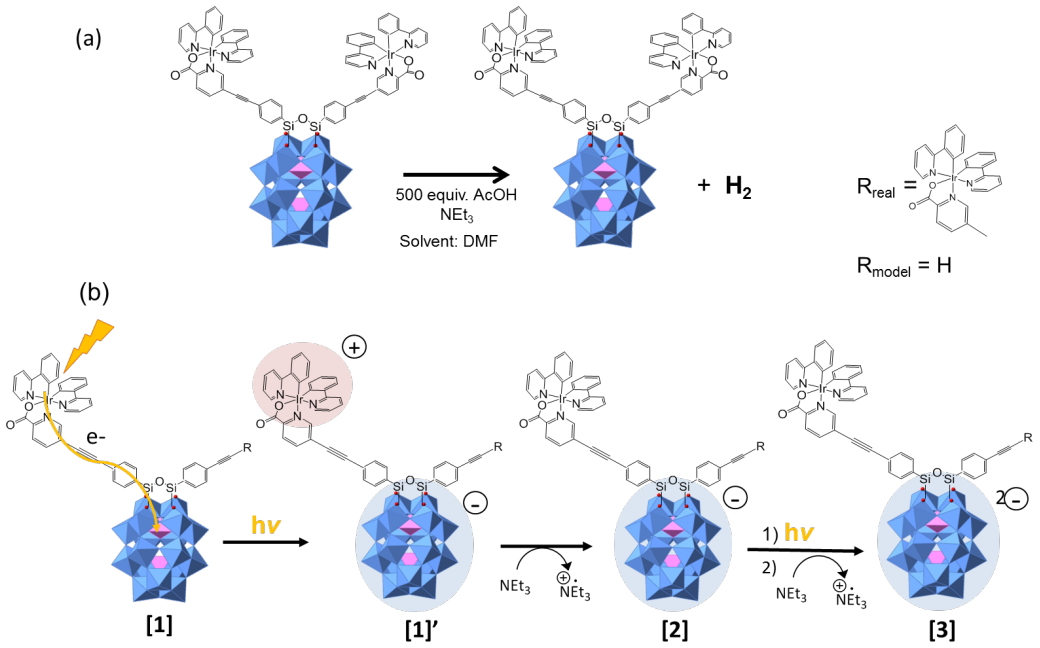

Figure 6. 1. Overview of the H_2 evolution process. The blue framework is the Wells-Dawson POM fragment with two silicon atoms, D_{Si}, and the organometallic fragment is the antenna, [Ir]. (a) Structure of the photosensitized POM species (D_{Si}[Ir] or [Ir]-POM) and reaction conditions reported in reference 1. R_{real} denotes the real structure of the [Ir] chromophore (two equivalent antennas) and R_{model} shows the model used in the calculations. (b) Structure and labeling of the relevant species involved in the generation of the possible activated complex [3].

The present DFT study examines the electronic structure of the [Ir]-POM system [1] and the intricate photoinduced stepwise H_2 evolution process reported in ref. 1. The characterization of the electronic structure and the knowledge of the associated properties of the reactants, intermediates and products is carried out. Also, time-dependent-DFT (TD-DFT) is applied to study the electronic transitions taking place in some of the systems upon visible-light irradiation. DFT is the most widely used computational method for the study of redox[42] and other properties of POM.[43]

6.2. Computational Details

DFT calculations were carried out using the ADF 2013 package.[44-46] Geometry optimisations of the transition states were first performed with the Quantum-regions Interconnected by Local Descriptors (QUILD) program, which acts as a wrapper around the ADF program.[47, 48] The exchange and correlation GGA functionals of Becke and Perdew (BP86) were employed to optimise all the equilibrium and transition state geometries.[49, 50] Relativistic corrections were included by means of the Zeroth Order Regular Approximation (ZORA) formalism.[51-53] Dispersion corrections were also incorporated (D3 method by Grimme).[54] Solvent effects in ADF calculations were included via the conductor-like screening model (COSMO).[55, 56] Slater-type basis sets of triple-ζ + double polarization (TZ2P) quality were used to describe the valence electrons of Ir, N, O, C, H, P and W. The following frozen cores were employed: 1s for C, N, O; 1s-2p for P; 1s-4d for Ir and 1s-4f shells for W, described by means of single Slater functions. TD-DFT calculations were performed using the Gaussian 09 program[57] with the B3LYP[58] functional and a 6-31G** basis set (LANL2DZ pseudopotentials[59] for W, P and Ir atoms), and using the Polarizable Continuum Model (PCM) for the solvent effects.[60]

6.3. Results and Discussion

The computational findings are based on model [1] and its derivatives. The structure of [1] is based on D_{Si}[Ir], the only difference between both being the replacement of one of the two equivalent [Ir] regions by H (see Figure 6.1a). Preliminary calculations on the full structure revealed that the two antennas are totally equivalent and independent, by virtue of the pairs of degenerate and chemically analogous orbitals associated to them. Thus, the target reaction can take place at the same time at each antenna separately, a case that our model holds. This approach simplifies our study without changing the general conclusions of the work.

6.3.1. Electronic Structure and Photochemistry

This section presents the electronic structure of the Ir-POM complex and the species generated upon light absorption. The correct understanding of the photochemical processes taking place in [1] requires a general view of its electronic structure, shown in Figure 6.2 as a molecular orbital sequence. It is composed of two distinctive and independent parts, one consisting of orbitals related with the organometallic fragment

(Ir-ligand), the other related with the inorganic metal-oxide framework (POM). This separation is respectively symbolized as the left- and right-hand halves of Figure 6.2. The occupied frontier orbitals of [1] (HOMO, HOMO–1 and HOMO–2) have π[Ir+(C^N)] nature, whereas the empty ones (LUMO to LUMO+4) are localized over the POM framework as combinations of d(W)-like orbitals. The higher-lying LUMO+6 is a π*(O^N) orbital, which is the first unoccupied orbital localized over the [Ir] region.

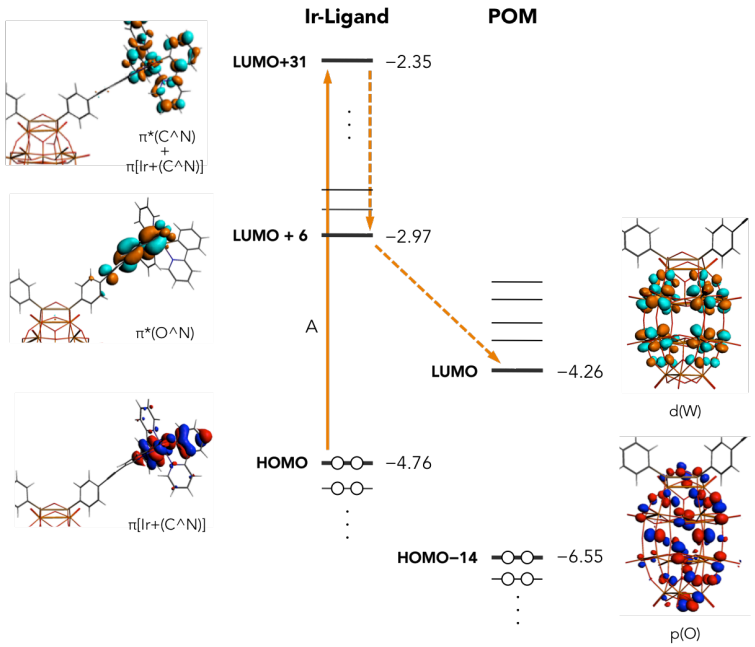

Figure 6. 2. Electronic structure of compound [1] represented as orbitals and electrons (circles). The energy levels (values in eV) on the left and right columns correspond to the organometallic antenna and the POM, respectively. The 3D orbital images are those labeled in the scheme. The solid and dashed orange lines represent the processes of light absorption and electronic relaxation, respectively, to produce the charge separated system [1′].

The central importance of the electronic transitions in the present study motivated the following TD-DFT calculations and analysis of [1]. The leading transitions simulated corresponding to [1] irradiated by a continuous visible-light irradiation (400 nm < λ < 800 nm) are represented in Figure 6.3. The most probable electronic transition in the low wavelengths region (300-500 nm) was computed to take place from HOMO to LUMO+31 with an energy of 2.94 eV (see Figure 6.2).[61] The band in the spectrum of Figure 6.3 has an oscillator strength f = 0.056 and has been characterized as a Metal to Ligand Charge Transfer (MLCT) localized on the iridium chromophore, π [Ir+(C^N)] → π* [(C^N)]. The [Ir+(C^N)] orbital has a mixed character of the (C^N) ligand orbital and a non-bonding orbital of the Ir atom.[62] The fate of this excited

state can take two routes: decay to the original ground state, or evolution to a second (lower energy) excited state in which the electron decays from LUMO+31 to LUMO+6, which acts as a channel for the electron, and finally to LUMO, the latter being localized in the POM framework (Figure 6.2). Overall, this is an [Ir] → POM charge migration process promoted by light irradiation, which requires 1.0 eV, leading to the charge separated species $[Ir]^+$-POM^-, or [1'].[62] These findings are in good agreement with the experiments by Izzet and co-workers, who proposed an initial excited state analogous to our most probable transition. Subsequently, the sacrificial reducing agent, NEt_3, restores Ir(III), yielding the one-electron reduced species [2] ([Ir]-POM^-).

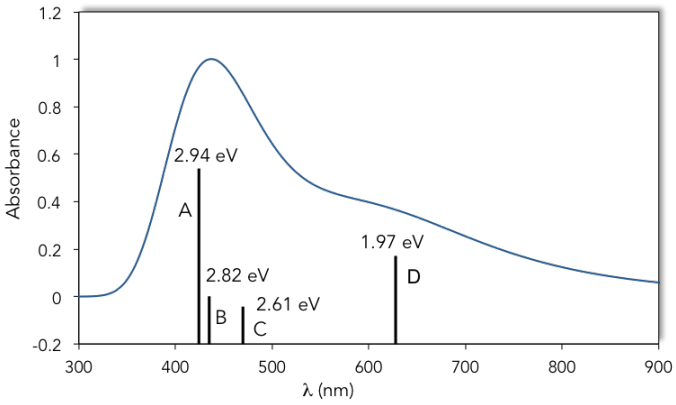

Figure 6. 3. Computed UV-vis spectrum for compound [1]. The main electronic transition A is schematically represented in Figure 6.2.

Table 6. 1. TD-DFT prediction of the most intense electronic excitations of compound [1] in the 400 nm < λ < 800 nm range. The transition energies, wavelengths, oscillator strengths and character are listed.

Label[a]	*E* (eV)	λ (nm)	Oscillator strength (*f*)	Main character[b]
D	1.97	627	0.0295	POM:p(O) → POM:d(W)
C	2.61	474	0.0127	POM:p(O) → POM:d(W)
B	2.82	439	0.0136	POM:p(O) → POM:d(W)
A	2.94	422	0.0564	p[Ir+(C^N)] → p*[Ir+(C^N)]

[a]Labels correspond to the transitions indicated in Figures 6.3 for compound [1]. [b]Only the transitions with more than 20% contribution are considered.

At high wavelengths (lower energies), the absorption bands of [1] are characterized by POM transitions, which are oxygen to metal charge transfer bands (bands B to D in Figure 6.3). The leading transitions are listed in Table 6.1. In summary, the most

probable electronic excitation is the MLCT on the [Ir] fragment with an oscillator strength f = 0.056 at 422 nm (transition A). The oscillator strength of transition D is somewhat larger than expected at the DFT level (it is well known that LMCT transitions are weak in oxidized POMs). This may originate in an overestimated orbital overlap computed by typical functionals when the implicated orbitals share the same region of the molecule.

The next stage of the process yields [2] after NEt_3 has restored the initial oxidation state of iridium. Then, excitation of the [Ir] complex takes place in an equivalent fashion as in [1], forming the second charge-separated state. Since the region of the molecule involved in light absorption is the same as in [1], the orbitals related with this second excitation are analogous to HOMO and LUMO+31, shown in Figure 6.2. From the excited state, the second charge transfer from [Ir]* to POM^- and another one-electron reduction of the complex gives the two-electron reduced species [3] ([Ir]-POM^{2-}). Present calculations show that the reduction of $[Ir]^+$ by TEA is slightly exothermic (–0.14 eV). Moreover, the energy required for leading to complex [2] is 0.86 eV (Eq. 6.1). The reduction process (Eq. 6.2) is more difficult (1.20 eV) than the first one, as expected. Therefore, the calculations are inline with the electrochemical measurements, that is, the first one-electron reduction is 0.34 eV easier than the second one-electron reduction in mild conditions.

$$[1] + NEt_3 \rightarrow [2] + NEt_3^{\bullet+} \quad \Delta E = 0.86 \text{ eV} \tag{6.1}$$

$$[2] + NEt_3 \rightarrow [3] + NEt_3^{\bullet+} \quad \Delta E = 1.20 \text{ eV} \tag{6.2}$$

In Figure 6.4, the spin densities of the charged-separated [1]' and the lowest doublet [2] are shown. The former has one unpaired electron localized over the equatorial region of the POM framework and the other electron localized in [Ir]. In [2], one electron is delocalized over the tungsten atoms of the POM.

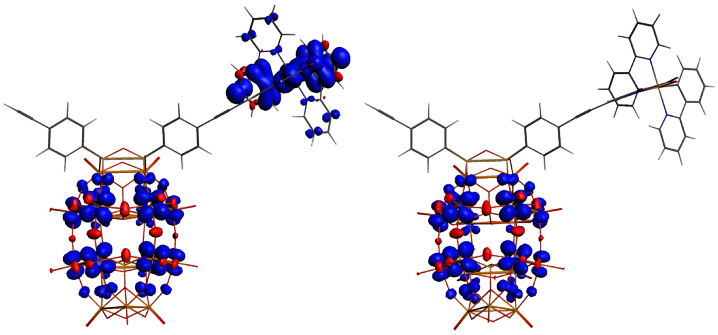

Figure 6. 4. Spin density representation (isosurface for ρ = 0.03) for the charge-separation state [1'] (left) and the lowest doublet state for compound [2] (right).

Reduction of [2] by irradiation and reduction yields [3], which sequence of molecular orbitals is shown in Figure 6.5. The only apparent difference between [1] and [3] is that the latter has two extra localized and paired electrons in the POM framework. The HOMO (corresponding to the LUMO in [1]) is a d(W)-like orbital, the next occupied orbitals having π[Ir+(C^N)] character. The lowest four unoccupied orbitals have very similar character to the HOMO, thus being also localized over the POM. The higher-lying LUMO+4 is a π*(O^N) orbital, which is the first unoccupied orbital localized over the [Ir].

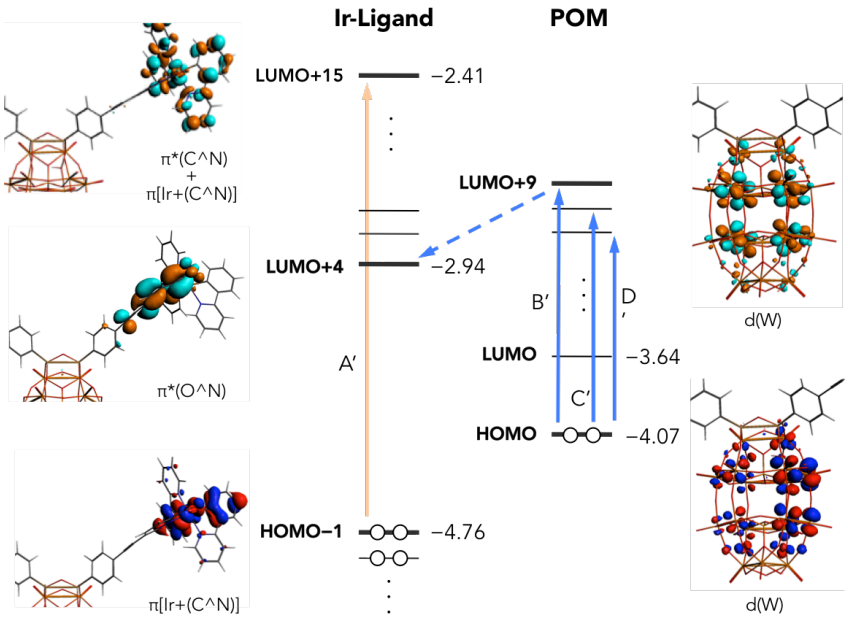

Figure 6. 5. Electronic structure of compound [3]. Energy levels and circles represent orbitals and electrons, respectively. Equivalently to Figure 2, solid and dashed blue lines represent excitation and relaxation processes. Excitation A′ is shown although it is not the most intense one. Orbital energies in eV.

The two-extra electrons in the POM can also be excited by UV-vis light, whose transitions are summarized in Table 6.2 with the highest oscillator strengths, and the spectrum shown in Figure 6.6. The most probable transition (B′: f = 0.09, 608 nm) is HOMO → LUMO+9, which costs 2.04 eV, and implies d(W)-like orbitals only. Similar excitations (C′, D′) appear in a nearby range of energies with slightly smaller intensities (Table 3.2). The bands in the electronic spectrum differ from those of [1], notably the most intense band, which is characterized by POM → POM transitions in the 600-800 nm range of d(W)-d(W) dominant character. Additionally, the absorption bands in the 400-500 nm region are MLCT transitions localized on the iridium chromophore. As

from [1], the most probable transition centred at the iridium chromophore appears at 2.94 eV (A'). It is worth saying that one could consider a direct transition from the HOMO of [3] to the first [Ir] unoccupied molecular orbital, LUMO+4 (not drawn). However, calculations show that this transition is unlikely (f = 0.0001, 570 nm), probably explained by the near-zero overlap between both orbitals, making this transition less relevant.

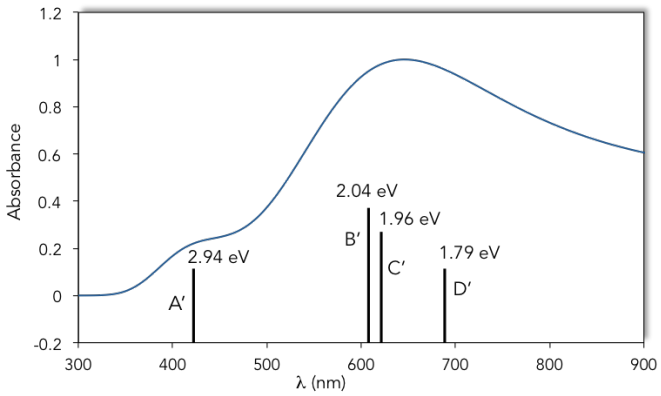

Figure 6. 6. Computed UV-vis spectrum for compound [3]. The main electronic transitions, A' to D', are sketched in Figure 6.5.

Table 6. 2. TD-DFT prediction of the most intense electronic excitations of compound [3] in the 400 nm < λ < 800 nm range. The transition energies, wavelengths, oscillator strengths and character are listed.

Label[a]	E (eV)	λ (nm)	Oscillator strength (f)	Main character[b]
D'	1.79	693	0.0655	POM:d(W) → POM:d(W)
	1.92[c]	645	0.0281	POM:d(W) → POM:d(W)
C'	1.96	623	0.0836	POM:d(W) → POM:d(W)
B'	2.04	608	0.0943	POM:d(W) → POM:d(W)
A'	2.94	422	0.0572	p[Ir+(C^N)] → p*[Ir+(C^N)]

[a]Labels correspond to the transitions indicated in Figures 6.6 for compound [3]. [b]Only the transitions with more than 20% contribution are considered. [c]Not indicated in the spectrum.

6.3.2. Basicity of the H_2 precursor

POMs can be protonated in acidic media, either in their fully oxidized state or upon/after reduction, depending on their chemical nature, molecular charge and size.[24, 63-66] Note that [3] is willing to protonation in the POM framework due to the two extra electrons. Calculations can predict where the protons are more likely localized in the POM surface. We computed the Molecular Electrostatic Potential map (MEP), shown in Figure 6.7, as well as atomic charges and protonation energies at several oxygen sites (Table 6.3). The results reveal that bridging oxygen sites have the largest affinity to protons in the system. In particular, the equatorial bridging oxygens A and B were found to be the most basic ones.

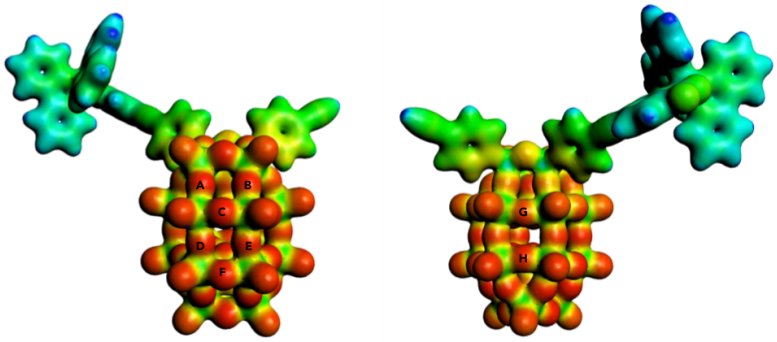

Figure 6. 7. Two views of the molecular electrostatic potential of the simplified model of two-electrons reduced D_{Si}[Ir] without one of the organometallic antennas, [3], used to assess the relative basicity of the POM framework. This qualitative approach gives information about the most basic sites. Orange-red colours identify the most nucleophilic regions and green-blue colours denotes less nucleophilic or electrophilic regions. The most nucleophilic sites of the system are bridging oxygens located in the POM framework. The protonation energies and atomic charges of the labelled sites are explored in Table 6.3.

Table 6. 3. Protonation energies[a] and atomic charges for the labelled oxygens of compound [3] (see Figure 6.7). MDC-q and Bader correspond to different methodologies to obtain atomic charges.

Oxygen site	Energy[a]	Atomic charges	
		MDC-q	Bader
A	-28.3	-0.8451	-1.1048
B	-28.4	-0.8440	-1.1042
C	-19.3	-0.8195	-1.1120
D	-22.2	-0.8116	-1.0944
E	-22.6	-0.8116	-1.0941
F	-18.7	-0.8073	-1.1101
G	-19.1	-0.8125	-1.0957
H	-21.6	-0.8295	-1.0904

[a]Protonation energies (in kcal·mol^{-1}) calculated for the reference compound (without the two organometallic antennas) and following the reaction: D_{Si} (2e$^-$-reduced) + H_3O^+ → D_{Si}[Ir] -H^+ (2e$^-$-reduced) + H_2O

The protonation energies from Table 6.3 show that the most basic sites of the two-electrons reduced D_{si} are A and B. The atomic charges also follow the same trends. Therefore, we have also computed reactions 6.3 and 6.4 for compound [3], where CH_3COOH and H_3O^+ are taken as source of protons, respectively. Reaction 6.3 only needs 2.4 kcal·mol^{-1}, whereas reaction 6.4, is exothermic by -27.1 kcal·mol^{-1}. Thus from now on we consider that [3]-H^+ is protonated by the presence of free H_3O^+.

$$[3] + CH_3COOH \rightarrow [3]\text{-}H^+ + CH_3COO^- \quad (6.\ 3)$$

$$[3] + H_3O^+ \rightarrow [3]\text{-}H^+ + H_2O \quad (6.\ 4)$$

For a better estimation of the protonation energy, we have calculated the Gibbs free energy following the scheme applied by López *et. al.*[24] for the accurate calculation of that energy. Following the same method from $[P_2W_{18}O_{62}]^{8-}$ to reach $[HP_2W_{18}O_{62}]^{7-}$ in DMF media, we have obtained a protonation energy of -24.94 kcal·mol^{-1}, considering H_3O^+ as a source of protons. The electronic energy of the same process is -28.46 kcal·mol^{-1}, rather close to the one obtained for compound [3] (see reaction 6.4), thus one can note that Gibbs free energies (which take a long time to obtain) are comparable to electronic energies in such systems. Moreover, for comparison purposes the Gibbs free energy of the protonation process in H_2O media have been calculated. Expectedly, the value obtained is -16.95 kcal·mol^{-1}, less exothermic since, in aqueous, solution the charged species are more stable than in DMF, the protonation being less favoured in H_2O than in DMF. We have also considered the protonation of [1] and [2] but the associated reaction energies are highly endothermic.

6.3.3. Redox Properties and H_2 Evolution

Additional points related with the photocatalytic H_2 evolution by confronting different energetic arguments are addressed. The reduced POM [3] being the activated species that ultimately catalyses H_2 evolution is assessed.

Structure [1] derives from the fully oxidised $[P_2W_{18}O_{62}]^{6-}$ POM, which features a LUMO at –4.42 eV computed in H_2O medium. This deep value explains the computed Reduction Energy (RE) = –4.32 eV, in complete agreement with the first pH-independent redox process measured (0.04 V vs SCE).[64] The second redox wave is also pH independent. The considerable stability of the 2e-reduced $[P_2W_{18}O_{62}\ 2e]^{8-}$ anion does not favour H_2 evolution in mild acidic aqueous conditions since the redox potential necessary for $2H^+ + 2e^- \rightarrow H_2$ cannot be thermodynamically compensated by the oxidation of $[P_2W_{18}O_{62}\ 2e]^{8-}$, demonstrating that $[P_2W_{18}O_{62}]^{6-}$ is a stronger oxidant than H^+. So, a catalyst-free solution with H^+ and P_2W_{18} would not produce H_2 unless (a)

the POM is highly reduced or (b) the pH is extremely acidic so that the $\Phi(H^+/H_2)$ gets sufficiently positive, following the Nernst equation, to remove the electrons accommodated in the reduced POM.

The liquid bulk (solvent + other species) greatly determines the redox behaviour of molecules, a fact that can be used to promote or impede reactions at will. For ionic species such as POMs, reduction in organic solvents is less favoured than in water, evidencing the limited ability of poorly polar media to stabilize anions. Calculations driven on $[P_2W_{18}O_{62}]^{6-}$ in DMF and H_2O attest this fact (see Table 6.4), which are supplemented with measurements and calculations for $[PW_{11}MoO_{40}]^{3-}$ and $[SiW_{11}MoO_{40}]^{4-}$.[67] The reduction energies (REs) and LUMO energies obtained for this series in two solvents show that REs of all species get more positive (RE *shift* > 0) when H_2O is replaced by DMF. It also arises that the compounds with higher negative charge densities experience larger RE shifts. The LUMO and RE for the reactant compound [1] match the values for the bare $[P_2W_{18}O_{62}]^{6-}$ system, revealing that the inorganic fragment in [1] keeps its chemical identity. The major difference is the more accentuated RE shift of +0.33 eV in [1] vs. $[P_2W_{18}O_{62}]^{6-}$. So, the reducing power of electron-rich POMs (provided they can be obtained) is enhanced in DMF. For the isostructural $[XW_{11}MoO_{40}]^{n-}$ Keggin derivatives, the increment of one charge unit as P is replaced by Si produces larger differences in the redox properties between H_2O and DMF (RE shift (P) = +0.08 eV, RE shift (Si) = +0.16 eV). For $P_2W_{18}O_{62}]^{6-}$, the change upon solvent replacement is even enlarged (+0.19 eV). The corresponding LUMO energies previous to reduction clearly explain the RE values. Analogous experimental measurements have shown how POMs modify their redox potentials by moderate to large extents upon solvent replacement owing to their anionic nature.[67] It must be mentioned that calculations follow the observed trend.

Table 6. 4. DFT computed LUMO and 1e-reduction energies[a] (RE) for selected POM compounds showing the effect of solvent replacement.

	H_2O		DMF		
	LUMO	RE	LUMO	RE	RE *shift*
$[P_2W_{18}O_{62}]^{6-}$	–4.42	–4.32	–4.27	–4.13	+0.19
[1]	–4.45	–4.42	–4.26	–4.09	+0.33
$[PW_{11}MoO_{40}]^{3-}$	–4.65	–4.62	–4.59	–4.54	+0.08
$[SiW_{11}MoO_{40}]^{4-}$	–4.40	–4.41	–4.28	–4.25	+0.16

[a]Values in eV. Recall that, formally, RE ≈ $-\Phi$.

Multi-electron reduction of [1] is a key step. In DMF, present calculations reproduce the trend of the cyclic voltammograms (see ref. 1) without and with excess AcOH. For the first reduction, with an observed potential shift of 60 mV, we consider that no protonation takes place, the shift coming from the bulk properties of the solution. Owing to the considerable potential shift of 280 mV observed in the second reduction of [1], the presence of acid was assumed to originate in protonation of the 2e-reduced species. Hence, the difference between adding the second electron to [1] when excess acid is present or not reveals that the protonated species is 150 meV easier to reduce than the unprotonated one, in qualitative agreement with the experiment, evidencing that the second reduction is associated with protonation of the POM. The computational overestimation may arise from an oversimplified computational model including no excess AcOH in the bulk, only the proton attached to the POM.

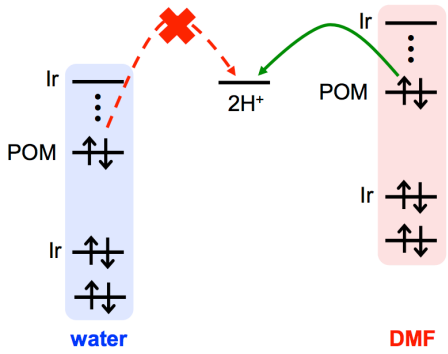

Figure 6. 8. The Ir-POM^{2-} complex in solution. Electronic structure of the reduced active form in water and DMF. Due to the anionic nature of Ir-POM, the molecular orbitals are found at more positive energies in DMF. The energy of the empty orbital of H^+ is much less sensitive to the nature of the solvent.

In the catalytic cycle represented in Figure 6.9, the initial energy gain of the complex upon light absorption is larger than ~1.5 eV (400 nm < λ < 800 nm), which is the energy required for excitation of the iridium chromophore and the necessary amount to overcome the energy requirements of the whole reaction. With some probability, the excited electron in the [Ir]* region will hop to the POM framework to generate the charge-separated [Ir]$^+$-POM$^-$ form (step 2). This process can occur again to give [Ir]$^+$-POM^{2-} (step 2'). In DMF, the extra electrons in the reduced POM$^-$ and POM^{2-} compounds are less stable than in water solution, as mentioned, and their energy approaches the amount of energy necessary to reduce H^+. It is represented in the oversimplified step 3 of Figure 6.8, with a reaction energy strongly depending on the actual source of protons.

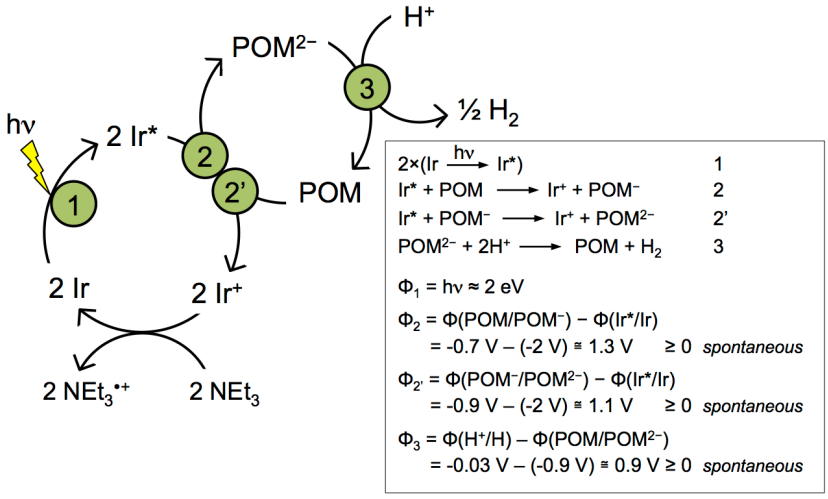

Figure 6. 9. Schematic diagram of H_2 evolution with the Ir-POM complex in DMF and excess acid with NEt_3 as the sacrificial reductant. The approximate electrochemical requirements of the various steps of process (1–3) are given. POM^{2-} = [3].

The thermodynamics of the $2H^+ + 2e \rightarrow H_2$ step is crucial. For a complete theoretical understanding of this process, a well-defined source of H^+ must be known, but it is not the case in this study. Trying to clarify this, calculations in DMF reveal that direct reaction of the 2e-reduced [3] with AcOH or NEt_3 as proton sources to produce H_2 is not favoured (> +20 kcal mol^{-1}). On the other hand, if H_3O^+ was present in the solution, reaction with [3] would spontaneously generate H_2 (–35.8 kcal mol^{-1}). That being said, H_3O^+ is expected to exist in DMF *only if* abundant moisture from the added AcOH is present and, thus, the acid is partially dissociated.

Going into more detail, species [3]-H^+ is a probable electron and proton source for H_2 evolution, as suggested above in this chapter. From the results obtained on the basicity of [3] and the thermodynamic *allowedness* of the protonated form, we can consider the 2e-reduced monoprotonated POM species, [3]-H^+, as the precursor of H_2. The reaction energy of process 6.5 was computed in water and DMF media to check if the previous arguments are solid, revealing a more favourable process in DMF (-8.7 kcal·mol^{-1}) than in water (0.4 kcal·mol^{-1}). Such dissimilar reaction energies bring to light one of the greatest advantages of using DMF instead of water as solvent for H_2 evolution.

$$[3]\text{-}H^+ + H_3O^+ \rightarrow [1] + H_2O + H_2 \qquad (6.\ 5)$$

At a purely electrochemical level, taking the experimental redox potentials in DMF (vs SCE), which are –0.9 V for the second reduction wave of D_{Si}[I][1] and –0.03 V for proton reduction (estimated from measurements with the $Fc^{+/0}$ electrode),[68] H_2 evolution is, step by step and overall, a favourable reaction from a thermodynamic point of view. Considering the simplest model, namely the bare H^+ surrounded by solvent, calculations indicate that the empty orbital of H^+ is placed at a rather constant energy of –0.7 eV both in DMF and H_2O, matching the stable $\Phi(H^+/H_2)$ reduction potential measured in both solvents.[68] On the other hand, the differences in redox behaviour of the Dawson species in H_2O and DMF are notable. In the 2e-reduced Dawson species, the highest occupied orbital lays at ca. –3.7 eV in DMF, considerably above in energy than in H_2O, where it is below –4.0 eV (see scheme in Figure 6.8). Thus, even if the origin of H^+ is unclear, the process [3] + $2H^+$ → [1] + H_2 is clearly enhanced in DMF.

Finally, we wish to remark that reduced hybrid POMs have been used for CO_2 reduction, where a Re-organic decorated phosphotungstate Keggin cluster acts as photo-sensitizer, electron reservoir and electron donor. [61, 62, 69] We can not discard that in parallel to the outer-sphere hydrogen evolution on the surface of the electron-rich POM, a fraction of excited electrons return to the Ir centres as represented in Figure 6.6 (dashed line), and then a hydride species as the one represented in Figure 6.10 is formed. Many organometallic complexes, which contain transition metals, can form a hydride to produce molecular hydrogen.[70-76] Such systems have focused a considerable interest, and over the last fifteen years numerous homogeneous molecular catalysts have been reported based on rare (Rh, Pd, Pt) or more abundant metals (Co, Ni, Fe, Mo) combined to various molecular photosensitizer (PS) as metallic complexes (Ru, Ir, Re, Os), porphyrins or organic dyes.[13] Some studies focus on iridium(III) as catalyst.[13, 76, 77] One of the most discussed mechanisms is the formation of a metal hydride which can react with a proton, resulting in H_2. We have checked that this species can evolve H_2 with relatively low energy barriers (<12 kcal·mol^{-1}), although this hypothesis needs experimental confirmation. So, more studies are needed in this direction.

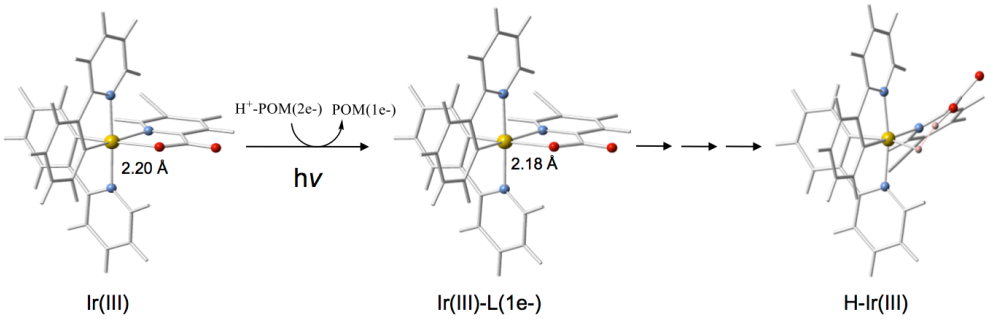

Figure 6. 10. An alternative process taking place at the organometallic fragment. Upon light irradiation of species [3], one or both electrons located in the two-electron reduced POM region migrate back to the antenna (first step), although this process is vaguely probable as TD-DFT calculations indicate (HOMO to LUMO+5 excitation in Figure 6.6). If this occurs, protons in the media can have an increased affinity for the Ir or the organic ligands surrounding it, and therefore H_2 can evolve in this region of the complex (second part of the mechanism). Color code for spheres: yellow-Ir, blue-N, red-O and pink-H.

6.4. Conclusions

A thorough DFT analysis on the photocatalytic H_2 evolution reaction reported by Matt *et al.* in ref. 1 is presented. We characterise the POM-based photosensitised reactant and intermediate species formed during the reaction mechanism, discussing photo- and electrochemical aspects. Calculations reveal that the two iridium-containing antenna of the reactant are chemically independent, justifying the theoretical simplified one-antenna model [1]. Electronic structure calculations show that the orbitals involved in the processes described here can be clearly classified as antenna- or POM-like upon their nature.

Photochemistry, studied with the TD-DFT formalism, confirm that, upon absorption of UV-vis light by the reactant, the most probable electron excitation involves the [Ir] chromophore localized in the antenna, with one electron transferred as π [Ir+(C^N)] → π* [(C^N)]. Partial relaxation of the excited stated generated might populate a d(W)-like empty orbital of the POM fragment, producing the charge-separated species. NEt_3 restores iridium to its initial oxidation state. After two excitation + reduction steps, the electron-rich species has extra electrons located in the POM fragment that might eventually reduce H^+.

From the electrochemical point of view of the reaction, we have identified the orbitals of the POM that are found at considerably more positive energies in DMF with respect to aqueous medium, whereas the energy of the empty orbital of H^+ is not as dependent on the solvent. Therefore, the $POM^{2-} + 2H^+ \rightarrow POM + H_2$ electron transfer is thermodynamically favoured in the reaction conditions, whereas in even very acidic aqueous conditions it is not, being the solvent the key point favouring the process. The energy of the hydrogen evolution process was computed in water and DMF media to check if the previous arguments are solid, revealing a more favourable process in DMF than in water. Such dissimilar reaction energies bring to light one of the greatest advantages of using DMF instead of water as solvent for H_2 evolution. The intricacies of the electron transfer from the two-reduced POM to H^+ is still an open issue in the present conditions; deeper comprehension remains a challenge that may help developing new systems with higher photocatalytic activity in this field.

6.5. Bibliography

[1] B. Matt, J. Fize, J. Moussa, H. Amouri, A. Pereira, V. Artero, G. Izzet, A. Proust, *Energy Environ. Sci.* **2013**, *6*, 1504.
[2] P. D. Tran, L. H. Wong, J. Barber, J. S. C. Loo, *Energy Environ. Sci.* **2012**, *5*, 5902.
[3] E. S. Andreiadis, M. Chavarot-Kerlidou, M. Fontecave, V. Artero, *Photochem. Photobiol.* **2011**, *87*, 946.
[4] A. Thapper, S. Styring, G. Saracco, A. W. Rutherford, B. Robert, A. Magnuson, W. Lubitz, A. Llobet, P. Kurz, A. Holzwarth, S. Fiechter, H. de Groot, S. Campagna, A. Braun, H. Bercegol, V. Artero, in *Green, Vol. 3*, **2013**, p. 43.
[5] A. C. Benniston, A. Harriman, *Mater. Today* **2008**, *11*, 26.
[6] S. W. Gersten, G. J. Samuels, T. J. Meyer, *J. Am. Chem. Soc.* **1982**, *104*, 4029.
[7] J. J. Concepcion, J. W. Jurss, J. L. Templeton, T. J. Meyer, *J. Am. Chem. Soc.* **2008**, *130*, 16462.
[8] F. Liu, J. J. Concepcion, J. W. Jurss, T. Cardolaccia, J. L. Templeton, T. J. Meyer, *Inorg. Chem.* **2008**, *47*, 1727.
[9] Y. V. Geletii, B. Botar, P. Kögerler, D. A. Hillesheim, D. G. Musaev, C. L. Hill, *Angew. Chem. Int. Ed.* **2008**, *47*, 3896.
[10] Q. Yin, J. M. Tan, C. Besson, Y. V. Geletii, D. G. Musaev, A. E. Kuznetsov, Z. Luo, K. I. Hardcastle, C. L. Hill, *Science* **2010**, *328*, 342.
[11] V. Artero, M. Fontecave, *Coord. Chem. Rev.* **2005**, *249*, 1518.
[12] M. L. Helm, M. P. Stewart, R. M. Bullock, M. R. DuBois, D. L. DuBois, *Science* **2011**, *333*, 863.
[13] A. J. Esswein, D. G. Nocera, *Chem. Rev.* **2007**, *107*, 4022.
[14] H. Imahori, D. M. Guldi, K. Tamaki, Y. Yoshida, C. Luo, Y. Sakata, S. Fukuzumi, *J. Am. Chem. Soc.* **2001**, *123*, 6617.
[15] M. Borgström, N. Shaikh, O. Johansson, M. F. Anderlund, S. Styring, B. Åkermark, A. Magnuson, L. Hammarström, *J. Am. Chem. Soc.* **2005**, *127*, 17504.
[16] M. Di Valentin, A. Bisol, G. Agostini, P. A. Liddell, G. Kodis, A. L. Moore, T. A. Moore, D. Gust, D. Carbonera, *J. Phys. Chem. B* **2005**, *109*, 14401.
[17] D. Gust, T. A. Moore, A. L. Moore, F. Gao, D. Luttrull, J. M. DeGraziano, X. C. Ma, L. R. Makings, S. J. Lee, *J. Am. Chem. Soc.* **1991**, *113*, 3638.
[18] M. R. Wasielewski, G. L. Gaines, G. P. Wiederrecht, W. A. Svec, M. P. Niemczyk, *J. Am. Chem. Soc.* **1993**, *115*, 10442.
[19] L. Le Pleux, Y. Pellegrin, E. Blart, F. Odobel, A. Harriman, *J. Phys. Chem. A* **2011**, *115*, 5069.
[20] M. T. Pope, A. Müller, *Angew. Chem.* **1991**, *30*, 34.
[21] L. Cronin, A. Muller, *Chem. Soc. Rev.* **2012**, *41*, 7333.
[22] C. L. Hill, *Chem. Rev.* **1998**, *98*, 1.
[23] M. Sadakane, E. Steckhan, *Chem. Rev.* **1998**, *98*, 219.
[24] J. A. Fernández, X. López, C. Bo, C. de Graaf, E. J. Baerends, J. M. Poblet, *J. Am. Chem. Soc.* **2007**, *129*, 12244.
[25] H. Chiba, A. Wada, T. Ozeki, *Dalton Trans.* **2006**, 1213.

[26] B. Keita, L. Nadjo, *J. Electroanal. Chem.* **1987**, *217*, 287.
[27] B. Keita, U. Kortz, L. R. B. Holzle, S. Brown, L. Nadjo, *Langmuir* **2007**, *23*, 9531.
[28] B. Keita, L. Nadjo, *J. Mol. Catal. A: Chem.* **2007**, *262*, 190.
[29] A. Proust, B. Matt, R. Villanneau, G. Guillemot, P. Gouzerh, G. Izzet, *Chem. Soc. Rev.* **2012**, *41*, 7605.
[30] A. Ioannidis, E. Papaconstantinou, *Inorg. Chem.* **1985**, *24*, 439.
[31] E. Papaconstantinou, *Chem. Soc. Rev.* **1989**, *18*, 1.
[32] C. L. Hill, D. A. Bouchard, *J. Am. Chem. Soc.* **1985**, *107*, 5148.
[33] T. Yamase, X. Cao, S. Yazaki, *J. Mol. Catal. A: Chem.* **2007**, *262*, 119.
[34] Y.-Q. Jiao, C. Qin, X.-L. Wang, F.-H. Liu, P. Huang, C.-G. Wang, K.-Z. Shao, Z.-M. Su, *Chem. Commun.* **2014**, *50*, 5961.
[35] X. Shang, R. Liu, G. Zhang, S. Zhang, H. Cao, Z. Gu, *New J. Chem.* **2014**, *38*, 1315.
[36] Z.-X. Yang, P. Huang, L. Zhao, M. Zhang, Y.-T. Zhang, Z.-M. Su, *Inorg. Chem. Commun.* **2014**, *44*, 195.
[37] J.-H. Son, J. Wang, W. H. Casey, *Dalton Trans.* **2014**, *43*, 17928.
[38] J.-H. Son, J. Wang, F. E. Osterloh, P. Yu, W. H. Casey, *Chem. Commun.* **2014**, *50*, 836.
[39] Z. Zhang, Q. Lin, S.-T. Zheng, X. Bu, P. Feng, *Chem. Commun.* **2011**, *47*, 3918.
[40] H. Lv, J. Song, H. Zhu, Y. V. Geletii, J. Bacsa, C. Zhao, T. Lian, D. G. Musaev, C. L. Hill, *J. Catal.* **2013**, *307*, 48.
[41] H. Lv, W. Guo, K. Wu, Z. Chen, J. Bacsa, D. G. Musaev, Y. V. Geletii, S. M. Lauinger, T. Lian, C. L. Hill, *J. Am. Chem. Soc.* **2014**, *136*, 14015.
[42] See, for instance, the recent studies: F. Doungmene, P. A. Aparicio, J. Ntienoue, C. S. Ayingone Mezui, P. de Oliveira, X. López and I. M. Mbomekallé, Elec. Acta, 2014, 125, 674-682. L. Parent, P. A. Aparicio, P. de Oliveira, A.-L. Teillout, J. M. Poblet, X. López and I. M. Mbomekallé, Inorg. Chem., 2014, 53, 5941-5949. K. Nishiki, N. Umehara, Y. Kadota, X. López, J. M. Poblet, C. S. Ayingone Mezui, A.-L. Teillout, I. M. Mbomekallé, P. de Oliveira, M. Miyamoto, T. Sano and M. Sadakane, Dalton Trans. 2016, 45, 3715-3726.)
[43] X. López, J. J. Carbó, C. Bo, J. M. Poblet, *Chem. Soc. Rev.* **2012**, *41*, 7537.
[44] ADF2013, SCM, Theoretical chemistry, Vrije Universiteit, Amsterdam, The Netherlands, https:// www.scm.com.
[45] C. Fonseca Guerra, J. G. Snijders, G. te Velde, E. J. Baerends, *Theor. Chem. Acc.* **1998**, *99*, 391.
[46] G. te Velde, F. M. Bickelhaupt, E. J. Baerends, C. Fonseca Guerra, S. J. A. van Gisbergen, J. G. Snijders, T. Ziegler, *J. Comput. Chem.* **2001**, *22*, 931.
[47] M. Swart, F. M. Bickelhaupt, *Int. J. Quant. Chem.* **2006**, *106*, 2536.
[48] M. Swart, F. M. Bickelhaupt, *J. Compt. Chem.* **2008**, *29*, 724.
[49] A. D. Becke, *Phys. Rev. A* **1988**, *38*, 3098.
[50] A. D. Becke, *J. Chem. Phys.* **1993**, *98*, 5648.
[51] E. V. Lenthe, E. J. Baerends, J. G. Snijders, *J. Chem. Phys.* **1993**, *99*, 4597.
[52] E. V. Lenthe, E. J. Baerends, J. G. Snijders, *J. Chem. Phys.* **1994**, *101*, 9783.
[53] E. V. Lenthe, A. Ehlers, E. J. Baerends, *J. Chem. Phys.* **1999**, *110*, 8943.
[54] S. Grimme, J. Antony, S. Ehrlich, H. Krieg, *J. Chem. Phys.* **2010**, *132*, 154104.
[55] A. Klamt, *J. Phys. Chem.* **1995**, *99*, 2224.

[56] A. Klamt, V. Jonas, T. Bürger, J. C. W. Lohrenz, *J. Phys. Chem. A* **1998**, *102*, 5074.
[57] M. J. T. Frisch, G. W.; Schlegel, H. B.; Scuseria, G. E.; Robb, M. A.; Cheeseman, J. R.; Scalmani, G.; Barone, V.; Mennucci, B.; Petersson, G. A.; Nakatsuji, H.; Caricato, M.; Li, X.; Hratchian, H. P.; Izmaylov, A. F.; Bloino, J.; Zheng, G.; Sonnenberg, J. L.; Hada, M.; Ehara, M.; Toyota, K.; Fukuda, R.; Hasegawa, J.; Ishida, M.; Nakajima, T.; Honda, Y.; Kitao, O.; Nakai, H.; Vreven, T.; Montgomery, J. A., Jr.; Peralta, J. E.; Ogliaro, F.; Bearpark, M.; Heyd, J. J.; Brothers, E.; Kudin, K. N.; Staroverov, V. N.; Kobayashi, R.; Normand, J.; Raghavachari, K.; Rendell, A.; Burant, J. C.; Iyengar, S. S.; Tomasi, J.; Cossi, M.; Rega, N.; Millam, J. M.; Klene, M.; Knox, J. E.; Cross, J. B.; Bakken, V.; Adamo, C.; Jaramillo, J.; Gomperts, R.; Stratmann, R. E.; Yazyev, O.; Austin, A. J.; Cammi, R.; Pomelli, C.; Ochterski, J. W.; Martin, R. L.; Morokuma, K.; Zakrzewski, V. G.; Voth, G. A.; Salvador, P.; Dannenberg, J. J.; Dapprich, S.; Daniels, A. D.; Farkas, Ö.; Foresman, J. B.; Ortiz, J. V.; Cioslowski, J.; Fox, D. J. Gaussian, Inc., Wallingford CT, (2009).
[58] C. Lee, W. Yang, R. G. Parr, *Phys. Rev. B* **1988**, *37*, 785.
[59] C. T. Lee, W. R. Wadt, *J. Chem. Phys.* **1988**, *82*, 270.
[60] S. Miertus, E. Scrocco, J. Tomasi, *Chem. Phys.* **1981**, *55*, 117.
[61] *Note that the orbital energy differences computed by DFT (Figure 6.2) and the electronic transition energies computed by TD-DFT (Figure 6.3) are not coincident.*
[62] B. Matt, X. Xiang, A. L. Kaledin, N. Han, J. Moussa, H. Amouri, S. Alves, C. L. Hill, T. Lian, D. G. Musaev, G. Izzet, A. Proust, *Chem. Sci.* **2013**, *4*, 1737.
[63] W. G. Klemperer, W. Shum, *J. Am. Chem. Soc.* **1977**, *99*, 3544.
[64] M. T. Pope, E. Papaconstantinou, *Inorg. Chem.* **1967**, *6*, 1147.
[65] X. López, C. Bo, J. M. Poblet, *J. Am. Chem. Soc.* **2002**, *124*, 12574.
[66] J. M. Maestre, J. P. Sarasa, C. Bo, J. M. Poblet, *Inorg. Chem.* **1998**, *37*, 3071.
[67] Y. Cui, L. Xu, W.-J. Wang, G.-G. Gao, E.-B. Wang, *Chin. J. Chem.* **2006**, *24*, 316.
[68] M. L. Pegis, J. A. S. Roberts, D. J. Wasylenko, E. A. Mader, A. M. Appel, J. M. Mayer, *Inorg. Chem.* **2015**, *54*, 11883.
[69] C. Ci, J. J. Carbó, R. Neumann, C. d. Graaf, J. M. Poblet, *ACS Catal* **2016**, *6*, 6422.
[70] Z. Han, L. Shen, W. W. Brennessel, P. L. Holland, R. Eisenberg, *J. Am. Chem. Soc.* **2013**, *135*, 14659.
[71] P. Zhang, P.-A. Jacques, M. Chavarot-Kerlidou, M. Wang, L. Sun, M. Fontecave, V. Artero, *Inorg. Chem.* **2012**, *51*, 2115.
[72] J. L. Dempsey, J. R. Winkler, H. B. Gray, *J. Am. Chem. Soc.* **2010**, *132*, 1060.
[73] C. Costentin, H. Dridi, J.-M. Savéant, *J. Am. Chem. Soc.* **2014**, *136*, 13727.
[74] W. C. Ou, T. R. Cundari, *ACS Catal.* **2015**, *5*, 225.
[75] A. Bhattacharjee, E. S. Andreiadis, M. Chavarot-Kerlidou, M. Fontecave, M. J. Field, V. Artero, *Chem. Eur. J.* **2013**, *19*, 15166.
[76] S. Fukuzumi, T. Kobayashi, T. Suenobu, *Angew. Chem. Int. Ed.* **2011**, *50*, 728.
[77] C. L. Pitman, A. J. M. Miller, *ACS Catal.* **2014**, *4*, 2727.

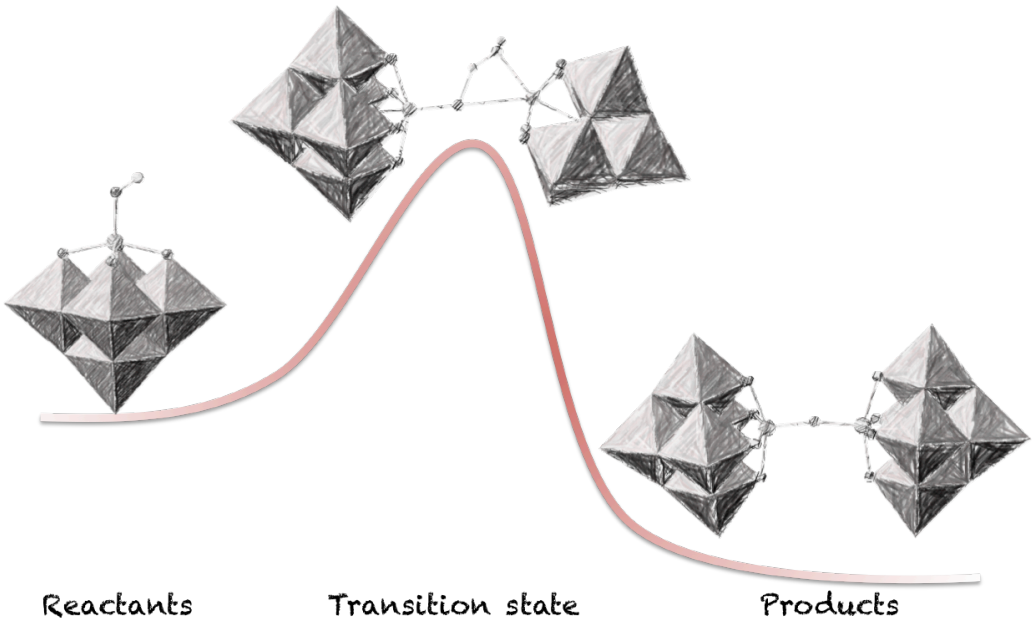

CHAPTER 7

Mechanistic Studies on Heterometallic Lindqvist and Keggin-type POMs

CHAPTER 7

Mechanistic Studies on Heterometallic Lindqvist and Keggin-type POMs

The research project described in this chapter started in Dr. Errington's group. They studied the protonolysis of different heterometallic Lindqvist and Keggin structures. Although all the compounds were synthesized, the different behaviour between diverse heterometallic POMs could not be easily explained. This motivated us to start a collaborative study on the mechanism of protonolysis taking place on different POMs. In the end, we have found a consistent explanation based on DFT calculations of why and how the reactions take place for different heterometallic molecules. At the end of the chapter, some experimental work related to the protonation of heterometallic Lindqvist POMs is reported.

7.1. Introduction

POMs are unrivalled in their chemical and structural diversity and provide a versatile platform for nanoscale molecular metal oxide science, but their rational synthesis with a pre-determined composition remains a major challenge. This fundamental capability, essential for the further development of POM chemistry, involves the following main approaches: (a) aggregation of small molecular precursors, (b) direct functionalization, *i.e.* reactions in which oxido ligands of the POM are replaced with other ligands without altering the metal-oxide structure and (c) incorporation of electrophilic groups into lacunary species.

Heterometallic POMs are of particular interest and they provide a unique opportunity to study the reactivity of isolated heterometal sites linked to a matrix of another metal oxide at the molecular level and, hence, to establish a basis of understanding for the

activity of a mixed oxide catalyst. One of the interests of heterometallic species is found in catalyst supports and soluble analogues of extended solid oxide materials.[1-3] Heterometallic POMs are potential models for heterogeneous catalysts in which an active metal site is supported on or within another metal oxide matrix.

Tungsten oxide supported on titania (TiO_2) was reported to be a solid acid catalyst with redox and photocatalytic activity.[4-8] Titanium-substituted polyoxotungstates offer an opportunity to elucidate features of the reactive sites in these materials, just as titanium-substituted Keggin-type POMs have provided mechanistic insight into titanium-catalysed H_2O_2-based oxidations.[9]

One of Errington's group interests is the non-aqueous chemistry of POMs. Consequently, they have developed different syntheses of these molecules in such media.[10-16] As a part of their programme to develop the metalorganic chemistry of POMs, they have studied the basic structural units of group VI Lindqvist-type hexametalates $[M_6O_{18}]^{2-}$ (M = W, Mo). Metathesis of oxide ligands in $[Mo_6O_{19}]^{2-}$ has been achieved in reactions involving a range of organic reactants.[17-20] However, the tungstate species, $[W_6O_{19}]^{2-}$, is inert under similar reaction conditions. The limited reactivity of these hexametalates has been ascribed to their low surface charge density and many of the reported organic derivatives have been prepared by indirect routes such as from $[WO_4]^{2-}$ or $[Mo_2O_7]^{2-}$.

A good way to design a reactive Lindqvist-type hexametalate is the replacement of M^{VI} in the relatively inert $[M_6O_{19}]^{2-}$ (M = W or Mo) by a lower-valent metal, thereby increasing the charge density at the surface of the resulting heterometal species, $[M'_xM_{6-x}O_{19}]^{n-}$. The problem with this type of compounds is that they are usually disordered in the solid state, making their real structure and reactivity difficult to establish. The introduction of a $\{M'L\}^{x+}$ unit instead of $[M'=O]^{x+}$, where $x < 4$, with a sufficiently bulky L ligand to prevent the disorder, is a procedure to solve the problem. This approach was first attempted by Klemperer[21, 22] and subsequently by Yagasaki.[23, 24] Errington's group has since developed a wide range of chemistry for this type of substitution.[10-16] Their strategy to expand the metalorganic chemistry of POMs has been to target heterometalates $[LM'M_5O_{18}]^{n-}$, which not only have a higher surface basicity than the parent $[M_6O_{19}]^{2-}$ but also possess labile M'-L bonds, permitting reactivity at the heterometal site. By employing a non-aqueous approach, they reported the alkoxide-substituted tungstate derivatives $[(RO)M'W_5O_{18}]^{n-}$, where M' = Ti, Zr, Hf, Sn and n = 3; M' = Nb and n = 2, and molybdates $[(RO)TiMo_5O_{19}]^{3-}$ derivatives. These studies revealed that there exist subtle differences in the protonolysis behaviour of the M'-OR group depending on the nature of M' and the $\{M_5O_{18}\}^{6-}$ lacunary oxide.[15]

Herein, we report a computational study to investigate (a) the effects of different lacunary oxide ligands $\{M_5O_{18}\}^{6-}$ on the protonolysis of the M'-OR bond and (b) the effects of different M' on the hydrolysis of heterometallic Lindqvist, $[(RO)M'W_5O_{18}]^{n-}$, and Keggin, $[(RO)M'W_{11}O_{39}]^{n-}$, polyoxotungstates.

In the last section of the chapter an experimental protonation study of heterometallic tungstate dimers is reported. This study provides an understanding their behaviour towards electrophiles in reactions that are producing a new family of functionalized POMs, where they act as chelating or pincer ligands.

7.2. Methods

7.2.1. Computational Details

DFT calculations were performed on a series of compounds using the Gaussian 09 suite of programs.[25] The minima (reactants, intermediates and products) as well as transition states were obtained using the B3LYP hybrid functional[26, 27] with a 6-31G** basis set. For heavy elements, we used the standard double-zeta basis set with LANL pseudopotentials of Hay and Wadt.[28] Transition states were identified by the characteristic calculation of Hessian matrices with only one imaginary frequency corresponding to the reaction coordinate. The calculations include solvent effects by means of the polarizable continuum model (PCM[29]) to simulate the effects of acetonitrile.

7.2.2. Experimental strategy

All reactions and manipulations were carried out under an atmosphere of dry, oxygen-free nitrogen in screw-top flasks fitted with PTFE screw valves using Schlenk and dry-box techniques.[30] Hydrocarbon and ether solvents were dried over and distilled from sodium benzophenone ketyl, acetonitrile was dried over and distilled from calcium hydride and methanol was pre-dried over 3A molecular sieves and distilled from magnesium methoxide immediately prior to use. 10% ^{17}O-enriched water and deuterated acetonitrile were purchased from Goss Scientific Instruments, and the latter was degassed and stored under nitrogen over calcium hydride or 3A molecular sieves.

Infrared spectra were recorded from powders on a Varian 800 FTIR spectrometer using a single reflectance ATR attachment. NMR spectra were recorded on a Jeol ECS 400

spectrometer operating at 399.78 MHz (^{1}H), 100.5 MHz (^{13}C) or 54.20 MHz (^{17}O). NMR spectra were referenced by sample replacement to $SiMe_4$ (^{1}H and ^{13}C) or water (^{17}O).

7.2.2.1. Preparation of $(TBA)_3[(MeO)TiW_5O_{18}]$

$(TBA)_2WO_4$ (2.73g, 3.74 mmol) and $Ti(OMe)_4$ (0.26 g, 1.49 mmol) were dissolved in MeCN (25 mL) and heated at 90 °C for about 2h. $WO(OMe)_4$ (2.82g, 8.691mmol) was dissolved in MeCN (25mL). The resulting solution of $WO(OMe)_4$ was transferred *via* cannula into the former solution. The mixture was heated at 90 °C for 10 minutes before adding ^{17}O-enriched H_2O (380 µL, 21.07 mmol). The mixture was heated overnight at 90 °C. After cooling to room temperature the volume was reduced by 30 % under reduced pressure. Crystals of $(TBA)_2[W_6O_{19}]$ formed at room temperature were filtered off and dried *in vacuo*. The filtrate was further reduced by 50% and cooled to -20 °C. Crystals formed were filtered, washed with diethyl ether (3 x 5 mL) and dried *in vacuo* to give the desired product. Clean spectra were obtained from ^{17}ONMR and ^{1}H NMR spectroscopy.

7.2.2.2. Hydrolysis of $(TBA)_3[(MeO)TiW_5O_{18}]$

$(TBA)_3[(MeO)TiW_5O_{18}]$ (0.6 g, 0.3 mmol) was dissolved in MeCN (15 mL) in a Schlenk flask. ^{17}O enriched H_2O (30 µl) was added and the mixture was heated overnight at 90 °C. The white product remaining after removal of the volatiles was recrystallized from MeCN (3.5 mL) and Et_2O (9 ml) to give crystalline solids were which were washed with diethyl ether (9mL) and dried *in vacuo*. The crystals were characterized by IR and ^{17}O NMR spectroscopy.[11]

7.2.2.3. Protonation of $(TBA)_6[(\mu\text{-}O)(TiW_5O_{18})_2]$

$(TBA)_6[(\mu\text{-}O)(TiW_5O_{18})_2]$ (40 mg, 0.01 mmol) was dissolved in MeCN (0.3 mL) in an NMR tube. A solution of $HBF_4.Et_2O$ (0.14 M) was prepared in MeCN, and aliquots were added to the solution in the NMR tube. The reaction was monitored by ^{17}O NMR spectroscopy.

7.2.2.4. Preparation of $(TBA)_3[ClTiW_5O_{18}]$

$(TBA)_2[(MeO)TiW_5O_{18}]$ (1.51g, 0.75 mmol) was dissolved in MeCN (15 mL) in a Schlenk flask and cooled in an acetone/liquid N_2 bath. In another Schlenk flask Me_3SiCl (95 µl)

was dissolved in MeCN (10mL) and cooled in an acetone/liquid N_2 bath. The solution of Me_3SiCl was transferred *via* cannula into the former flask. The mixture was left overnight with stirring during which time the solution finally became clear. The product remaining after the removal of volatiles was washed with diethyl ether (3 x 5 mL), dried *in vacuo* and recrystallized from MeCN (7 mL) at -20 °C. Crystals formed were filtered and dried in vacuo to give the desired product. Clean spectra were obtained from ^{17}O NMR and ^{1}H NMR spectroscopy.

7.2.2.5. Synthesis of $(TBA)_4[(TiW_5O_{18})_2]$

$(TBA)_3[ClTiW_5O_{18}]$ (0.50 g, 0.50 mmol) was dissolved in MeCN (10 mL) in a Schlenk flask. In another Schlenk flask $AgBF_4$ (480 mg) was dissolved in MeCN (10mL). The resulting solution of $AgBF_4$ was transferred *via* cannula into the former flask. The mixture was left overnight during which time a purple solid appeared (AgCl). The AgCl was removed from the solution by filtration. The product remaining after the removal of volatiles was washed with diethyl ether (3 x 5mL), dried *in vacuo* and recrystallized from MeCN (7 mL) at -20 °C. Crystals formed were filtered and dried *in* vacuo to give the desired product. Clean spectra were obtained from ^{17}O NMR spectroscopy.

7.2.2.6. Hydrolysis of $(TBA)_4[(TiW_5O_{18})_2]$

$(TBA)_6[(TiW_5O_{18})_2]$ (40 mg, 0.01 mmol) was dissolved in MeCN (0.3 mL) in an NMR tube. An aliquot amount of ^{17}O-enriched H_2O was added to the solution in the NMR tube and the reaction was monitored by ^{17}O NMR spectroscopy.

7.3. Protonolysis of Heterometallic Lindqvist Compounds

Errington's group reported[11] the synthesis and protonolysis of $[(MeO)TiW_5O_{18}]^{3-}$ with a variety of protic molecules H_nX in order to explore the Ti-OMe bond reactivity leading to anions $[(X)(TiW_5O_{18})_n]^{3-}$.

$$n[(MeO)TiW_5O_{18}]^{3-} + H_nX \rightarrow [(X)(TiW_5O_{18})_n]^{3-} + nMeOH \qquad (7.1)$$

They studied by ^{1}H NMR the methanolysis of Ti-O bond with MeOH in order to prove the reactivity of titanium in the comparatively rigid coordination environment provided by the $W_5O_{18}^{6-}$ cage. The 2D EXSY ^{1}H NMR revealed that the value of MeO-exchange was considerably lower than initially expected. It was pointed out that this low rate of exchange implies that the activation energy for the proton process is high.

One of the most basic sites in heterometal-substituted tungstates are MOW bridging oxygens.[31, 32] The slow rates of the reported reactions[11] suggested that the activation energy associated with the proton transfer process, involving seven-coordinate titanium as in mechanism shown in Figure 7.1, is likely to be elevated because of the reluctance of titanium in $[XTiW_5O_{18}]^{3-}$ anions to increase its coordination number.

It was also suggested that, in addition to the concerted mechanism represented in Figure 7.1, initial interaction of the proton from HX might occur with either OMe or WOTi. In the first case, the seven-coordinate transition state of the concerted mechanism would be generated in the absence of prior H-X dissociation, whereas the intermediate $[(MeOH)TiW_5O_{18}]^{2-}$ would result if H-X dissociation occurred, in which case dissociation of methanol followed by coordination of X^- would give $[(X)TiW_5O_{18}]^{3-}$. In the second case, interaction at WOTi with dissociation of H-X would result in the formation of the protonated intermediate $[(MeO)TiW_5O_{18}H]^{2-}$, while non-dissociative interaction of HX with WOTi might reduce the rate of reaction at TiOMe. The second pathway requires migration of the proton from the metal oxide cage to the alkoxide prior to lose of the methanol and coordination of X^-.

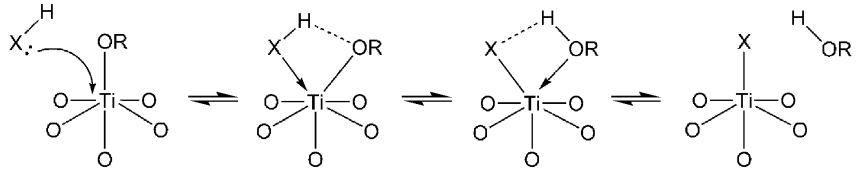

Figure 7. 1. Concerted reaction mechanism between $[(RO)TiW_5O_{18}]^{3-}$ and HX, reported in ref. [11]

Moreover, in computational studies reported by Poblet *et. al*,[33] pathways involving protonation at either Ti=O and TiOW for the conversion of $[O=TiW_5O_{18}]^{4-}$ to $[(\mu\text{-}O)(TiW_5O_{18})_2]^{6-}$ were considered. Calculations showed that both processes are exothermic, but the protonation is preferred at Ti=O and formation of the dimeric intermediate with seven-coordinate titanium prior to the elimination of water is endothermic. However, all the calculations of that study correspond to energy minima, that is, no reaction energy barrier whatsoever was explored.

Recently, Errington *et. al*[15] reported a comparative study related to $[LM'M_5O_{18}]^{3-}$ anions. They studied the methanolysis of $[(MeO)TiMo_5O_{18}]^{3-}$ by 2D EXSY ^1H NMR. Contrary to what was reported for $[(MeO)TiW_5O_{18}]^{3-}$, in this case no exchange peaks related to TiOMe appeared. This implied that the exchange in $[(MeO)TiMo_5O_{18}]^{3-}$ is slower than for $[(MeO)TiW_5O_{18}]^{3-}$ despite the fact that polyoxomolybdates are usually regarded as being more labile than homologous tungstates. The interpretation of those results was made considering different mechanisms for polyoxomolybdates and

polyoxotungstates. They supposed that the oxometalate cage would be involved in the protonolysis reaction, which should be considered in the study of the ligand exchange mechanism. In a single-site alkoxide $[(RO)TiM_5O_{18}]^{3-}$, the unwillingness of Ti to increase its coordination number beyond six makes a proton-assisted S_N1 ligand exchange mechanism more likely than S_N2. However, the basicity of TiOM bridging oxygens in these POMs provides an additional complication since the initial interaction with a protic reagent HL may occur at either OR or TiOM (Figure 7.2). The higher basicity of TiOMo compared to TiOW may therefore result in protonation at TiOMo in $[(RO)TiMo_5O_{18}]^{3-}$ but at OR group in the less basic $[(RO)TiW_5O_{18}]^{3-}$ and, given that an extra proton-transfer would be required before loss of ROH in $[(RO)TiMo_5O_{18}H]^{2-}$, dissociation would likely be slower than in $[(ROH)TiW_5O_{18}]^{3-}$. The authors suggested that this may explain why the alcohol exchange was too slow to be observed by 2D ^{1}H EXSY NMR in the reaction between $[(MeO)TiMo_5O_{18}]^{3-}$ and MeOH, whereas an exchange peak was observed in the tungstate system.

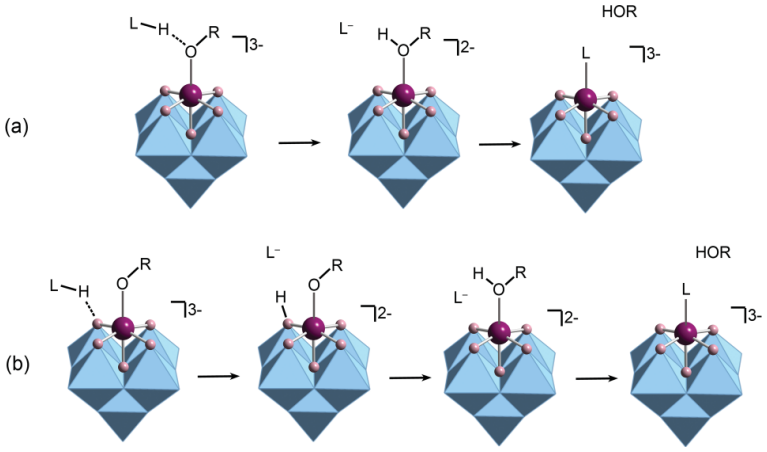

Figure 7.2. (a) Possible mechanisms of protonolysis of the TiOR bond in $[(RO)TiM_5O_{18}]^{3-}$ POMs with HL involving either direct protonation of the alkoxido ligand (b) or protonation of the oxometalate cage at TiOM with subsequent proton transfer to the alkoxido ligand (Figure obtained from ref. [15])

Considering all the results presented above, we have examined the species involved in the protonolysis of $[(MeO)TiMo_5O_{18}]^{3-}$ and $[(MeO)TiW_5O_{18}]^{3-}$ to confirm both mechanisms. DFT calculations have been crucial for the determination of the whole mechanism in solution. We have examined the intermediates involving direct protonation at the alkoxido ligand and protonation at the oxometalate cage, labelled Int-1 and Int-2 (Figure 7.3).

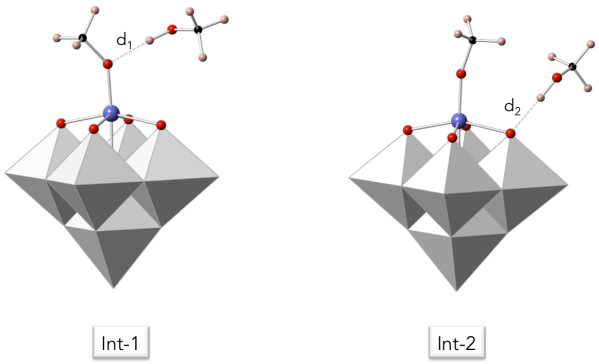

Figure 7.3. Polyhedral representation of Int-1 and Int-2. Color code: Grey polyhedra-W, red-O, purple-M, black-C and pink-H.

The relative energies and the O-H distances (d_1 and d_2) of the intermediates are shown in Table 7.1. It can be seen that there is only a slight difference between int-1 and int-2. In both cases, the protonation at the cage is preferred rather than at the alkoxide substituent. However, the energy difference between the two intermediates is around 2 kcal·mol^{-1}, a modest difference. Furthermore, the distances are also very similar suggesting that the basicity of those oxygens are similar.

Table 7. 1. Relative energies with respect to reactants in kcal·mol^{-1} and distances in Å related to intermediates 1 and 2.

Anion	E_{int-1}	d_1(O-H)	E_{int-2}	d_2(O-H)	$\Delta E_{int2-int1}$
$[(MeO)TiW_5O_{18}]^{3-}$	-6.1	1.87	-8.4	1.80	2.3
$[(MeO)TiMo_5O_{18}]^{3-}$	-6.9	1.86	-8.9	1.79	2.0

Inspection of these first results suggests that the mechanism presented in Figure 7.2 could be misinterpreted. It was proposed that $[(MeO)TiW_5O_{18}]^{3-}$ might be preferentially protonated at the alkoxide group and $[(MeO)TiMo_5O_{18}]^{3-}$ at the oxometalate cage. However, DFT calculations show no such big difference. Therefore, an exploration of the potential energy surface (PES) along different reaction coordinates was carried out. First, we focused on $[(MeO)TiMo_5O_{18}]^{3-}$. As initial 2D 1H EXSY NMR results suggested that MeOH exchange with $[(MeO)TiMo_5O_{18}]^{3-}$ was slower than with $[(MeO)TiW_5O_{18}]^{3-}$, we explored different reaction coordinates of the PES from Int-2: (a) the Ti-O and (b)

the O-H distances. The scans along these coordinates are shown in the graphics shown in Figure 7. 4.

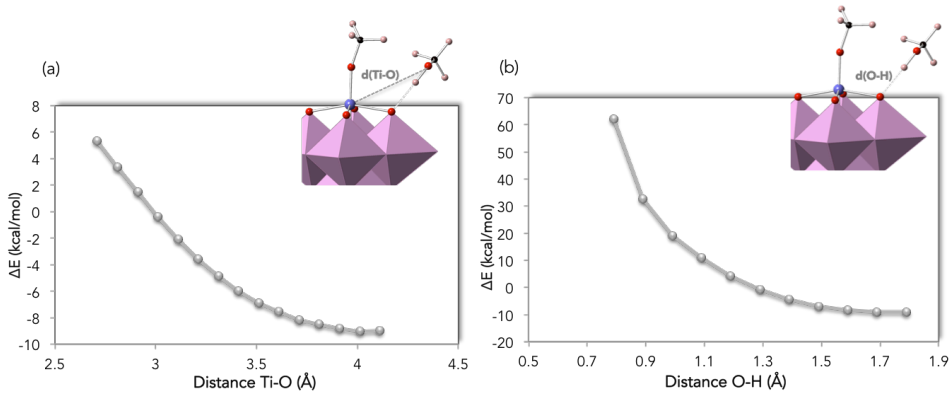

Figure 7. 4. Relative energy scans along the reaction coordinates of the PES of $[(MeO)TiMo_5O_{18}]^{3-}$: (a) Ti-O and (b) O-H.

No energy barrier was detected along the coordinate scans analysed since there is a monotonous energy decrease. It arises that the first protonation at the oxometalate cage would not occur since the energy increases up to 60 kcal·mol^{-1}. Therefore, this first step is unlikely due to the instability of the MeO^- anion. It is worth noting that both steps can take place at the same time, meaning that as the oxometalate cage is protonated the titanium is coordinated to the alkoxide. However, experimentalists didn't consider such concerted mechanism (Figure 7.1).

On the other hand, we explored the PES along different reaction coordinates of $[(MeO)TiW_5O_{18}]^{3-}$ in order to clarify the mechanism. From Int-1, we performed two energy-coordinate scans of the PES: (a) Ti-O and (b) O-H coordinates (Figure 7.5).

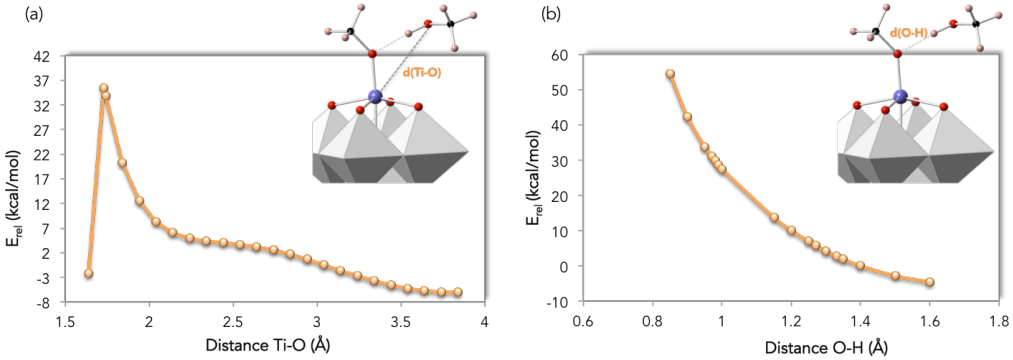

Figure 7. 5. Relative energy scans along the reaction coordinates of the PES of $[(MeO)TiW_5O_{18}]^{3-}$: (a) Ti-O and (b) O-H.

An energy barrier appears when the oxygen from the methanol group approaches the titanium (Figure 7.5a), and this prompted us to search and find a transition state (TS_1) in that region. In TS_1, oxygen from the methanol group becomes bonded to the titanium, and the proton from methanol is transferred to the methoxide group. The new methanol molecule formed leaves (Figure 7.6). The energy barrier is 16.4 kcal·mol^{-1}.

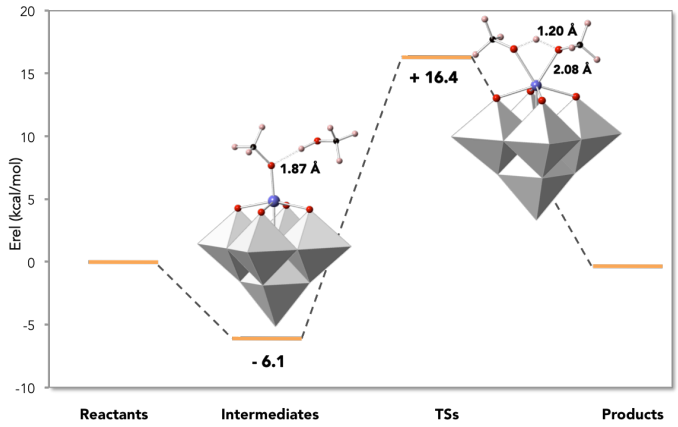

Figure 7. 6. Energy profile for protonolysis reaction for $[(MeO)TiW_5O_{18}]^{3-}$.

To rule out other mechanisms, the same TS was calculated for $[(MeO)TiMo_5O_{18}]^{3-}$. Results show (Figure 7.7) that the reaction can follow the same mechanism. First, a stabilization of the system takes place leading to Int-1 (-6.95 kcal·mol^{-1}). As in the case of $[(MeO)TiW_5O_{18}]^{3-}$, the energy barrier of 16.3 kcal·mol^{-1} is accessible at working conditions. Finally, the MeOH leaves and the product is formed.

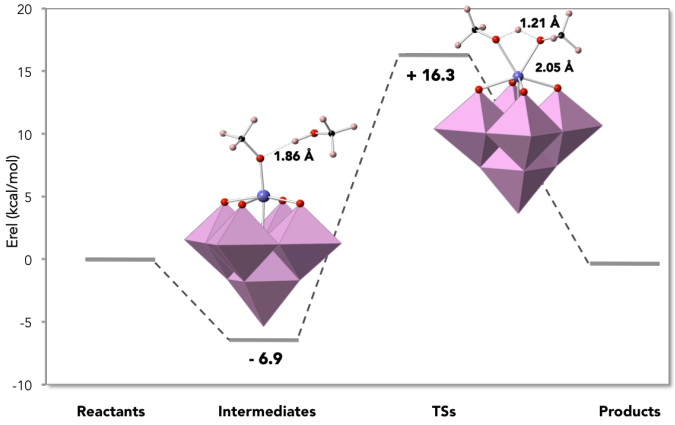

Figure 7. 7. Energy profile for protonolysis reaction for $[(MeO)TiMo_5O_{18}]^{3-}$.

From Int-2 of $[(MeO)TiMo_5O_{18}]^{3-}$ another reaction coordinate was studied. Considering that no energy barrier was identified for the previous reaction coordinate, we performed an energy scan varying the distance between the oxygen of the methoxide and the hydrogen of the methanol (Figure 7.8a). This reaction coordinate is the pathway for going from Int-2 to Int-1. Figure 7.8 shows that this step takes place through an almost imperceptible process of 2.9 kcal·mol^{-1} as estimated from the scan, so this process can be considered almost barrierless. For comparison purposes, the same reaction coordinate was explored for $[(MeO)TiW_5O_{18}]^{3-}$ and the same trend was found (Figure 7.8b). We have also computed the harmonic frequencies in order to know if these energy barriers correspond to the pathways to get Int-1 from Int-2 in both compounds. The results showed activation energies of 2.5 and 3.3 kcal·mol^{-1} for molybdenum and tungsten compounds, respectively.

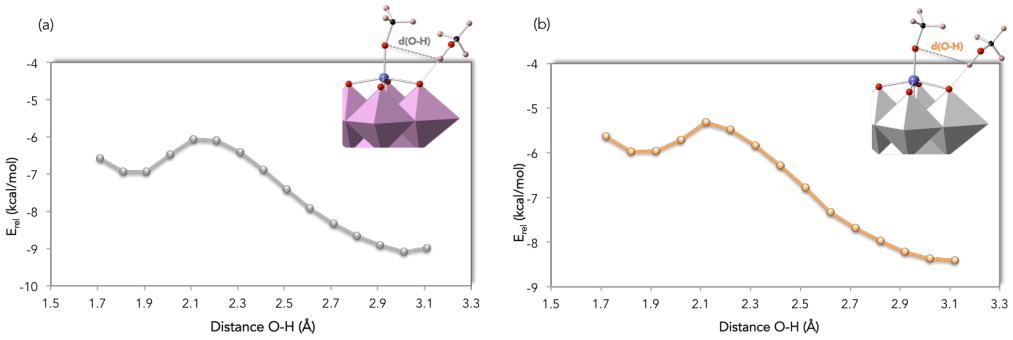

Figure 7. 8. Scans along the d(O-H) reaction coordinates and relative energies for (a) $[(MeO)TiMo_5O_{18}]^{3-}$ and (b) $[(MeO)TiW_5O_{18}]^{3-}$.

So, these results show that the pathway from int-2 to int-1 is spontaneous in the reaction conditions. Then, present results suggest that the protonolysis mechanism of $[(MeO)TiMo_5O_{18}]^{3-}$ and $[(MeO)TiW_5O_{18}]^{3-}$ should be the same, involving initial approach of MeOH towards TiOW and then TiOMe with subsequent transfer of H to TiOMe and loss of MeOH.

These results prompted further investigations of these systems and it is worth noting that recent repeat 2D EXSY ^{1}H NMR studies of $[(MeO)TiW_5O_{18}]^{3-}$ methanolysis have *not* shown MeOH/TiOMe exchange peaks, which reinforces the conclusions from the computational studies described above.

7.4. Hydrolysis of Heterometallic Lindqvist Compounds

The second part of this project is a comparison of the reactivity of titanium- and tin-substituted Lindqvist tungstates. The hydrolytic behaviours of $[(MeO)TiW_5O_{18}]^{3-}$ and $[(MeO)SnW_5O_{18}]^{3-}$ anions differ significantly and we have tried to explain this difference by DFT calculations.

Hydrolysis of this type of heterometallic Lindqvist-type POMs leads to the hydroxido Lindqvist compounds (step 1) and the hydroxides $[(HO)MW_5O_{18}]^{n-}$ can undergo condensation giving the corresponding oxido-bridged dimer, $[(\mu\text{-}O)(MW_5O_{18})_2]^{2n-}$ (step 2) as shown in Figure 7.9.

The experimental study of the reactions in Errington's group have revealed that the hydrolysis of $(TBA)_3[(MeO)SnW_5O_{18}]$ is much faster than that of $(TBA)_3[(MeO)TiW_5O_{18}]$ and gives the hydroxide $(TBA)_3[(HO)SnW_5O_{18}]$, which undergoes slow condensation to $(TBA)_6[(\mu\text{-}O)(SnW_5O_{18})_2]$. In the case of $(TBA)_3[(MeO)TiW_5O_{18}]$, when the reaction was heated to drive the reaction to completion, the product was $(TBA)_6[(\mu\text{-}O)(TiW_5O_{18})_2]$ rather than $(TBA)_3[(HO)TiW_5O_{18}]$.

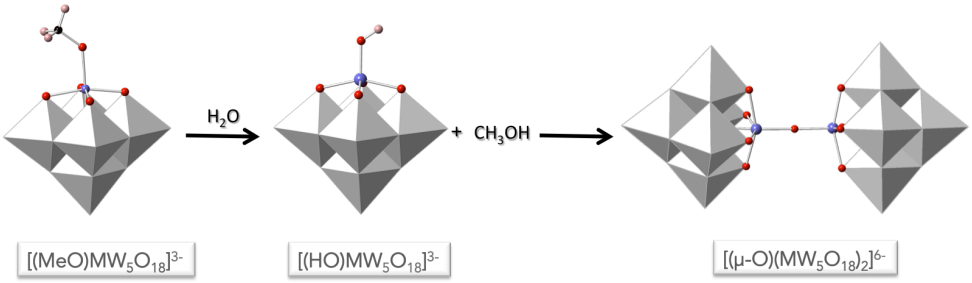

Figure 7. 9. Polyhedral and ball-and-stick representation of hydrolysis reaction for $[(MeO)MW_5O_{18}]^{3-}$. Color code: Grey polyhedra-W, red-O, purple-M, black-C and pink-H.

Since we verified the mechanism of protonolysis in previous section, now we search the energy barriers for H_2O instead of MeOH as reactant. We have also studied the thermodynamics and kinetics of the reactions in order to explain such differences in behaviour.

Table 7.2 shows the relative energies with respect to reactants for the transition state and the products of step 1 of the hydrolysis. The energy barrier for $[(MeO)TiW_5O_{18}]^{3-}$ (15.8 kcal·mol^{-1}) is higher than $[(MeO)SnW_5O_{18}]^{3-}$ (9.8 kcal·mol^{-1}), in accordance with the fact that the hydrolysis of $[(MeO)SnW_5O_{18}]^{3-}$ is faster than in $[(MeO)TiW_5O_{18}]^{3-}$.

Moreover, the reaction energies confirm that the $[(HO)SnW_5O_{18}]^{3-}$ is easy to isolate because it is 3.1 kcal·mol^{-1} more stable than the reactants, whereas $[(HO)TiW_5O_{18}]^{3-}$ is not so stabilized with respect to reactants.

Table 7. 2. Relative energies with respect to reactants for transitions state and products for step 1 of the hydrolysis of $[(MeO)MW_5O_{18}]^{3-}$, where M = Sn and Ti.

Reactant	$E_{rel.step1}$ TS1[a]	$E_{rel.step1}$ Product[a]
$[(MeO)TiW_5O_{18}]^{3-}$	15.8 (26.4)	1.1 (0.3)
$[(MeO)SnW_5O_{18}]^{3-}$	9.8 (20.2)	-3.1 (-4.0)

[a] Relative energies with respect to reactants (in kcal·mol^{-1}); in parenthesis, relative Gibbs free energies (in kcal·mol^{-1}) for step1 of the hydrolysis.

It is worth mentioning that the transition state structures (Figure 7.10) have demonstrated that the distances shown in the tin compound ($TS1_{Sn}$) are longer and, thus, their bonds easier to cleave than for the titanium analogue ($TS1_{Ti}$). Therefore, the $[(MeO)SnW_5O_{18}]^{3-}$ species would be more reactive than $[(MeO)TiW_5O_{18}]^{3-}$.

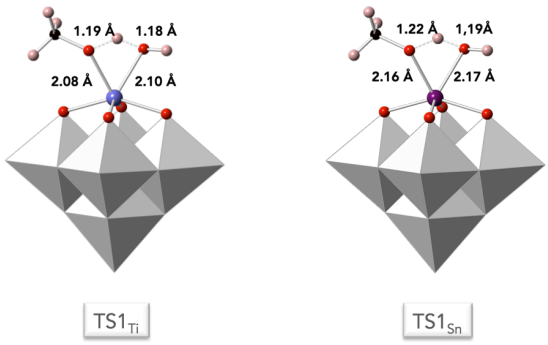

Figure 7. 10. Optimized transition state structures of step 1 for the $[(MeO)TiW_5O_{18}]^{3-}$ (right) and $[(MeO)SnW_5O_{18}]^{3-}$ (left). Color code: Grey polyhedra-W, red-O, purple-Ti or Sn, black-C and pink-H.

The second step of the hydrolysis was also studied. In the mechanism studied, the dimer is directly generated (Figure 7.11). We have calculated all species related to this pathway for tin and titanium compounds.

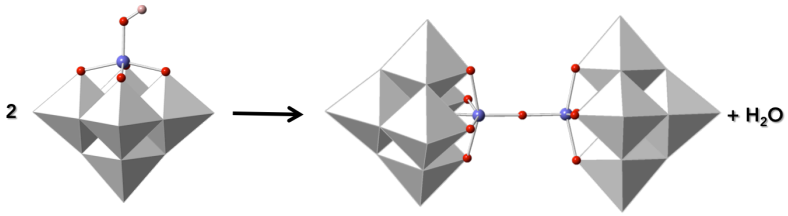

Figure 7.11. Scheme of the studied pathway for step 2 of the hydrolysis reaction for $[(MeO)MW_5O_{18}]^{3-}$. Color code: Grey polyhedra-W, red-O, purple-M and pink-H.

The computed relative energies of the reactants, products and transition states are shown in Table 7.3. We should point out that in the formation of $[(\mu\text{-}O)(SnW_5O_{18})_2]^{6-}$ two different energy barriers were found, corresponding to, first, the Sn-O bond formation ($TS2_1$) and, second, the proton transfer from one oxygen to the other ($TS2_2$). Nevertheless, only one transition state including both processes, Ti-O formation and proton transfer, was found in the formation of $[(\mu\text{-}O)(TiW_5O_{18})_2]^{6-}$.

Table 7. 3. Relative energies with respect to reactants for different transitions states and products for step 2 of the hydrolysis of $[(MeO)MW_5O_{18}]^{3-}$, where M = Sn and Ti.

Reactant	$E_{rel.}$ $TS2_1$[a]	$E_{rel.}$ $TS2_2$[a]	$E_{rel.step2}$ Product[a]
$[(HO)TiW_5O_{18}]^{3-}$	21.1 (38.8)		3.6 (7.5)
$[(HO)SnW_5O_{18}]^{3-}$	12.7 (29.6)	20.8 (40.6)	9.0 (12.1)

[a] Relative energies with respect to reactants (in kcal.mol^{-1}); in parenthesis, relative Gibbs free energies (in kcal.mol^{-1}) for step2 of the hydrolysis.

The relative energies of the transition states confirm that the energy barriers are accessible at working conditions. One would expect formation of $[(\mu\text{-}O)(SnW_5O_{18})_2]^{6-}$ to be more demanding energetically since there exist two energy barriers. We have not been able to determine an intermediate between them, but it is not necessary for comparing the behaviour with the titanium analogue. The $[(\mu\text{-}O)(SnW_5O_{18})_2]^{6-}$ is less stable than the reactants (9.0 kcal·mol^{-1}), which is consistent with the easier isolation of $[(HO)SnW_5O_{18}]^{3-}$ than the corresponding dimer. Moreover, dimeric $[(\mu\text{-}O)(TiW_5O_{18})_2]^{6-}$ is slightly less stable (3.6 kcal·mol^{-1}) than $[(HO)TiW_5O_{18}]^{3-}$ consistent with the need to heat the reaction for complete condensation to occur. Transition state structures are shown in Figure 7.12. In $TS2_{Ti}$, the Ti-O bond (2.63 Å) is forming at the same time that the proton is transferred to give $[(\mu\text{-}O)(TiW_5O_{18})_2]^{6-}$. As mentioned, $TS2_{1Sn}$ is the first transition state related to the formation of the Sn-O bond (2.71 Å) and $TS2_{2Sn}$ corresponds to the proton transfer leading to $[(\mu\text{-}O)(SnW_5O_{18})_2]^{6-}$.

As a general conclusion, our results are consistent with all experimental observations related to the hydrolysis of $[(MeO)MW_5O_{18}]^{3-}$, where M = Ti and Sn. We have shown

that the hydrolysis of $[(MeO)TiW_5O_{18}]^{3-}$ leads directly to the dimer (unless precautions are taken to prevent the condensation step), whereas in the case of $[(MeO)SnW_5O_{18}]^{3-}$, it is easier to obtain $[(HO)SnW_5O_{18}]^{3-}$.

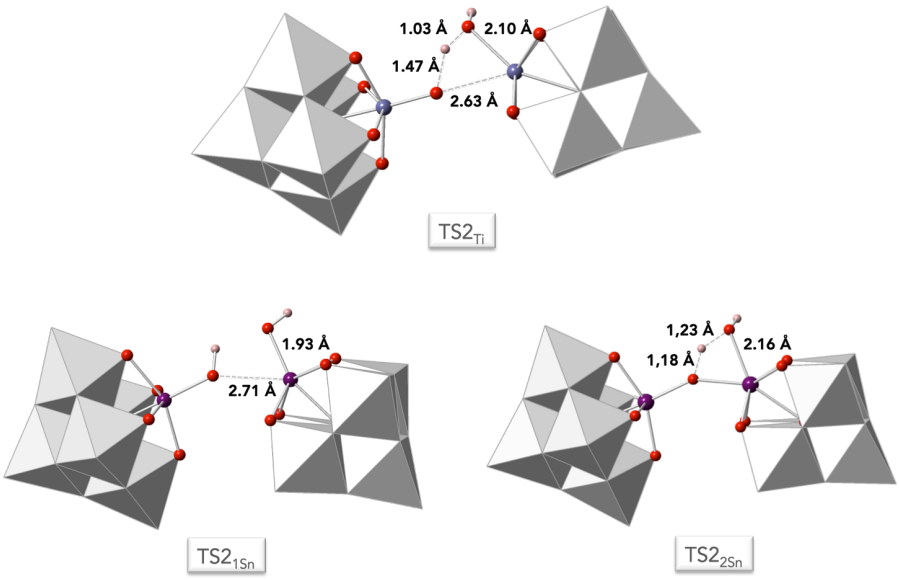

Figure 7.12. Optimized transition state structures of step 2 for the formation of $[(\mu\text{-}O)(TiW_5O_{18})_2]^{6-}$ (top) and $[(\mu\text{-}O)(SnW_5O_{18})_2]^{6-}$ (bottom). Color code: Grey polyhedra-W, red-O, purple-Ti or Sn and pink-H.

7.5. Hydrolysis of Heterometallic Keggin Compounds

Errington's group has also studied the hydrolysis of Keggin anions. They found that $(TBA)_4[(MeO)SnPW_{11}O_{39}]$ is very sensitive towards hydrolysis and the hydroxide $(TBA)_4[(HO)SnPW_{11}O_{39}]$ is easily formed. Although they have evidence of the formation of $(TBA)_8[(\mu\text{-}O)(SnPW_{11}O_{39})_2]$, they noted that it is readily hydrolysed to give $(TBA)_4[(HO)SnPW_{11}O_{39}]$. Hence, we have studied the mechanism of $[(MeO)SnPW_{11}O_{39}]^{4-}$ hydrolysis in order to understand these trends. We have also studied the hydrolysis of the titanium analogue, $[(MeO)TiPW_{11}O_{39}]^{4-}$ to obtain data for comparison purposes.

As in the Lindqvist case, we studied the reaction in two different steps. Step 1 corresponds to the formation of $[(HO)MPW_{11}O_{39}]^{4-}$, where M = Ti and Sn (Figure 7.13).

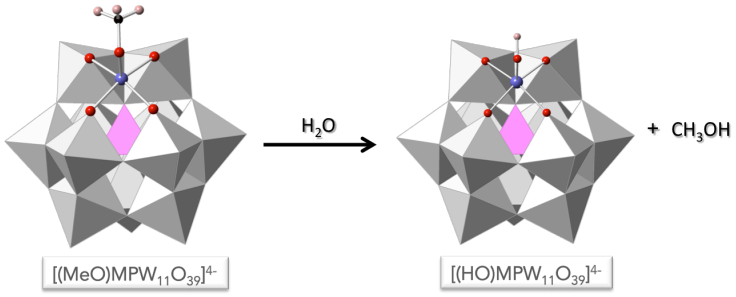

Figure 7.13. Polyhedral and ball-and-stick representation of step 1 of the hydrolysis reaction for $[(MeO)MPW_{11}O_{39}]^{4-}$. Color code: Grey polyhedra-W, pink polyhedra-P, red-O, purple-M, black-C and pink-H.

We have calculated all the reactants, transition states and products. We found that the transition state structures are similar to those found in the Lindqvist hydrolysis reaction. Step 1 for $[(MeO)SnPW_{11}O_{39}]^{4-}$ is slightly exothermic (-2.7 kcal·mol^{-1}). Conversely, hydrolysis of $[(MeO)TiPW_{11}O_{39}]^{4-}$ is endothermic by 2.1 kcal·mol^{-1} (Table 7.4).

Table 7. 4. Relative energies of different transition states and products for step 1 of the hydrolysis of $[(MeO)MPW_{11}O_{39}]^{4-}$, where M = Sn and Ti.

Reactant	$E_{rel.step1}$ TS1[a]	$E_{rel.step1}$ Product[a]
$[(MeO)TiPW_{11}O_{39}]^{4-}$	19.0 (30.3)	2.1 (1.76)
$[(MeO)SnPW_{11}O_{39}]^{4-}$	8.8 (26.4)	-2.7 (-4.0)

[a] Relative energies with respect to reactants (in kcal·mol^{-1}); in parenthesis, relative Gibbs free energies (in kcal·mol^{-1}) for step 1 of the hydrolysis.

The energy barrier for $[(MeO)SnPW_{11}O_{39}]^{4-}$ is only 8.8 kcal·mol^{-1}, a small value that explains why this species is easily hydrolysed in comparison with the Ti analogue, which features a much higher energy barrier. Moreover, the product $[(HO)SnPW_{11}O_{39}]^{4-}$ is more stable than the reactants, so the reaction is expected to occur readily.

As indicated, the transition states are similar to those found for the Lindqvist hydrolysis (Figure 7.14) and the same trends can be shown related to M-O bonds, where M = Sn and Ti, meaning that the Sn-O are longer than Ti-O ones.

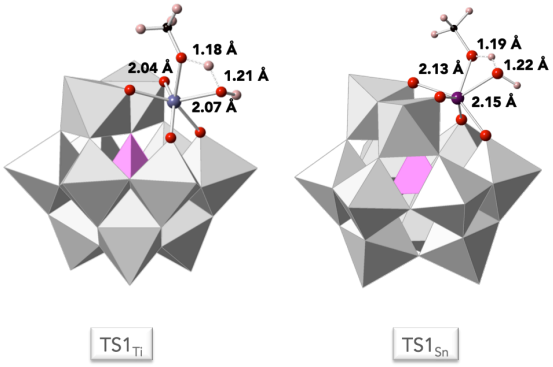

Figure 7.14. Optimized transition states structures of step 1 for the formation of $[(HO)TiPW_{11}O_{39}]^{4-}$ (right) and $[(HO)SnPW_{11}O_{39}]^{4-}$ (left). Color code: Grey polyhedra-W, pink polyhedra-P, red-O, purple-Ti or Sn, black-C and pink-H.

For the formation of the dimeric $[(\mu\text{-}O)(MPW_{11}O_{39})_2]^{8-}$, similar trends were found as for the Lindqvist analogues (Figure 7.15). Concerning the formation of $[(\mu\text{-}O)(SnPW_{11}O_{39})_2]^{8-}$, two different energy barriers were found. The first one implies formation of the Sn-O bond and the second one corresponds to proton transfer. However, only one energy barrier was found for the formation of $[(\mu\text{-}O)(TiPW_{11}O_{39})_2]^{8-}$ implying the same two atom concerted migration processes.

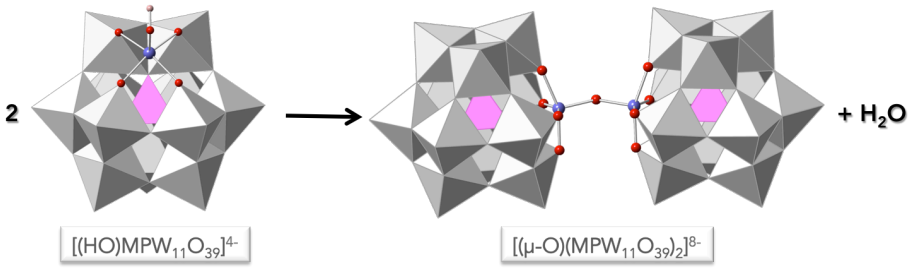

Figure 7.15. Polyhedral and ball-and-stick representation of step 2 of the hydrolysis reaction for $[(MeO)MPW_{11}O_{18}]^{4-}$. Color code: Grey polyhedra-W, pink polyhedra-P, red-O, purple-M and pink-H.

It was observed that $[(\mu\text{-}O)(SnPW_{11}O_{39})_2]^{8-}$ is unstable and is rapidly hydrolysed. It seems that this reaction is controlled by the instability of the dimer (12.9 kcal·mol^{-1}) considering that the energy barriers (Table 7.5) are not so high in energy under the reaction conditions. The formation of $[(\mu\text{-}O)(TiPW_{11}O_{39})_2]^{8-}$ (3.6 kcal·mol^{-1}) is largely more favourable than $[(\mu\text{-}O)(SnPW_{11}O_{39})_2]^{8-}$ and the energy barrier is accessible under normal reaction conditions.

Table 7. 5. Relative energies of different transition states and products for step 2 of the hydrolysis of $[(MeO)MPW_{11}O_{39}]^{4-}$, where M = Sn and Ti.

Reactant	$E_{rel.}$ TS2$_1$[a]	$E_{rel.}$ TS2$_2$[a]	$E_{rel.step2}$ Product[a]
$[(HO)TiPW_{11}O_{39}]^{4-}$	22.9 (45.8)		3.6 (7.6)
$[(HO)SnPW_{11}O_{39}]^{4-}$	15.4 (31.2)	23.8 (37.3)	12.9 (16.7)

[a] Relative energies with respect to reactants (in kcal·mol^{-1}); in parenthesis, relative Gibbs free energies (in kcal.mol^{-1}) for step 2 of the hydrolysis.

The results have revealed why it is so difficult to isolate $[(\mu\text{-}O)(SnPW_{11}O_{39})_2]^{8-}$. In addition, Keggin anions are larger than Lindqvist anions, so steric interactions are expected to play an important role in the reaction.

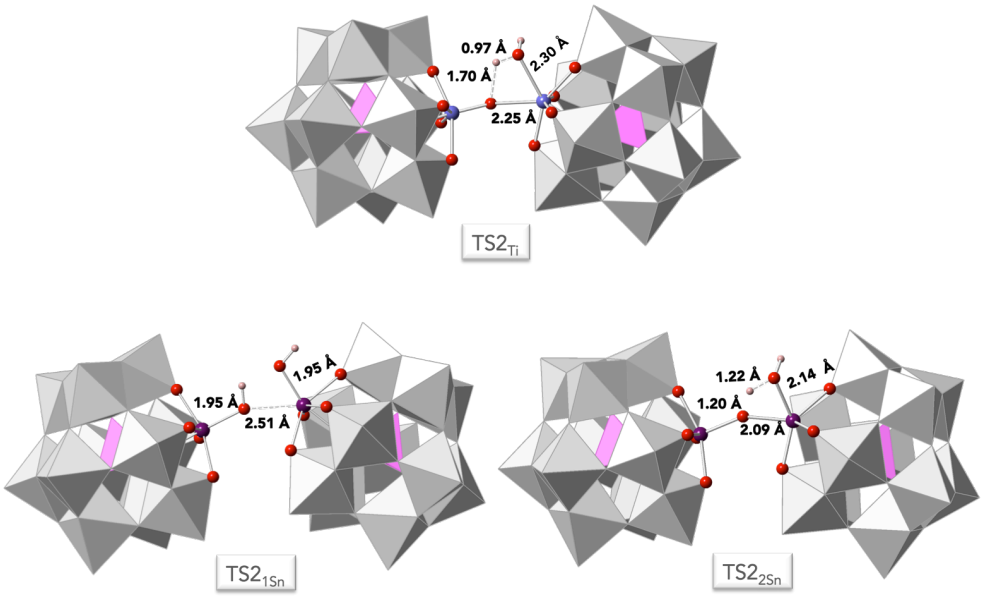

Figure 7.16. Optimized transition state structures of step 2 for the formation of $[(\mu\text{-}O)(TiPW_{11}O_{39})_2]^{8-}$ (top) and $[(\mu\text{-}O)(SnPW_{11}O_{39})_2]^{8-}$ (bottom). Color code: Grey polyhedra-W pink polyhedra-P, red-O, purple-Ti or Sn and pink-H.

In the structure of the transition state in the formation of $[(\mu\text{-}O)(TiPW_{11}O_{39})_2]^{8-}$ (Figure 7.16, TS_{2Ti}) the Ti-O bond (2.25 Å) is forming while the proton is transferred. The TS2$_1$ structure shows the transition state where the Sn-O (2.51 Å) is forming and the TS2$_2$ structure shows the second transition state to reach $[(\mu\text{-}O)(SnPW_{11}O_{39})_2]^{8-}$, where the proton transfer takes place.

Gathering all these results, we conclude that the formation of the $[(\mu\text{-O})(SnPW_{11}O_{39})_2]^{8-}$ does not readily occur due to the instability of this dimer, and it is easily hydrolysed to form $[(HO)SnPW_{11}O_{39}]^{4-}$. On the other hand, it seems easier to form $[(\mu\text{-O})(TiPW_{11}O_{39})_2]^{8-}$ by hydrolysis of $[(MeO)TiPW_{11}O_{39}]^{4-}$.

7.6. Protonation of $(TBA)_6[(\mu\text{-O})(TiW_5O_{18})_2]$

This section is related to the experimental work that I carried out during my two periods in Errington's group in Newcastle University (UK).

As previously mentioned, Errington and co-workers have developed rational synthetic routes to new POMs, a modified strategy in which soluble oxoalkoxo anions could be accessible from hydrolysis reactions between mononuclear WO_4^{2-} and metal alkoxides in organic solvents. The same group have reported the hexanuclear heterometallic $[(RO)MW_5O_{18}]^{n-}$ Lindqvist-type anions as an entry to MW_5 synthesis. This strategy has enabled the preparation of new alkoxide-substituted polyoxoanions with the systematic introduction of the reactive surface site into the structures.

POMs constructed with heterometal akoxido groups M-OR can provide a single reactive metal site within the more inert $[W_5O_{18}]^{6-}$ lacunary framework, but details of protonation on these hexametalate systems still remain unclear. Herein, we have investigated $[(\mu\text{-O})(TiW_5O_{18})_2]^{6-}$ as a way of gaining an in-depth understanding of protonation sites. We have explored two different routes to the protonated dimeric anion $[(\mu\text{-O})(TiW_5O_{18}H)_2]^{4-}$ in order to compare the two routes.

7.6.1. Synthesis and characterization of $(TBA)_6[(\mu\text{-O})(TiW_5O_{18})_2]$

As mentioned above, $(TBA)_6[(\mu\text{-O})(TiW_5O_{18})_2]$ can be obtained from hydrolysis of $[(MeO)TiW_5O_{18}]^{3-}$ (Figure 7.9), as reported by Errington *et.al* in 2007.[11] First of all, we obtained $(TBA)_3[(MeO)TiW_5O_{18}]$ by hydrolysis of a mixture of $Ti(OMe)_4$, $WO(OMe)_4$ and $(TBA)_2WO_4$ in acetonitrile with the stoichiometry shown in Eq. 7.1.

$$3WO_4^{2-} + 7WO(OMe)_4 + 2Ti(OMe)_4 + 17H_2O \rightarrow 2[(MeO)TiW_5O_{18}]^{3-} + 34MeOH \quad (7.1)$$

Crystals were obtained after the removal of the volatiles and recrystallization from $MeCN\text{-}Et_2O$. It was characterized by ^{17}O NMR spectroscopy (Figure 7.17).

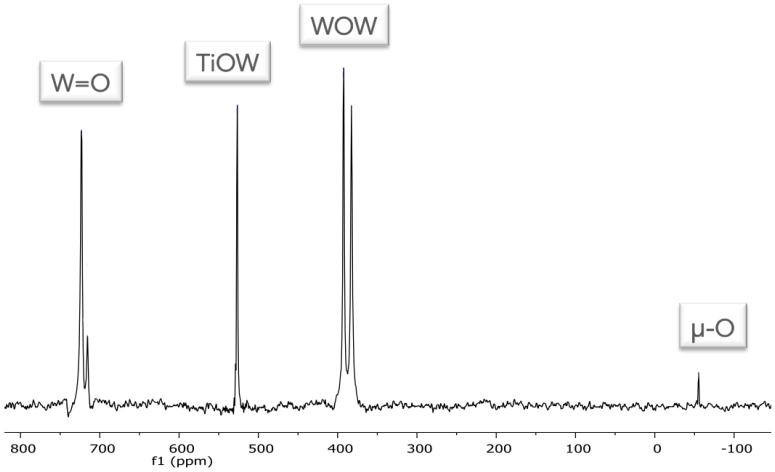

Figure 7.17. ^{17}O NMR spectrum of $(TBA)_3[(MeO)TiW_5O_{18}]$ in CH_3CN. Chemical shift: -58 ppm (μ-O), 380 and 390 ppm (WOW), 525 ppm (WOTi) and, 713 and 721 ppm (W=O).

The ^{17}O NMR spectrum shows four different oxygen environments. The central oxygen coordinated to six metals which is the most shielded with a value of chemical shift of -58 ppm; two types of terminal oxygen W=O, found at 713 and 721 ppm. Between these two regions, the signal corresponding to the bridging TiOW oxygens is found at 525 ppm. The two types of bridging WOW sites are responsible of two close peaks at 380 and 390 ppm.

As confirmed by DFT calculations, the hydrolysis of $[(MeO)TiW_5O_{18}]^{3-}$ leads to $(TBA)_6[(\mu\text{-}O)(TiW_5O_{18})_2]^{6-}$ rather than $[(HO)TiW_5O_{18}]^{3-}$. The hydrolysis takes place in acetonitrile with the stoichiometry shown in Eq. 7.2.

$$2[(MeO)TiW_5O_{18}]^{3-} + H_2O \rightarrow [(\mu\text{-}O)(TiW_5O_{18})_2]^{6-} + 2MeOH \qquad (7.2)$$

In the hydrolysis product, the peaks observed by ^{17}O NMR were consistent with the TiW_5 Lindqvist core structure. A peak at 676 ppm appears in the ^{17}O NMR spectrum (Figure 7.18), which was assigned to TiOTi, an indication of the formation of $[(\mu\text{-}O)(TiW_5O_{18})_2]^{6-}$. These facts are therefore consistent with calculations predicting that the product of hydrolysis of $[(MeO)TiW_5O_{18}]^{3-}$ is the $[(\mu\text{-}O)(TiW_5O_{18})_2]^{6-}$ anion instead of $[(HO)TiW_5O_{18}]^{3-}$.

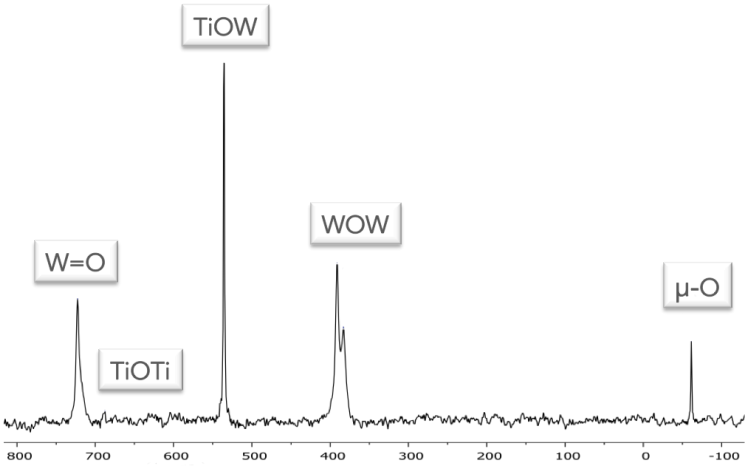

Figure 7.18. ^{17}O NMR spectrum of $[(\mu\text{-}O)(TiW_5O_{18})_2]^{6-}$ in CH_3CN. Chemical shift: -63 ppm (μ-O), 381 and 390 ppm (WOW), 534 ppm (WOTi), 676 pmm (TiOTi) and 720 ppm (W=O).

7.6.2. Synthesis and characterization of $(TBA)_4[(TiW_5O_{18}H)_2]$

The dimer $(TBA)_4[(TiW_5O_{18})_2]$ can be obtained from $(TBA)_3[ClTiW_5O_{18}]$ through a halide abstraction reaction. The halide was synthesized from the reaction between $(TBA)_3[(MeO)TiW_5O_{18}]$ and Me_3SiCl in acetonitrile, with the stoichiometry shown in Eq. 7.3.

$$(TBA)_3[(MeO)TiW_5O_{18}] + Me_3SiCl \rightarrow (TBA)_3[ClTiW_5O_{18}] + Me_3SiOMe \quad (7.3)$$

White crystals of $(TBA)_3[ClTiW_5O_{18}]$ appeared after recrystallization from MeCN-Et_2O. It is well known that halogenated POMs are useful precursors for different types of reactions such as hydrolysis, ligand metathesis, ligand abstractions and so on, providing a large variety of functionalized POMs. Hence, we took advantage of this reactivity to obtain $(TBA)_4[(TiW_5O_{18})_2]$ (Figure 7.19). We treated the $(TBA)_3[ClTiW_5O_{18}]$ with $AgBF_4$ with the aim of removing the chloride anion as AgCl, to generate $[TiW_5O_{18}]^{2-}$ with a vacant coordination site on titanium, which would dimerise to give $(TBA)_4[(TiW_5O_{18})_2]$ (Eq. 7.4). However, $(TBA)_4[(TiW_5O_{18})_2]$ is easily hydrolysed if traces of water are present in the solution (Eq. 7.5).

$$2(TBA)_3[ClTiW_5O_{18}] + 2AgBF_4 \rightarrow (TBA)_4[(TiW_5O_{18})_2] + 2AgCl + 2(TBA)BF_4 \quad (7.4)$$

$$(TBA)_4[(TiW_5O_{18})_2] + H_2O \rightarrow (TBA)_4[(\mu\text{-}O)(TiW_5O_{18}H)_2] \quad (7.5)$$

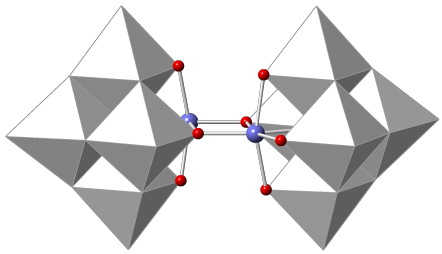

Figure 7. 19. Crystal structure of $(TBA)_4[(TiW_5O_{18})_2]$. Color code: Grey polyhedra-W, red-O and purple-Ti.

The ^{17}O NMR spectrum of the crystals obtained from reaction 7.4 is shown in Figure 7.20. No peak was observed for the TiOTi bridging oxygen, which was present in the spectrum related to $(TBA)_6[(\mu\text{-}O)(TiW_5O_{18})_2]$ (Figure 7.18), a circumstance that we attribute to the fact that this site is derived from H_2O that is not ^{17}O-enriched. However, all the peaks occur at significantly higher chemical shifts compared to those of $[(\mu\text{-}O)(TiW_5O_{18})_2]^{6-}$, indicating a lower charge on the oxometalate framework. Therefore, it is proposed that the product is the protonated one (Eq. 7.5), considering that there were some traces of water in the solution, as it can be seen in Figure 7. 20.

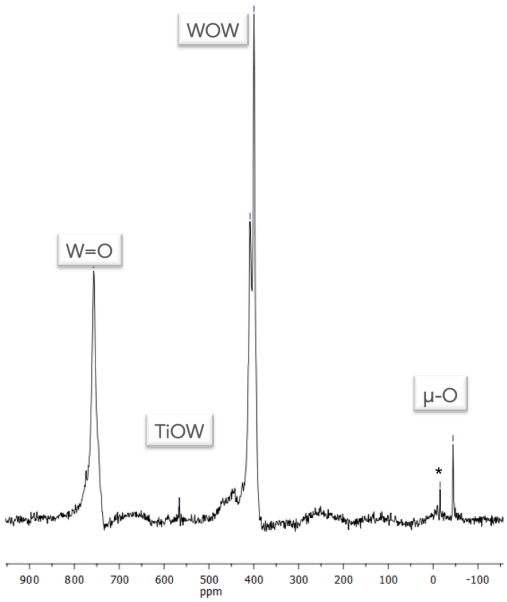

Figure 7.20. ^{17}O NMR spectrum obtained from the reaction between $(TBA)_3[ClTiW_5O_{18}]$ and $AgBF_4$ in CH_3CN. The H_2O peak is marked with an asterisk. Chemical shift: -45 ppm (μ-O), 399 and 408 ppm (WOW), 567 ppm (WOTi) and 756 ppm (W=O).

The protonated product of this reaction is of great interest since it confirms that some oxygens are prone to protonation. It is worth mentioning that one would expect that if a reaction with an electrophile takes place, the electrophile would be localized at the region where the protons are located. To confirm an existence of a nucleophilic region in the $[(\mu\text{-O})(TiW_5O_{18})_2]^{6-}$ anion, two different reactions were studied. First, an excess of water was added to the product obtained from the reaction between $(TBA)_3[ClTiW_5O_{18}]$ and $AgBF_4$ to complete reaction shown in Eq. 7.5. Secondly, $[(\mu\text{-O})(TiW_5O_{18})_2]^{6-}$ was reacted with two equivalents of HBF_4.

The ^{17}O NMR registered for both reactions is similar (Figure 7.21). The lack of the TiOTi signal in the protonation of $[(\mu\text{-O})(TiW_5O_{18})_2]^{6-}$ is due to the fact that this oxygen is not ^{17}O-enriched. Except for that peak, both spectra show the same chemical shifts, confirming that the product from the different pathways is the same. The chemical shifts are displaced to more positive values revealing that the charge is lower than for $[(\mu\text{-O})(TiW_5O_{18})_2]^{6-}$. Both suggested the formation of $[(\mu\text{-O})(TiW_5O_{18}H)_2]^{4-}$ anion.

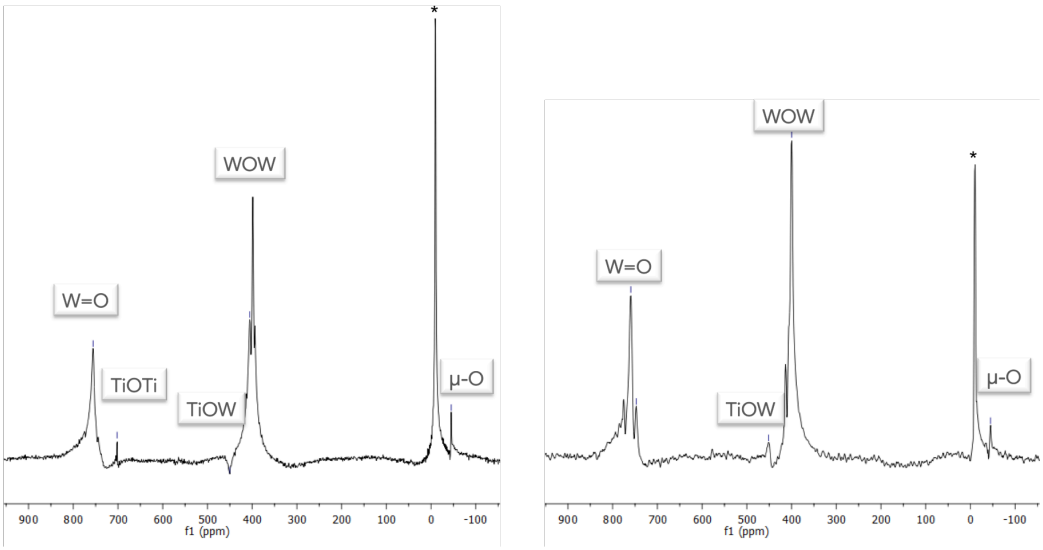

Figure 7.21. (Right) ^{17}O NMR spectrum obtained from the protonation of $[(\mu\text{-O})(TiW_5O_{18})_2]^{6-}$ anion. Peaks assigned to H_2O are marked with asterisks. Chemical shift: -45 ppm (μ_6-O), 405 ppm (WOW), 450 ppm (WOTi), 702 ppm (TiOTi) and 752 ppm (W=O). (Left) ^{17}O NMR spectrum obtained from the hydrolysis of the product obtained upon reaction with $(TBA)_3[ClTiW_5O_{18}]$ and $AgBF_4$ in CH_3CN. Chemical shift: -45 ppm (μ_6-O), 399 ppm (WOW), 452 ppm (WOTi) and 759 ppm (W=O).

Note that in the presence of H_2O, peaks due to TiOW are not well resolved, presumably due to exchange of the protons associated with TiOW. In the absence of H_2O, a peak is observed at 490 ppm, which corresponds to TiOW (Figure 7.22).

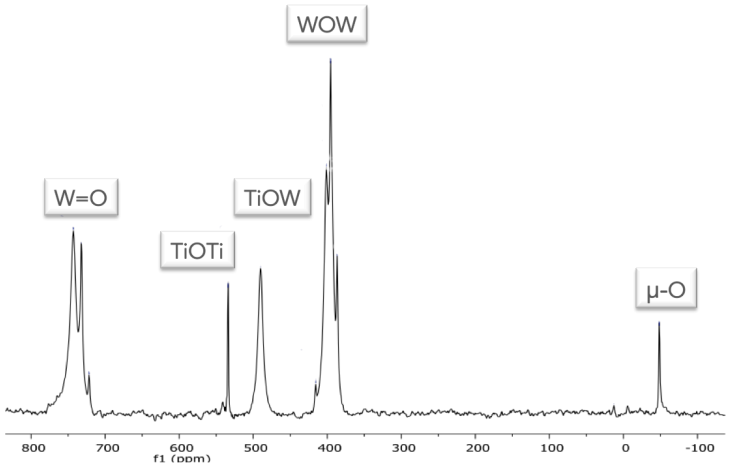

Figure 7.22. ^{17}O NMR spectrum obtained from the protonation of $[(\mu\text{-}O)(TiW_5O_{18})_2]^{6-}$ anion. Chemical shift: -48 ppm (μ_6-O), 387, 396 and 401 ppm (WOW), 490 ppm (TiOW), 743 and 732 ppm (W=O). Peaks at 534 and 721 ppm are starting material, $[(\mu\text{-}O)(TiW_5O_{18})_2]^{6-}$, and the peak at 415 ppm (W_6O_{19}) bridging oxygen.

In support of this proposal Dr. Errington's research group have characterized a compound with a dimethyl sulfoxide (DMSO) hydrogen bonded to $[(\mu\text{-}O)(TiW_5O_{18}H)_2]^{4-}$ (Figure 7.23). The structure consists of two protonated hexametalate tungsten cages structures, with titanium heteroatoms, which are linked by an oxygen bridge. DMSO then bridges the gap between the two-protonated oxygens of the hexametalate structures held by two hydrogen bonds. The crystal structure of the DMSO adduct $[(\mu\text{-}O)(TiW_5O_{18}H)_2(dmso)]^{4-}$ provides further evidence for protonation at the TiOW sites.

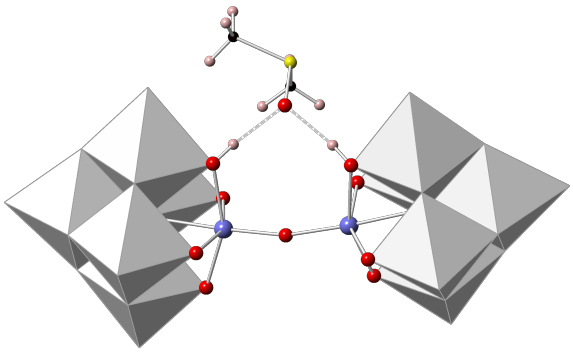

Figure 7. 23. Crystal structure of the dmso adduct $[(\mu\text{-}O)(TiW_5O_{18}H)_2(dmso)]^{4-}$. Color code: Grey polyhedra-W, red-O, purple-Ti, yellow-S, black-C and pink-H.

7.7. POMs as potential inorganic chelating or pincer ligands

The experiments mentioned in the previous section revealed that $[(\mu\text{-O})(TiW_5O_{18})_2]^{6-}$ anion has a nucleophilic region able *to trap* electrophiles. This led us to think that the reaction of $[(\mu\text{-O})(TiW_5O_{18})_2]^{6-}$ with an organometallic compound will result in a product where the organometallic framework will be placed in the same region as the protons were located upon reaction shown in Eq. 7.5. It is worth noting that the size of the organometallic framework is an important factor, which has to be optimal in order to fit into the *pocket*.

Preliminary results has showed that the reaction between $[(\mu\text{-O})(TiW_5O_{18})_2]^{6-}$ and Me_2SnCl_2 (Eq. 7.6) was successful and a crystal structure was obtained (Figure 7.24).

$$(TBA)_6[(\mu\text{-O})(TiW_5O_{18})_2] + Me_2SnCl_2 \rightarrow (TBA)_4[(\mu\text{-O})\{TiW_5O_{18}\}_2(Me_2Sn)] + 2(TBA)Cl \quad (7.6)$$

DFT calculations were performed in order to evaluate the structure. The most characteristic bond distances characterized by X-ray were rather well reproduced: Ti-O(Ti) 1.83 Å , O-Sn(O) 2.16 Å and 2.10 Å Ti-O(Sn).

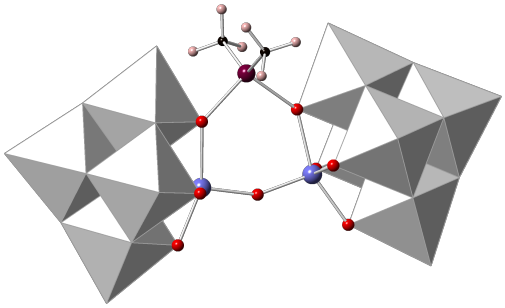

Figure 7.24. X-ray crystal structure of the anion $[(\mu\text{-O})\{TiW_5O_{18}\}_2(Me_2Sn)]^{4-}$. X-ray distances: Ti-O(Ti) 1.79 Å , O-Sn(O) 2.03 Å and 2.03 Å Ti-O(Sn). Color code: Grey polyhedra-W, red-O, light purple-Ti, purple-Sn, black-C and pink-H.

Moreover, analysis of the electronic structure revealed that the highest occupied molecular orbitals are combinations of mainly p atomic orbitals of bridging oxygens. The first seven unoccupied molecular orbitals (LUMO to LUMO+6) are localized over titanium and tungsten d-like orbitals. The LUMO+7 is localized over the tin atom, specifically at the 6s orbital, with some participation of the tungsten d orbitals (Figure 7.25).

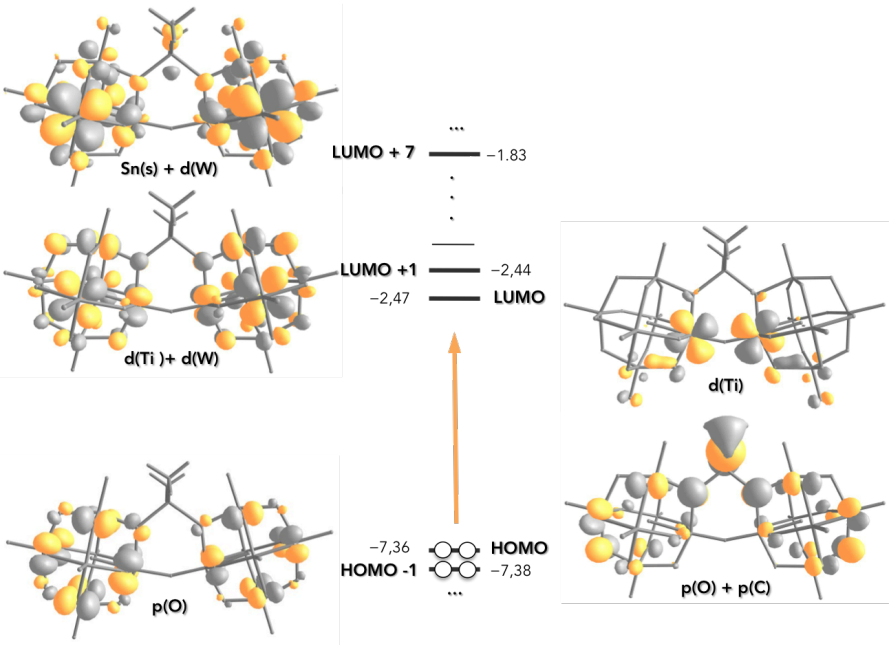

Figure 7.25. Electronic structure of $[(\mu\text{-O})\{TiW_5O_{18}\}_2(Me_2Sn)]^{4-}$ with circles representing electrons and values in eV. The 3D orbital images are those labelled in the scheme.

The $(TBA)_6[(\mu\text{-O})(TiW_5O_{18})_2]$ was treated with $CsAuCl_4$ to known if $\{AuCl\}^{2+}$ organometallic framework was optimal to fit the *pocket*. ^{17}O NMR spectrum of the reaction between $[(\mu\text{-O})(TiW_5O_{18})_2]^{6-}$ has shown that the chemical shifts are correspondent to a polyoxometalate structure with a smaller charge than the reactant. These preliminary results has evidenced that the reaction between and $(TBA)_6[(\mu\text{-O})(TiW_5O_{18})_2]$ $CsAuCl_4$ can be seen as Eq. 7.7.

$$(TBA)_6[(\mu\text{-O})(TiW_5O_{18})_2] + CsAuCl_4 \rightarrow (TBA)_4[(\mu\text{-O})\{TiW_5O_{18}\}_2(AuCl)] + 2(TBA)Cl + CsCl \qquad (7.7)$$

We have analysed the electronic structure of $[(\mu\text{-O})\{TiW_5O_{18}\}_2(AuCl)]^{4-}$ to examine its stability (Figure 7.26). The electronic structure revealed that the highest occupied molecular orbital from $\{AuCl\}^{2+}$ framework is localised at HOMO-11. The orbitals from HOMO-11 to HOMO are combinations of mainly p atomic orbitals of bridging oxygens. The first unoccupied molecular orbital (LUMO) is localized over the Au d-like orbitals, the Cl p-like orbitals and O p-like orbitals. The next unoccupied molecular orbitals (LUMO+1 to LUMO+3) are localized in titanium and tungsten d-like orbitals.

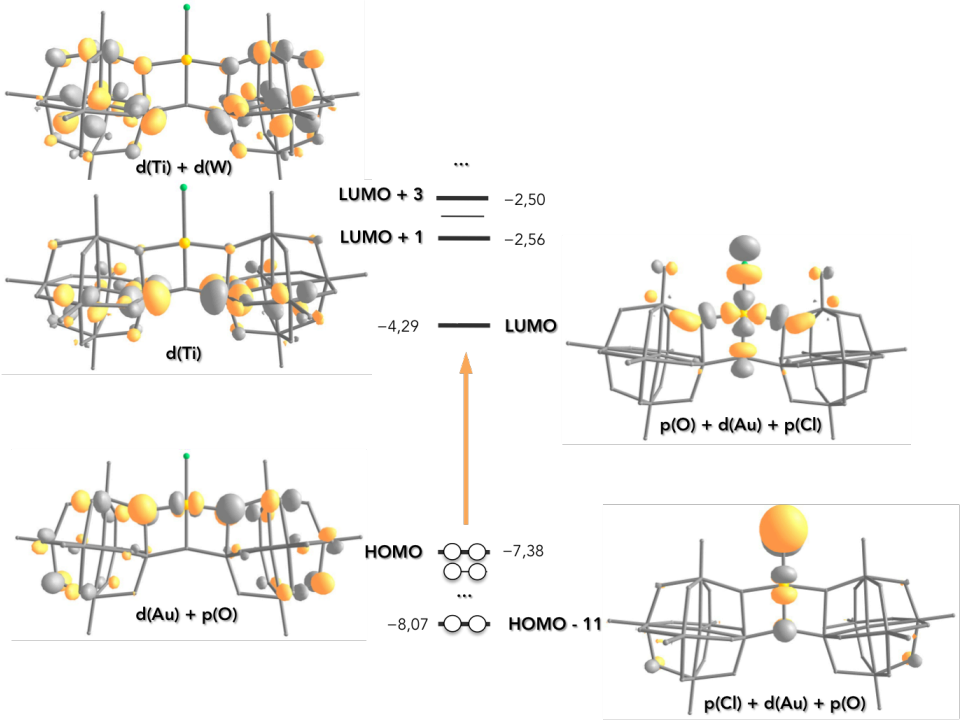

Figure 7.26. Electronic structure of $[(\mu\text{-O})\{TiW_5O_{18}\}_2(AuCl)]^{4-}$ with circles representing electrons and values in eV. The 3D orbital images are those labelled in the scheme.

7.8. Conclusions

The mechanism of protonolysis of different heterometallic Lindqvist and Keggin anions was thoroughly studied. An understanding of the comparative differences in behaviour between polyoxomolybdates and -tungstates is not complete, since our calculations predict the same mechanism in both cases. Moreover, substituted Ti- and Sn-substituted Lindqvist and Keggin polyoxotungstates were also compared. The experimental trends have been reproduced by calculations, and relative stabilities and energy barriers are in complete agreement with measurements. We have found that hydroxido-derivatives of titanium-substituted polyoxotungstates formed by hydrolysis of alkoxides dimerise readily by condensation. In contrast, oxido-bridged dimers of Sn-substituted polyoxotungstates are somewhat unstable and they are easily hydrolysed to the more stable hydroxido form.

In addition, two different pathways to the di-protonated form of $(TBA)_6[(\mu\text{-}O)(TiW_5O_{18})_2]$ were studied. We have found that the protonated form is stable and it is easily synthesized. This leads us to predict the behaviour of electrophiles when they interact with this class of oxo-bridged dimer. Consequently, we have been able to synthesize and analyse the structure of the anion $[(\mu\text{-}O)(TiW_5O_{18})_2Sn(CH_3)_2]^{4-}$ where an organometallic framework is placed in the *pocket* formed between the two $\{TiW_5O_{18}\}$ fragments. Moreover, the reaction between $(TBA)_6[(\mu\text{-}O)(TiW_5O_{18})_2]$ and $CsAuCl_4$ was attempted to know if $\{AuCl\}^{2+}$ was optimal to fit into the *pocket*. These behaviours provide the opportunity to construct a new family of functionalized POMs that can act as chelating or pincer ligands.

7.9. Bibliography

[1] *Polyoxometalates: From Platonic Solids to Anti-retroviral Activity*, Ed. M.T. Pope and A. Müller, Kluwer, Dordrecht, The Netherlands, **1994**.
[2] *Polyoxometalate Chemistry: From Topology via Self-assembly to Applications*, ed. M. T. Pope and A. Müller, Kluwer, Dordrecht, The Netherlands, **2001**.
[3] C. L. Hill, *Chem. Rev.* **1998**, *98*, 1.
[4] T. Kim, A. Burrows, C. J. Kiely, I. E. Wachs, *J. Catal.* **2007**, *246*, 370.
[5] I. E. Wachs, T. Kim, E. I. Ross, *Catal. Today* **2006**, *116*, 162.
[6] S. Eibl, B. C. Gates, H. Knözinger, *Langmuir* **2001**, *17*, 107.
[7] D. S. Kim, M. Ostromecki, I. E. Wachs, *J. Mol. Catal. A: Chem* **1996**, *106*, 93.
[8] F. Hilbrig, H. E. Göbel, H. Knözinger, H. Schmeiz, B. Lengeier, *J. Phys. Chem.* **1991**, *95*, 6973.
[9] O. A. Kholdeeva, R. I. Maksimovskaya, *J. Mol. Catal. A: Chem.* **2007**, *262*, 7.
[10] R. J. Errington, S. S. Petkar, P. S. Middleton, W. McFarlane, W. Clegg, R. A. Coxall, R. W. Harrington, *J. Am. Chem. Soc.* **2007**, *129*, 12181.
[11] R. J. Errington, S. S. Petkar, P. S. Middleton, W. McFarlane, W. Clegg, R. A. Coxall, R. W. Harrington, *Dalton Trans.* **2007**, 5211.
[12] R. J. Errington, G. Harle, W. Clegg, R. W. Harrington, *Eur. J. Inorg. Chem.* **2009**, 5240.
[13] R. J. Errington, L. Coyle, P. S. Middleton, C. J. Murphy, W. Clegg, R. W. Harrington, *J. Clust. Sci.* **2010**, *21*, 503.
[14] R. Bakri, A. Booth, G. Harle, P. S. Middleton, C. Wills, W. Clegg, R. W. Harrington, R. J. Errington, *Chem. Commun.* **2012**, *48*, 2779.
[15] L. Coyle, P. S. Middleton, C. J. Murphy, W. Clegg, R. W. Harrington, R. J. Errington, *Dalton Trans.* **2012**, *41*, 971.
[16] B. Kandasamy, C. Wills, W. McFarlane, W. Clegg, R. W. Harrington, A. Rodríguez-Fortea, J. M. Poblet, P. G. Bruce, R. J. Errington, *Chem. Eur. J.* **2012**, *18*, 59.
[17] W. Clegg, R. J. Errington, K. A. Fraser, S. A. Holmes, A. Schäfer, *Chem. Commun.* **1995**, 455.
[18] Y. Du, A. L. Rheingold, E. A. Maatta, *J. Am. Chem. Soc* **1992**, *114*, 345.
[19] H. Kwen, V. G. Young, E. A. Maatta, *Angew. Chem. Int. Ed.* **1999**, *38*, 1145.
[20] J. B. Strong, R. Ostrander, A. L. Rheingold, E. A. Maatta, *J. Am. Chem. Soc* **1994**, *116*, 3601.
[21] W. G. Klemperer, W. Shum, *J. Chem. Soc., Chem. Commun.* **1979**, 60.
[22] T. M. Che, V. W. Day, L. C. Francesconi, W. G. Klemperer, *Inorg. Chem.* **1992**, *31*, 2920.
[23] H. Akashi, J. Chen, T. Sakuraba, A. Yagasaki, *Polyhedron* **1994**, *13*, 1091.
[24] H. Akashi, J. Chen, H. Hasegawa, M. Hashimoto, T. Hashimoto, T. Sakuraba, A. Yagasaki, *Polyhedron* **2003**, *22*, 2847.
[25] M. J. T. Frisch, G. W.; Schlegel, H. B.; Scuseria, G. E.; Robb, M. A.; Cheeseman, J. R.; Scalmani, G.; Barone, V.; Mennucci, B.; Petersson, G. A.; Nakatsuji, H.; Caricato, M.; Li, X.; Hratchian, H. P.; Izmaylov, A. F.; Bloino, J.; Zheng, G.; Sonnenberg, J. L.; Hada, M.; Ehara, M.; Toyota, K.; Fukuda, R.; Hasegawa, J.; Ishida, M.; Nakajima, T.; Honda, Y.;

Kitao, O.; Nakai, H.; Vreven, T.; Montgomery, J. A., Jr.; Peralta, J. E.; Ogliaro, F.; Bearpark, M.; Heyd, J. J.; Brothers, E.; Kudin, K. N.; Staroverov, V. N.; Kobayashi, R.; Normand, J.; Raghavachari, K.; Rendell, A.; Burant, J. C.; Iyengar, S. S.; Tomasi, J.; Cossi, M.; Rega, N.; Millam, J. M.; Klene, M.; Knox, J. E.; Cross, J. B.; Bakken, V.; Adamo, C.; Jaramillo, J.; Gomperts, R.; Stratmann, R. E.; Yazyev, O.; Austin, A. J.; Cammi, R.; Pomelli, C.; Ochterski, J. W.; Martin, R. L.; Morokuma, K.; Zakrzewski, V. G.; Voth, G. A.; Salvador, P.; Dannenberg, J. J.; Dapprich, S.; Daniels, A. D.; Farkas, Ö.; Foresman, J. B.; Ortiz, J. V.; Cioslowski, J.; Fox, D. J. Gaussian, Inc., Wallingford CT, (2009).

[26] C. Lee, W. Yang, R. G. Parr, *Phys. Rev. B* **1988**, *37*, 785.

[27] P. J. Stephens, F. J. Devlin, C. F. Chabalowski, M. J. Frisch, *J. Phys. Chem.* **1994**, *98*, 11623.

[28] P. J. Hay, W. R. Wadt, *J. Chem. Phys.* **1985**, *82*.

[29] S. Miertus, E. Scrocco, J. Tomasi, *Chem. Phys.* **1981**, *55*, 117.

[30] R. J. Errington, *Advanced Practical Inorganic and Metalorganic Chemistry*, Blackie Academic & Professional, London, **1997**.

[31] X. López, C. Bo, J. M. Poblet, *J. Am. Chem. Soc.* **2002**, *124*, 12574.

[32] J. A. Fernández, X. López, J. M. Poblet, *J. Mol. Catal. A: Chem.* **2007**, *262*, 236.

[33] X. López, I. A. Weinstock, C. Bo, J. P. Sarasa, J. M. Poblet, *Inorg. Chem.* **2006**, *45*, 6467.

CHAPTER 8

Concluding Remarks

CHAPTER 8

Concluding Remarks

This last chapter is the endpoint of the project. It summarizes the most important achievements and conclusions presented along this thesis. As seen, the main goals have been reached and we have succeeded in most of the projects combining computational and experimental disciplines. On the other hand, we have also tackled very challenging projects and it has been complex to reach part of the objectives that we wished at the beginning.

The present thesis represents a step forward in the understanding of POMs' behavior. Different aspects of their unmatched chemistry have been tackled, from spectroscopic properties to reaction mechanisms. Taking advantage of the past experience accumulated at the computational level, the present work was performed searching high standards in accuracy. The first block of results, devoted to NMR properties, presents optimal computational strategies in this direction, whereas the last two chapters analyse in detail two interesting reactions. All in all, the field of POMs is in continuous progress, computational chemistry being a key interpreting and predicting source of knowledge.

Chapter 3. ^{17}O NMR Chemical Shifts in Oxometalates

It is worth mentioning that the principal objectives in this project were reproducing and rationalizing the factors affecting the ^{17}O chemical shifts The main conclusions arising from the extensive study of ^{17}O NMR developed are:

- A well-defined computational strategy based on DFT has been established for accurately computing ^{17}O NMR chemical shifts of oxometalates. The OPBE/TZP//PBE/TZ2P (NMR//optimization) combination gives the best results. The mean average errors can be reduced to ~26 ppm over a large set of compounds by means of a linear fitting after the calculation is performed.

- The principal factor of the ^{17}O NMR chemical shift is the paramagnetic contribution to the shielding, thus we have studied and interpreted the main factors governing it, namely the transitions from occupied orbitals to unoccupied ones, which have a higher oxygen contribution. The electronegativity of the metal linked to the oxygen is a key point in order to understand the chemical shift values.

- DFT helps understanding how important protonation is and how it must be properly taken into account to reproduce and correctly interpret $\delta(^{17}O)$ in oxometalates. When a molecule has many similar or equivalent oxygen sites that can accept an itinerant proton, the change in $\delta(^{17}O)$ signals is almost undetectable. On the other hand, when a molecule has very few distinctively basic sites, the proton gets trapped in one or a few sites and the change in $\delta(^{17}O)$ signals is more evident.

Chapter 4. ^{31}P NMR Calculations on Polyoxometalates

Following our objective of understanding NMR properties of POMs, we also propose a computational strategy for reproducing ^{31}P NMR chemical shifts. The conclusions acquired are:

- The study of the influence of the basis set and the density functional concluded that the best method for an accurate determination of $\delta(^{31}P)$ is using TZP/PBE for NMR calculation and TZ2P/OPBE for geometry optimization, very similar to ^{17}O NMR.

- The main variations in $\delta(^{31}P)$ come from the paramagnetic contribution, which is highly related to occupied-virtual transitions with P contribution. Thus, the variations in $\delta(^{31}P)$ are directly linked to the differences in the energy gap of those transitions. The smaller the gap, the higher the $\delta(^{31}P)$.

Chapter 5. Thalium(III) Containing POM: Structure and NMR

As introduced, the three groups working in this project succeeded to identify and characterize this thallium-containing POM. The conclusions that can be extracted of this project are:

- The thallium-containing POM has been structurally and electronically characterized by both computational and experimental disciplines.
- DFT calculations revealed that there are low energy differences between different di-protonated anions and, thus, the protons can be mobile. Moreover, the protons are linked to O_C in the solid state due to the inaccessibility to the other oxygen types, which are blocked by counter cations.
- The ^{205}Tl NMR chemical shifts are perfectly reproduced by DFT methodology. However, the spin-spin coupling between two thallium atoms is not as easy to reproduce and it is still some work to be done in this direction.

Chapter 6. Photochemical H_2 Evolution by an Iridium (III)-photosensitized Polyoxometalate

We have reported a DFT analysis on the photocatalytic H_2 evolution reported by Matt *et. al. in Energy Environ. Sci.* ***2013****, 6, 1504* is presented. We have studied in detail the relevant photosensitized POM reactant and the species formed during the proposed mechanism reaction. The principal conclusions of this project are:

- TD-DFT calculations confirm that, upon light excitation, electrons can be transferred from the [Ir] chromophore to the d(W)-like orbitals of the POM. The nature of these transitions and the orbitals involved are theoretically identified.
- We propose that the catalytic species for the H_2 evolution reaction is the two-reduced POM framework, which can transfer those electrons to protons to form the H_2.
- Calculations corroborate that POM orbitals are higher in energy in DMF compared to aqueous media, whereas the energy of the empty orbital H^+ are not dependent on the media. Thus, this is the key point for H_2 evolution in *our* conditions taking place more easily.

- Detailed understanding of how the electron transfer process from the two-electron reduced POM to the protons occurs is still a big challenge.

Chapter 7. Mechanistic Studies on Heterometallic Lindqvist and Keggin-type POMs

The mechanism of protonolysis for different heterometallic Lindqvist and Keggin POMs was studied. Moreover, some experimental data based on protonation are reported. Some conclusions can be extracted:

- The behavior of polyoxomolybdates and polyoxotungstates towards protonolysis is predicted to be the same by DFT calculations.
- The comparative study between the protonolysis mechanism of substituted Tin and Titanium Lindqvist and Keggin polyoxotungstates is in excellent agreement with experimental results.
- The protonated form of $(TBA)_6[(\mu\text{-}O)(TiW_5O_{18})_2]$ is stable and easily synthetized and this leads us to introduce a new family of POMs.
- The characterization of a POM acting as a chelating ligand is reported, which is $(TBA)_4[(\mu\text{-}O)(TiW_5O_{18})_2Sn(CH3)_2]$, where an organometallic framework is placed in the *pocket* which is formed between the two $\{M_5O_{18}\}^{6-}$ monomers

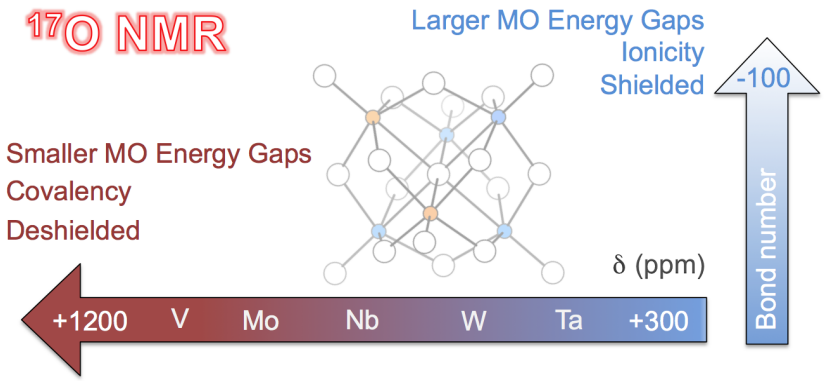

ANNEX A

^{17}O NMR Chemical Shifts in Oxometalates

Tables. All the data are in ppm. There were obtained 17 signals with each methodology. The MAE values are referred to the experimental values listed in parentheses in Table 3.3 of the main text (see references in the rightmost column). The missing values (×) were not calculated assuming that they hardly affect the MAEs of that site and, consequently, the average ones. This assumption arises from the values in Table A6, for which the complete study was carried out. The errors obtained are so similar that we decided to compute only one of these W_2O sites, that of Nb_2W_4.

Table A1. Computed ^{17}O chemical shifts with the B3LYP/TZP//B3LYP/TZ2P methodology.

Anion	M_6O	W_2O	MWO	M_2O	W=O	M=O
$[W_6O_{19}]^{2-}$	–57	499	–	–	842	–
$[Ta_2W_4O_{19}]^{4-}$	–41	×	477	464	×	633
$[Nb_2W_4O_{19}]^{4-}$	–41	449	507	572	757	805
$[V_2W_4O_{19}]^{4-}$	–20	×	608	1034	×	1348
MAE	24	77	75	92	67	119

Table A2. Computed ^{17}O chemical shifts with the PBE/TZ2P//PBE/TZ2P methodology.

Anion	M_6O	W_2O	MWO	M_2O	W=O	M=O
$[W_6O_{19}]^{2-}$	–23	459	–	–	749	–
$[Ta_2W_4O_{19}]^{4-}$	–1	×	467	459	×	631
$[Nb_2W_4O_{19}]^{4-}$	11	444	502	571	712	759
$[V_2W_4O_{19}]^{4-}$	–9	×	571	824	×	1046
MAE	58	54	54	41	24	61

Table A3. Computed ^{17}O chemical shifts with the BP86/TZP//B3LYP/TZ2P methodology.

Anion	M_6O	W_2O	MWO	M_2O	W=O	M=O
$[W_6O_{19}]^{2-}$	–30	497	–	–	790	–
$[Ta_2W_4O_{19}]^{4-}$	–18	×	469	466	×	642
$[Nb_2W_4O_{19}]^{4-}$	–13	445	501	572	713	572
$[V_2W_4O_{19}]^{4-}$	52	×	583	884	×	1140
MAE	59	74	60	42	19	14

Table A4. Computed ^{17}O chemical shifts with the PBE/TZP//B3LYP/TZ2P methodology.

Anion	M_6O	W_2O	MWO	M_2O	W=O	M=O
$[W_6O_{19}]^{2-}$	–32	490	–	–	784	–
$[Ta_2W_4O_{19}]^{4-}$	–18	×	468	465	×	640
$[Nb_2W_4O_{19}]^{4-}$	–13	445	501	555	711	759
$[V_2W_4O_{19}]^{4-}$	53	×	584	888	×	1139
MAE	61	70	60	38	15	15

Table A5. Computed ^{17}O chemical shifts with the PBE/TZP//PBE/QZ4P methodology.

Anion	M_6O	W_2O	MWO	M_2O	W=O	M=O
$[W_6O_{19}]^{2-}$	–41	488	–	–	790	–
$[Ta_2W_4O_{19}]^{4-}$	–26	×	466	460	×	636
$[Nb_2W_4O_{19}]^{4-}$	–20	443	500	572	717	764
$[V_2W_4O_{19}]^{4-}$	–34	×	575	830	×	1048
MAE	33	68	55	34	21	63

Table A6. Computed ^{17}O chemical shifts with the PBE/TZP//PBE/TZ2P methodology.

Anion	M_6O	W_2O	MWO	M_2O	W=O	M=O
$[W_6O_{19}]^{2-}$	–48	459	–	–	757	–
$[Ta_2W_4O_{19}]^{4-}$	–26	445	460	466	700	637
$[Nb_2W_4O_{19}]^{4-}$	–20	443	501	575	719	767
$[V_2W_4O_{19}]^{4-}$	–34	444	574	831	726	1049
MAE	31	58	55	37	28	52

Table A7. Computed ^{17}O chemical shifts with the OPBE/TZP//OPBE/TZ2P methodology.

Anion	M_6O	M_2O	$M'MO^c$	M'_2O	M=O	M'=O
$[W_6O_{19}]^{2-}$	–46	457	–	–	748	–
$[Ta_2W_4O_{19}]^{4-}$	–31	×	437	434	×	601
$[Nb_2W_4O_{19}]^{4-}$	–24	414	472	548	679	731
$[V_2W_4O_{19}]^{4-}$	–40	×	536	784	×	993
MAE	31	48	22	46	20	96

Table A8. Computed ^{17}O chemical shifts with the KT2/TZP//PBE/TZ2P methodology.

Anion	M_6O	W_2O	MWO	M_2O	W=O	M=O
$[W_6O_{19}]^{2-}$	–46	448	–	–	784	–
$[Ta_2W_4O_{19}]^{4-}$	–23	×	456	450	×	637
$[Nb_2W_4O_{19}]^{4-}$	–17	419	493	572	712	770
$[V_2W_4O_{19}]^{4-}$	–32	×	571	817	×	1038
MAE	34	36	50	38	15	71

Table A9. Computed ^{17}O NMR chemical shifts with the OPBE/TZP//PBE/TZ2P methodology.

Anion	M_6O	W_2O	MWO	M_2O	W=O	M=O
$[W_6O_{19}]^{2-}$	–52	445	–	–	732	–
$[Ta_2W_4O_{19}]^{4-}$	–30	432	452	443	700	612
$[Nb_2W_4O_{19}]^{4-}$	–23	430	491	563	696	749
$[V_2W_4O_{19}]^{4-}$	–39	430	563	808	702	1015
Partial MAE	27	40	41	41	24	76

Table A10. Computed (OPBE/TZP//PBE/TZ2P) and experimental ^{17}O NMR chemical shifts for compounds in Table 3.3.

Anion	M_6O	W_2O	WMO	M_2O	W=O	M=O
$[W_6O_{19}]^{2-}$	–52 (–80)	445 (413)	-	-	732 (772)	-
$[Mo_6O_{19}]^{2-}$	–33 (–32)	611 (563)	-	-	930 (933)	-
$[TaW_5O_{19}]^{3-}$	–38 (–71)	452 (394)	485 (426)	-	732 (732)	648 (666)
$[NbW_5O_{19}]^{3-}$	–30 (–67)	450 (393)	516 (456)	-	730 (731)	810 (799)
$[VW_5O_{19}]^{3-}$	–43 (–75)	451 (392)	597 (562)	-	734 (731)	1053 (1217)
$[Ta_2W_4O_{19}]^{3-}$	–30 (–40)	432	452	443 (454)	700	612
$[Nb_2W_4O_{19}]^{3-}$	–23 (–67)	430 (379)	491 (435)	563 (493)	696 (691)	749 (753)
$[V_2W_4O_{19}]^{3-}$	–39 (–65)	430 (378)	563 (530)	808 (848)	702 (687)	1015 (1162)
$[(MeO)SnW_5O_{18}]^{3-}$	71 (17)	443,455 (363,383)	428 (395)		713,670 (720,684)	
$[(MeO)ZrW_5O_{18}]^{3-}$	–12 (–58)	438,441 (385,377)	517 (484)		715,703 (711,691)	
$[(MeO)TiW_5O_{18}]^{3-}$	–17 (–58)	438,444 (380,390)	566 (525)		718,723 (721,713)	
$[(\mu\text{-}O)(TiW_5O_{18})_2]^{6-}$	–26 (–63)	441,448 (381,390)	576 (534)	759 (697)	721,717 (722,714)	
$[\{(\mu\text{-}HO)ZrW_5O_{18}\}_2]^{6-}$	–23 (–58)	435,444 (378,387)	530 (479)		711,700 (712,692)	
MAE	38	60	44	59	7	69

Table A11. Computed ^{17}O chemical shifts[a] for the Non-protonated ($V_{10}O_{28}^{6-}$) and two monoprotonated ($HV_{10}O_{28}^{5-}$) forms of the Decavanadate anion. The 28 oxygen positions are labeled in the Figure. The chemical shifts of the protonated oxygens in each case (two rightmost columns) are highlighted in bold.

	$V_{10}O_{28}^{6-}$	$HV_{10}O_{28}^{5-}$	
O label		O_C	O_B
1	108	113	166
8	790	827	814
9	826	826	833
10	826	832	827
11	785	828	803
12	498	509	526
13	498	533	556
14	785	**199**	816
15	499	516	572
16	784	832	788
17	784	807	805
18	499	521	**77**
19	994	1027	1010
20	995	1028	1019
21	1005	1032	1023
22	1005	1038	1031
27	108	158	166
28	791	810	814
29	827	837	834
30	826	851	827
31	785	801	804
32	785	799	816
33	785	806	789
34	784	804	805
35	994	1014	1009
36	994	1010	1018
37	1005	1026	1023
38	1005	1023	1031

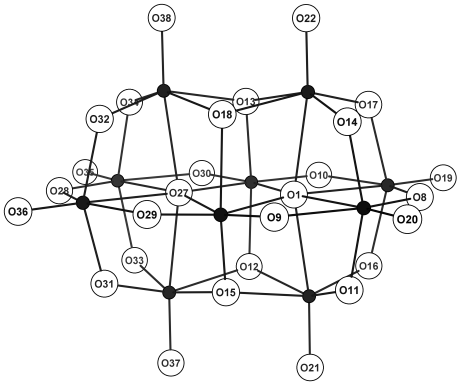

[a]Values in ppm.

List of publications

[1]. **^{17}O NMR chemical shifts in oxometalates: from the simplest monometallic species to mixed-metal polyoxometalates**

M. Pascual-Borràs, X. López, A. Rodríguez-Fortea, R. J. Errington and J.M. Poblet, *Chem. Sci.* 2014, 5, 2031.

[2]. **Accurate calculations of ^{31}P NMR chemical in polyoxometalates**

M. Pascual-Borràs, X. López and J.M. Poblet, Phys. Chem. Chem. Phys. 2015, 17, 8723.

[3]. **Synthesis, Structure, and Antibacterial Activity of Thallium(III)-Containing Polyoxometalate, $[Tl_2\{B\text{-}\beta\text{-}SiW_8O_{30}(OH)\}_2]^{12-}$**

W. W. Ayass, T. Fodor, Z. Lin, R. M. Smith, X. Xing, K. Abdallah, I. Tóth, L. Zékány, M. Pascual-Borràs, A. Rodríguez-Fortea, J. M. Poblet, L. Fan, J. Cao, B. Keita, M. S. Ullrich, U. Kortz, *Inorg. Chem.* 2016, 55, 10118.

[4]. **Computational insight into photochemical H_2 evolution by an iridium(III)-photosensitized polyoxotungstate.**

M. Pascual-Borràs, G. Izzet, A. Proust, X. López and J.M. Poblet. *(To be submitted)*

[5]. **Mechanistic studies on heterometallic Lindqvist and Keggin-type Polyoxometates**

D. Lebbie, B. Kandasamy, T. Izuagie, M. Pascual-Borràs, X. López, C. Wills, J.M. Poblet and R. J. Errington. *(To be submitted)*

Posters and Oral Presentations

^{17}O Chemical Shifts determination in polyoxometalates

XXIX Annual Meeting of the Reference Network of R+D+i on Theoretical and Computational Chemistry

Barcelona (Spain)-July 2013

Oral Presentation

^{17}O NMR Chemical Shifts: From monometallic species to metal-mixed polyoxometalates

Frontiers in Metal Oxide Cluster Science (FMOCS)

Paris (France)-July 2014

Oral Presentation.

Predicting NMR Parameters in POMs: Chemical Shifts and Coupling Constants

Novena Trobada de Joves Investigadors dels Països Catalans

Perpignan (France)-Febrary 2016.

Oral Presentation

Computational insight into photochemical H_2 evolution by an iridium(III)-photosensitized polyoxotungstate

Frontiers in Metal Oxide Cluster Science (FMOCS)

Newcastle (UK)-July 2016.

Poster Presentation

Mechanistic studies on heterometallic Lindqvist and Keggin-type Polyoxometates

Frontiers in Metal Oxide Cluster Science (FMOCS)

Newcastle (UK)-July 2016

Oral Presentation

Collaborations

Newcastle University
Dr. R. John Errington

Jacobs University
Dr. Ulrich Kortz

Sorbonne Universités, UPMC Université Paris06, Université Pierre et Marie Curie
Dr. Guillaume Izzet and Prof. Anna Proust

Research stay abroad

Projects	Electronic Effects in Heterometallic Lindqvist Hexametalates
Supervisor	Dr. R. John Errington
Center	Newcastle University
Period	September-December 2013 April 2016